Monographs of the School of Doctoral Studies in Environmental Engineering
8

Lagrangian trajectory analysis for the identification of moist airflows producing intense precipitation events over the Alps

Alessio Bertò

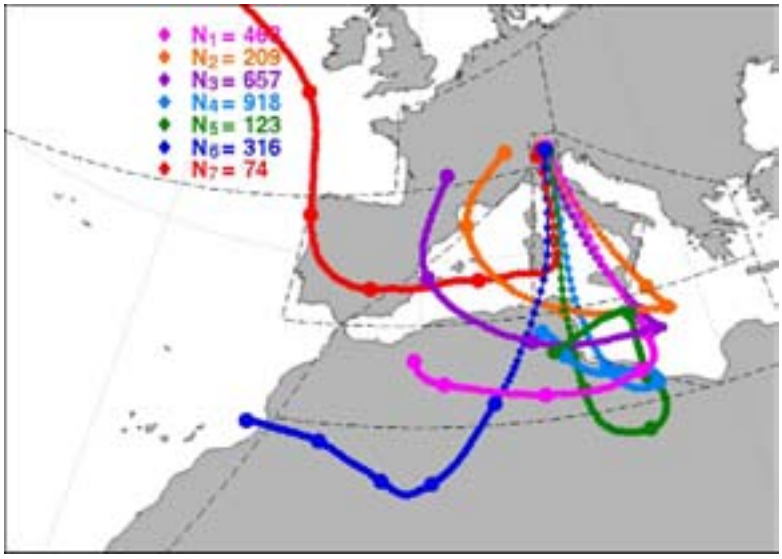

UNIVERSITÀ DEGLI STUDI DI TRENTO
Dipartimento di Ingegneria Civile e Ambientale

2005

Based on the Doctoral thesis in Environmental Engineering (XVII cycle)
defended in February 2005 at the Faculty of Engineering of the University of Trento
Supervisors: Dino Zardi and Andrea Buzzi

On the cover: Trajectory analysis for the historical flood event of 03-05 November 1966

Direttore della collana: Marco Tubino
Segreteria di redazione: Laura Martuscelli e Fabio Bernardi
Dipartimento di Ingegneria Civile ed Ambientale
Università degli Studi di Trento, Italia
Aprile 2005
ISBN: 88-8443-101-8

To my wife and my parents

Acknowledgements

This work has been supported by the Fondo Unico della Ricerca of the Provincia Autonoma di Trento under the project AQUAPAST. An acknowledgment to the European Center for Medium Range Weather Forecasting for providing analysis data and to ISAC-CNR of Bologna for providing the BOLAM model.

Many thanks to prof. Dino Zardi, dr. Andrea Buzzi and dr. Silvia Frisia for their help and comments. Special acknowledges go to Andreas Stohl, Paul James and Heini Wernli for their illuminating suggestions about the use of trajectory models. Stimulating comments and suggestions by Andrea Rossa were of great help in focussing on the problem.

Contents

List of Figures

List of Tables

1 Summary

The present work has been performed in the framework of the research project AQUAPAST. The main focus of AQUAPAST is the reconstruction of past climate changes in the Alpine and the Mediterranean regions based on the analysis of the isotopic content of cave speleothems in the Trentino Province.
This research is motivated by the need to study the climate of the past in order to understand and detect the causes of the climate changes we are witnessing today (ICCP, 2001), and, if possible, to provide the basis for simulating future scenarios by means of suitable global climate models (GCM). The interest of the scientific community in the climate changes of the past is proved by the increasing amount of papers (Ayalon et al., 1998; Baldini et al., 2002; McDermott et al., 2001; Genty et al., 2003), workshops and reports. In particular, the target of the climatological studies is to understand the climate response to both the natural (solar -Hansen et al., 1997-, volcanic and so on) and anthropogenic forcing (greenhouse gases -WMO, 1999-, sulfate aereosol). The most monitored variables to detect climate changes are air temperature and precipitation. Besides overall properties of the series of daily or monthly average of these variables the frequency of extreme values are investigated. The analysis can be refined by studying the evolution of the previous variables on a regional scale pointing out local variabilities in atmospheric and oceanic circulations: El Niño-Southern Oscillation (ENSO), Monsoons, the North Atlantic Oscillation (NAO), the Artic Oscillation (AO) and so on. In fact the project AQUAPAST aims also at relating the past climatological changes to modifications in the atmospheric circulation and in particular in the water vapour transport mechanism over the Mediterranean region.
The contribution of the present Thesis to the research project consists in setting up a methodology for the reconstruction and the analysis of the airstreams governing the transport of water vapour to the Trentino area. The technique requires as input the output of both global meteorological and climatological models. A testing phase was necessary whereby the methodology has to be applied to the study of strong precipitation events occurring in the last decades over the Alps.

The Alps affect atmospheric dynamics on a broad range of horizontal scales (as classified by

Orlanski, 1975), the most relevant ones ranging from the meso-α (e.g. lee cyclogenesis and modification of upper level troughs, Tibaldi et al., 1990), through meso-β (e.g. modification of fronts by orography, Hoinka et al., 1990; Buzzi and Alberoni, 1992) up to the meso-γ (e.g. circulations in individual valleys and inside individual clouds).
Recent studies, especially those developed in connection with the Mesoscale Alpine Programe (Bougeault et al., 2001), have focused on the synoptic-scale situations which are most likely to produce severe precipitation events in the southern Alpine region. The physical mechanism of orographic precipitation has been explored in depth (Buzzi et al., 2003; Gheusi and Stein, 2002; Medina and Houze, 2003; Rotunno and Ferretti, 2001, 2003). However, at present little is known about the relationship between detectable local and regional flow structures and the larger scale processes determining the moisture fluxes at lower atmospheric levels and the water vapour transport and evaluation at upper levels.
Isotopic composition of water can be used as suitable tracer to detect the origin of precipitating water. Measurements of the isotopic composition of precipitated water samples show that oxygen and hydrogen isotopes may vary considerably depending on the measurement location and the area where precipitating water originally evaporated (Longinelli and Selmo, 2003). The history of water vapour can be also evaluated from the meteorological analysis of data and from the reconstruction of trajectories associated with precipitating systems. Lagrangian analysis provides a method to understand the relationship between precipitation in a certain region and recurring specific meteorological features, such as PV-streamers (Massacand et al., 1998; Wernli et al., 2002) or peculiar interactions between large scale patterns of transport of water vapour in far regions where the air masses come from (Keil et al., 1999).

A detailed discussion on the motivations of the project AQUAPAST, as well as of the present work, is proposed in chapter 2, where the atmospheric mechanisms governing the water transport of vapour during cyclonic events are discussed in detail along with the method of Lagrangian analysis as an optimal way to understand them.
Chapter 3 provides a review of literature about the techniques of trajectory computation. In particular the various types of errors affecting the computation and their order of magnitude are estimated and discussed. As an example the numerous applications of the trajectory techniques to the long range pollution transport are briefly sketched. Finally an introduction is reported to the applications available so far in literature about this method to the transport of water vapour.
The choice of the case studies to test the Lagrangian analysis as well as the results from the computation of ensembles of back trajectories are shown in chapter 4. The selected events are the flood events of 3-5 November 1966, 16-18 November 2000 and 24-26 November 2002. Empha-

sis is given to the regional budget analysis over the Mediterranean basin and in particular to the estimation of the evaporation fluxes contributing to increase the moisture content of airstreams producing intense precipitation over the Alps during the selected events.
The identification of the flow patterns mostly contributing to precipitation requires suitable gathering of the ensemble trajectories into few most remarkable bundles. Clustering techniques applied to this purpose are presented in chapter 5. The attention here is mainly concentrated on the adoption of the most suitable phase space where trajectories can be represented as points and the "distance" between two trajectories is easily evaluated as the euclidean distance between the respective points. This allows for gathering similar trajectories of the ensemble to obtain a small number of clusters (cf. also Bertò et al., 2004).
Chapter 6 outlines comments and results deriving both from the budget and the cluster analysis and a conceptual model describing the airstreams flowing over the Mediterranean basin during extreme precipitation events is proposed. This provides a preliminary basis for the classification of meteorological situations producing intense precipitation events over selected target area in the Alps. Finally a preliminary test of the sensitivity of the trajectory method to the resolution of input data is reported.
The conclusions as well as possible future developments are summarized in chapter 7.

2 A general overview and formulation of the problem

In recent years it has been more and more frequent to hear about extreme precipitation events. The growing attention to these phenomena can be partially explained by the role of media in spreading information and to hit the sensitivity of the public. Indeed the frequency of tropical hurricanes, which are the most impressive among extreme events (in 2004 they caused a lot of damages in Japan, in the Caribbean islands and in the South of USA), is not increasing (ICCP, 2001). No appreciable variation has been ever registered in the number and in the intensity of the storms associated to the Indian monsoon affecting the South-East of Asia. On the contrary the ICCP stresses that a widespread increase in the heavy and extreme precipitation events has been found in regions where total precipitation has increased, e.g. the mid- and high latitudes of the Northern Hemisphere. This is the case of the flood event in the Central Europe in 2002 (Fig. 2.2, 2.1), of the flash floods in the western Mediterranean basin (in Morocco in 2002, in Spain and in the south of France in 2003, in Sardinia in December 2004) and of the severe storms hitting the Alps in the 90s (a summary can be found in CIPRA, 2002). As opposed to extreme precipitation events, frequent extreme drought events occurr. A remarkable case was provided by the summer of 2003 in Europe as well as by many winters without snow over the Alps in the '90s (CIPRA, 2002).

Figure 2.1: Region of the Central Europe interested by floods in the August of 2002

Figure 2.2: Flooded villages, factories and fields in the surroundings of Dresden in the August of 2002

Most of the engineering applications related to extreme weather events have connection with "civil protection". In fact, the evaluation of the intensity of extreme weather events corresponding to a specific return period is necessary to design the hydraulic structures and devices to be used for the protection of people and social or economic activities. On the other hand, knowing the frequency of occurrence of extreme or remarkable events is also crucial for the "water resource management". For example, in the case of an extreme precipitation event, it can be useful to know the V water reserve to meet the agricultural, energetic and human needs given a probability P of no more precipitation in the next n months.
However, the classical engineering approach based on the statistical analysis of the historical instrumental records shows some limits. Firstly, they could be not sufficiently long (especially for high return periods); furthermore they could be no longer useful since the sample results to be "old". The latter situation can occur because the "climate system has a weak structural stability with respect to the parameters which reflect the way the system is solicited by external forcing or by the boundary conditions" (Nicolis, 2003). For example a small perturbation of the temperature of the Gulf Current could lead to a sudden modification of the atmospheric circulation and of the climate over Europe. So if a climate change is really occurring today the instrumental records are no longer right for the engineering applications.
To understand whether a climate change is happening today the atmospheric circulation associated to different climatological periods of the past can be studied.

2.1 The project AQUAPAST

The present work has been performed and financed in the framework of the project AQUAPAST. AQUAPAST is a three-year project (2002-2004) coordinated by the Museo Tridentino di Scienze Naturali (dr. S. Frisia) and funded by the Fondo Unico per la Ricerca of the Province of Trento. The main focus of AQUAPAST is the reconstruction of past climate changes over the Alpine and the Mediterranean regions based on the analysis of the isotopic content of cave speleothems in the Trentino Province.
A cave is an isolated environment filtering the short term weather signal such as spurious effects. It is therefore an optimal site (Fig.2.3) to monitor the seasonal evolution of temperature, precipitation and many other physical and chemical quantities (e.g. CO_2 concentration).

The study of cave speleothemes, and in particular of stalagmites, provides further information about the climate of the past. Firstly the sequence of laminae (Fig.2.4) results to be a relatively easy and precise dating system. In fact it is possible to detect 2 different kinds of laminae for each year, especially in the caves close to the surface: a dark lamina whose color is caused by the loam

Figure 2.3: Sampling of dripping water in the cave of Giazzera cave (near Folgaria in the Province of Trento) during the project AQUAPAST. The cave is characterized by various forms of speoleothemes: small stalactites (hanging from the vault of the cave), stalagmites (rising up from the bottom) and some columns.

washed from the above terrain during persistent precipitation events, especially in autumn, and a translucent lamina, slowly growing in spring and summer due to water dripping produced by ice and snow melting.

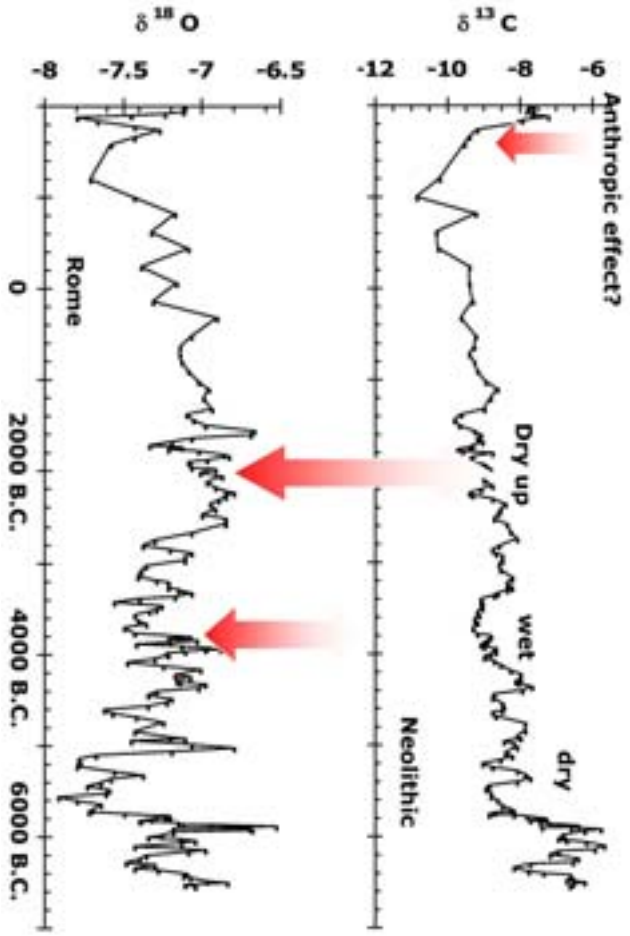

Figure 2.4: Example of stalagmite section taken away from the cave of Ernesto at the boundary between the Province of Trento and the Region of Veneto. The main scale factor is the centimeter.

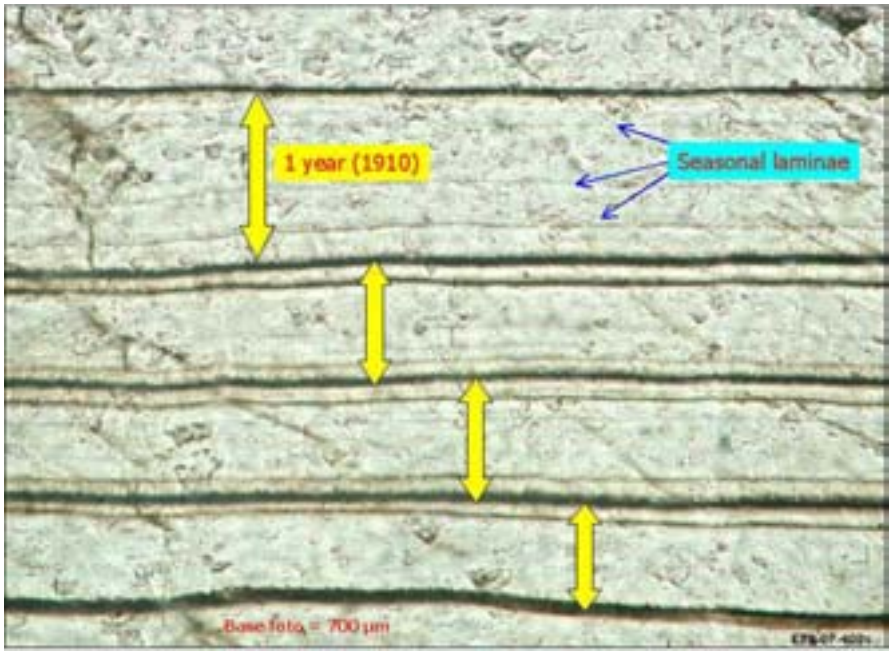

Figure 2.5: Example of seasonal laminae observed in the section of a stalagmite from the cave of Ernesto. The dark bands correspond to periods of persistent precipitation events when the loam is washed away from the above terrain by the seeping water.

Furthermore, the thickness of each lamina (Fig.2.5) gives information about the intensity of precipitation and about the indoor temperature in past times.
The isotopic concentration in each lamina results to be a complementary quantity to derive conclusions about the climate in past eras. The isotopic content of a sample is given by the δ-expression: this provides the isotopic concentration anomaly in the sample with respect to the concentration in standard (the *reference* content). Eq.2.1 exemplifies this definition with the formula used to quantify the concentration of the isotope 18 of oxygen (Frisia et al., 2004).

$$\delta^{18}O = \frac{\left(m^{18}O/m^{16}O\right)_{sample} - \left(m^{18}O/m^{16}O\right)_{reference}}{\left(m^{18}O/m^{16}O\right)_{reference}} \tag{2.1}$$

The evolution of the isotopic content of $\delta^{13}C$ and $\delta^{18}O$ can be derived from the chemical analysis of stalagmite.
Precipitating or melting water seeps into the soil and captures CO_2 forming a weak acid which dissolves the carbonates of rocks or the organic carbon of vegetation. When the water droplets reach the cave, the partial pressure of CO_2 in the cave air is less than in the solution. So CO_2 degasses and $CaCO_3$ precipitates contributing to the formation of a new lamina.
It is clear that $\delta^{13}C$ composition depends on the origin of the carbon in the carbonate of stalagmites. The $\delta^{13}C$ is almost zero if the carbon derives from the surrounding rocks or atmosphere, while the heavy isotopic concentration is depleted ($\delta^{13}C$ = -27 ‰) if it derives from plants organic carbon. The $\delta^{18}O$ composition is determined by:

(a) the oxygen isotopic concentration of the water dripping from the cave ceiling

(b) the cave temperature

For any value of $\delta^{18}O$ in dripping water the equation governing the isotopic content in the stalagmite is:

$$t = 16,9 - 4,2\left(\delta_{18}O_{carb} - \delta_{18}O_{water}\right) + 0,13\left(\delta_{18}O_{carb} - \delta_{18}O_{water}\right)^2 \tag{2.2}$$

where t is the temperature in centigrade degrees. Note that the higher is the temperature in the cave, the most depleted is the isotopic concentration in the cave speleothemes.
In Fig.2.6 the evolution in time of $\delta^{13}C$ and $\delta^{18}O$ is reported from the analysis of a stalagmite in the Ernesto cave (in Eastern Trentino, at the boundary with Veneto region). Starting from the correlation of the two signals one can hypothesize the climate changes in the past eras in the area of the cave (Frisia et al., 2004).
The objective of AQUAPAST is not only the analysis of the stalagmite records. The project also aims to relating the past climatological changes to modifications in the atmospheric circulation

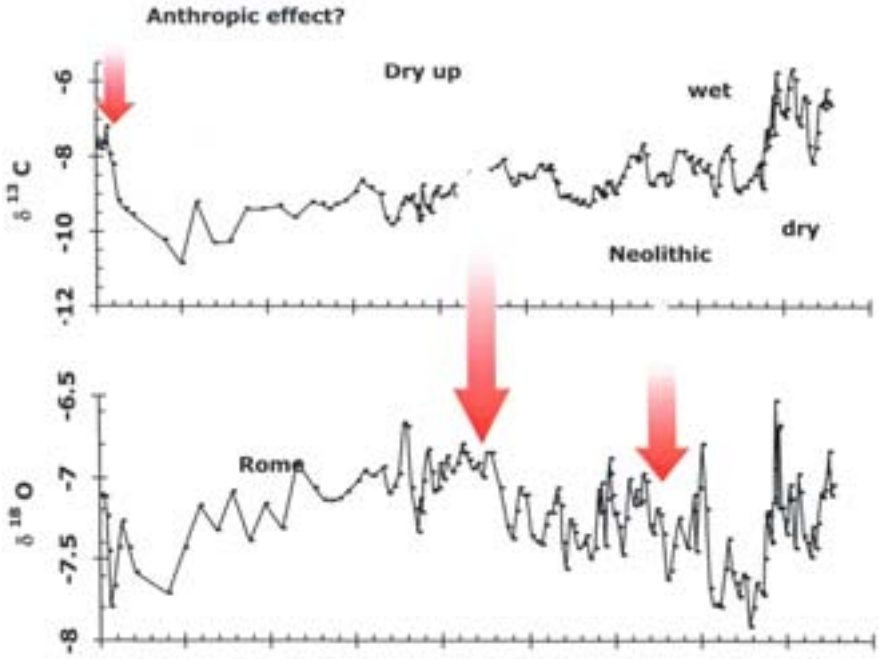

Figure 2.6: Trend of the isotopic content of $\delta^{13}C$ and $\delta^{18}O$ from the analysis of the stalagmite of the Ernesto cave. Possible interpretations of the correlation or of the anticorrelation between the two signals (Frisia et al., 2004).

and in particular in the water vapour transport mechanism over the Mediterranean area. In fact, beside the indoor temperature and the chemical reactions in the terrain, the isotopic concentration of $\delta^{18}O$ in the carbonate of cave speleothemes depends on the isotopic content in the precipitation parcels. In turn, $\delta^{18}O$ in the water vapour producing precipitation is determined by the type of water sources ($\delta^{18}O$ is equal to zero or lightly negative over the Atlantic Ocean, equal to -5 $\%_o$ over the Mediterranean Sea, strongly negative over the mainland) and on the temperature of condensation along the trajectory of the cloud fronts.

In fact Longinelli and Selmo (2003) showed that the distribution of the mean isotopic content in the precipitated water over a time period of 1-8 years in the '90s is strongly correlated to the orography of the Italian peninsula (Fig.2.7). It seems to confirm the dependence of the isotopic signal on the average height (and temperature) at which water vapour condenses producing precipitating water Ayalon et al. (1998).

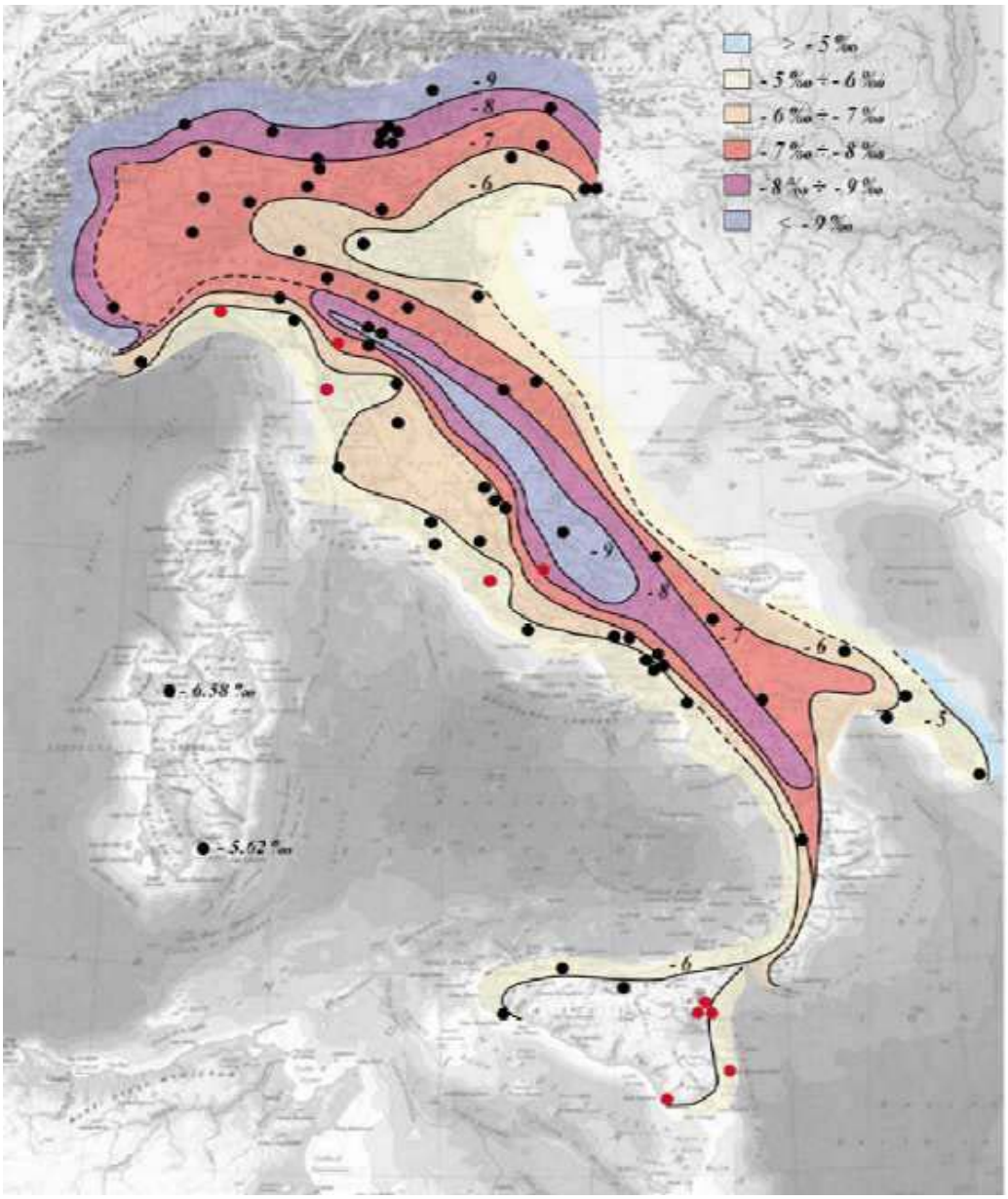

Figure 2.7: Spatial distribution over the Italian peninsula of the mean isotopic content in the precipitated water (Longinelli and Selmo, 2003). The $\delta^{18}O$ concentration is equal to -5 $\%_o$ along the coasts and it decreases almost linearly with ground elevation.

To understand the climatological influence of the atmospheric circulation on the isotopic signal in speleothemes the path of single air parcel should be monitored. This can be done by means of a suitable trajectory model, starting from the output of the Global Climate Models. The present

work aims at setting up a methodology for the reconstruction and analysis of the air mass trajectories governing the transport of water vapour.
The Lagrangian procedure has been developed and applied to recent precipitation events. Moreover, a sampling network (Fig.2.8) has been set up in Trentino during the entire duration of the project (2002-2004) to compare the results of the numerical model with the $\delta^{18}O$ content in collected samples of precipitating water.
As an example, the average monthly isotopic signal in precipitated water is reported for November 2002 and November 2003 in Fig. 2.9. In November 2003 the isotopic concentration is lower than in November 2002 (Fig.2.9). The difference has to be related to the origin of the air masses: in November 2002 the southerly slopes of the Alps were affected by Mediterranean cyclonic systems driving air masses from the South-West. In November 2003 they were hit by east-southeasterly winds originating in the regions of Eastern of Europe. So in November 2003 the mean condensation temperature over the North of Italy was lower than in 2002, but the air masses were already driving from the East water vapour with a weaker continental isotopic signal.
Note that the climatological analysis of the water vapour mechanisms should also explain the atmospheric anomalies expressed by the NAO index (Fig.2.10).

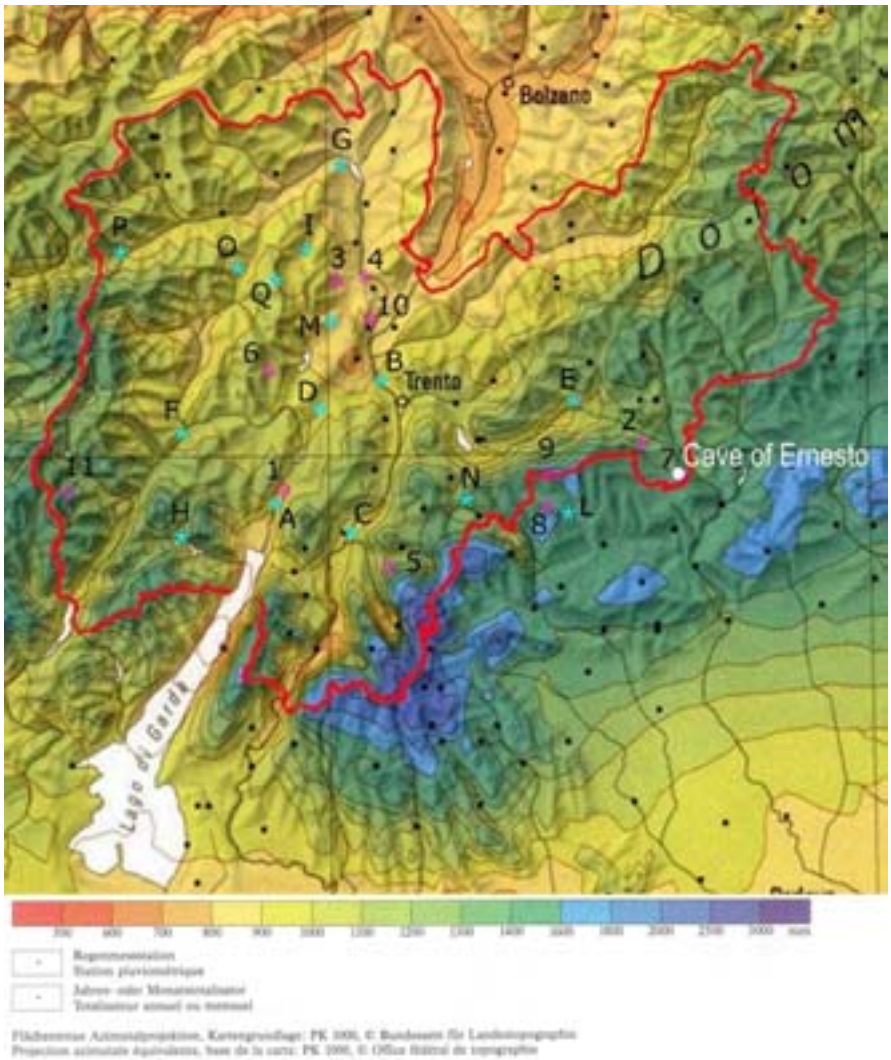

Figure 2.8: Climatological map of the average yearly precipitation ((Frei and Schär, 1998)). The dark blue color corresponds to a daily precipitation larger than 2500 mm; the dark green color larger than 1400 mm; the yellow-ocher color larger than 700 mm. Minima of 500 mm are registered in the Adige valley near Egna-Ora, maxima of 3500 mm over the Monti Lessini. The light blue asterisks mark the positions of the meteorological stations used for the monthly sampling of the precipitation water during the project AQUAPAST (Frisia et al., 2004). The magenta asterisks mark the positions of the monitored caves.

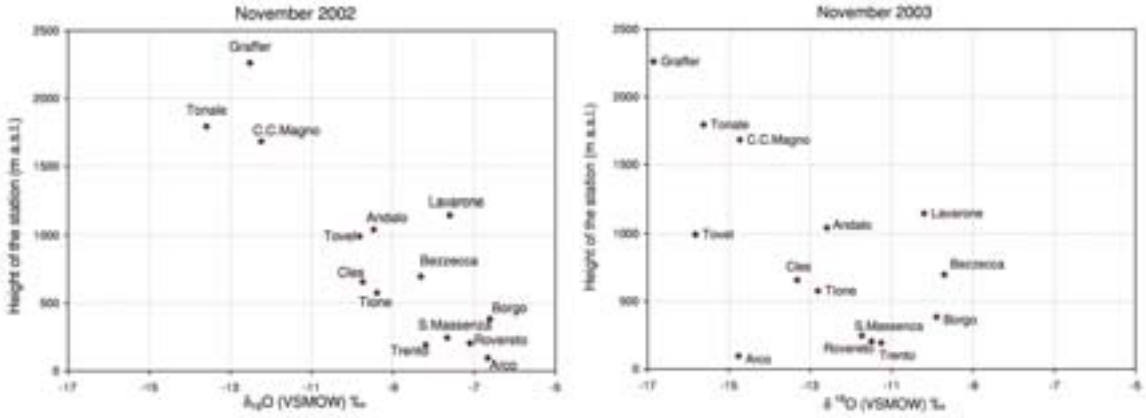

Figure 2.9: Plot of the mean monthly isotopic concentration in the precipitated water against the altitude of each meteorological station (Fig.2.8) for November 2002 and for November 2003

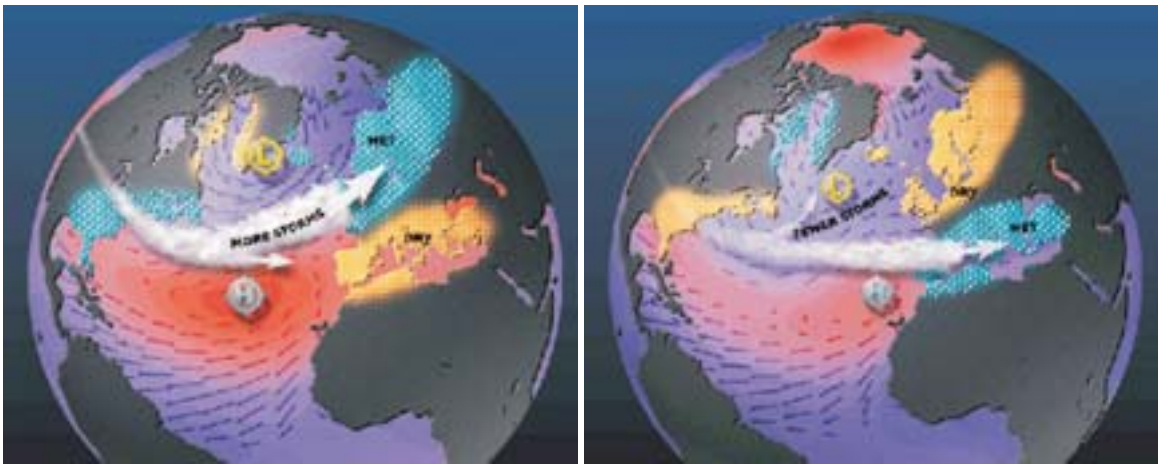

Figure 2.10: Atmospheric circulation and distribution of the precipitation over Europe and over the North Atlantic Ocean during the periods of positive and negative NAO. The positive pressure anomaly over the North Atlantic favours the zonal flow, while a negative anomaly produces a deepening of the North Atlantic through centers.

The positive pressure anomaly (NAO+) over the North Atlantic Ocean favours the zonal flow with precipitations over the north of Europe, while a negative anomaly (NAO-) produces a deepening of the North Atlantic through centers enhancing the probability of floods in the western Mediterranean basin. In the report of ICCP (2001) it is shown that in the last 3 decades Europe

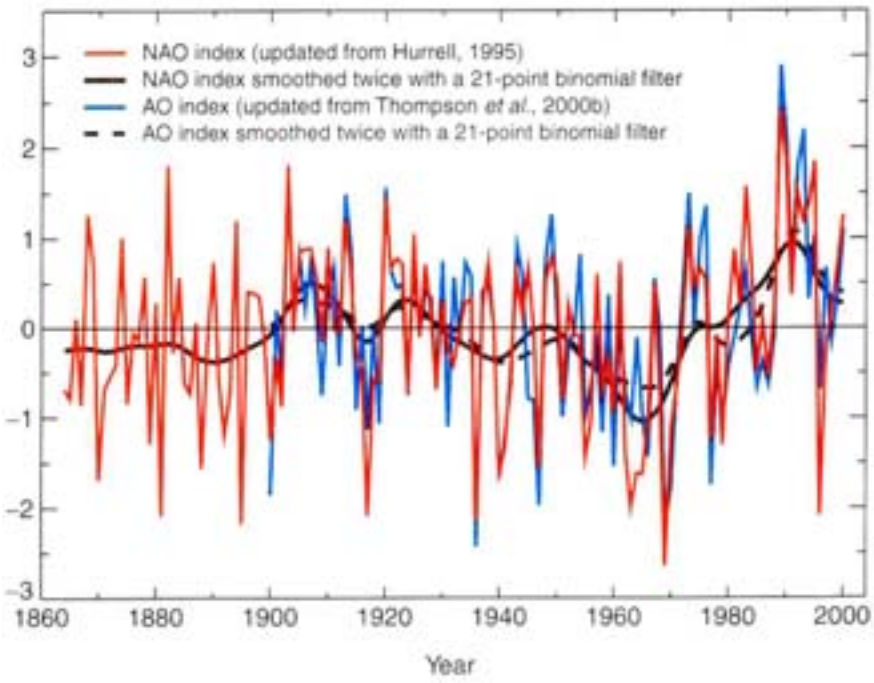

Figure 2.11: December to March North Atlantic Oscillation (NAO) indices, 1864 to 2000, and Arctic Oscillation (AO) indices, 1900 to 2000 (ICCP, 2001).

has been characterized by a dominant positive NAO signal (Fig. 2.11).

2.2 Large scale forcing of the water vapour transport

In the present section some studies are presented about the synoptic scale mechanisms forcing the transport of water vapour. These studies aim to reconstruct the water budget on a global scale or, at least, on the scale of the northern hemisphere. Moreover they outline the way some intense meteorological events (tropical storms) can influence the precipitation regime over the Mediterranean basin.

2.2.1 Tropical storms

Some authors have recently investigated the role of tropical storms in contributing to extreme weather events over the Mediterranean region (Pinto et al., 2001; Reale et al., 2001). Pinto et al. (2001) considered the 30 most extreme events from 1958 to 2000 over Northwest Italy monitoring their relationship with concomitant disturbances. Three different types of influences were proposed after the climatological analysis (see figure 2.12):

A. A tropical system recurves over the Central North Atlantic and, after extratropical transition, moves directly into the Western Mediterranean Basin (direct influence).

B. A tropical system recurvs over the Western or Central North Atlantic. The systems undergoes a transition in an extratropical system cyclone, inducing strong humidity advection from the subtropics to the extratropics, and part of the moisture is advected across the Atlantic over the Central North Atlantic (indirect influence).

C. A tropical system, recurving near the US East Coast, connects with an approaching upper-tropospheric mid-latitude trough. The extreme temperature contrasts between the tropical and the extra-tropical air masses lead to a strong baroclinic development which induces the development of a trough-ridge-trough system over the Atlantic. The eastern trough over the Iberian Peninsula is located at the optimal geographical position to induce a south-westerly flow from the Eastern Atlantic near coasts of Morocco into the Mediterranen (remote influence).

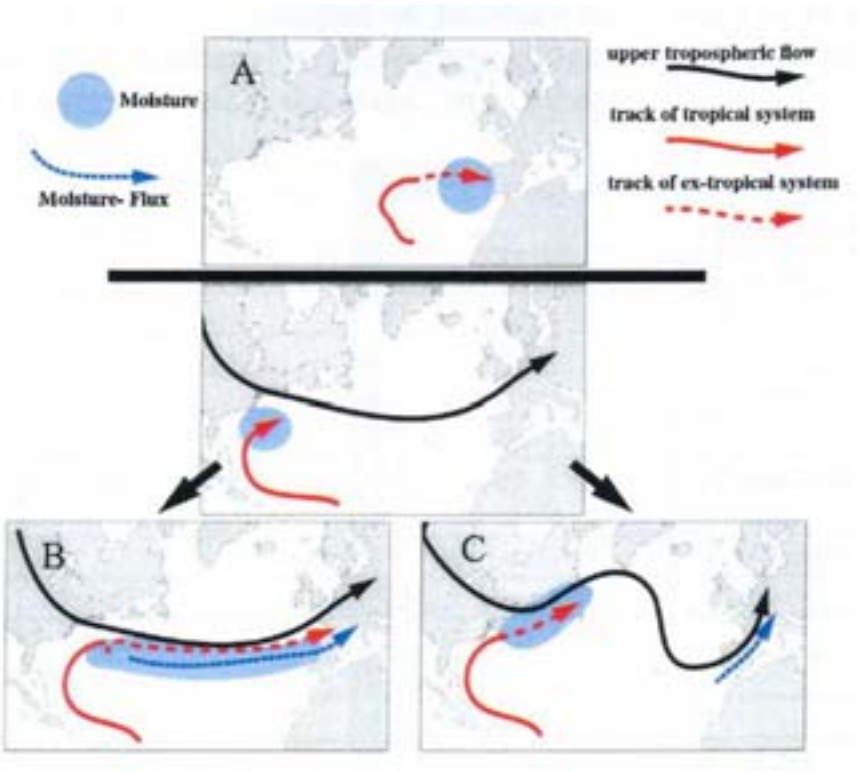

Figure 2.12: Basic mechanism of extratropical-extratropical interaction related to extreme precipitation events over the western Mediterranean Basin. Upper panel (case A), bottom left panel (case B), bottom right panel (case C). From Pinto et al. (2001).

The influence type *A*. happens quite rarely; types *B*. and *C*. are the most common. The last case (*C*.) can justify the unusual deepening of a subtropical upper level through over the eastern Atlantic reinforcing the tropical plumes flowing along the Africa coasts, marked by a dashed arrow in the scheme of Pinto et al. (2001).

2.2.2 African tropical plumes

Other large scale features conditioning both the cyclogenesis and the cyclone deepening over the temperate regions are the tropical plumes (TPs). They are evident as white quasi-stationary features (either in the $Infrared$ (I) images as bands of mid- and upper-level clouds -see figure 2.13- or in the $WaterVapour$ (WV) images as streams of moist air masses) having a lenght of several thousand kilometers and extending poleward and eastward from the tropics into the subtropics where the band typically recurves anticyclonically (McGuirk et al., 1987). TPs are common feature of tropical-extratropical interactions troughout the tropics, but they are particularly frequent

over the eastern Pacific and the central Atlantic (Iskenderian, 1995) and often occur in the transition seasons (Kuhnel, 1989). These areas are well known as westerly ducts, where both westerlies and transients from the midlatitudes are common. Knippertz et al. (2002) have investigated the

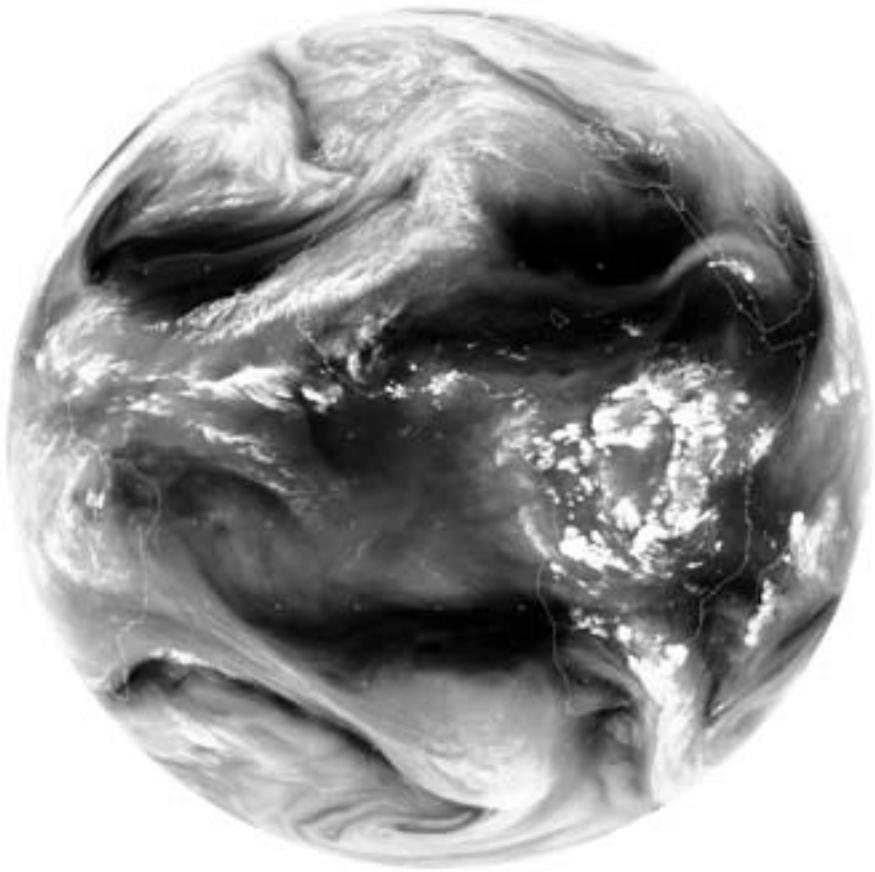

Figure 2.13: Meteosat WV satellite image at 1500 UTC 23 November 2002. A TP is evident over Mauritania, Morocco and Algeria, while a midlatitude moist stream stretches over the Atlantic. Both air streams seem to contribute to the subsequent cyclogenesis over the Mediterranean Sea.

evolution of African TPs flowing northward and eastward over the coasts of north-west Africa (Mauritania and Morocco) showing that the TPs are closely related to the development of pronounced upper-level troughs in the subtropical jet (STJ) at a latitude of 20° N -30° N. In summer (June-August) upper level subtropical highs over Africa and the Atlantic build a high pressure belt suppressing tropical-extratropical exchanges. The autumnal formation of troughs is not extraordinary because of the reinforcement of the STJ (with Rossby waves inside it favouring the equatorward amplification and the zonal contraction of the jet) and the northernmost position of the intertropical convergence zone (ITCZ) at this time. The peculiar element is the quasi-stationarity

of some troughs (centred at 35°W) favouring a persistent moist stream on their eastern side characterized by anomalous high wind speeds at upper levels (250 mbar) (Kuhnel, 1990). Rarely the through can deepen contrasting the low level north-easterly trade (Wallace and Hobbs, 1977) and modifying the dry, isentropic and hot Saharian PBL; more often it evolves into an extratropical western Mediterranean cyclone at the end of its life. Trajectory analysis of Knippertz et al. (2002) and Fink and Knippertz (2003) suggests that high levels clouds (300 -400 mbar) originate from the tropical Atlantic Ocean and are advected in south-west to north-east direction. On the contrary, the mean levels plume (700-400 mbar) originates over Central Africa in the ITCZ zone from the outflow of convective systems triggered by the African easterly waves, flows anticyclonically over the West Africa and converges in the TP over Morocco.
Knippertz et al. (2002) analysed rainy episodes in the southern foothills of the Atlas Mountains where the convection was initiated, inside the moist plumes, by large scale convergence due to the baric configuration and by the triggering orographic effect of the mountains. Unfortunatelly that they did not concentrate on cases of interaction of the upper level subtropical troughs (with their TPs) either with midlatitude troughs moving into the Mediterranean from the Atlantic or even with the polar jet (Ziv, 2001), which could be of some relevance for the present aims.

2.3 Extratropical cyclones and the Lagrangian viewpoint

Besides the very large scale forcing depicted in the previous section the basic focus of the present work is the reconstruction of the water budget over a large portion of the Mediterranean basin. In fact on a regional scale the transport of water vapour producing precipitation over the Alps is strictly related to the dynamics of the cyclones affecting the westerly and central part of the Mediterranean regions.
The heterogeneous kinematic features of airstreams forming an extratropical cyclone are the reason for its complex evolution. In fact the whole low system moves with a mean horizontal velocity of 0-15 m/s, but the cyclone shows a complicated 3D structure with respect to the low center with various airstreams at different levels and in different sectors. Some regions are characterized by strong vertical lifting of airmasses.

2.3.1 Analysis of extratropical cyclones in the literature

Different types of analysis have been applied to characterize extratropical cyclogenesis case studies. The first type is based upon the potential temperature (θ) and potential vorticity (PV) perspective and wants to recognize the influence of distinct flow features (PV anomalies) on the evolution of a cyclone system (Hoskins et al., 1985; Stein and Alpert, 1993). The second approach is based

on the omega equation which sheds light on the vertical motion fields (Hoskins et al., 1978; Keyser, 1994; Clough et al., 1995). Finally a third type seeks to identify physically and dynamically significant airstream patterns (Browning, 1990; Carlson, 1991). The Eulerian viewpoint is suitable to deal with the fixed coordinates of most observing systems, to analyse the atmospheric flow systems (fronts, cyclones and anticyclones), since they are characterized by spatially coherent structures that evolve smoothly in time, and to predict their evolution by means of numerical models. On the contrary, the Lagrangian framework is suitable to the asynoptic non routine airflow-tracking measurements. Furthermore it allows for the characterization of homogeneous but convoluted forms inside the flow motion. Although there is more uncertainty regarding the existence of temporally coherent Lagrangian structures within synoptic systems, the Lagrangian framework is more physically based, as it stems from the view point of "Classic Mechanics".

Early studies of surface measurements (Dove, 1840; Fitzroy, 1863) pointed to the existence of distinct air currents and airmasses within synoptic systems. Analysis of the path of an isolated volume of air and calculations of surface trajectories associated with low pressure systems (Shaw, 1903; Shaw and Lempfert, 1906) served to emphasize the occurrence of distinct airmasses and revealed significant bands of flow convergence and divergence. These same Lagrangian notions also featured prominently in the development of the classical Bergen frontal model (Bjerknes, 1919).

Later isentropic Lagrangian analyses suggested the existence of dry descending and moist ascending tongues of air insight cyclones and anticyclones (Rossby, 1937; Namias, 1939). Several studies (Rossby, 1945; Palmén, 1953; Danielsen, 1980; Young et al., 1987) have contributed to describe the descending tongues, commonly assuming a hammer head shape to the west of the surface cyclone and called *cold conveyor belts*. Other contributions (Green et al., 1966; Harrold, 1973; Browning and Mason, 1981) provided a detailed analysis of the ascending tongues assuming a narrow elongated form ahead of the cold fronts and called *warm conveyor belts*. The cold conveyor belt can be either rearward-sloping or forward-sloping depending on their relative movement with respect to the cold front (Fig.2.14).

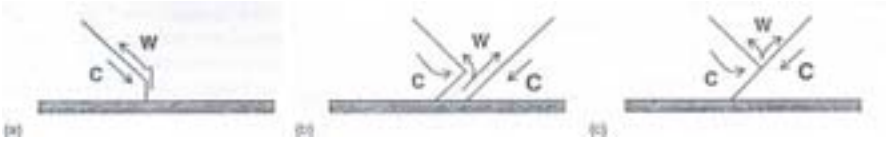

Figure 2.14: Relative motion of cold (C) and warm (W) air masses along the section of a rearward-sloping cold front (a), of a forward-sloping cold front lying just behind a warm front (b) and of an occluded front (c).

2.3.2 The scheme of cyclone proposed by Browning and Roberts (1994)

In the 90s much work was devoted to investigate the structure and dynamics of extratropical cyclones, starting from the publication of the Palmén Memorial Volume (Newton and , Eds.) which was a combination of theoretical, observational and modelling approaches. Later a synthetic analysis scheme was proposed by Browning and Roberts (1994). Their scheme was obtained from the diagnosis of a mid-latitude cyclone over the Eastern Atlantic Ocean, which did not undergo "explosive cyclogenesis" (i.e. 24mb in 24h) according to the definition of Sanders and Gyakum, 1980 but nevertheless showed many of the characteristics of major cyclones (Uccellini, 1990).

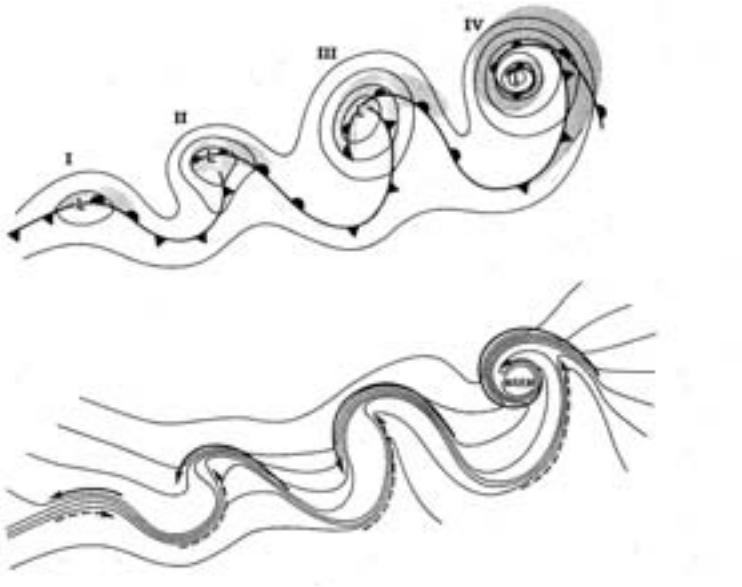

Figure 2.15: Conceptual model of the development of a cyclone starting from a secondary wave perturbing the polar front: I. Continuous and broad front - birthplace of incipient frontal cyclone; II. Frontal fracture in the vicinity of the cyclone centre and scale contraction of the discontinuous warm and cold frontal gradients; III. Bent-back warm front - midpoint of cyclogenesis; IV. Warm-core seclusion within northward side of polar air stream (Shapiro and Keyser, 1990).

In Browning and Roberts (1994) the authors concentrated their attention on the third phase of the conceptual model of the development of a cyclone (see Fig. 2.15).

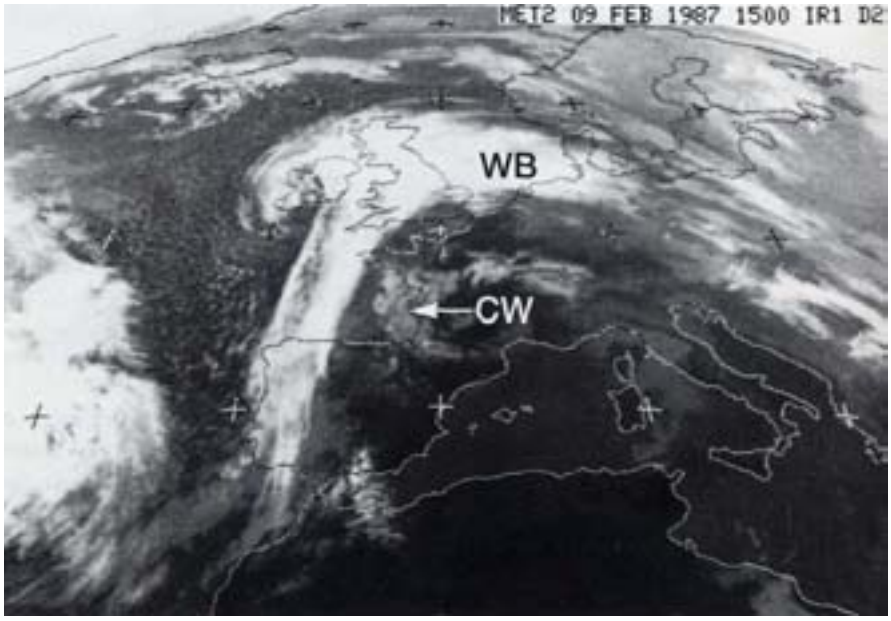

Figure 2.16: Meteosat IR image for 9 February 1987 1500 UTC when a cyclone is developing over England. The "cloud head", the warm and the cold fronts are clearly visible.

Figure 2.17: MODIS image of a cyclone over the central-eastern USA (20 April 2000)

Although they do not consider the last phase of deepening cyclogenesis (4th plot of Fig. 2.15) and although the Mediterranean cyclones may display different and peculiar features, their study is here briefly reported: in the meantime it has become a classical reference of the "conveyor belt" theory.

From Fig. 2.16 (from Bader et al., 1990) or Fig. 2.17 one may clearly detect the cold front, the warm front and the "cloud head" (which is a region of clouds with a sharp convex outer edge poleward of the main polar-front cloud band and intruded by a dry slot of cold air). Generally, in the cloud heads, the cloud tops are quite low toward the edge near the dry slot. Moreover beneath the north-western part of the cloud head, precipitation evaporates before reaching the surface, while it is heavy in the south-easterly region of low clouds, even characterized by convection.

Browning and Robert (1994) analysed the relative flow of air streams with respect to the mean speed of the cyclone (Fig. 2.18). To this purpose they looked at the flow within moist isentropic

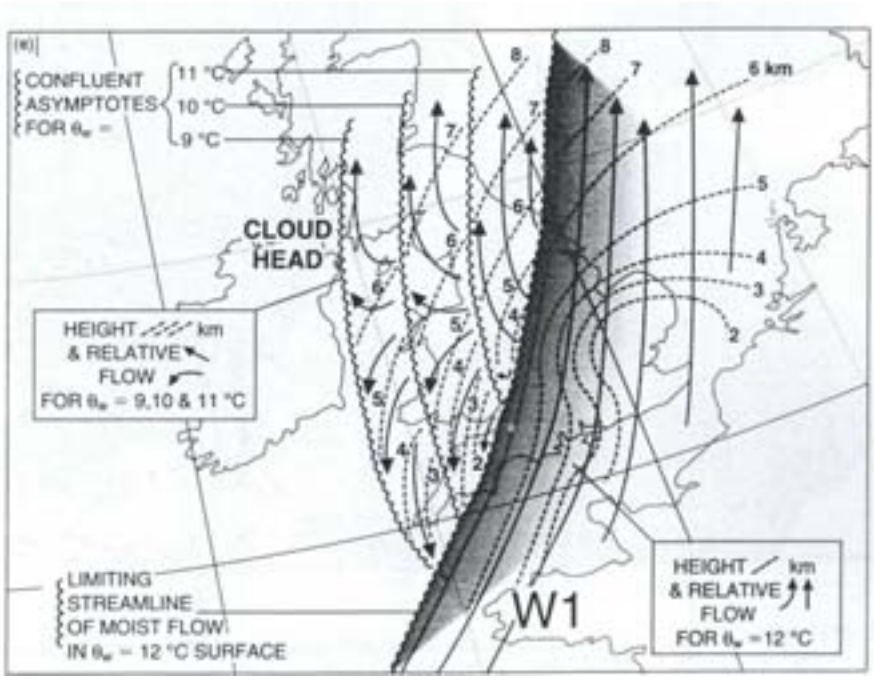

Figure 2.18: Moist isentropic flow relative to the cyclone flowing at 15 UTC 13 January 1993 over England (Browning and Roberts, 1994). The selected θ_e-surfaces correspond to 9°C, 10°C, 11°C and 12°C. The arrows represent the relative air motion over each θ_e-surface with respect to the mean velocity of the cyclone. Dashed curves are the height at 1 km intervals of the θ_e-surfaces.

surface, since the equivalent potential temperature is the most closely conserved quantity along the trajectories of air parcels. The superposition of various surface analyses reproduces the 3D structure of the center of the cyclone (Fig. 2.18). On the right hand side there is the core (W1)

of the warm conveyor belt flow: the warm conveyor belt (Harrold, 1973) is a strong, well defined flow of air with high wet-bulb potential temperature (θ_e) that advances, as a tongue, poleward ahead of the cold front. In the proximity of the surface low center the W1, moving in the middle troposphere, ascends over the preexisting cold air to form the warm front: after that it tends to move anticyclonically toward the East.
The lowest air mass near the warm front (W2), at the base of the warm conveyor belt ($\theta_e = 11°C$), peels off toward the west to form a portion of the upper part of the cloud head (Young et al., 1987): such warm airstream is the portion of fluid which experience the highest ascent inside the cyclone. The rearward relative flow of W2 toward the cold front (see also Fig. 5.1) is due to the ageostrophic circulation in the ABL induced by a frictional effect: this feature is a well-known symptom of cyclogenesis (Evans, 1994).
The two other airstreams of Fig. 2.18 ($\theta_e = 9°C$ and $\theta_e = 10°C$) are preexisting colder air, originating just ahead and beneath the warm front. These flows ascend while travelling westward, in a system relative sense, within the cloud head and around the low center: they correspond to the upper part of the cold conveyor belt (Carlson, 1980). At the westernmost limit of these flows, where they emerge from beneath the warmer air, there is a fanning out of the streamlines: the part turning toward the north continues ascending and producing precipitation, the other part turns towards the south and decelerates to ascend producing low level clouds. From the above description it is clear that, close and right to the cyclone center, there is no sharp demarcation between the two conveyor belts, both ascending and producing precipitation.
South of the low center there is an incipient intrusion of dry air above saturated warmer air corresponding to the W2 stream. The weak large scale ascent in this region is sufficient enough to trigger convective precipitation: this line has to be marked as a cold front, although it is often confused with an occluded front, developing only in the last phases of the cyclone development.
From a look at satellite images or radar images, a major break in the cold front is evident. The frontal fracture is due to the dry intrusion which is associated with a tropopause fold penetrating down from the stratosphere west of the surface cyclone center, which penetrates south-westerly, especially in the middle levels of troposphere. At the surface there is no line convection, while the edge of the intrusion produces an upper level cold front (or moisture front) hundreds of kilometer ahead of the surface cold front and inside the core of the warm conveyor belt. At the surface patchy rain can be observed. The resulting cold split front (in the vertical) can be explained by a the kata-cold front transverse flow structure: note that such fronts are weekly defined in terms of θ, while they are better-defined in terms of θ_e due to a remarkable decrease in humidity.
As a summary of their analysis, Browning and Roberts (1996) proposed the scheme reported in Fig. 2.19 and 2.20, which slightly differs from the customary cyclone representation with the cold,

warm and occluded fronts.

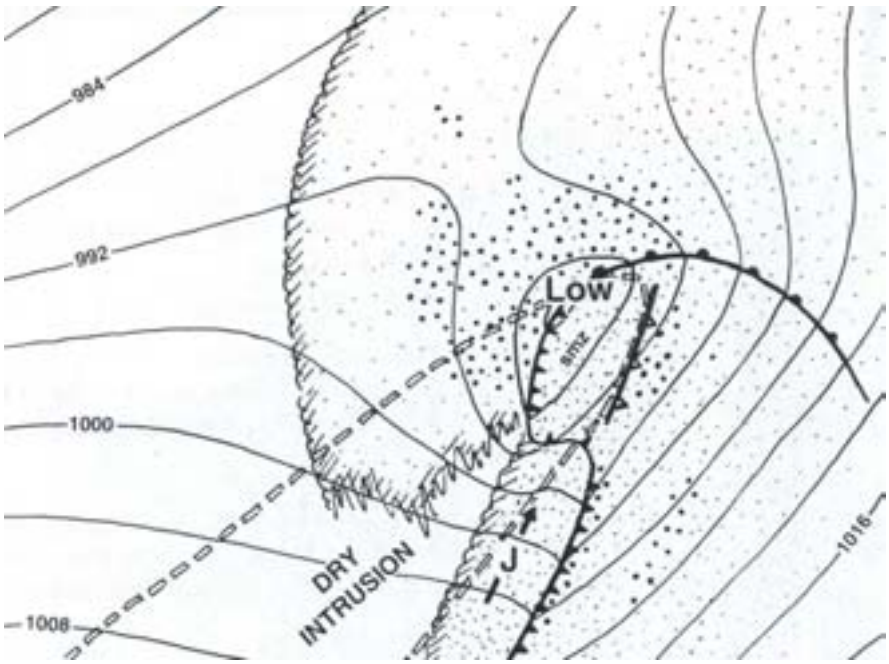

Figure 2.19: Analysis scheme for a cyclone with cloud head and frontal structure, before rapid deepening. See Fig.2.20 for the symbols.

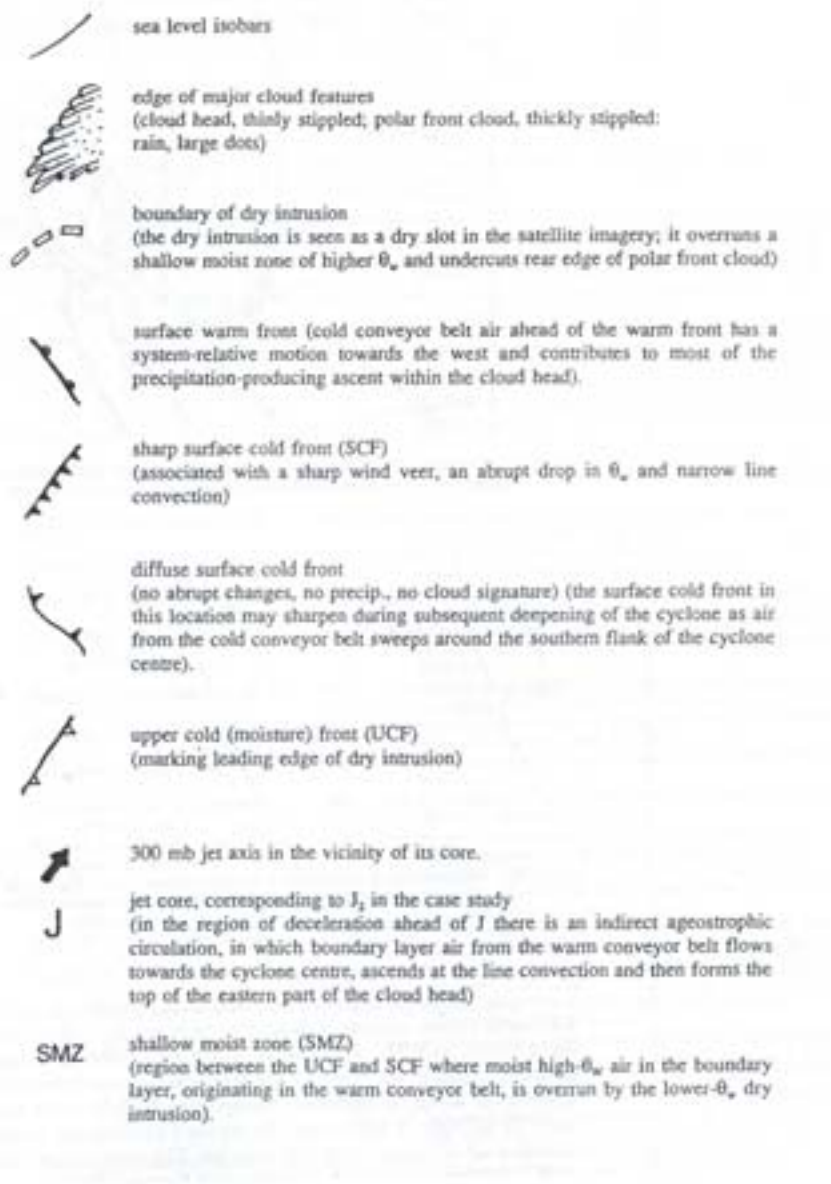

Figure 2.20: Explanation of the analysis scheme of Fig.2.19

In the northern part of the cold front, within even several hundred kilometers of the cyclone center in the last phases of the cyclone deepening, the dry intrusion overrides a narrowing tongue of relative high-θ_e air and advances ahead of the surface cold front to give a structure consistent with the split-cold front, as shown by the same authors in (Browning and Roberts, 1996). Farther south, in the trailing part of the cold front, there is always an ana-cold front along which the high-

θ_e air in the warm conveyor belt tends to ascend above descending low-θ_e air 2.14. The structure of the rain bands in the two parts is quite different: along the ana-cold front there is a classical 2D continuos convective line; along the split front there are convective elements oriented in the direction of the geostrophic flow and not of the cold front itself.

2.4 Trajectories of air masses

In the last 20 years trajectory computation has been successfully used in the environmental studies of the long range transport of pollutants, dust or stratospheric ozone (James et al., 2003; Kahl et al., 1989b; Merrill and Moody, 1996; Haagenson et al., 1990; Nodop, 1997b; Maryon and Heasmann, 1988). In these works one or few trajectories, representative of the air masses arriving over or leaving from a specific target point, are computed every day to obtain a climatology over some seasons or years. Consequently the statistical properties of various meteorological scenarios and of the concentration of tracers are derived, in order to compute the probability of occurrence of hazardous conditions for that specific target.
Sometimes a small number of trajectories is computed too to describe flow patterns or, generally, peculiar meteorological configurations occuring in specific case studies. See for example the papers of Danielsen (1961), Rotunno and Ferretti (2001) and Gheusi and Stein (2002) or some other works especially those published within the Mesoscale Alpine Programme (MAP) community. The latter approach seems to be less appropriate since it aims to describe a phenomenon by a trajectory whose starting or ending points have been chosen quite arbitrarily.
At the end of the 90s some researchers, especially from the Swiss School (Institute of Atmospheric Sciences, ETH Zuerich), have developed an objective method of Lagrangian analysis which computes a large number of trajectories to give a complete representation of the air masses in the 3D-space and in the entire period of the studied synoptic event. After that they identify macro air-parcels, called CETs (Coherent Ensembles of Trajectories), displaying a marked time coherency. The method has also been applied to identify numerically the theoretical conveyor belts inside a developing synoptic and extratropical cyclone (Schär and Wernli, 1993; Wernli and Davies, 1997; Rossa, 1995). In this context Swiss researchers have developed a theory for the stratospheric-tropospheric exchange and above the role of PV-banners and PV-anomalies as precursors of cyclogenesis. Less attention has been paid to the warm-conveyor belt, with the exception of two papers by Wernli and Davies (1997) and Wernli (1997) where synoptic cyclones developing over the Atlantic Ocean are simulated. Apart from a few attempts (Massacand et al., 1998) the extension of results to the mesoscale, as well as a detailed trajectory study of cyclones developing in the Mediterranean area has been left still untried. Moreover it seems interesting to resume a quantita-

tive approach which attempts at defining water budget associated with Lagrangian flow structures (Turato, 2003; Bertò et al., 2004; Stohl et al., 2004).

2.4.1 Water budget

The Lagrangian computation of trajectories is commonly used as an instrument yielding a qualitative illustration of the airstreams. Only few authors have already developed analytical techniques which allow to reconstruct evaporation maps that provide the distribution and the quantification of the sources of only the water vapour contributing to the precipitation over a specific target area (Stohl and James, 2004).
In the present thesis a water vapour budget analysis has been developed in detail. Through the application of the method to a large ensemble of precipitation events over the Alps during a long period, the climatology of the atmospheric portion of the hydrological cycle over the Mediterranean region has been obtained.

2.4.2 Atmospheric transport and water isotopic concentration

The following chapter shows that the reconstruction of air mass trajectories can be affected by large errors. An estimation of such errors requires the knowledge of the *true* reference trajectories. This is possible by tagging an air parcel by a mathematical tracer that is conserved along the trajectory.

Mathematical tracers

The Liouville theorem is valid for Hamiltonian systems of material points. "In the phase space, defined by the spatial coordinates and by the components of the impulses $f(x,y,z,i_x,i_y,i_z)$, a generic scalar quantity of the system of points is an invariant along the trajectory followed by the system." The above stated Liouville theorem is true if the system of points takes up an infinitesimal volume, i.e. a volume so small that it can be deformed but not disaggregated in the considered time period. In particular it is possible to write that the density D in the phase space

$$D = \frac{dN}{dV} \tag{2.3}$$

is constant in time, that is

$$\frac{dD}{dt} = 0. \tag{2.4}$$

where N is the number of parcels and V is the volume of the system of points in the phase space. The density ρ in the physical space can be written as

$$\rho = \iiint_{-\infty}^{+\infty} D\, du dv dw, \tag{2.5}$$

while the velocity distribution h as

$$h = \iiint_{-\infty}^{+\infty} D\, dx dy dz. \tag{2.6}$$

Therefore, if the variation of one of the two quantities is known, then it is possible to derive information about the evolution of the second one resorting to the conservation principle stated by the Liouville theorem.
In the case of continuous systems, e.g. the atmospheric fluids, it is possible to derive a similar Hamiltonian formulation of the theorem by writing:

$$\frac{dG}{dt} = 0 \tag{2.7}$$

where G is a generic integral quantity in the physical space:

$$G = \iiint g\, dx dy dz. \tag{2.8}$$

It is clear that for the continuous systems the Liouville theorem results to be less usable just because G must be an integral quantity. Furthermore, the system, to be Hamiltonian, must display conservative properties which are not easily found in the real atmosphere. So the only remaining possibility is to resort to physical tracers to check the reliability of the computed trajectories.

Physical tracers

Ideal physical tracers are ballons or light, rather than reactive substances (ozone, inert gases, fine dust).
While the study of large scale pollutant transport is commonly based on conservative tracers, this is not the case when analysing the transport of water vapour. The condensation/evaporation processes along air mass trajectories strongly affect the conservation of the water vapour. The only possible conservative tracer, therefore, could be the isotopic composition of water vapour if its values at the source areas were known. Although this is not the main purpose of the AQUAPAST project it is clear that the isotope signal can be also used:

- to test the trajectory methodology pointing out the type error which mostly hit the trajectory

computation

- to distinguish between the numerical errors and the real upper tropospheric mixing due to the Lagrangian chaos (von Hardenberg et al., 2000). It is useful to remember, however, that a flow tube on a isentropic chart equates to a Lagrangian flow pattern only if the system is conservative, steady and in uniform translation.

3 Back trajectories: methodology

In the present chapter a review of the existing literature is proposed regarding the technique of trajectory computation. In particular the various types of possible errors and their order of magnitude are discussed. An hint at the numerous applications of the trajectory techniques to the long range pollution transport follows. Finally, an introduction concerning the rare applications of the methodology to the water vapour transport in the literature and in the present work is reported.

3.1 Computation of trajectories

The trajectory of a specific infinitesimally small air parcel is defined by the differential equation

$$\frac{d\mathbf{X}}{dt} = \dot{\mathbf{X}}[\mathbf{X}(t)] \tag{3.1}$$

with t being time, $\mathbf{X}$ the vector identifying the parcel position at time t and $\dot{\mathbf{X}}$ the air parcel velocity vector. Recalling that at each time t the velocity of the air parcel $\dot{\mathbf{X}}$ (Lagrangian velocity) is equal to the value assumed by the wind field $\mathbf{u}$ (Eulerian velocity) in the point where the air parcel is flowing at that specific time t, then the equation 3.1 can be written as

$$\frac{d\mathbf{X}}{dt} = \mathbf{u}[\mathbf{X}(t)]. \tag{3.2}$$

Once the initial position of the parcel $\mathbf{X}_0$ at time t_0 and the wind field $\mathbf{u}$ are known, the trajectory of air parcel is completely determined through equation 3.2. We can write

$$\mathbf{X}(t) = \mathbf{X}(\mathbf{X}_0, t). \tag{3.3}$$

Based on equation 3.2 we can compute either forward trajectories ($t > t_0$) or backward trajectories ($t < t_0$). The spatial coordinates $\mathbf{X}_0$ at time t_0 provide a means for identifying each air parcel at each time. These initial coordinates are called *material* or *Lagrangian coordinates* (Dutton, 1986). An important feature of trajectories is that particles that are initially neighbors remain

neighbors at least for finite time lags (which is not true for infinite time lags). So a line of particles at time t_0 remains an unbroken line at time t, no matter how it is distorted by the motion. This can be expressed by

$$\lim_{\Delta X_0 \to 0} |\mathbf{X}(\mathbf{X}_0 + \Delta\mathbf{X}_0, t) - \mathbf{X}(\mathbf{X}_0, t)| = 0. \tag{3.4}$$

The most important property of equation 3.4 is that particles that are inside a closed surface at time t_0 remain separated from those outside. Any closed surface which moves with the flow is called a *material surface*. An interesting application of this feature is contour advection (Waugh and Plumb, 1994).

It has to be noted that trajectories are different from *streamlines*. A streamline identifies the direction of flow at a fixed instant of time and thus is everywhere tangent to the velocity vectors:

$$\frac{dx}{u} = \frac{dy}{v} = \frac{dz}{w}. \tag{3.5}$$

Only during *stationary conditions* the trajectories and the streamlines coincide.

The idealized concept discussed above is not fully applicable to finite dimension parcels in the real atmosphere. A real parcel of finite size may become distorted so strongly in a divergent flow that it is turn apart; in particular it is deformed, at least in ABL, by turbulent and convective motions. Hence, a computed trajectory is representative for the path of an air parcel only for very limited time lags.

3.1.1 Solution of the trajectory equation

In general Eq. 3.2 can be integrated only by means of numerical methods. For meteorological applications a finite-difference numerical approximation can be used (Walmsley and Mailhot, 1983). Expanding $\mathbf{X}(t)$ in a Taylor series about $t = t_0$ and evaluating it at another instant$t_1 = t_0 + \Delta t$ (see Fig. 3.1.1), one obtains

$$\mathbf{X}(t_1) = \mathbf{X}(t_0) + (\Delta t)\left.\frac{d\mathbf{X}}{dt}\right|_{t_0} + \frac{1}{2}(\Delta t)^2\left.\frac{d^2\mathbf{X}}{dt^2}\right|_{t_0} + \cdots. \tag{3.6}$$

The first order approximation to equation 3.6 is

$$\mathbf{X}(t_1) = \mathbf{X}(t_0) + (\Delta t)\dot{\mathbf{X}}(t_0). \tag{3.7}$$

This is a *'zero acceleration'* solution of equation 3.1 that is computationally cheap since it involves no iteration. It is accurate to the first order, which means that differences between the real (the

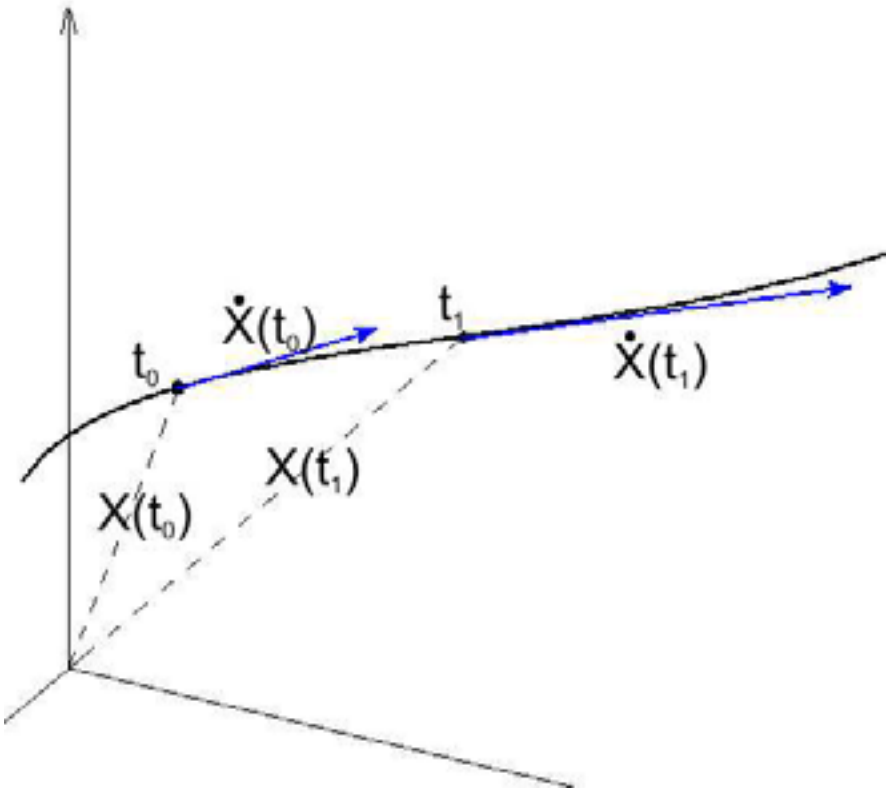

Figure 3.1: Position and velocity vectors of an air parcel along its trajectory at time t_0 and t_1

"*reference trajectory*") and the numerical solution will occur from the omission of the second- and higher-order terms. If trajectories are calculated using very short integration time steps, equation 3.7 might be accurate enough for pratical purposes. However, more accurate approximations at acceptable computational costs do exist. If $\mathbf{X}(t)$ is also expanded in a Taylor series about $t = t_1$ and evaluated a $t = t_0$, the following yields:

$$\mathbf{X}(t_0) = \mathbf{X}(t_1) - (\Delta t)\left.\frac{d\mathbf{X}}{dt}\right|_{t_1} + \frac{1}{2}(\Delta t)^2\left.\frac{d^2\mathbf{X}}{dt^2}\right|_{t_1} - \cdots . \tag{3.8}$$

Combining equations 3.6 and 3.8, we obtain

$$\mathbf{X}(t_1) = \mathbf{X}(t_0) + \frac{1}{2}(\Delta t)[\dot{\mathbf{X}}(t_0) + \dot{\mathbf{X}}(t_1)] + \frac{1}{4}(\Delta t)^2\left[\left.\frac{d\dot{\mathbf{X}}}{dt}\right|_{t_0} - \left.\frac{d\dot{\mathbf{X}}}{dt}\right|_{t_1}\right] + \cdots . \tag{3.9}$$

If only the first two terms on the right-hand side of equation 3.9 are retained, we obtain the "*constant acceleration*" *solution*

$$\mathbf{X}(t_1) = \mathbf{X}(t_0) + \frac{1}{2}(\Delta t)[\dot{\mathbf{X}}(t_0) + \dot{\mathbf{X}}(t_1)]. \tag{3.10}$$

(Walmsley and Mailhot, 1983). This approximation is identical to the well known Petterssen (1940) scheme, originally a graphical method used to manually trace isobaric trajectories from weather charts. Equation 3.9 is accurate to the second order. It has to be solved by iteration starting with equation , since $\dot{\mathbf{X}}(t_1)$ is not known *a priori*:

$$\begin{aligned}
\mathbf{X}^1(t_1) &\approx \mathbf{X}(t_0) + (\Delta t)\dot{\mathbf{X}}(t_0) \\
\mathbf{X}^2(t_1) &\approx \mathbf{X}(t_0) + \frac{1}{2}(\Delta t)[\dot{\mathbf{X}}(t_0) + \dot{\mathbf{X}}^1(t_1)] \\
&\vdots \\
\mathbf{X}^i(t_1) &\approx \mathbf{X}(t_0) + \frac{1}{2}(\Delta t)[\dot{\mathbf{X}}(t_0) + \dot{\mathbf{X}}^{i-1}(t_1)]
\end{aligned} \tag{3.11}$$

The superscripts indicate the number of iteration, and $\dot{\mathbf{X}}^i(t_1)$ is taken at the position $\dot{\mathbf{X}}^i(t_1)$. Sometimes, the third term on the right-hand side of equation 3.9 is retained ("*variable acceleration*" *method*). In principle, this solution gives higher accuracy at the cost of increasing computing time with the disadvantage that the accelerations at two times have to be evaluated. This can introduce inaccuracy because wind fields are often available only at large temporal intervals. Hence, the variable acceleration method may result even less accurate than the constant acceleration method. All solutions discussed so far are *kinematic*, as they use the wind information only. Danielsen (1961) developed a technique to trace trajectories by tagging air parcels with $(quasi-)conservative$ quantities such as potential temperature. Although two-dimensional kinematic trajectories can also be constructed on isentropic surfaces, Danielsen (1961) method is *dynamic* because it uses velocity and mass field information and *dynamic equations* linking the two (Merrill et al., 1986). However, Stohl and Seibert (1998) showed that dynamic trajectories calculated through an explicit method can perform unrealistic ageostrophic oscillations. Since accurate wind fields with high space and time resolution are available, kinematic trajectories are more accurate (Stohl and Seibert, 1998).

3.1.2 Sensitivity to the initial conditions and errors

The inaccuracy inherent to the numerical integration of trajectories can be evaluated by introducing a suitable concept of error. The measure of trajectory errors mostly adopted in the literature is the

absolute horizontal transport deviation (Kuo et al., 1985; Rolph and Draxler, 1990)

$$AHTD(t) = \left\{[X(t) - x(t)]^2 + [Y(t) - y(t)]^2\right\}^{1/2} \tag{3.12}$$

where (X, Y) is the location of the test trajectory and (x, y) is the location of the reference trajectory at the travel time t. A similar measure can be defined in the vertical dimension.
Another parameter often used is the relative horizontal transport deviation (RHTD), which is defined as the AHTD divided by the lenght of the reference trajectory. Various types of possible errors and their order of magnitude are discussed in the following subsections.

Truncation errors

The so-called *truncation errors* occur when the equation 3.1 is approximated by a finite-difference scheme neglecting higher order terms in the Taylor series expansion. Walmsley and Mailhot (1983) show that the truncation error is proportional to Δt for the zero order scheme (Eq. 3.7), proportional to $(\Delta t)^2$for the constant (Eq. 3.10) and variable acceleration method. It can be kept below any given limit by using sufficiently small Δt.
Considering that in most situations the time step requirements will be less demanding, while on the other hand a few situations may even be more demanding, Seibert (1993) recommended to use a scheme that automatically adjusts the time step to the actual flow situation. Hence, since no grid cell must be skipped during a time step to reproduce the smallest features in the trajectories, the Courant-Friedrichs-Lewy criterion

$$\Delta t < \frac{\Delta x_i}{|v_i|}, \tag{3.13}$$

where Δx_i are the grid distances and v_i are the wind components, may serve as an upper limit for the flexible time step (Seibert, 1993).

Interpolation errors

Wind data are, in general, available only at discrete locations in space and time, either as irregularly spaced observations or as the gridded output of meteorological models. In both cases, the wind speed must be estimated at the trajectory position by the trajectory model. This interpolation causes errors that substantially affect the trajectory accuracy.
To examine the errors caused by the spatial interpolation of the wind fields obtained by prognostic meteorological models (either forecasts or initialized analyses), the usually adopted method is to degrade artificially the grid resolution, interpolate the wind data to the original grid and compare them with the undegraded data. Similar tests can be adopted to estimate errors deriving from the

Spatial resolution (km)	Temporal resolution			
	2h	4h	6h	12h
90	0	250	411	734
180	166	281	418	733
360	417	444	517	730

Table 3.1: Mean horizontal trajectory position deviation (km) from the higher resolution reference trajectories after 96 h travel time for various spatial and temporal resolutions of the input data (Rolph and Draxler, 1990)

interpolation in time.

Stohl et al. (1995) evaluated the performance of several different interpolation methods. They found that linear interpolation in time is very accurate, but interpolation methods of higher order in space reduce errors as compared to linear interpolation. Stohl et al. (1995) also found that interpolation of the vertical wind component *w* produces larger errors than the interpolation of the horizontal components because of its high-frequency variability. The effect of degrading the wind field resolution on trajectory accuracy has been examined in several other studies (Kuo et al., 1985; Doty and Perkey, 1993; Rolph and Draxler, 1990). One finding of these studies is that the growth of trajectory position errors with travel time caused by interpolation is approximately linear, but the most important result is that "the spatial and temporal resolution of the wind fields must be in balance in order to limit the trajectory errors" (Rolph and Draxler, 1990). An increase in spatial resolution alone results in just marginally more accurate trajectories when the temporal resolution is low. On the contrary, increasing the temporal resolution alone is also not so effective when the spatial resolution is low. In any case, a minimum resolution of 6 h is required if diurnal variations in the flow field are to be resolved. The recent availability of analysis fields with 3 h temporal resolution has improved substantially the trajectory computation.

As an example, the results of Rolph and Draxler (1990) are summarized in Table 1. At high spatial resolution, trajectories are more sensitive to a reduction of the temporal resolution than to a reduction of the horizontal resolution. However, at 360 km resolution, except for the 12 h case, the coarse spatial resolution becomes the dominant cause of trajectory errors. The effect of interpolation errors on trajectory accuracy may also depend on the complexity of the flow situation. For example Stohl et al. (1995) found larger sensitivity to interpolation errors for trajectories crossing the Alps than for others.

Errors resulting from the evaluation of the wind vertical component

Trajectory errors are also related to different assumptions about the wind vertical component w. In contrast to the horizontal wind component no routine observations of w are available, since the wind vertical component has an order of magnitude of only some cm/s which is comparable with the measurement errors. So fields of w are solely producted by NWP models, and hence they are usually less accurate than the fields of the horizontal wind. Note that a small error in the estimation of the vertical displacement of an air parcel can induce big errors in its horizontal trajectory because of the strong vertical gradient of the horizontal wind field. Fuelberg et al. (1996) pointed out that it is more accurate to obtain vertical velocities directly from a dynamically consistent numerical model. Vertical motions diagnosed from the horizontal wind components using the principle of mass conservation (i.e continuity equation) are much less accurate. Trajectories computed with these vertical velocity components sometimes determine unrealistically large diabatic heating or cooling rates of the air parcel, whereas dynamically consistent vertical motions keep the diabatic heating and cooling rates within the limits expected on theoretical basis. The simplest alternative to three-dimensional trajectories is neglecting w. This results in two-dimensional trajectories in various coordinate systems:

1. *isobaric* trajectories,
2. *isosigma* trajectories, i.e. terrain following trajectories,
3. *isentropic* trajectories.

The third family of trajectories is the most realistic, since the atmospheric motion at synoptic scale to mesoscale is generally adiabatic and inviscid. In fact, they were computed for a long time before the arrival of variational analyses. However, large problems can be met in the ABL and in saturated moist air where diabatic effects are not negligible. Morover, in the ABL, calculated 3D-trajectories are often far from being representative of the path of single air parcels as the latter quickly loose their identity due to turbulent mixing. Accordingly, stochastic Lagrangian particle dispersion models have been applied to simulate the transport in the ABL, but they are relatively demanding on computer resources and not easily applicable. Alternatively trajectories are often used that are advected with the vertically averaged wind in the ABL (Heffter, 1980; Rao et al., 1983). This approach, which was found to agree best with the dispersion of tracer material (Haagenson et al., 1987), has been adopted in the present work. Of course this method gives only a crude approximation of the real complexities occurring in real turbulent flows.

Wind field errors

In many cases the largest source of error for trajectory reconstruction derives from the underlying wind fields obtained either from forecasts or from analyses.

The analysis fields. Most of the trajectory models use the analysis fields available from two meteorological centers, the European Centre for Medium-Range Weather Forecast (ECMWF) and the U.S. National Centers for Environmental Prediction (NCEP). The analyses are obtained from the *data assimilation* process, which combines the meteorological observations with a short range forecast, yielding meteorological fields that are as close as possible to the observations and at the same time fulfill the dynamic model constraints. The most advanced assimilation technique at ECMWF (White, 2002) is a four-dimensional algorithm (4DVar) working on a time period Δt called "assimilation window" (currently 12 h) extending from the time of analysis t_0 to the time $t_a = t_0 + \Delta t$. The analysis (valid at time t_0) is adjusted iteratively to minimize a so-called "cost function" (Fig. 3.2). The latter is given by the sum of both the deviation at time t_0 of the new analysis from the "background" forecast (initialized on the previous analysis valid at time $t_{-a} = t_0 - \Delta t$) and of the deviation of the short forecast (initialized on the new analysis) from the observations:

$$J(x) = J_b(x) + J_o(x) = (x - x_b)^T B^{-1}(x - x_b) + (y - H(x))^T R^{-1}(y - H(x)) \tag{3.14}$$

where x is the vector of analysis variables (surface pressure, temperature, wind, specific humidity and ozone), x_b is the vector of background forecast, y is the vector of observations , B is the background error covariance matrix, R_i is the observation covariance matrix and H is the observation operator which interpolates the background on the observation point and on the time of observation (see White (2002) for details).

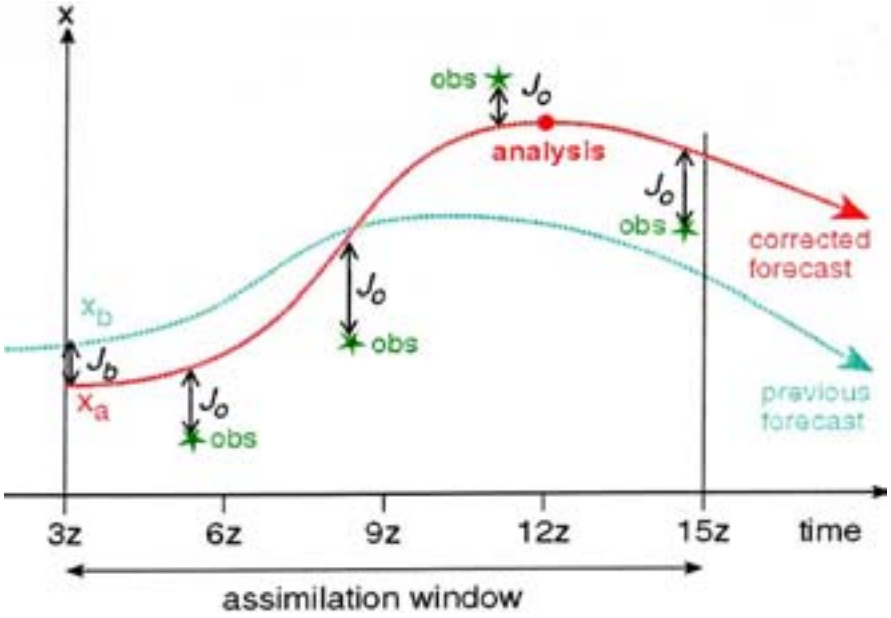

Figure 3.2: 4DVar assimilation technique used at ECMWF (White, 2002). J_b is the deviation at time t_0 of the new analysis x_a from the "background" forecast x_b (initialized on the previous analysis); J_o is the deviation of the short forecast (initialized on the new analysis) from the observations.

The impact of analysis and forecast errors on trajectory computation. Most of the trajectory models avoid using the fully consistent fields from forecast models in favour of the analysis data because the forecast errors increase exponentially with time. Nevertheless, as shown in Stohl et al. (2004), the nondiffusive character of the Lagrangian methods can be partially spoiled by the use of a series of dynamically inconsistent wind fields produced by the assimilation procedure. In fact the short range forecast initialized on the analysis field valid at time t_0 is as close as possible to the observations and at the same time fulfill the dynamic model constraints only during the *assimilation window* of that analysis (from t_0 to $t_0 + \Delta t$). The short range forecast initialized at time t_0 is instead not dynamically consistent with the short range forecasts initialized respectivelly on time $t_0 - \Delta t$ and on time $t_0 + \Delta t$.

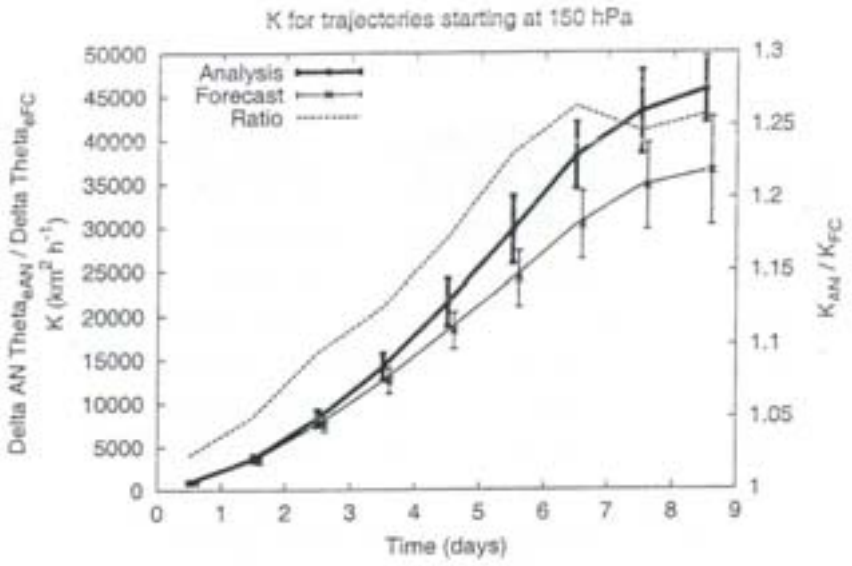

Figure 3.3: The Lagrangian diffusion coefficient is defined as $K(t) = 0.5\frac{d\overline{r^2(t)}}{dt}$ where $\overline{r^2(t)}$ is the mean square separation of particles at time t (Stohl et al., 2004).

As a consequence the Lyapunov exponents and the diffusion coefficient (measure of the dispersion tendency of a set of trajectories) can result statistically relevant even starting from analyses data (Fig. 3.3). In summary the Lagrangian mixing obtained from the forecast data can be wrong but the mixing from the analyses is generally overestimated although closer to the real Lagrangian dispersion. Such a result has been obtained by Stohl et al. (2004) from a 1-year climatology (2002) of a set of 10 million trajectories representative of the troposphere and tropopause of the whole Northern Emisphere. Moreover, a similar overestimation of the variations of some conservative properties (PV, θ_e and q) along the trajectories has been detected. This is particularly important in atmospheric chemistry, since many chemical reactions show a non-linear dependence on the concentration of the reactants, including water vapour. Luckily, the effect is more evident at higher levels (tropopause) than at lower ones, where it is dumped by the extra noise from turbulent mixing. The tendency of the water vapour content in the middle and low troposphere is thus the most important issue in the present work.

Starting position errors and ensemble methods

The starting positions of trajectories are commonly not exactly known. For example, the differences between the model topography and the real topography makes the selection of a starting height difficult. This introduces some inaccuracy in the reconstruction of back-trajectories (es-

pecially in the case of convergent flow). Note that trajectory divergence is due not only to the occurrence of initial position errors, but also to the wind shear and to the divergence of the flow. Fortunately in the present work an ensemble of trajectories starting form a grid box has been computed (see section 3.3.2), thus reducing the impact of such error source.

3.1.3 Combination of errors

The overall accuracy of a trajectory is determined by the integral effect of all the errors discussed in the previous section. Its assessment is difficult because it requires the determination of a *true* reference trajectory. This is possible by tagging an air parcel with a tracer that is conserved along the trajectory. Many different tracers have been used, but none of them is ideally suited, either because it is not well conserved, or because its determination is difficult, or because it is not commonly available. Many studies performed in the 80s and 90s were based on three different classes of tracers, balloons (*constant level* or *manned baloons*), material (smoke plumes, inert gases and so on) and dynamical tracers (PV). These culminated in some continental experiments ($Cross-Appalachian\ Tracer\ Experiment$ -CAPTEX-; *Across North America Tracer Experiment* -ANATEX- and *European Tracer Experiment* -ETEX-). A brief summary of literature estimates is reported in Stohl (1998) (see figure 3.4).

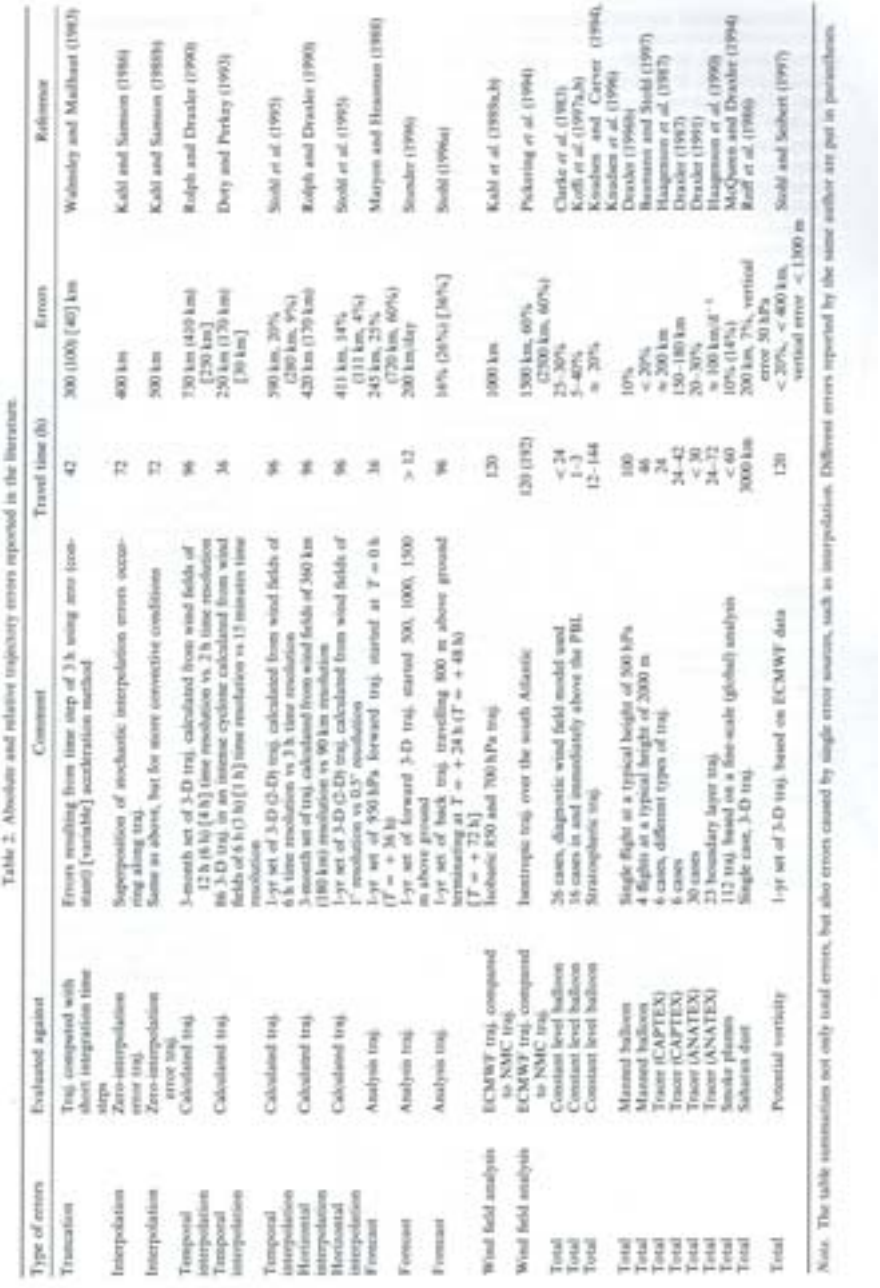

Table 2. Absolute and relative trajectory errors reported in the literature.

Type of errors	Evaluated against	Comment	Travel time (h)	Errors	Reference
Truncation	Traj. computed with short integration time steps	Errors resulting from time step of 3 h using zero (constant) [variable] acceleration method	42	300 (100) [40] km	Walmsley and Mailhot (1983)
Interpolation	Zero-interpolation error traj.	Superposition of stochastic interpolation errors occurring along traj.	72	400 km	Kahl and Samson (1986)
Interpolation	Zero-interpolation error traj.	Same as above, but for more convective conditions	72	500 km	Kahl and Samson (1988b)
Temporal interpolation	Calculated traj.	3-month set of 3-D traj. calculated from wind fields of 12 h (6 h) [4 h] time resolution vs 2 h time resolution	96	730 km (410 km) [250 km]	Ralph and Draxler (1990)
Temporal interpolation	Calculated traj.	86 3-D traj. on an intense cyclone calculated from wind fields of 6 h (3 h) [1 h] time resolution vs 15 minutes time resolution	36	250 km (170 km) [30 km]	Doty and Perkey (1993)
Temporal interpolation	Calculated traj.	1-yr set of 3-D (2-D) traj. calculated from wind fields of 6 h time resolution vs 3 h time resolution	96	590 km, 39% (280 km, 9%)	Stohl et al. (1995)
Horizontal interpolation	Calculated traj.	3-month set of traj. calculated from wind fields of 360 km (180 km) resolution vs 90 km resolution	96	420 km (170 km)	Ralph and Draxler (1990)
Horizontal interpolation	Calculated traj.	1-yr set of 3-D (2-D) traj. calculated from wind fields of 1° resolution vs 0.5° resolution	96	411 km, 14% (111 km, 4%)	Stohl et al. (1995)
Forecast	Analysis traj.	1-yr set of 950 hPa forward traj. started at $T = 0$ h ($T = +36$ h)	36	345 km, 25% (720 km, 60%)	Maryon and Heasmann (1988)
Forecast	Analysis traj.	1-yr set of forward 3-D traj. started 500, 1000, 1500 m above ground	> 12	200 km/day	Stunder (1996)
Forecast	Analysis traj.	1-yr set of back traj. travelling 800 m above ground terminating at $T = +24$ h ($T = +48$ h) [$T = +72$ h]	96	16% (26%) [36%]	Stohl (1998a)
Wind field analysis	ECMWF traj. compared to NMC traj.	Isobaric 850 and 700 hPa traj.	120	1000 km	Kahl et al. (1989a,b)
Wind field analysis	ECMWF traj. compared to NMC traj.	Isentropic traj. over the south Atlantic	120 (192)	1300 km, 60% (2500 km, 60%)	Pickering et al. (1994)
Total	Constant level balloon	26 cases, diagnostic wind field model used	< 24	25–30%	Clarke et al. (1983)
Total	Constant level balloon	16 cases in and immediately above the PBL	1–3	5–40%	Kraft et al. (1997a,b)
Total	Constant level balloon	Stratospheric traj.	12–144	≈ 20%	Knudsen and Carver (1994), Knudsen et al. (1996)
Total	Manned balloon	Single flight at a typical height of 500 hPa	100	10%	Draxler (1996b)
Total	Manned balloon	4 flights at a typical height of 2000 m	46	< 20%	Beerends and Stohl (1997)
Total	Tracer (CAPTEX)	6 cases, different types of traj.	24	≈ 200 km	Haagenson et al. (1987)
Total	Tracer (CAPTEX)	6 cases	24–42	150–180 km	Draxler (1987)
Total	Tracer (ANATEX)	30 cases	< 30	20–30%	Draxler (1991)
Total	Tracer (ANATEX)	23 boundary layer traj.	24–72	≈ 100 km d^{-1}	Haagenson et al. (1990)
Total	Smoke plumes	112 traj. based on a fine-scale (global) analysis	< 60	10% (14%)	McQueen and Draxler (1994)
Total	Saharan dust	Single case, 3-D traj.	3000 km	200 km, 7%, vertical error 50 hPa	Reiff et al. (1986)
Total	Potential vorticity	1-yr set of 3-D traj. based on ECMWF data	120	< 20%, < 400 km, vertical error < 1000 m	Stohl and Seibert (1997)

Note. The table summarizes not only total errors, but also errors caused by single error sources, such as interpolation. Different errors reported by the same author are put in parentheses.

Figure 3.4: The table (from Stohl (1998)) summarizes various trajectory error estimations derived from Baumann and Stohl (1997), Doty and Perkey (1993), Clarke et al. (1983), Draxler (1996), Haagenson et al. (1987), Haagenson et al. (1990), Kahl et al. (1989a), Kahl et al. (1989b), Kahl and Samson (1986), Kahl and Samson (1988), Knudsen and Carver (1994), Knudsen et al. (1996), Nodop (1997a), Nodop (1997b), Maryon and Heasmann (1988), McQueen and Draxler (1994), Pickering et al. (1994), Reiff et al. (1986), Rolph and Draxler (1990), Stohl (1996), Stohl and Wotawa (1995), Stohl et al. (1995), Stunder (1996), Walmsley and Mailhot (1983), Draxler (1991), Draxler (1987), and Stohl and Seibert (1998),.

It turns out to be easier the estimation of the relative contribution of a specific source of error. For example the truncation errors (section 3.1.2) can be computed reconstructing the *reference trajectory* by integrating Eq. 3.2 using a very short time step: obviously this *reference trajectory* does not correspond to the real physical track, which could even be very different since the *reference trajectory* shows the effects of the other errors. Another typical approach is the intercomparison of various Lagrangian models which again can only help to point out the possible gaps of a particular model (Stohl et al., 2001). The advantages of this strategy is the possibility to build a sort of error climatology, which is impossible in the case of tracer experiments.

3.1.4 Other models

Trajectory models are the main instrument to estimate the long range transport of tracers in the atmosphere. Nevertheless the description of transport phenomena in *turbulent flows* by single trajectories is not exhaustive (Seibert, 1997).
Both Eulerian models and Lagrangian Particle Dispersion Models (LPDM) are currently used to study the turbulent transport on a fine scale. LPDM have no artificial numerical diffusion like Eulerian models (Nguyen et al., 1997) and hence have a greater potential to resolve fine-scale structures of the flow. LPDM numerically simulate the transport and diffusion of a passive scalar tracer by calculating the Lagrangian trajectories of tens or hundreds of thousands of tagged particles. These trajectories are calculated according to the relation:

$$\mathbf{X}(t+\Delta t) = \mathbf{X}(t) + (\Delta t)[\bar{\mathbf{v}}(t) + \mathbf{v}'(t)] \tag{3.15}$$

where $\bar{\mathbf{v}}$ is the *resolvable scale wind vector* obtained directly from a meteorological model, and $\mathbf{v}'$ is the *turbulent wind vector* that describes the turbulent diffusion of the tracer in the ABL. The concentration of the tracer at a specific location at a given time is linearly proportional to the number of particles per unit volume. It can be evaluated simply by counting all particles that reside within a certain volume or, more favorably, by using a kernel method (Lorimer, 1986; Uliasz, 1994; Thomson, 1987; Wilson and Sawford, 1996; Rodean, 1996).
The core problem of LPDM is the determination of the turbulent velocities $\mathbf{v}'$. These are estimated from the Langevin equation (Thomson, 1987):

$$dv_i' = a_i(\mathbf{X}, \mathbf{v}', t)dt + b_{ij}(\mathbf{X}, \mathbf{v}', t)d\mathbf{W}_j(t) \tag{3.16}$$

where a and b are functions of $\mathbf{X}$, $\mathbf{v}'$ and t and the $d\mathbf{W}_j$ are the increments of a vector-valued *Wiener process* with independent components. The $d\mathbf{W}_j$ represent Gaussian white noise with

mean zero and variance dt; increments $d\mathbf{W}_i$ and $d\mathbf{W}_j$ occurring at different times, or at the same time with i $\neq$ j, are independent. LPDM can simulate, in addition to the dispersion, all linear processes, such as dry and wet deposition, radioactive decay, and linear chemical transformations, but a major drawback is that, currently, nonlinear chemical reactions cannot be accounted for.
Otherwise Lagrangian *box models* can be employed. Firstly, a back trajectory is calculated from this location. Then, a box is moved forward along this trajectory and the changes in the concentrations in the box caused by chemical reactions and deposition are calculated. Compared to zero-dimensional Eulerian models, Lagrangian box models are more practical because no advection from outside the box occurs and hence no boundary conditions are required. However, such models are fully applicable only at higher levels of the atmosphere (Sparling, 1995) where turbulence is weak. For the calculation of the turbulent vertical exchange in the ABL it is necessary that the boxes representing an air column remain exactly above each other. In reality, however, a vertical shear of the horizontal wind would separate the boxes. To avoid this *grid tangling*, the wind shear must be neglected and the whole column of boxes must be advected along a single trajectory. It is for this reason Lagrangian column models are less accurate than three-dimensional Eulerian models in the ABL (Peters, 1995).

3.2 Source areas of air pollution

In 1995 Ashbaugh et al. (1985) developed a method based on Lagrangian trajectories to identify source areas of air pollutants ("source oriented model"). They calculated a large set of back trajectories, each consisting in a number of segments separated by specific time increments and characterized by their positions and time, respectively. Then they covered the area of study with a regular analysis grid.
If N is the total number of trajectory segments, n_{ij} is the number of segments falling in the (i, j) grid cell and $P[A_{ij}] = \frac{n_{ij}}{N}$ is the probability that a randomly selected air parcel resides in the (i, j) grid cell. If m_{ij} is the number of segments in the (i, j) grid cell, but only for those trajectories which arrive at the receptor when a certain criterion value for the pollutant concentration is exceeded, then $P[B_{ij}] = \frac{m_{ij}}{N}$ represents the residence time of high pollutant concentration air parcels in the (i, j) grid cell. The conditional probability of the event B_{ij}, given that event A_{ij} occurs, is $P[B_{ij}|A_{ij}] = \frac{m_{ij}}{n_{ij}}$. Regions with high conditional probability have a large potential to adversely affect the air quality at the receptor site when they are crossed by a trajectory. They do not necessarily make a large contribution to long-term air pollutant concentrations, since this also depends on the frequency at which air parcels actually travel over that region.
Later on Seibert et al. (1994a) and Seibert et al. (1994b) modified the method to obtain the pol-

lutant concentration fields. They calculate a logarithmic mean concentration for each grid cell according to

$$\overline{C_{ij}} = \frac{1}{\sum_{l=1}^{N} \tau_{ijl}} \sum_{l=1}^{N} log(c_l)\tau_{ijl} \tag{3.17}$$

where i, j are the indices identifying the horizontal grid, l the index of the trajectory, N the total number of trajectories, c_l the concentration observed on arrival of trajectory l and τ_{ijl} the time spent in grid cell (i, j) by trajectory l. The previous formula assumes that the pollutant concentration is conserved along the trajectory: so a high value of $\overline{C_{ij}}$ means that, on average, air parcels passing over cell (i, j) result in high concentrations at the receptor site. Note that this statistical approach acts in such a way to determine gridded concentration field maps representing, at each grid cell, the vertical average column concentration of the pollutant from the surface to the free troposphere, which make it possible to localize the spatial distribution of sources and sinks. Seibert et al. (1994b) showed that the computed fields exhibit small-scale variations which are not necessarily statistically significant. So a 9-point filter must be applied to smooth the concentration field, imposing the restriction that the values must be kept within their confidence interval. The smoothing is iteratively repeated until the change in the concentration field is less than a prescribed value. This procedure assures that significant variations are preserved while most of the insignificant ones are removed. Stohl et al. (1995) further refined the method performing an iterative redistribution of the concentrations along the trajectories.

The described method has been widely used. For example Ferrarese et al. (2002) applied the previous *source oriented model* to calculate the concentration fields of atmospheric CO_2 starting from the pluri-annual measurements of CO_2 at the observing stations of Plateau Rosà (3480m a.s.l., in the western Alps) and Zugspitze (2937 m, in the eastern Alps). Subsequently they compared the computed fields with the sea-surface temperature (SST) patterns, forestation maps, forest fires and the anthropogenic emissions in order to identify with high spatial resolution the most relevant areas of CO_2 sources and sinks (Apadula et al., 2003).

The procedures of Ashbaugh et al. (1985) and of Seibert et al. (1994b) underestimate the spatial gradients of the "true" source fields because a measured concentration is attributed equally to all segments of its related trajectory. Moreover it has been shown that these methods have problems with species produced by non-linear chemistry. A possible solution is the new approach of Seibert (1997) establishing trajectory-derived source-receptor relationships. It is not based on statistics, but on inverse modeling, viewing trajectories as the output of a primitive Lagrangian dispersion model. This is an ill-posed inverse problem, since the dimensions of the receptor-concentration-vector and of the source-vector are not equal. Seibert (1997) overcomes this difficulty by introducing additional constraints, but the effect of these constraints has to be further explored.

3.3 Application of the Lagrangian Analyses to long range water vapour transport

Precipitation falling on a given area is a mixture of water transported from many different sources: some water originated locally (from local evaporation or transpiration), some other has been advected from remote sources of moisture (both terrestrial and oceanic). Transport of water vapour can be reproduced by means of numerical modelling concepts similar to those outlined in previous sections. However some processes specific of this species have to be carefully taken into account, namely:

- the mass conservation principle has to be applied to all the various phases of water: water vapour, atmospheric liquid droplet and ice particles (Seibert et al., 1994b),
- phase transformations imply energy fluxes between the air parcels and water drops (or ice crystals).

3.3.1 The approach of Dirmeyer and Brubacker (1999)

In the work of Turato (2003) the approach of quasi-isentropic back-trajectory algorithm of Dirmeyer and Brubacker (1999) is applied and extended to other case studies. The surface sources of water evaporating and later producing rainfall during the event were determined through the calculation of back trajectories of water vapour in a quasi-isentropic way: in fact the trajectories can not be considered isentropic as the height of parcels at each time step is calculated on isentropic surfaces, but the wind which is used to move the parcels from a gridbox to another is defined on isobaric surfaces. Note that the method assumes that there is sufficient stratification and absence of significant diabatic processes to permit *tagging* single air parcels by means of their potential temperature. Three dimensional fields (horizontal wind, temperature and specific humidity), provided as part of the NCEP reanalysis archive (Kistler et al., 2001), are instead originally available on a 1.875° $\times$ 1.875° global grid and 28 vertical levels, with only 8 levels under the 300 hPa height: the vertical structure of humidity and wind fields in the planetary boundary layer is therefore coarsely resolved.
Back-trajectory calculations are performed from each specified grid square i where precipitation has occurred, at a rate proportional to the precipitation rate on the same grid box: each parcel represents a unit of precipitation onto the grid box i. The assumption is that a precipitation parcel can fall from any level: for this reason, the computation of the air parcel back trajectory is started from a random level in the vertical. The vertical probability distribution of the random function depends on the precipitable water content in the atmospheric column below each vertical

level. Column-integrated precipitable water PW between the surface and a specific vertical level is calculated according to the equation:

$$PW = \frac{p_s}{g} \int_{\sigma}^{1} q d\sigma \tag{3.18}$$

where the variables q and p_s represent respectively the specific humidity and the surface pressure, g is the acceleration of gravity and σ is the vertical sigma-coordinate given by $\sigma = \frac{p}{p_0}$ (p_0 is equal to 1000 hPa and p is the pressure at the σ-level). To randomly sample the starting height from

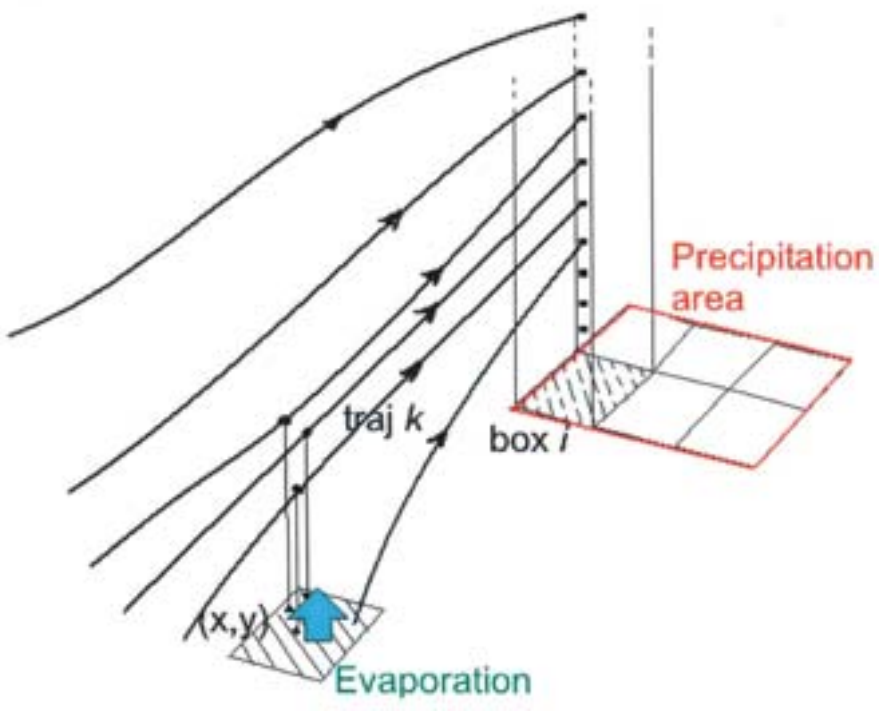

Figure 3.5: Scheme of water vapour transport adopted in the approach of Dirmeyer and Brubacker (1999)

σ = 0 to 1, a cumulative distribution function is assigned, so that the probability P_c of the back trajectory whose integration starts from $\sigma <$ c is

$$P_c = 1 - \frac{PW_c}{PW_i} \tag{3.19}$$

where PW_i is the total precipitable water in the column over grid box i and PW_c is $PW_c = \frac{p_s}{g} \int_c^1 q d\sigma$. Each water vapour parcel in the precipitation column is assumed to have an equal probability of being rained out; it follows that the larger portion of precipitation comes from the lower levels,

where the concentration of water vapour is higher.
In the model of Dirmeyer and Brubacker (1999), as a parcel k is tracked back in time from the grid box i, the evaporative sources contributing to increase its water vapour content over the grid box underlying the parcel at the time t are evaluated, whereas the horizontal moisture convergence in the same gridbox is not taken into account (Fig. 3.3.1). The rate of evaporation is computed at each time step of the trajectory integration as

$$R_{i,k}(x,y,t) = \frac{E(x,y,t)}{PW_i} \tag{3.20}$$

where $E(x,y,t)$ is the evaporation from the grid box (x,y) underlying the parcel k at the time t, $R_{i,k}(x,y,t)$ is the contribution of the grid box (x,y) to the total column precipitable water PW_i, at the time of the rain event over the grid box i. Equation 3.20 implies that the evaporated moisture is well mixed in the lower troposphere: the assumption is well verified for the low atmosphere layers at the time when most evaporation occurs, i.e. during daytime. So after m parcels have been launched from the target area A, formed by n grid squares, the water mass contribution of evaporation from grid square (x,y) to precipitation onto area A is given by

$$E_A(x,y) = \sum_{i=1}^{n} \sum_{k=1}^{m} \sum_{\tau=0}^{t_f} R_{i,k}(x,y,t_p+\tau) \tag{3.21}$$

where t_p is the time when precipitation occurs, τ is given by $\tau = -n\Delta t$ (with Δt the integration time step), $-t_f$ (where $t_f = -n_f\Delta t$) is the duration of the longest back-trajectory. By this formulation of the evaporation contribution to the final precipitation the possible phase changes along the path, which could modify the moisture and energy content of the parcel (condensation, re-evaporation of cloud liquid water) are not taken into account. The assumption is that along the path there are no sources or sinks of water vapour other than surface evaporation and rainfall events in the area A. In fact, in the method proposed by Dirmeyer and Brubacker (1999), all the parcels which are over the grid box (x,y) at the same time, lost over it the same amount of water as a contribution to local evaporation, without taking into account their height and the real thermodynamic profile over the grid box, which gives information on the actual vertical distribution of specific humidity. In conclusion the method adopted by Turato (2003) presents a lot of weak points:

1. Quasi-isentropic backtrajectories are affected by large errors.
2. Analysis fields display a coarse spatial and temporal resolution.
3. The assumption that a precipitation parcel can fall from any level does not take into account the state of saturation of various vertical levels.

4. The condition of well mixed distribution of water vapour within the troposphere is not always verified.

5. Sources or sinks of water vapour along the path are not taken into account.

6. The method has to get as an input the evaporation field too, besides the 3D field of water vapour concentration

3.3.2 The method proposed here

In the paper of Turato (2003) the method from Dirmeyer and Brubacker (1999) is used to analyse single events: probably it would be more suitable to climatological studies where computational errors could compensate each other. In the present work a more restrictive approach is followed both in the computation of trajectories and in the analysis of water vapour budget (chapter 4).

The model

Five-day back-trajectories are computed using the Lagrangian model FLEXTRA (Stohl and Wotawa, 1995), which integrates fully 3D-trajectories interpolating wind records to current particle position and implementing the Petterssen (1940) scheme (section 3.1.1). The Petterssen (1940) scheme is accurate to the second order. The integration time step is not fixed: it corresponds to the time lag which simultaneously satisfies the Courant-Friedrichs-Lewy criterion $\Delta t < \frac{\Delta x_i}{|v_i|}$ (Seibert, 1993) for the 3D components and for all the trajectories. FLEXTRA interpolation of the wind field is linear in time, bicubic in the horizontal and polinomial in the vertical 3.1.2.
Representative ending points for the trajectories to be calculated have been selected as the grid-points of a 3D-grid with a $0.5\ ^\circ \times 0.5^\circ$ horizontal resolution and 200m vertical resolution (from 1500m to 5900m above sea level). This implies a total number of $N_z = 23$ horizontal levels; on each of them $N_x \times N_y = 5 \times 4$ grid points are set, resulting in an overall number of $N_T = 460$ endpoints over Trentino (see Fig. 3.3.2 and Bertò et al. (2004)). It is implicitly assumed that 460 ending points properly represent sufficiently properly the thermodynamic state of the air masses producing precipitation over the target area. Note that a minimum height of 1500m s.l.m. has been chosen to end trajectories over ECMWF orography. A maximum height of 5900m s.l.m has been set assuming the contribution of upper troposphere to the precipitation be negligibile.
Then 460 back-trajectories arriving over Trentino have been computed every 3 hours. Each parcel is tracked until it leaves the model domain. Anyway the parcels are never backtracked for more than 5 days.

Figure 3.6: 3D-grid of the trajectory ending points over Trentino having 0.5° × 0.5° horizontal resolution and 200m vertical resolution

3.3.3 Choice of events and case studies

In the present thesis a method of analysis of strong precipitation over Trentino has been developed to study and decipher in detail the water budget of single case studies. As a consequence the attention was first driven on the most important recent extreme events of November 2000 and November 2002. Moreover this allowed to use 4d-Var analyses as input fields for the model. These type of analyses, produced operationally by ECMWF since November 1997, are very accurate: the model forecast is adjusted iteratively to minimize the deviation of the analysis from both the forecast and the observations in the whole assimilation time window (see section 3.1.2). Wind and other fields are provided every 3 hours on a regular grid of 0.5° × 0.5° and 60 levels in the vertical. Note that a net improvement is guaranteed by the time resolution of analyses: many authors outlined in their works the bad performances related to the use of analysis fields every 6 hours (Stohl, 1998; Wernli and Davies, 1997; Turato, 2003; Stohl et al., 2004). As a consequence it was necessary to increase the high spatial resolution too (section 3.1.2).
In the most recent meteorological literature numerical modelling has been applied to exemplary

case studies because they were representative of recurrent meteorological conditions or because they occurred during intense measurements campaigns, as it was the case of MAP (Buzzi and Foschini, 2000; Gheusi and Stein, 2002; Keil et al., 1999; Rotunno and Ferretti, 2001; Medina and Houze, 2003). These special events happened quite recently, i.e. since the global numerical models became operational and since the global assimilation network became sufficiently dense to initializate the global models themself. Actually in the past more extreme events occurred which were more worth of attention, at least for the amount of precipitation. For two years the European Center for Medium Range Weather Forecast (ECMWF) has made possible to access ERA40 by all users from the Member States. ERA40 are high resolution analyses obtained by the modern 4d-Var assimilation system for the time period from 1954 to 1994. This dataset allows, for the first time, to study all the extreme precipitation events of the last 50 years. The most intense meteorological event occurred in Italy (and in particular the considered target area) was the alluvional event of 1966.

In conclusion the events most carefully described and reported in the following section are the alluvional events of November 1966, November 2000 and November 2002. The model algorithm and the type of data were the same except for the time resolution of analyses since ERA40 are given every 6 hours. Furthermore it is realistic to associate larger errors to the ERA40 fields, as they were obtained from rare observation data.

Note that the considered events fall in November: in fact the most abundant precipitation on the meridional slopes of Alps are always registered in October or November. Sometimes they are even preceded by colder episodes producing snow: the high temperatures and the high rate of precipitation can produce a sudden snow melting increasing the risk of flooding, while summer storms were not considered. Sometimes they can be really extreme but most of the water vapour has a local origin (i.e. from evapo transpiration): this kind of water transport has not been analysed in the present work.

4 Back trajectories: applications

The choice of the case studies to test the Lagrangian analysis as well as the results from the computation of ensembles of back trajectories are shown. The chosen extreme precipitation events are the flood events of 3-5 November 1966, 16-18 November 2000 and 24-26 November 2002. Emphasis is given to the regional budget analysis over the Mediterranean basin and in particular to the estimation of the evaporation fluxes contributing to increase the moisture of airstreams producing intense precipitation over the Alps during the selected events.

4.1 Synoptic characterization of selected events

A comparison among the three synoptic conditions is presented which produced the intense precipitation events.

4.1.1 Flood event of 3-5 November 1966

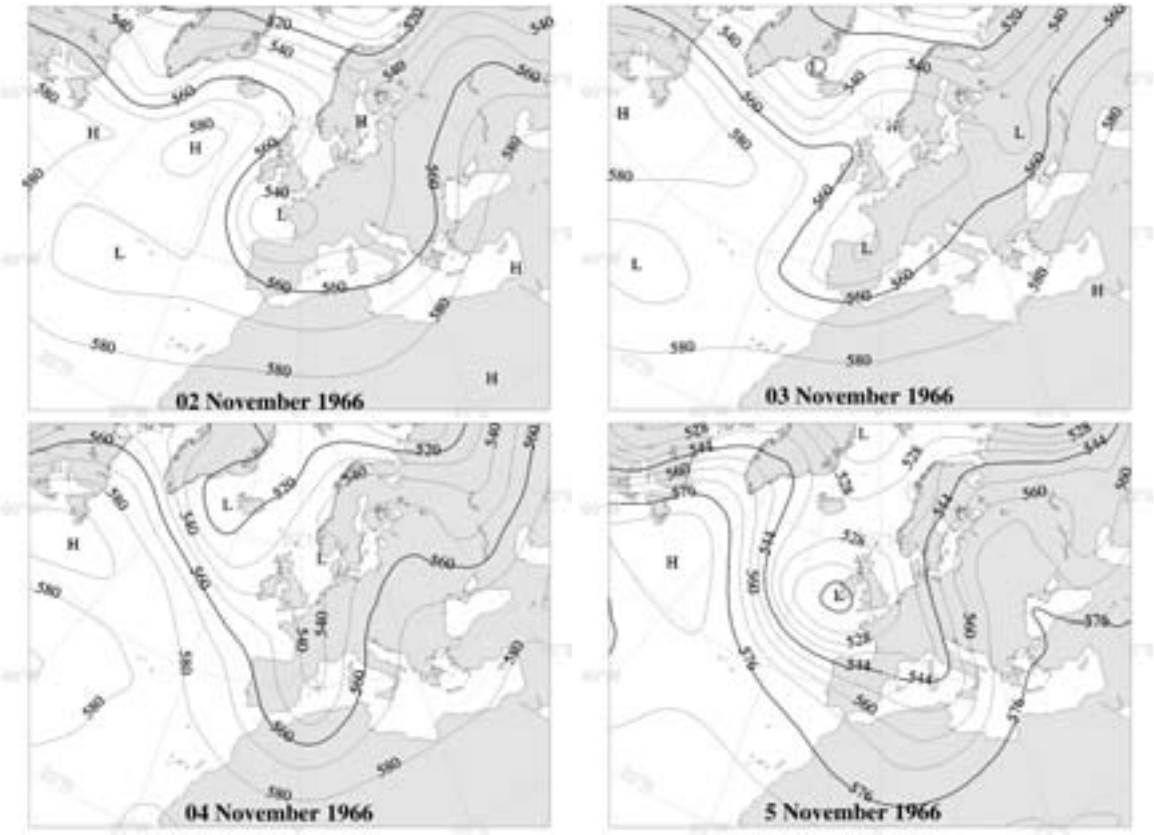

Figure 4.1: 500 hPa geopotential maps from ERA40 reanalyses for 02, 03, 04 and 05 November 1966 at 00 UTC.

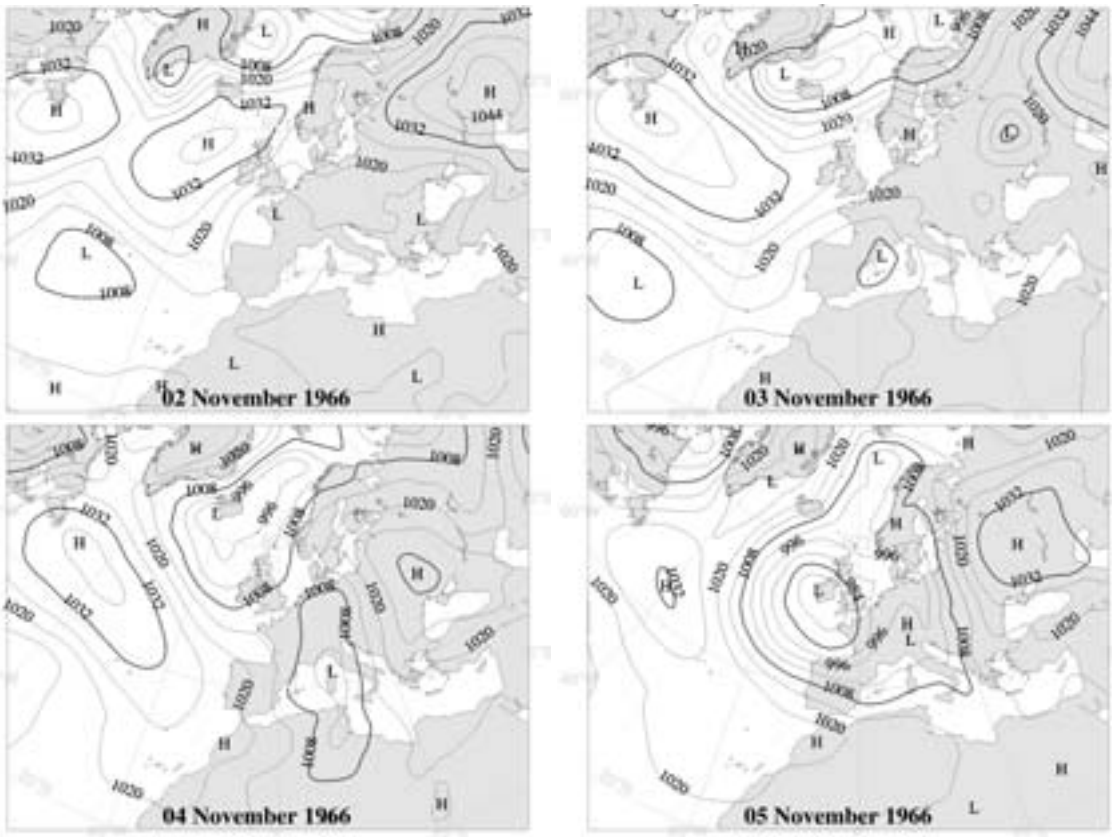

Figure 4.2: Surface pressure maps from ERA40 reanalyses for 02, 03, 04 and 05 November 1966 at 00 UTC.

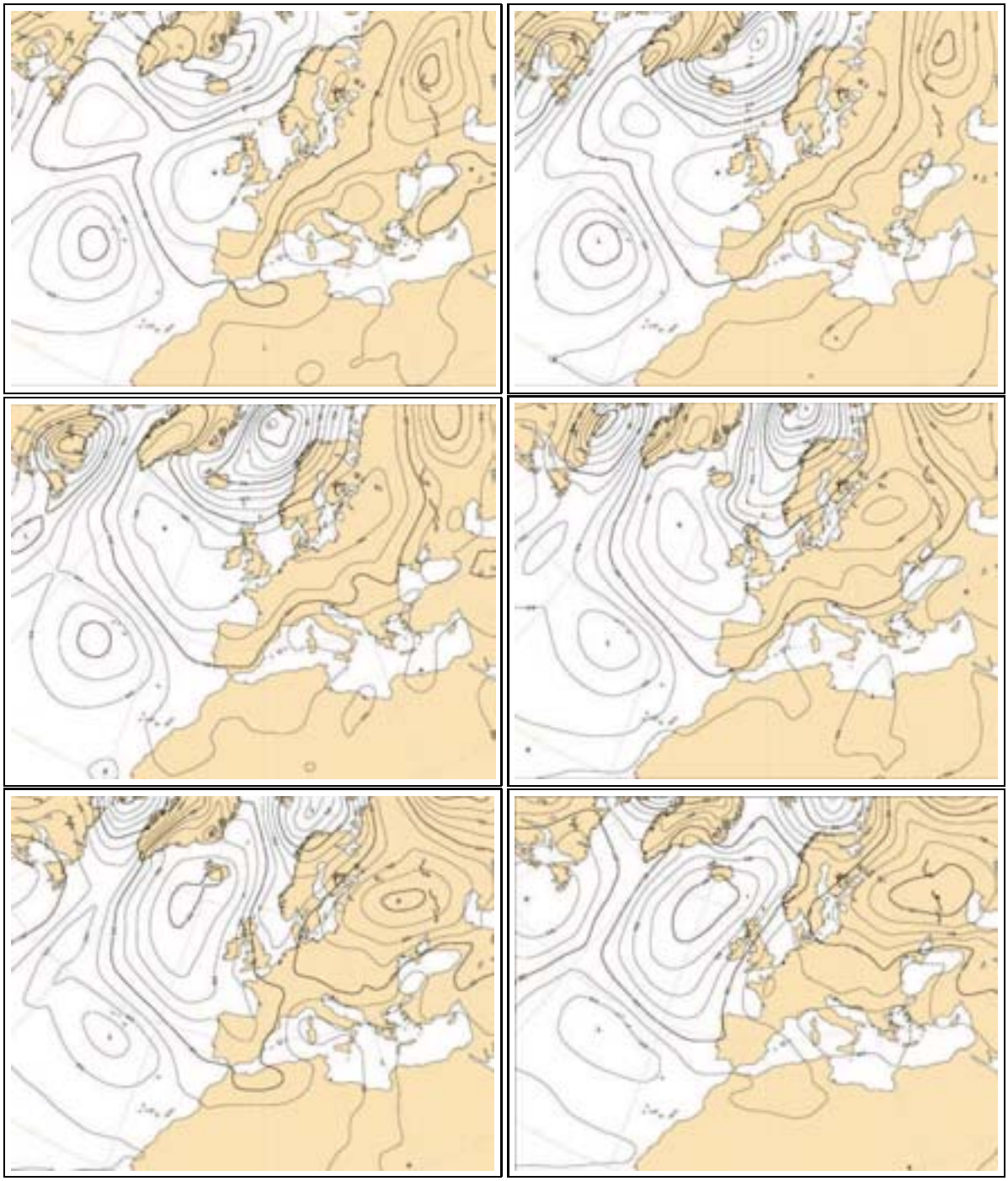

Figure 4.3: Surface pressure maps from ERA40 reanalyses for 30 October 1966 00 UTC and 12 UTC, the same for 31 October and 01 November.

The alluvional precipitation event which hit Italy in 1966 originated in Sardinia in the early hours of 03 November and ended over Friuli in the late hours of 05 November. The event, short but intense, was preceded by anomalous climatic conditions (Fea et al., 1968): surface temperature data show appreciable deviations (-6°C in the Artic area and +4°C over the Mediterranean Sea) from the mean values of the previous 30 years. Artic air invasions of the warm Mediterranean basin were announced destabilizing the temperate air masses residing over there and enhancing cyclogenetic conditions.
In figure 4.1 500 hPa geopotential height from ECMWF analysis is reported for 02, 03, 04 and 05 November 1966 at 00 UTC. In the previous days a strong ridge extended northward over the Atlantic Ocean favouring the formation of a trough over Europe and the descent of cold air toward the Mediterranean Sea and the Northern Africa on 2-3-4 November. At the beginning (2 November) the trough seemed to be cut off from the main zonal air stream, but during 3 November a new intense small scale wave, moving over the North Atlantic Ocean along the isobars of the wider low, contributed to the deepening of the latter in the meridional direction. At the beginning of 4 November the pressure configuration was dominated by a narrow and elongated trough over Europe drawing, on its west side cold air from Greenland, over Spain and over the Sahara desert in Algeria; on its east side warm and wet air from the Mediterranean Sea towards Scandinavia.
The surface pressure map of 2 November (Fig. 4.2) showed an unusual synoptic configuration: a band of anticyclones around 45° - 60°N and a low pressure band around 30° - 45°N. Within the latter one 4 low centers can be distinguished:

- a center over the Atlantic Ocean which was related to the 500 hPa trough extending toward the western Spain; this low was going to migrate westward losing importance for the Mediterranean area;
- a weak low between Turkey and the Balcans moving north-eastward;
- a low center over France and a lee side low between Morocco and Algeria, which were going to merge and to deepen on 3 November over the western Mediterranean Sea; this was the low system producing a lot of precipitation over Italy between the 3rd and 4th of November.

During the 3 and 4 November, the initial zonal configuration changed into a dipole with an area of low pressure over the eastern Atlantic Ocean and Europe and two areas of high pressure over the central Atlantic Ocean and over the East of Europe.
Over Italy, the event was announced by an increase in surface pressure over the Adriatic Sea and over North-Eastern of Italy in the night between 2 and 3 November, due to a barrier effect: cold and dense air masses at low tropospheric levels were driven from the Balcans by south-southeasterly

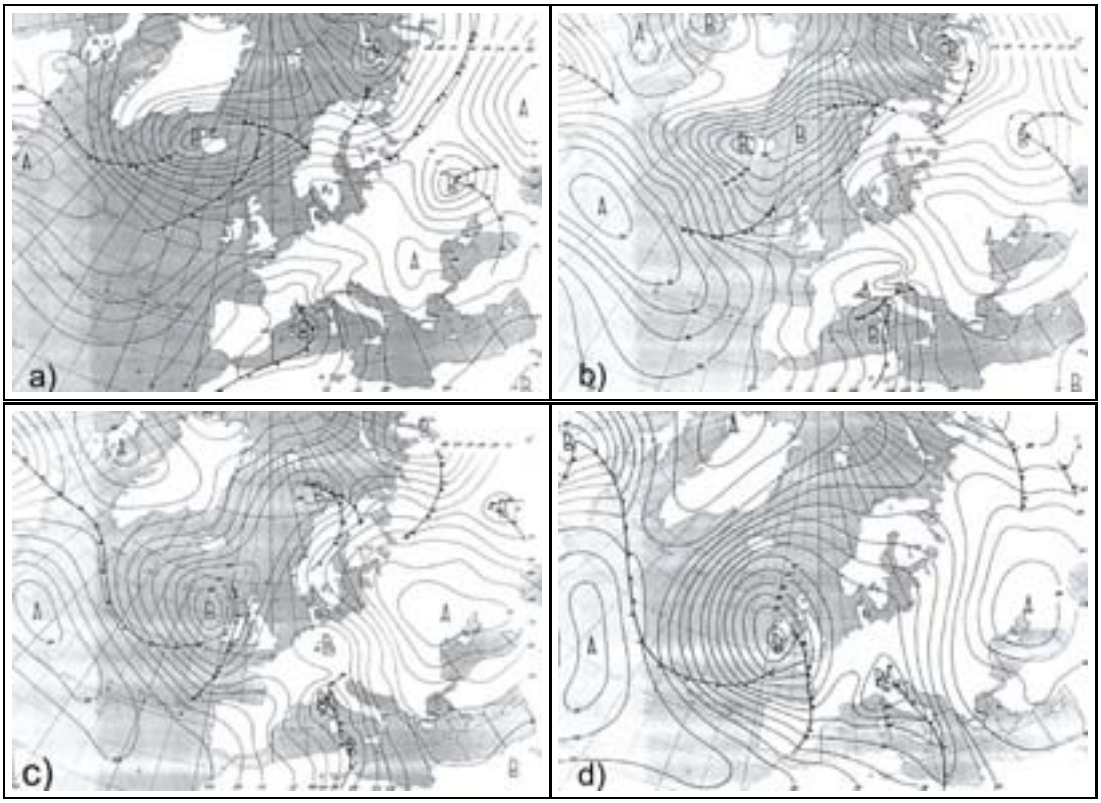

Figure 4.4: Surface front charts on 03 November 1966 06 UTC (a), 03 November 1966 18 UTC (b), 04 November 1966 06 UTC (c), 04 November 1966 18 UTC (d) from Fea et al., 1968. Pressure isolines differ for 4 hPa. The letter *A* stands for high pressure, the letter *B* for high pressure.

winds and trapped in the Po Valley between the Alps and the Apennines. During the day after a cold meridionally oriented front, organized in convective bands, extended from the Northern of Italy towards the South, moved very slowly eastward strongly affecting Liguria and Tuscany in the night between 3 and 4 November (Fig. 4.4). The convective cold front, clearly seen by the radar of Aeronautica Militare Italiana (Fea et al., 1968), caused the well known Arno flood which in particular hit the city of Florence.

East of the cold front, a strong pressure gradient arose generating a narrow warm prefrontal jet with extraordinary high values of the surface wind intensity over the Adriatic Sea, the South of Italy, Sardinia and Tunisia. In Venice the highest ever tide was measured: 1.98 m above the mean sea level. Locally there was also a contribution of the orographic effects, Appennines being oriented north-west to south-east and forming a sort of funnel with the meridional cold front, forced the uplift. The warm front, being east of the cold front and ahead of the ”warm conveyor belt”, moved

quickly along the Adriatic Sea toward the Alps. Nevertheless, although warm air stepped over the Alpine chain, a cold pool remained trapped at very low level during 3 November 1966. So the upper warmer air entered the Central Europe, but a sort of surface warm front remained apparently stable over the Po Valley until 4 November 00 UTC.
In Trentino, most of the precipitation occurred from 3 November 21 UTC to 4 November 12 UTC (Fig. 4.5). This was mostly produced by the progressive erosion of the cold pool along the Alps.

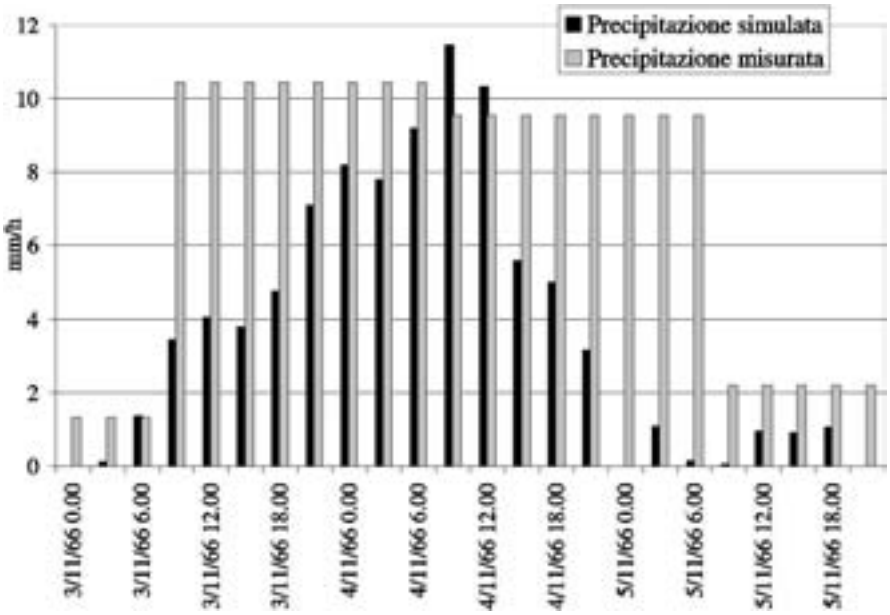

Figure 4.5: Mean precipitation over Trentino so as simulated from Lagrangian specific humidity variations in $mm\,(3h)^{-1}$ in the period from 03/11/66 00 UTC to 05/11/66 21 UTC.

The process was accompanied by temperature rising and conversion of solid precipitation into rain even at relatively high levels (Fea et al., 1968).
Fea et al. (1968) already performed the evolution of the spatial distribution of specific humidity on the 850 hPa isobaric surface at 00 UTC of 02, 03, 04, 05 November 1966 starting from the data of various scattered radiosondes (Fig. 4.6). On this basis they proposed that much of moisture, producing strong precipitation over Italy, had been advected over the Mediterranean Sea from the Atlantic a few days before the event: in the following chapters this hypothesis will be examined.

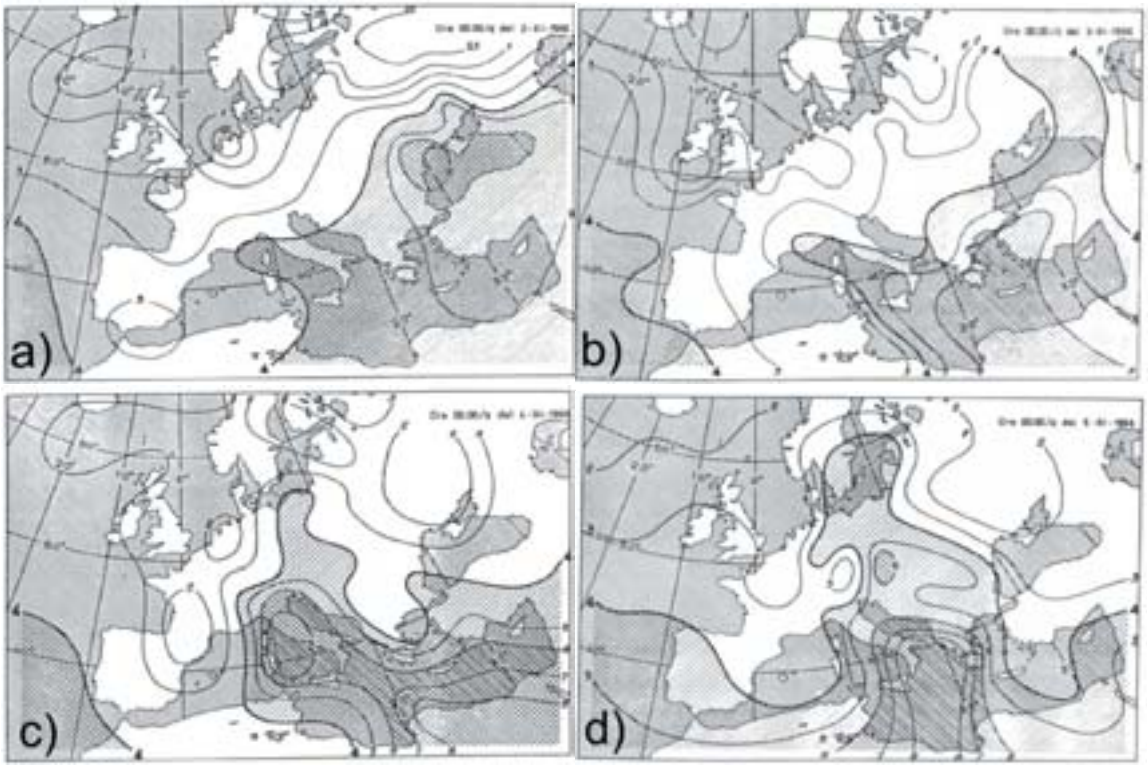

Figure 4.6: Spatial distribution of specific humidity on the 850 hPa isobaric surface at 00 UTC of 02 (a), 03 (b), 04 (c), 05 (d) November 1966 (Fea et al., 1968). Contours indicate specific humidity isolines with intervals of 1 gkg^{-1} (thin contours); bold contour marks 4 gkg^{-1} isoline (shaded where $q > 4\ gkg^{-1}$).

4.1.2 Flood event of November 2000

On the isobaric surface, 500 hPa a trough developed on 15 November (Fig. 4.7) over Central Europe extending towards the Iberian Peninsula. Such a configuration resembles the initial synoptic pressure distribution of November 1966 (Fig. 4.1): in November 2000 the through was more elongated and there was no a cut off from the mean zonal flow. The main long wave (the through) extended to a latitude of 45° with the 560 dam geopotential height; the short wave moved from Spain (15 November) eastward. This first short wave was followed by a second one descending from the North-West of Europe (Greenland, England) to the South of France: after that (17 November) the two short waves merged, enhancing a low pressure tongue extending from the North-Atlantic Ocean to the western Mediterranean Sea.

The strong winds over Gibraltar on the 15th of November, associated with the cold front, flew over the Atlas chain thus favouring the formation of a lee-side surface depression (Fig. 4.8). After that

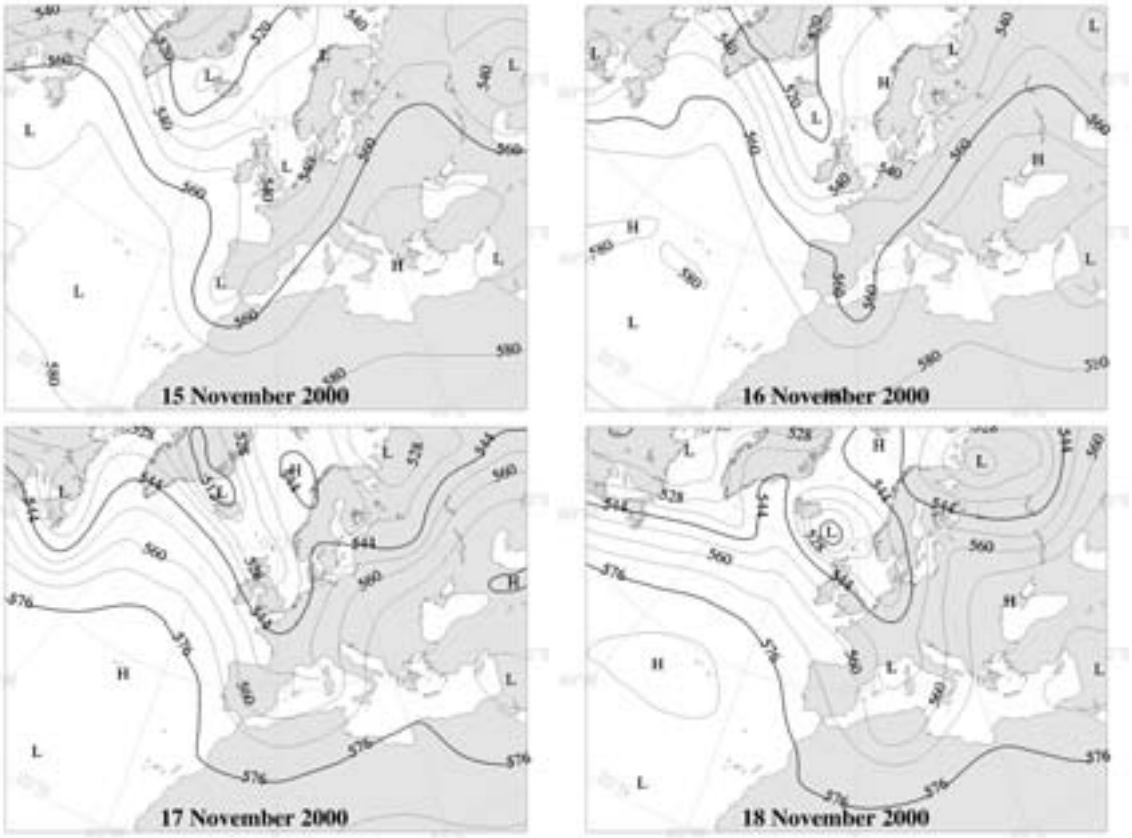

Figure 4.7: 500 hPa geopotential maps from ECMWF reanalyses for 15, 16, 17 and 18 November 2000 at 00 UTC.

the surface low moved north-eastward embedded in the previous cold front (Fig. 4.9) and reinforced by the deepening of the upper level baroclinic trough which was located only a few hundred kilometers westward. On the 17th November the surface low moved over the Gulf of Genoa as well as the 500 hPa trough: then the mean hourly precipitation over the target area reached its maximum values (Fig. 4.10).

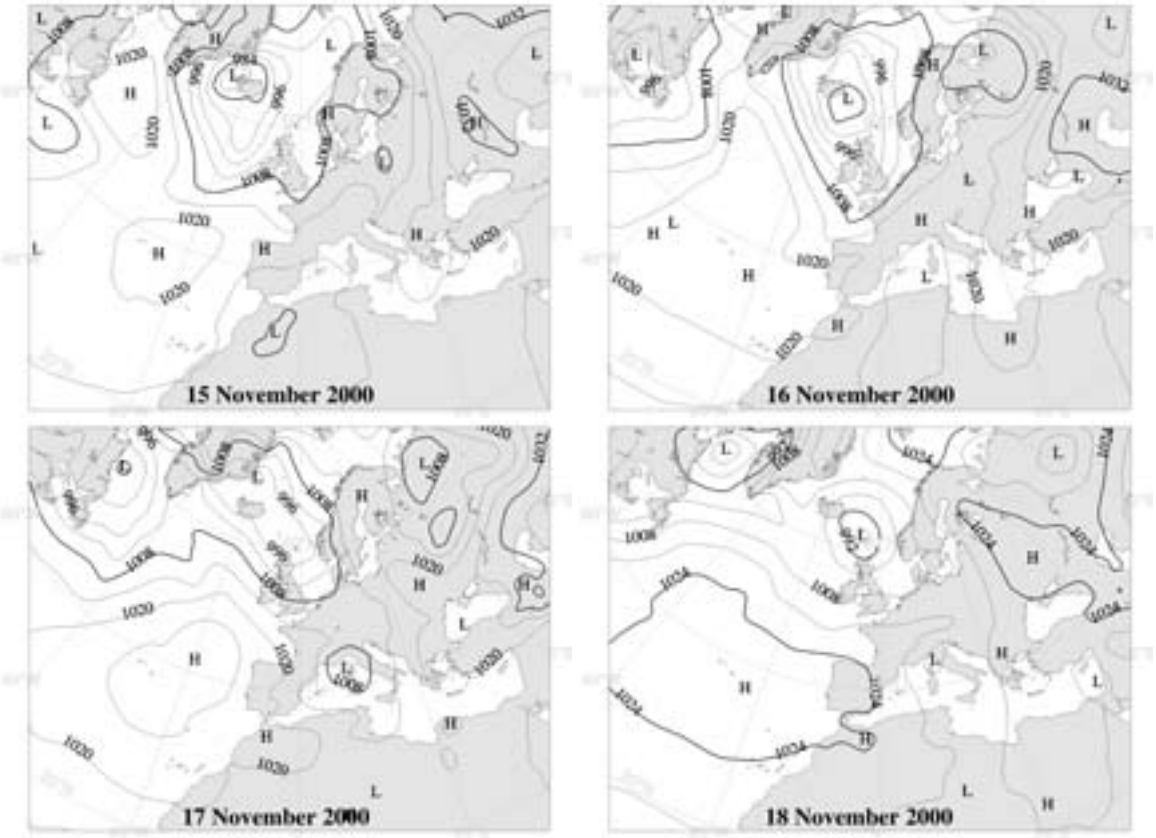

Figure 4.8: Surface pressure maps from ECMWF reanalyses for 15, 16, 17 and 18 November 2000 at 00 UTC.

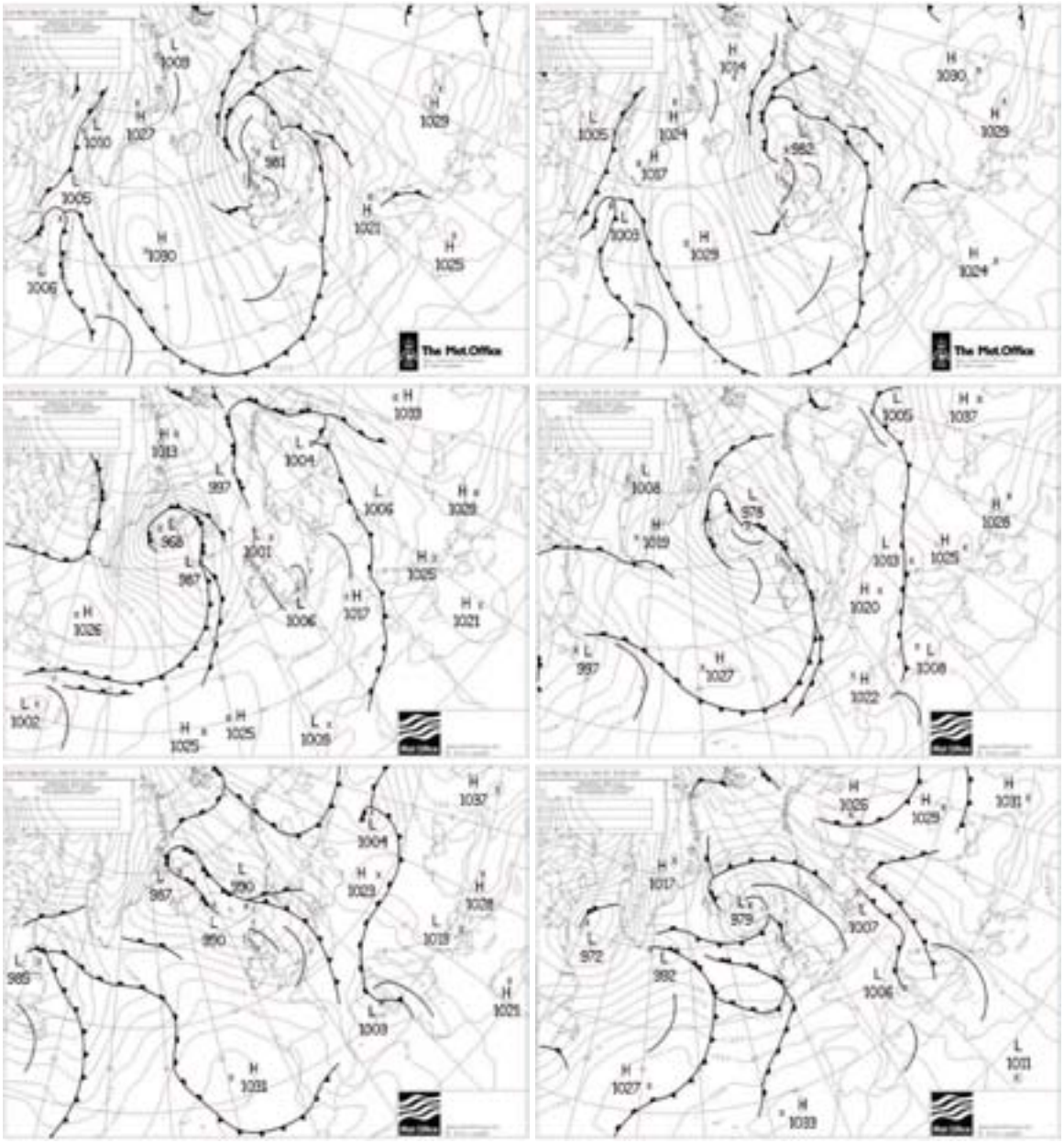

Figure 4.9: UKMO surface front charts on 13 November 2000 00 UTC, 14 November 2000 00 UTC, 15 November 2000 00 UTC, 16 November 2000 00 UTC, 17 November 2000 00 UTC, 18 November 2000 00 UTC (pressure isolines differs° for 4 hPa). The letter *H* stands for high pressure, the letter *L* for high pressure.

In summary, in the event of 2000, the cold front moved slowly from West to East over the Tyrrhenian Sea and then over Central Italy in the south of the low center. The warm front was driven by southerly winds against the alpine barrier. It was slightly oriented north-eastward and not exactly along the zonal direction as in the flood event of 3-5 November 1966.
As previously explained a number of elements are common to both the events. The following differences have, however, been recognized:

1. In 1966 the narrow and elongated trough extending along the meridians (Fig. 4.1) was more or less 20 dam deeper: on the 3th November 1966 the 540 dam isoline reached Sardinia, whereas on the 17th November 2000 it was over Denmark.

2. In 1966 the deeper upper level trough produced a more marked surface pressure gradient over Italy in the zonal direction causing a stronger wind jet in the meridional direction: over the southern Adriatic Sea isolines differing by 8 dam were separated by about only 250 km, roughly corresponding to a wind velocity of 30 m/s. In fact in 1966 the East of Europe was dominated by a surface anticyclone on 3-4 November, while in 2000 the original cold front was extended, oblique to meridians, from the West Mediterranean Sea to Polonia and Russia, thus favouring the deepening of some low centers along the front.

3. In the 2000 case study, the surface low originated essentially over the North Africa, in 1966 besides this contribution, there was already a lee side low over France, amenable to the preexisting cut-off upper-level low of 2 November. The resulting surface low system over Italy resulted to be wider and deeper (minimum less than 1000 hPa).

4. The surface high pressure on the East Europe was stronger in 1966 (the 1024 isolines are over the Balcans and over the south of Italy on 4th November), thus favouring also a marked pressure gradient at the surface.

5. In 2000 the cold front was rather short, extending north of the coasts of Africa: the cold air behind could not reach the Sahara desertic region, failing to start a meridional low-level jet over Southern Italy and over the coasts of Tunisia (Fig. 4.9).

The deepening and extending of the low during the 1966 event over the entire central and western Europe was combined with the weakening of the preexisting high pressure system, which migrates westward toward the north Atlantic coasts of America. This anticyclone forced the zonal flow to move at a very high latitude (60-70°). So air masses contributing to precipitation did not come from the Atlantic, but from northern Europe or North Africa.
In 2000 synoptic conditions were similar but not so extreme. The main low remained farther

North, near Iceland and the anticyclone over the Eastern Europe remained very weak. So the surface low over Italy was not attracted by the main trough, and it became a surface cutoff low persisting over the Gulf of Genoa. The cold front moved toward the South-East being uncoupled from the low system; on the contrary, the orographic precipitation persisted on 18-19 November over the Alps, fed by the "Stau" effect.

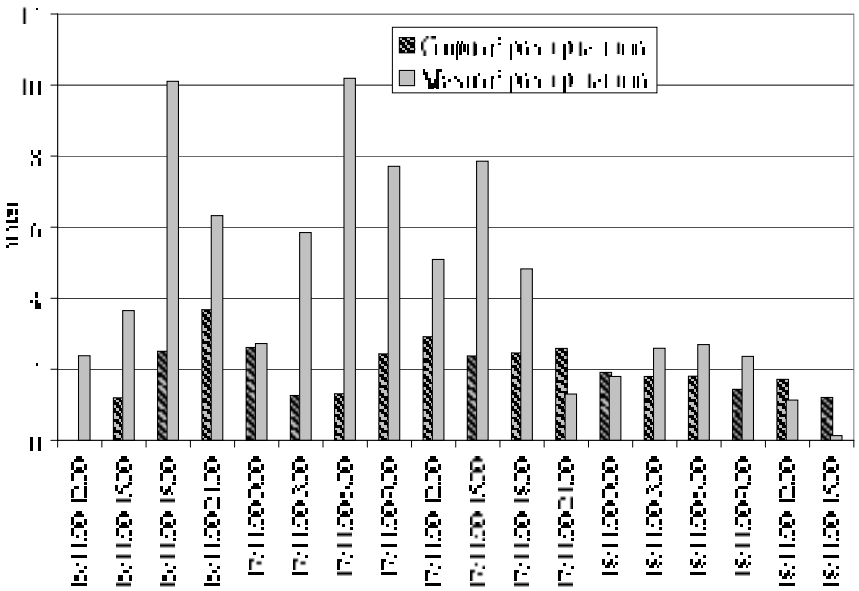

Figure 4.10: Mean precipitation over Trentino so as simulated from Lagrangian specific humidity variations in $mm\,(3h)^{-1}$ in the period from 15/11/66 00 UTC to 18/11/66 21 UTC.

In 2000, extreme values of precipitation were not recorded, but the event lasted for several days (Fig. 4.10). In Trentino it provoked landslides, but not floods.

4.1.3 Flood event of November 2002

In November 2002, Trentino was hit by an intense precipitation event. The hourly average precipitation over the whole Province is shown in Fig. 4.11: estimations, based on the lagrangian analysis (section 4.2.1), agree with rain gauge measurements (within $\pm$ 5 %) in the first day of the event, but they systematically overestimate precipitation amount (about + 45 %) in the second day, with the exception of the "tail" of the event, when precipitation was decreasing. The total measured precipitation amount (average over the area) was 125 mm, but maxima of 255 mm were recorded at some weather stations. This uneven distribution may be ascribed to the effects of complex orography, which is poorly reproduced by the ECMWF models. Two main precipitation spells can be

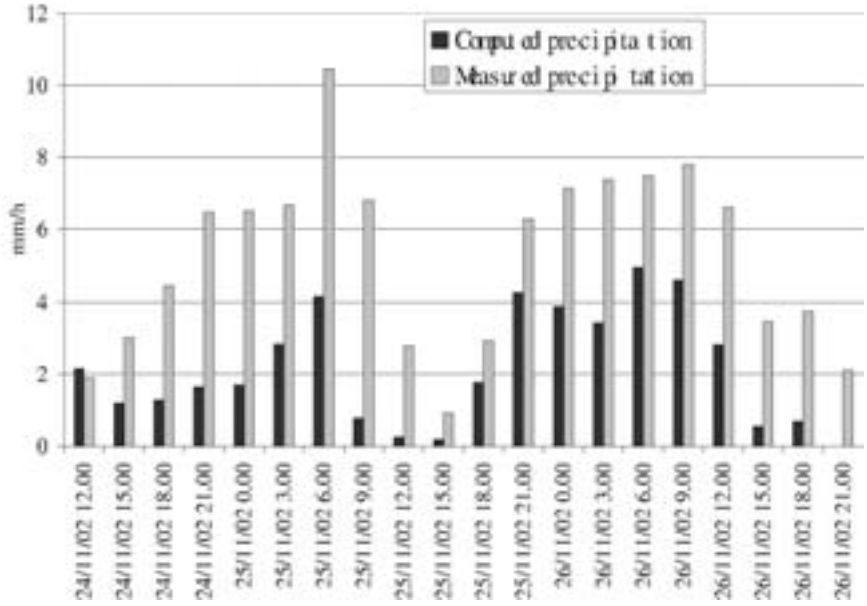

Figure 4.11: Mean precipitation over Trentino so as simulated from Lagrangian specific humidity variations in $mm\,(3h)^{-1}$ in the period from 24/11/02 00 UTC to 27/11/02 21 UTC.

recognized in Fig. 4.11: the first between 24 and 25 November and the second between 25 and 26 November.

The 500-hPa geopotential height maps from ECMWF 4d-Var analyses (Fig. 4.12) display a baroclinic wave extending from the East Atlantic to northern Europe, with a cut-off low over England. At the sea surface, an intense cyclone, with a minimum of 976 hPa, affected north-central Europe (Fig. 4.13). By 24 November the wave became deeper and extended its main axis southward, as the deepening short wave migrated from the mid-Atlantic toward the Iberic peninsula, while the upper level jet moved toward Spain and the Atlas (Fig. 4.12). As a consequence, a surface low-pressure system developed downstream of the trough axis near Spain and Morocco (Fig. 4.13) and an intense south-westerly moisture advection developed in the low and mid troposphere from the Atlantic Ocean toward northern Italy (Fig. 4.14).

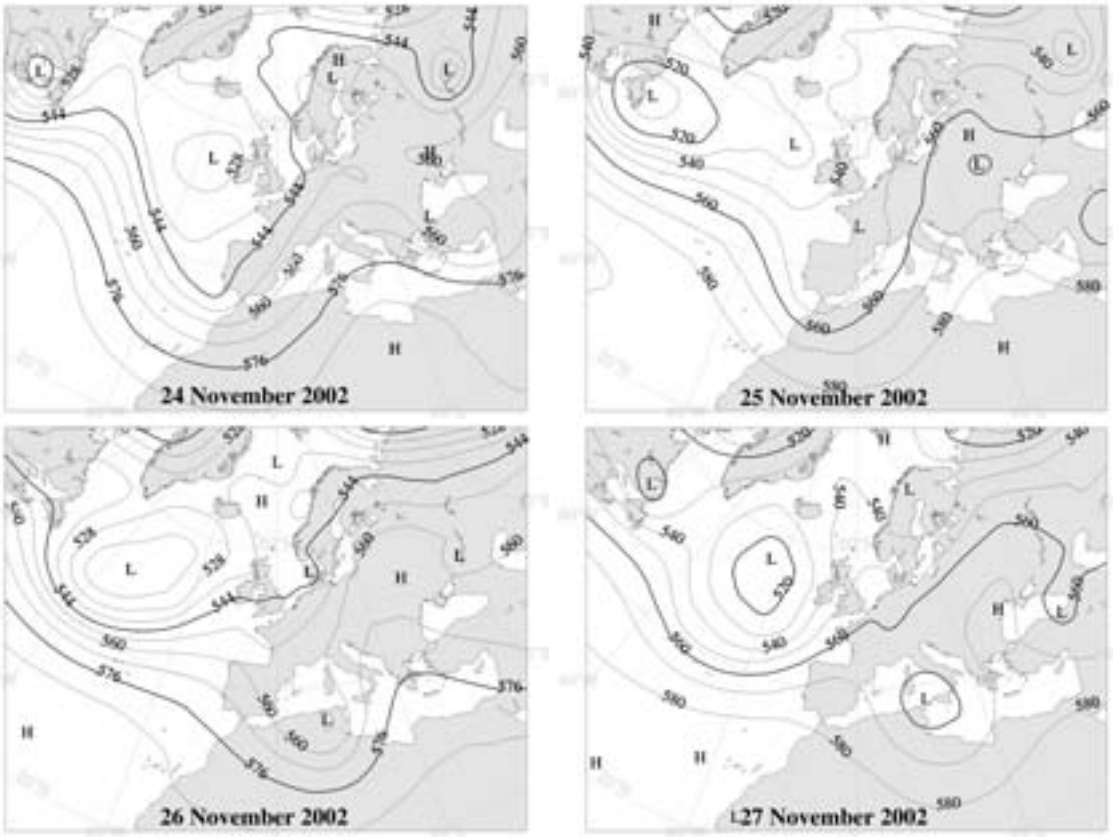

Figure 4.12: 500 hPa geopotential maps from ECMWF reanalyses for 24, 25, 26 and 27 November 2002 at 00 UTC.

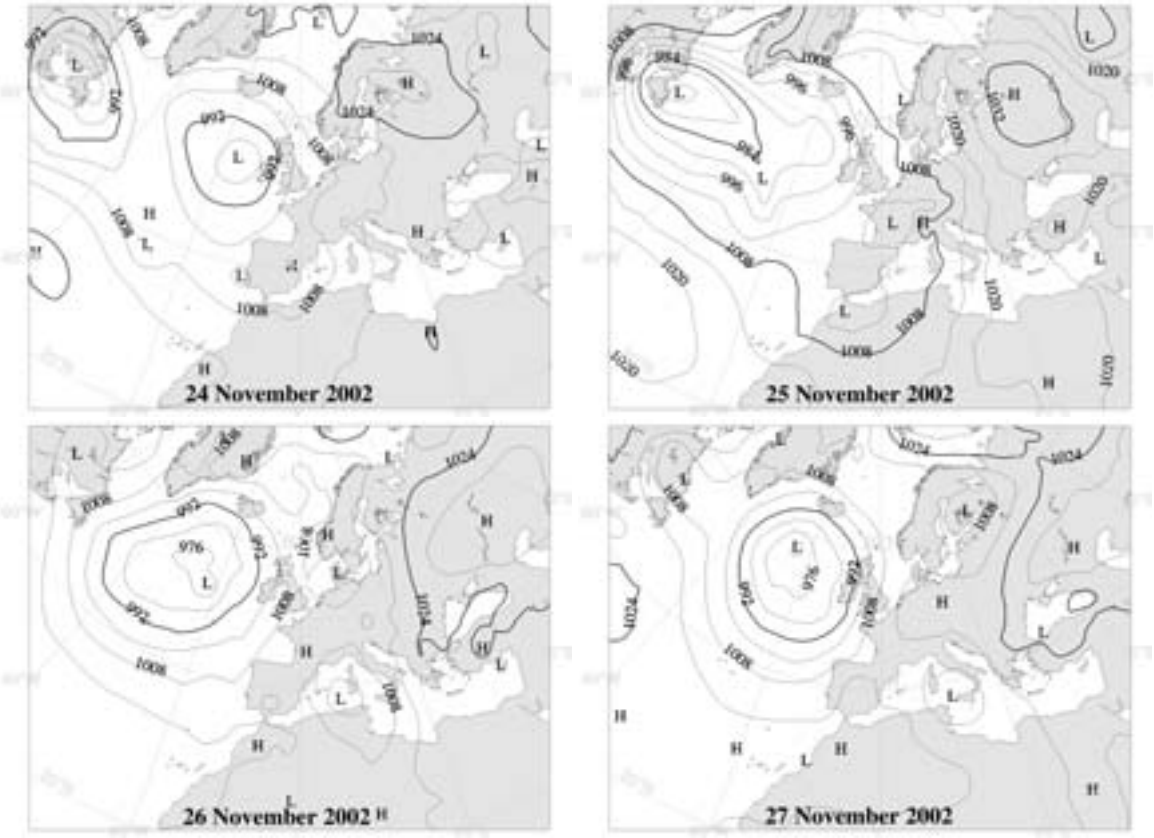

Figure 4.13: Surface pressure maps from ECMWF reanalyses for 24, 25, 26 and 27 November 2002 at 00 UTC.

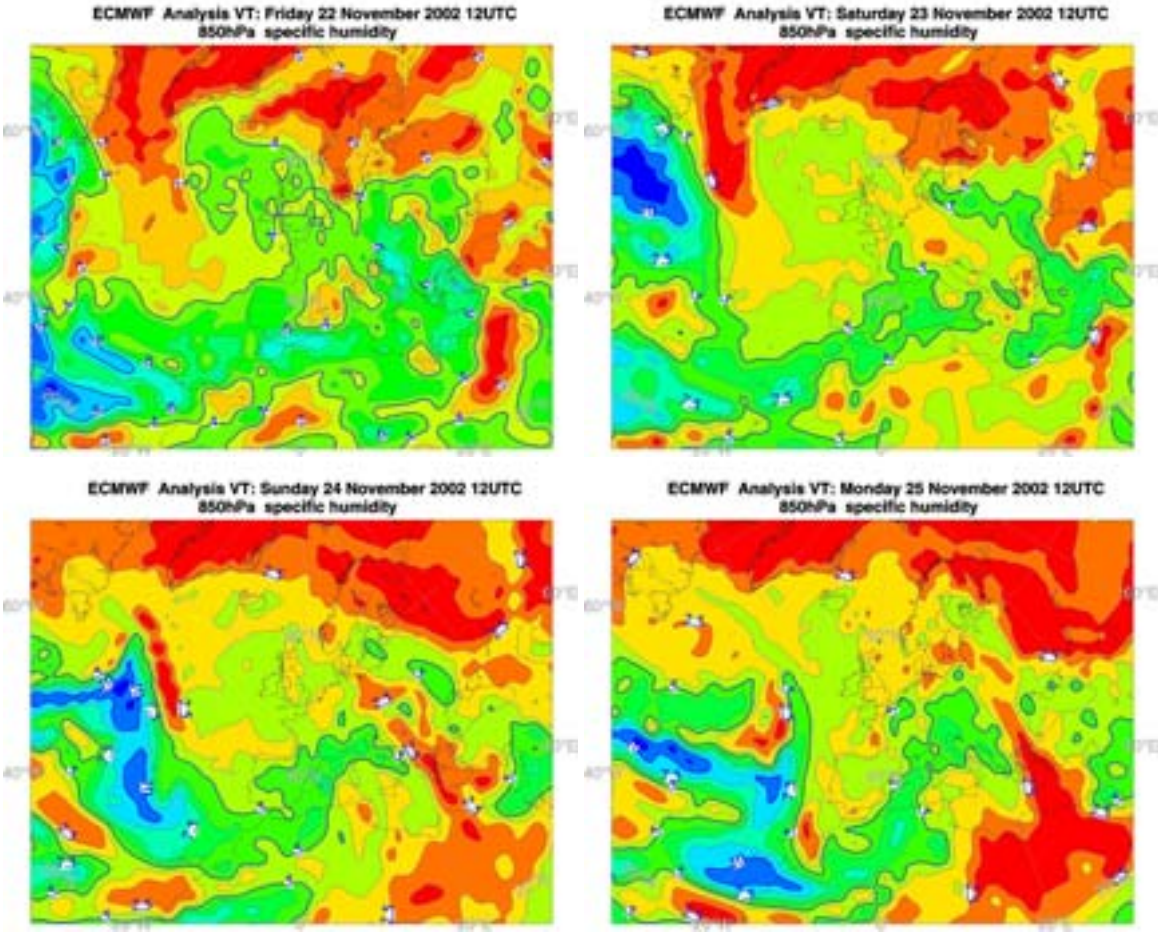

Figure 4.14: Specific humidity maps over 850 hPa surface from ECMWF reanalyses for 22, 23, 24 and 25 November 2002 at 12 UTC.

At some stages of the event, this moisture stream was enhanced by the contribution of mid-tropospheric "plumes" from the equatorial African region through the Sahara desert, as it will be shown in the following sections. Note that the synoptic configuration for the 2002 event is different from the former:

1. The trough at 500 hPa was over the Atlantic ocean: there was no anticyclone blocking the zonal flow occurring, with an upper level jet, at a latitude of 40°.

2. The upper level trough favoured the development of two surface lows on 25 November. One of the two lows moved into the Mediterranean Sea toward Southern Italy (26 November).

3. In 2002 neither an elongated trough over Italy in the meridional direction occurred (but rather a cut-off low well developed at all levels), nor a strong pressure gradient producing strong wind (Fig. 4.9).

4. At a first phase the target area was characterized by south-westerly winds produced by the approaching low (at the end of 24th November) and later by south-easterly winds induced by the cyclonic *return* effect (on 26th November).

The position of the surface cyclone as well as the direction of the warm front were quite similar to the case of 2000. But in 2002 event the cyclone moved alone in a south-eastward direction (in 2000 north-eastward in connection with the cold front). Moreover it had a longer cold front forcing meridional wind over the Gulf of Syrte as well as over the Tyrrhenian and the Adriatic Sea.

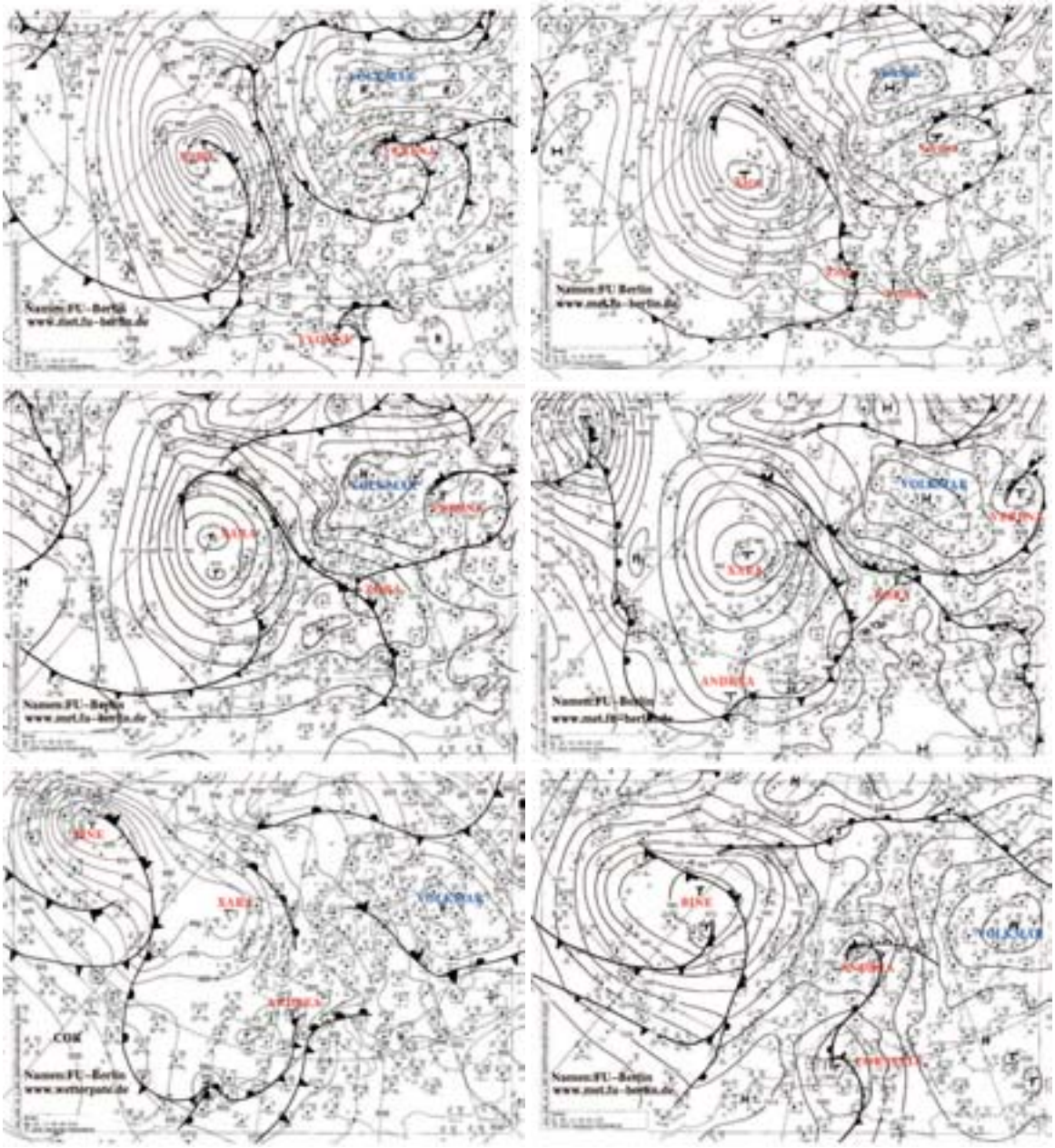

Figure 4.15: FU-Berlin surface front charts for 21 November 2002 00 UTC, 22 November 2002 00 UTC, 23 November 2002 00 UTC, 24 November 2002 00 UTC, 25 November 2002 00 UTC, 26 November 2002 00 UTC (pressure isolines differs for 4 hPa). The letter H stands for high pressure, the letter T for low pressure.

4.2 "Macro-area" analysis and evaporation

Analyses and numerical models provide fields of various quantities at high spatial resolution. Because of the large amount of data, the analysis domain has been subdivided into 12 macro-areas shown in Fig. 4.16. Each area corresponds roughly to a distinct geographical domain: the

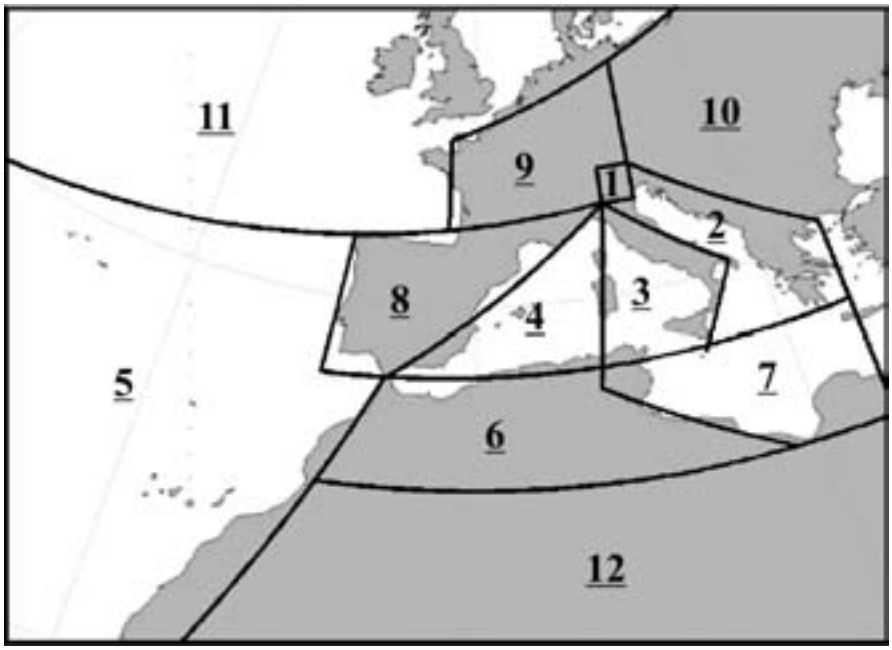

Figure 4.16: Subdivision of domain in areas

target area (1), the Adriatic and Ionic Sea (2), the Tyrrhenian Sea (3), the West Mediterranean (4), the central Atlantic Ocean (5), the Atlas chain and the northern side of Sahara (6), the rest of Sahara (12), the central Mediterranean Sea (7), Spain (8), central Europe (9), eastern Europe (10) and the northern Atlantic Ocean (11). Boundaries of selected areas have been commonly traced along meridians and paralleles. Lines easily defined by simple analytical expression have been drawn. Such a choice allows for condensing most of information in few parameters: this can be done when a detailed analysis is not necessary, as in the case of the study of water vapour source distribution. In Fig. 4.18 the spatial and temporal average of evaporation from various areas is reported summarizing information coming from 16 more figure than Fig. 4.17. Note that the latent heat flux field has been remapped from ERA40 reanalyses resolution to a resolution of 0.16° by means of bi-cubic interpolation to get Fig. 4.17.

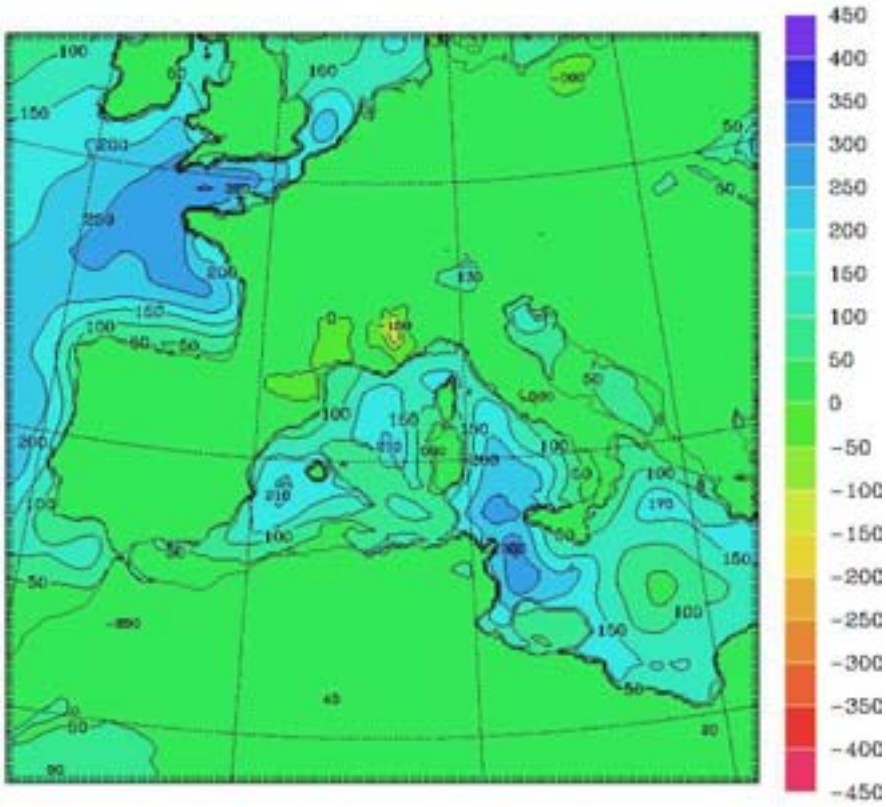

Figure 4.17: Latent heat remapped to a resolution of $0.16° \times 0.16°$ starting from ERA40 analyses valid on 02 November 18 UTC

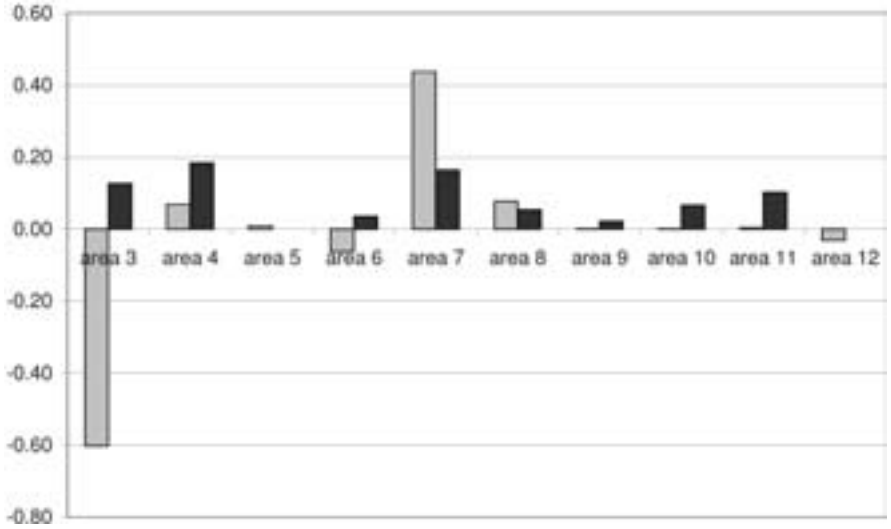

Figure 4.18: Average in time and in space of evaporation and of Lagrangian specific humidity variation (computed following the method described in the present paragraph) in kg m^{-2} h^{-1} over various areas (x-axis) in the period from 31/10/66 00 UTC to 04/11/66 00 UTC.

The latent heat is used to estimate the evaporation rate (per hour) through the simple formula:

$$ev = \frac{Q_l}{L(T)} \times 3600 \tag{4.1}$$

where ev is the evaporation, Q_l the latent heat flux of evaporation and L the latent heat coefficient which depends on absolute temperature (T). The mean evaporation ev_k over a specific macro-area is obtained by

$$\overline{ev_k} = \frac{1}{A_k} \int_{A_k} ev\,(\phi, \lambda)\, d\phi d\lambda \tag{4.2}$$

where ϕ is the longitude and λ the latitude, while A_k is the area of the domain.

4.2.1 Use of macroareas for Lagrangian budgets

Macroareas can be used to summerize information from Lagrangian analysis too. For example the mean values of position, temperature, humidity, etc. of parcels along their trajectories in passing over a specific macroarea is simply derived by the following formula:

$$\overline{y_k} = \frac{1}{\sum_{i=1}^{N_k} M_{i,k}} \sum_{i=1}^{N_k} \sum_{j=1}^{M_{i,k}} y_{i,j,k} \tag{4.3}$$

where $\overline{y_k}$ is the mean value of the physical quantity y over the k macroarea, $y_{i,j,k}$ the value of the physical quantity y for i-trajectory at the time step j in the passing over the k macro-area, N_k the number of trajectories passing over k macro-area and $M_{i,k}$ the number of time steps at which i trajectory passes over the k-th macro-area.
In the same way the mean variations of position, temperature, humidity, etc. of parcels along their trajectories, flowing over a specific macroarea, is obtained from the following formula:

$$\overline{\delta y_k} = \frac{1}{N_k} \sum_{i=1}^{N_k} \delta y_{i,k} \tag{4.4}$$

where $\overline{\delta y_k}$ is the mean variation of the physical quantity y over the k macroarea, $\delta y_{i,k}$ the variation of the physical quantity y for i-trajectory in the passing over the k macro-area from the entry to the exit.
It is also possible to define a variance for the variation of the physical quantity δy_k over the k macroarea as:

$$\sigma^2_{\delta y_k} = \frac{1}{N_k - 1} \sum_{i=1}^{N_k} \left(\delta y_{i,k} - \overline{\delta y_k} \right)^2 \tag{4.5}$$

Such a formula is used to evaluate the mean values of each physical quantity for parcels over the macroarea of interest. A similar formula is used to compute the variance σ_{y_k} of the values of the physical quantity y over the k macroarea.
In Tab. 4.1 the average values and variances of various parameters over the 12 areas are reported for all the trajectories ending over Trentino from 03/11/66 21 UTC to 04/11/66 12 UTC.

	N_k	$\overline{z}$[dam]	$\overline{q}[\frac{g}{kg}]$	$\overline{PV}$[PVU]	$\overline{\theta}$[K]	$\overline{\theta_e}$[K]	$\overline{h}$[dam]	t[h]
1	2760	354 (137)	4.22 (1.74)	0.78 (0.21)	304.0 (6.8)	317.0 (2.7)	79 (21)	1 (1)
2	2223	209 (146)	6.15 (1.84)	0.57 (0.36)	298.6 (6.5)	316.9 (3.1)	23 (12)	3 (4)
3	2747	139 (80)	6.80 (1.60)	0.40 (0.23)	296.0 (4.5)	316.0 (6.2)	14 (8)	11 (5)
4	1309	202 (133)	3.80 (2.31)	0.30 (0.21)	292.7 (6.3)	303.9 (7.2)	20 (14)	16 (12)
5	302	228 (57)	4.07 (1.65)	0.37 (0.20)	300.5 (5.1)	313.1 (8.4)	13 (13)	17 (14)
6	2123	156 (78)	5.43 (2.34)	0.23 (0.18)	298.3 (3.7)	314.6 (7.8)	37 (20)	24 (20)
7	2516	104 (47)	6.44 (1.63)	0.22 (0.18)	296.0 (3.7)	315.0 (6.0)	12 (20)	29 (23)
8	1060	258 (157)	1.87 (1.23)	0.56 (0.29)	290.6 (7.8)	296.2 (5.1)	47 (20)	15 (9)
9	629	321 (186)	1.64 (1.07)	0.61 (0.29)	291.0 (9.5)	295.9 (7.3)	49 (27)	11 (9)
10	30	268 (85)	1.51 (0.54)	0.68 (0.19)	288.4 (5.0)	293.1 (4.3)	39 (19)	12 (12)
11	167	364 (170)	1.30 (1.13)	0.69 (0.22)	295.2 (7.2)	299.2 (5.0)	5 (8)	21 (20)
12	1061	129 (54)	6.18 (1.67)	0.22 (0.22)	301.2 (2.7)	319.9 (3.5)	42 (9)	43 (26)

Table 4.1: Table summarizing the number of trajectories flowing at least for one time step over the 12 macroareas of Fig. 4.16 during the event of November 1966. The average values (along with the respective variances) of the height above the surface, of the specific humidity, of the potential vorticity, of the potential temperature, of the equivalent potential temperature and of the height of the surface underneath are reported for the the air parcels staying over the various macroareas. The last column gives the average number of time steps spent by trajectories over each area.

A similar table (Tab. 4.2) is used to report the average variations and the variances of variations for the same case study. A separate explanation has to be devoted to the quantity in the last column in table 4.2. It has been obtained by the following formula

$$\delta Q_{TOTk} = \frac{3h}{\frac{1}{N_k}\sum_{i=1}^{N_k} t_{i,k}} \frac{mass(i)}{10^6 \cdot A_1} (\sum_{i=1}^{N_k} \delta q_{i,k}) \tag{4.6}$$

where $t_{i,k}$ are the time steps spent by the i trajectory over area k, $\delta q_{i,k}$ the variation of specific humidity along the i trajectory over area k and $mass(i)$ is the mass of the volume represented by i trajectory (it is hypothesized that $mass(i)$ is conserved along trajectories, while the volume can change as the air density varies). $Mass(i)$ is computed multiplying the density at the ending time for the subvolume represented by i trajectory over the final 3D-box ($0.5^\circ \times 0.5^\circ \times 200m$). Note that the quantity of water vapour gained or lost by all the trajectories over area k is divided by the surface of the target area. So the formula gives the height of water (in mm) that should evaporate

	δz[dam]	$\delta q[\frac{g}{kg}]$	δPV[PVU]	$\delta\theta$[K]	$\delta\theta_e$[K]	δh[dam]	$\delta Q_{TOT}[\frac{kg}{m^2 h}]$
1	57 (37)	-1.04 (0.82)	0.01 (0.15)	2.30 (1.59)	-0.60 (1.34)	48 (32)	-0.054
2	36 (31)	-0.28 (0.97)	0.08 (0.19)	0.87 (1.30)	0.06 (2.03)	16 (15)	-0.014
3	147 (149)	-1.74 (2.57)	0.36 (0.34)	4.67 (5.01)	-0.05 (3.98)	14 (17)	-0.092
4	6 (63)	0.76 (1.46)	-0.02 (0.24)	1.28 (3.03)	3.43 (4.87)	-2 (36)	0.020
5	-24 (32)	0.29 (0.72)	-0.02 (0.15)	-0.85 (1.27)	-0.07 (2.34)	41 (25)	0.001
6	-12 (66)	-0.14 (1.32)	0.03 (0.30)	-0.03 (2.58)	-0.37 (3.72)	-12 (31)	-0.008
7	-55 (73)	2.78 (2.56)	-0.03 (0.27)	-0.25 (2.63)	7.60 (7.50)	-8 (16)	0.176
8	-51 (47)	0.54 (0.68)	-0.21 (0.35)	0.40 (2.11)	1.95 (3.12)	-14 (36)	0.011
9	-48 (46)	0.12 (0.29)	0.07 (0.35)	-2.17 (2.37)	-1.88 (2.09)	-7 (26)	0.002
10	-6 (23)	0.16 (0.22)	0.07 (0.13)	-1.01 (1.96)	-0.55 (2.29)	24 (17)	0.000
11	-46 (65)	0.58 (0.94)	-0.04 (0.28)	-0.79 (2.72)	0.90 (3.96)	0 (59)	0.002
12	-11 (58)	-0.49 (1.61)	-0.12 (0.58)	1.64 (3.43)	0.43 (3.93)	-1 (27)	-0.008

Table 4.2: The mean variations (as well as the respective variances) of the height of the trajectories in passing over various macroareas (Fig. 4.16) are reported for the event of November 1966. The same is done for the variations of the specific humidity, of the potential vorticity, of the potential temperature, of the equivalent potential temperature and of the height of the surface underneath of the parcels. The last column gives the quantity of water vapour (computed by the formula 4.6) gained or lost by all the trajectories over each area.

(or precipitate) over area 1 to have the same overall gain (or loss) of water mass. Furthermore the computed quantity is normalized to a time lag of 3 hours.

The evolution of θ, θ_e and PV

In the above table the evolution of potential vorticity PV, potential temperature θ and equivalent potential temperature θ_e along trajectories flowing over the 12 macro-areas is reported to help understanding the physical effects associated to the airflow dynamics and thermodynamics. The main equations governing the evolution of such parameters require a brief comment.
The Ertel potential vorticity is defined as

$$PV = \frac{1}{\rho}\Delta\theta \cdot \xi_a \approx -g\,(f+\xi)\,\frac{\partial\theta}{\partial p} \tag{4.7}$$

where ρ is the air density, f the Coriolis parameter and ξ_a the absolute vorticity. The conservation of the potential vorticity PV can be described by its budget equation (Haynes and McIntyre, 1987):

$$\frac{dPV}{dt} = \Delta \cdot \left(g\dot{\theta} \cdot \xi_a + g\mathbf{F} \times \Delta\theta\right) \tag{4.8}$$

which states that the change of *PV* along trajectories is brought about by the diabatic heating $\dot{\theta}$ in the presence of absolute vorticity ξ_a, and frictional forces **F**, including effects of turbulence or dissipation. If the frictional term is negligible, the conservation of the Ertel potential vorticity *PV* can be rewritten with some further approximation $|\xi_a| \approx f$ as

$$\frac{dPV}{dt} = \frac{f}{\rho}\frac{\partial \dot{Q}}{\partial \theta} \tag{4.9}$$

The effect implied by equation 4.9 is schematically depicted in Fig. 4.19a. A positive heating

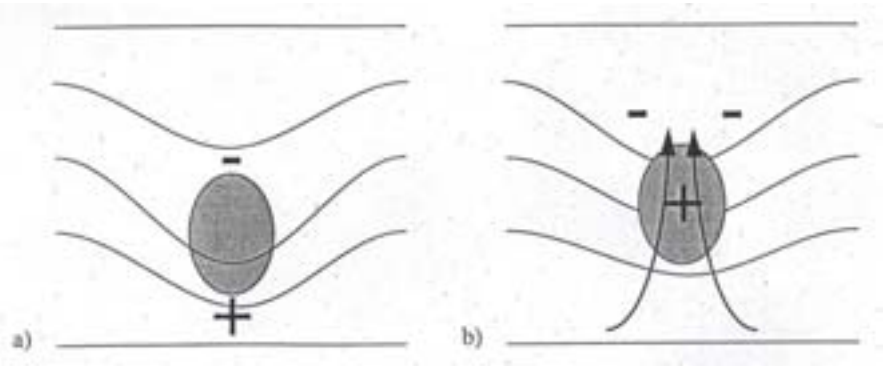

Figure 4.19: Impact of diabatic heating (shaded) on the budget of potential vorticity (thin lines denote potential temperature contours, arrows denote an updraft, and plus/minus signs refer to the potential vorticity budget). Panel a) depicts instantaneous tendencies, panel (b) a state of quasi balance (Perrson, 1995).

anomaly induces positive (negative) tendencies for the potential vorticity underneath (aloft). So for a given stratification the diabatic heating acts to deform isentropes so as to increase (decrease) the static stability below (above) the air mass where the forcing acts.
From another point of view the diabatic heating induces an updraft with compensatory convergent (divergent) flow at low (aloft) levels and concurrent vortex stretching (shrinking). Yet, the involved vertical motion advects the locally produced potential vorticity upward as pointed out by Perrson (1995). For a very detailed budget calculation on a real case of cold front he demonstrated that in a state of quasi balance a maximum of potential vorticity is established at the level of maximum heating (see Fig. 4.19b).

Water budget and evaporation

The equation for conservation of water mass along a single trajectory can be written as follows:

$$\frac{dq}{dt} = F_{qDISP} + F_{qMICRO} \tag{4.10}$$

$$\frac{dc_l}{dt} = F_{c_lDISP} + F_{c_lMICRO} \tag{4.11}$$

$$\frac{dc_s}{dt} = F_{c_sDISP} + F_{c_sMICRO} \tag{4.12}$$

where q is the specific humidity of the air parcel flowing along the trajectory, c_l is the concentration of the cloud liquid water particles inside the air parcel (i.e. the mass of liquid water particles per unit of air mass), c_s the concentrations of the cloud solid particles (ice, snow particles). On the right hand side of each conservation equation the first term $F_{...DISP}$ accounts for molecular diffusion and turbulent transport, the second term $F_{...MICRO}$ for microphysical processes occuring inside the air parcel, such as phase transitions, transformation of cloud particles into precipitation particles and so on. Another budget equation can be written for the microphysical processes:

$$F_{qMICRO} + F_{c_lMICRO} + F_{c_sMICRO} = F_{PREC} \tag{4.13}$$

where F_{PREC} represents the net flux of water precipitating outside the air mass.
So, neglecting terms related to the turbulent fluxes, which can be relevant only in the ABL, Eq. 4.10 becomes:

$$\frac{dq}{dt} + \frac{dc_l}{dt} + \frac{dc_s}{dt} = F_{PREC} \tag{4.14}$$

As it will be shown in the following chapter, the second and the third term on the left hand side of equation 4.14 are often negligible with respect to the specific humidity variations. The exact quantification of the microphysical processes demands for knowledge of all the microphysical variables along each trajectory at high spatial resolution. Thus, on the large scale water budget aiming at quantifying precipitation from an air parcel can be written as:

$$F_{PREC} = \frac{dq}{dt} \tag{4.15}$$

Nevertheless for air parcels flowing in the ABL the previous equation must be corrected:

$$F_{PREC} = \frac{dq}{dt} - F_{qDISP} \tag{4.16}$$

where the term F_{qDISP} represents the turbulent fluxes which transfer water vapour originating from sea surface evaporation to the air parcel.
In order to have an estimate of the mean evaporation over a specific macro-area, the Lagrangian analysis (from now on called "lagrangian evaporation") is probably more affected by uncertainties and inaccuracies than the Eulerian budget (from now on called "Eulerian evaporation"). First of all the variation of specific humidity along a trajectory over an area is generally due both to the evaporation from the sea and to the re-evaporation of rain droplets falling from higher atmospheric layers. Lagrangian analysis cannot provide any well based criterion suited to distinguish between the two contributions. Furthermore there are kinematic difficulties. Taking for granted that the evaporation corresponds to the variation of air humidity (which is true for trajectories close to the surface) it is possible to compute the evaporation fluxes through the following formula:

$$ev_k = \frac{1}{A_{eqk}} \sum_{i=1}^{N_k} \frac{\delta q_{i,k} m_i}{\delta t_{i,k}} \tag{4.17}$$

where ev_k is the mean evaporation over the k macroarea, $\delta q_{i,k}$ and $\delta t_{i,k}$ the specific humidity variation and the time lag for i-trajectory in the passing over the k macro-area, m_i the mass of air volume represented by parcel i, A_{eqk} the horizontal projection over the area k of the volume represented by all parcels passing over k macro-area and N_k the number of trajectories passing over k macro-area. By the numerical discretization, at the ending point, a trajectory is a parcel representative of a specific quadrangular volume around it ($0.5° \times 0.5° \times 200$m). So, over the area 1, $A_{eqk} = A_k$. Far away from the end point, the same volume results to be stretched and deformed in an unknown way and the the horizontal projection of that volume is undefined.

If we assume that, at time t, $A_{eqk} = A_{eq1} = A_1$ so as at the ending point, mean evaporation over various macroareas estimated starting from the Lagrangian analysis is reported in figure 4.18 (in this case evaporation estimates are the temporal average over the period from 31/11/66 00 UTC to 04/11/66 00 UTC).

Another possibility is to take into account both the variation of air density along trajectories (the higher is the air density, the smaller is the area of air parcel subject to the computed evaporation) and variation of the vertical thickness of the atmospheric layer explored by the trajectories. The squared root of variance for the altitude of trajectories passing over area k can be adopted as an estimator of the vertical thickness, but it does not contain all information deriving from vertical distribution of particles over the generic macroarea k. The troposphere, 10 km high (H), is subdivided in $M = 30$ vertical layers: $z^*(s) = \left(s + \frac{1}{2}\right) \frac{H}{M}$ is the average height of the layer s. Once

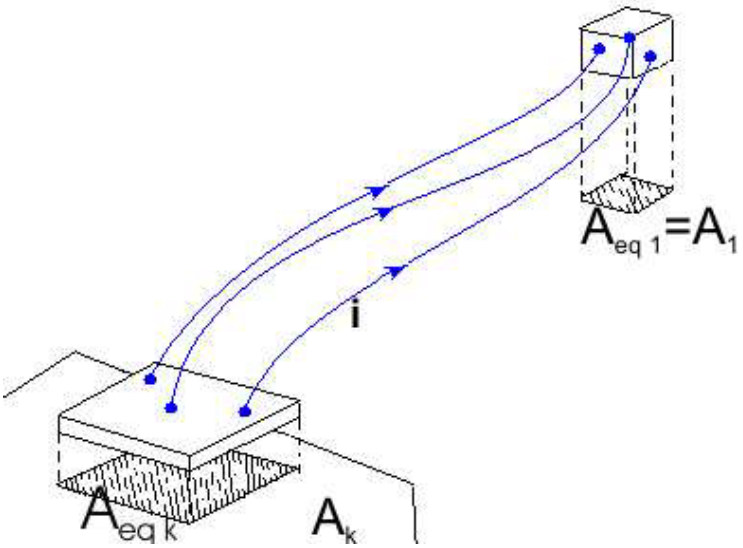

Figure 4.20: Scheme representing some trajectories flowing over macroarea k end ending over area 1. The projection A_{eqk} of the volume represented by all parcels passing over k macro-area is shown.

defined the function $F(z(s),k) = \frac{1}{N_k}\sum_{s^*=1}^{s} i_k(s^*)$, it is instead possible to derive $z_{y\,percentile}$ such as $F(z_{y\,percentile},k) = y$. $i_k(s^*)$ is the number of parcels flowing in the atmospheric layer s over area k. So, even though being slightly arbitrary in the choice of the percentile, the vertical thickness can be computed as $d_k = z_{85\,percentile} - z_{15\,percentile}$. The refined formula for the evaporation is

$$ev_k = \left(\frac{d_z(k)}{d_z(1)}\frac{\rho_0}{\rho_k}\right)\left(\frac{1}{A_1}\sum_{i=1}^{N_k}\frac{\delta q_{i,k} m_i}{\delta t_{i,k}}\right) \tag{4.18}$$

This formulation has given better results as shown in figure 4.21.

4.3 Analysis of the water budget for the 3 case studies

4.3.1 Event of November 1966

The duration of the precipitation event was 3 days (Fig. 4.5), but it is more meaningful to take into account a shorter time period when most of the precipitation occurred (from 3 November 21 UTC to 4 November 12 UTC). This allows to describe the properties of the air masses that actually contributed to the flood. As expected, from an Eulerian perspective, most evaporation took place over the sea (Fig. 4.18 and Fig. 4.17). Nevertheless a look to trajectories ending to the target area

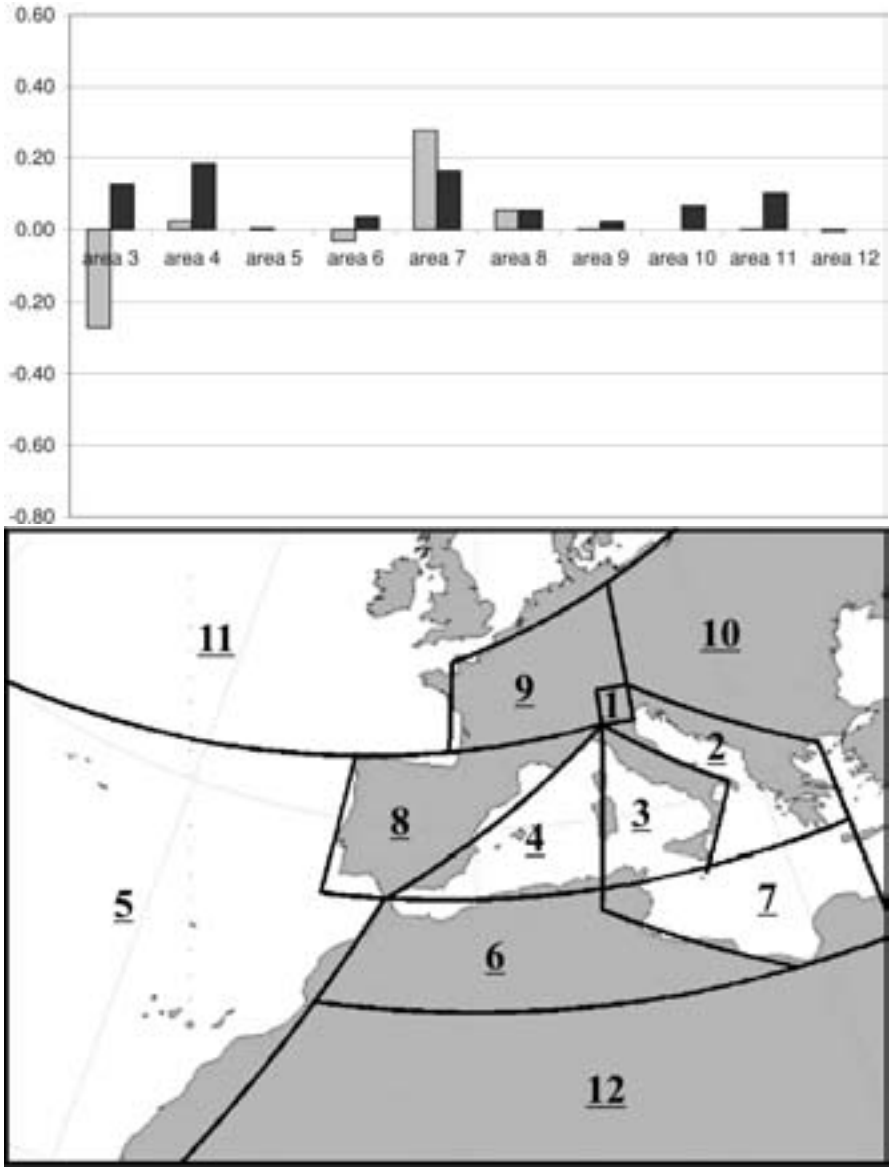

Figure 4.21: Average in time and in space of evaporation and of Lagrangian specific humidity variation (computed following the refined method of Eq. 4.18) in $kg\,m^{-2}h^{-1}$ over various areas (x-axis) in the period from 31/10/66 00 UTC to 04/11/66 00 UTC. The subdivision of domain in areas is also reported.

on 04/11/1966 00 UTC (Fig. 4.22) clearly shows that areas 3, 4, and 7 are the most contributions to evaporation which can provide water for the subsequent precipitation over the Alps (within 4 days from the arrival time).

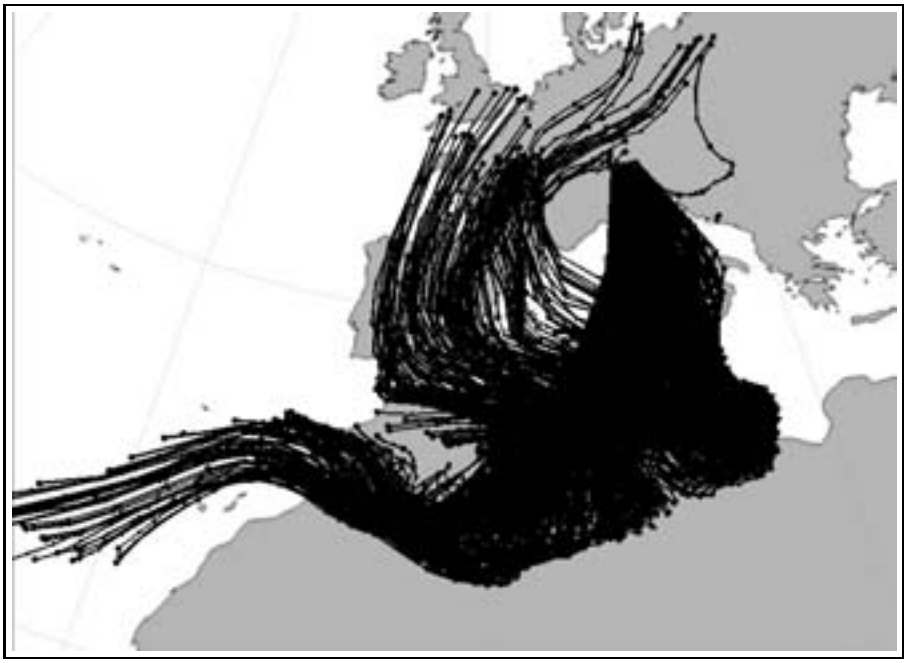

Figure 4.22: Five-days backtrajectories ending over Trentino at 04/11/1966 00 UTC.

The lagrangian water budget (Tab. 4.1 and Tab. 4.2 and Fig. 4.5), evaluated as explained in the previous section, indicates that the main source of water vapour is over area 7, i.e. the Central Mediterranean in front of the coasts of Tunisia and Lybia. It is indead reasonable that the most remarkable gain of water vapour along trajectories over area 7 was mainly due to the evaporation over the sea. Trajectories were, on average, 1000m high above sea level, which means that many of them gained water vapour by the turbulent fluxes within the boundary layer. This hypothesis is confirmed by the large increase of equivalent potential temperature (+7.60 K), whereas the potential temperature remained rather constant (-0.25 K). Air was far from saturation state and there was a supply of water vapour from outside.
Moreover the latter is a region where trajectories underwent a mean descending motion: as a consequence potential temperature was constant and the relative humidity RH decreased. Nevertheless evaporation was so strong that RH increased along the trajectories (+12 %).
By contrast, over the Tyrrhenian Sea (area 3) air parcels displayed a considerable increase in potential temperature (+4.67 K), almost costant values of equivalent potential temperature (-0.05 K), and trajectories flew at an average height of 1400 m a.s.l. In the period relative to the studied event area 3 was directly affected by a cold front. Trajectories were too high to gain water vapour through mechanical turbulent fluxes. Trajectories were almost at saturation and, therefore their ascent (+1470m), characterized by increasing values of PV (+0.36 PVU), caused the condensation

of water vapour to form cloud droplets (-1.74 g/kg of specific humidity).
Projections of trajectories flowing over area 3 on the underlying horizontal surface displayed a gentle rising (+140m). This seems to indicate that the orographic effect on precipitation was quite negligible over the Tyrrenian Sea in comparison to the cyclonic ascent ahead the cold front (warm conveyor belt). It might be important over the Alps (area 1): the slope of the trajectories was considerably lower than the corresponding slope of the underlying topography. There should be a "shrinking" effect, at least for lower air masses.

Over area 4, trajectories flew at a costant height experiencing increasing values of both potential temperature (+1.28 K) and equivalent potential temperature (+3.43 K). This means that there was a double contribution of latent heat fluxes from outside (the evaporation on the sea surface resulting in an increase of θ_e) and from the condensation of water vapour, resulting in the increase of θ. Reasonably the first effect can be ascribed to the trajectory behaviour in the southern part of the area 3 (at the boundary with areas 6 and 7), while the condensation of water vapour was more effective in the north-western part close to area 3.

Back to Figure 4.21, Lagrangian analysis shows us that most of the precipitation over Italy, as detectable using the ECMWF analysis, was related to the evaporation over the Gulf of Gabes and over the Sicily Channel. Therefore surface evaporation at areas 3 and area 4, as inferred after Eulerian analysis, was only partially contributing to the water budget of the air volume moving from an irregular space over the Mediterranean Sea to the rectangular ending-box over Trentino.
Figure 4.23 shows the evolution of the evaporation rate over the areas of interest. Looking at a small subarea within area 7 (Fig. 4.25), over which most of the trajectories flew, the Eulerian analysis points out that the highest evaporation rate took place from 01 November 00 UTC to 02 November 6 UTC (Fig. 4.24).

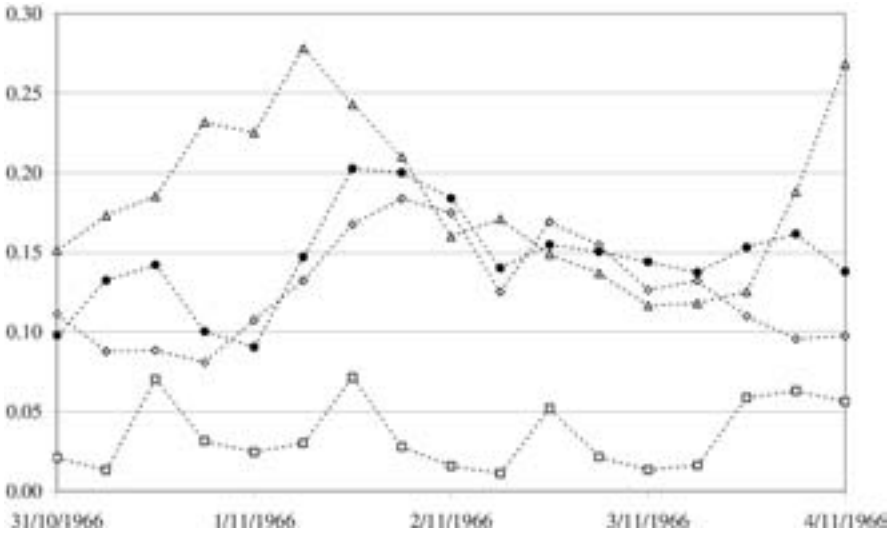

Figure 4.23: Evolution of mean "Eulerian evaporation" rate ($kg\,m^{-2}h^{-1}$) over four areas (diamonds for area 3, triangles for area 4, squares for area 6 and bold circles for area 7).

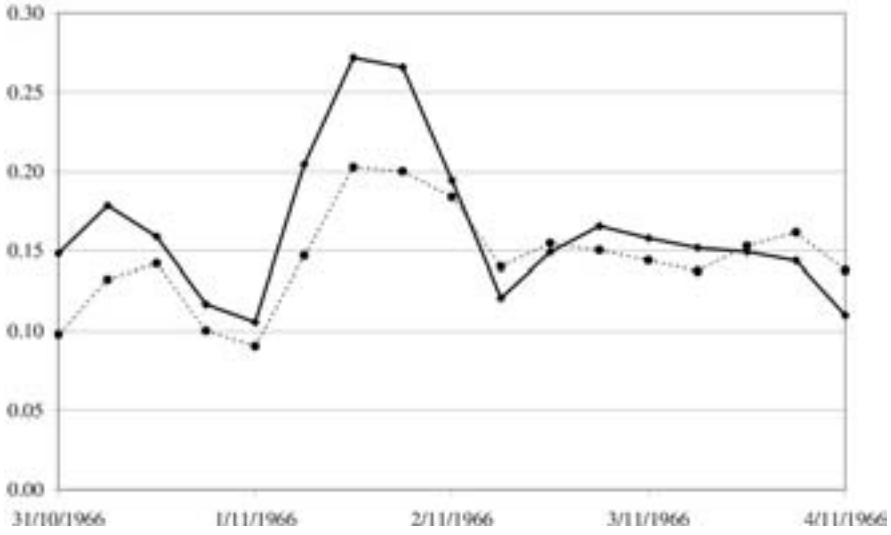

Figure 4.24: Evolution of mean "Eulerian evaporation" rate ($kg\,m^{-2}h^{-1}$) over area 7 and over a smaller area inside it.

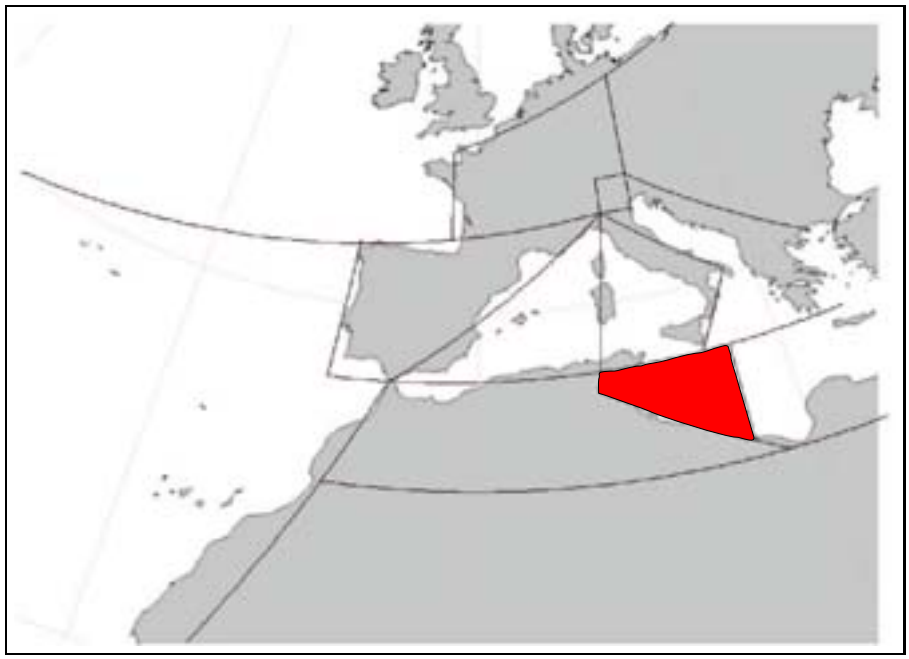

Figure 4.25: Boundaries of the sub-area within area 7 used to estimate the sensitivity of the evaporation rate to the macro-area dimension

4.3.2 Event of November 2000

In the case study of November 2000 the average precipitation recorded over Trentino from 16/11/00 21 UTC to 17/11/00 21 UTC was of 5-6 $mm\,h^{-1}$ (Fig. 4.10). In 1966 the measured value of mean precipitation over 3 and 4 November was 10 $mm\,h^{-1}$, but since precipitation occured essentially over the central 24 hours, a realistic value of the mean precipitation was 18 $mm\,h^{-1}$. So, in the event of 2000, less than 70 % of the mean precipitation of the 1966 event was recorded. This is a clear difference in intensity of the two events.
Simulated precipitation is underestimated by a 50 % (Fig. 4.26): it seems to be a typical bias of the trajectory method that has been implemented in the present work. Probably it is not only to be ascribed to the algorithm itself but to the ECMWF analyses data. Note that the climatology of precipitation forecast by the ECMWF deterministic model is systematically characterized by a considerable underestimation of the precipitation rate over Trentino (Schmidli et al., 2002; Rubel and Rudolf, 2001).

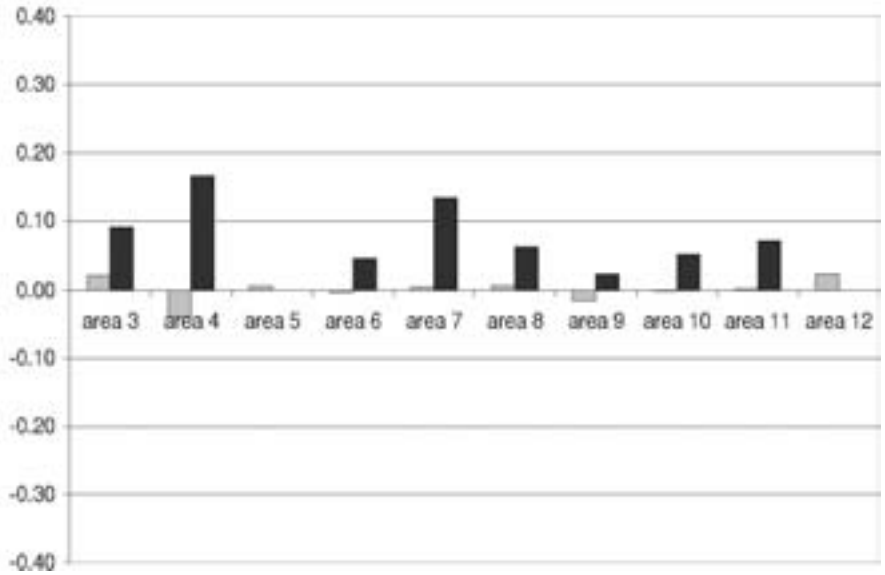

Figure 4.26: Average in time and in space of evaporation and of Lagrangian specific humidity variation (computed following the refined method of Eq. 4.18) in $kg\,m^{-2}h^{-1}$ over various areas (x-axis) in the period from 16/11/00 21 UTC to 17/11/00 21 UTC.

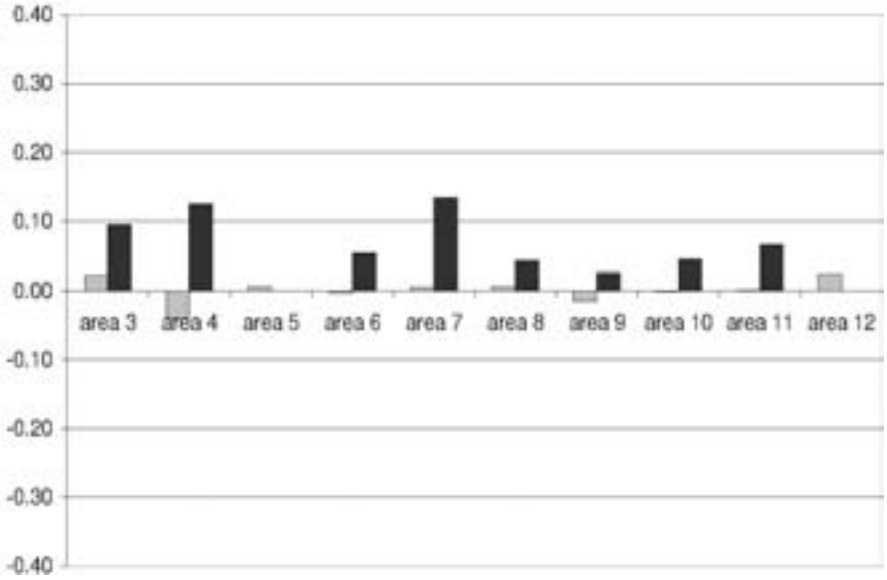

Figure 4.27: Average in time and in space of evaporation and of Lagrangian specific humidity variation (computed following the refined method of Eq. 4.18) in $kg\,m^{-2}h^{-1}$ over various areas (x-axis) in the period from 16/11/00 21 UTC to 17/11/00 21 UTC. Here the "Eulerian evaporation" has been computed averaging the evaporation fields only over the time during which trajectories flow over the each specific macroarea.

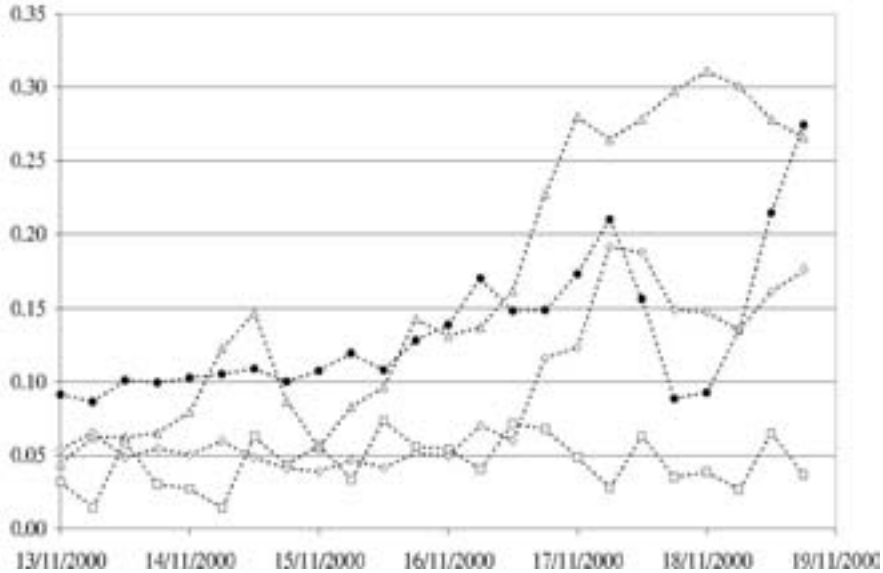

Figure 4.28: Evolution of mean evaporation rate ($kg\,m^{-2}h^{-1}$) over 4 areas (diamonds for area 3, triangles for area 4, squares for area 6 and bold circles for area 7) 16/11/00 21 UTC to 17/11/00 21 UTC.

A comparison between "Eulerian" and "Lagrangian" evaporation estimates (Fig. 4.26 and 4.28) show very different values. Nevertheless it is clear that, even in nature, the (Eulerian) evaporation over a geographical area does not correspond to the specific humidity increments experienced by an air mass along its trajectory (see also 4.3 and 4.3). This is the case, for example, of trajectories flowing aloft in the mid-troposphere without the effects of real surface evaporation. So the apparent strong underestimation outlined in Fig. 4.26 may be interpreted as if, during the event of November 2000, the air masses flowing along the trajectory carried the water vapour from far away, outside the analysed domain.
In order to avoid as much as possible that such discrepancies derive from the adopted formulas a slight change has been performed in the Eulerian estimation of evaporation. The average evaporation has been computed on a selected temporal window instead of over the whole event. For each one of the 12 macroareas, the average times of trajectory entry and exit have been computed: the two times define the period during which trajectories probably had change in the moisture content because of the evaporation (or the precipitation) over that area. Figure 4.27 clarifies that there are no big differences in the results for the 2000 event. Anyway such a correction has been automatically adopted also for the other cases.
The mean "Eulerian evaporation" computed over various areas is only the 20-30 % lower than in the case of 1966: strong evaporation alone over the Mediterranean Sea (or high sea surface temperature) is not a good index for forecasting extreme precipitation.
A further interpretation of the water mass budget for the 2000 event is provided in chapter 6 on the basis of cluster analysis.

4.3.3 Event of November 2002

In the case of 2002 the average precipitation recorded in Trentino from 24/11/02 18 UTC to 26/11/02 18 UTC was 5 $mm\,h^{-1}$ (Fig. 4.11). The event can be subdivided into two phases: the first from 24 November 18 UTC to 25 November 09 UTC, the second from 25 November 21 UTC to 26 November 12 UTC. In each phase the recorded mean precipitation rate was 6 to 7 mm, that is 70 % less than the mean precipitation in 1966 (as in the case of 2000).

First phase

In the first phase, simulated precipitation is underestimated by 70 % while there is a tendency to the overestimation of the evaporation over the macro-areas 3, 4 and 7 (Fig. 4.29). In other words ECMWF analyses seem to be too dry. Another possibility is that there was strong convection over the target area: the precipitation measured by rain gauges was balanced by strong humidity fluxes

	N_k	$\overline{z}$[dam]	$\overline{q}[\frac{g}{kg}]$	$\overline{PV}$[PVU]	$\overline{\theta}$[K]	$\overline{\theta_e}$[K]	$\overline{h}$[dam]	t[h]
1	4140	352 (140)	3.39 (1.75)	0.61 (0.26)	300.7 (6.2)	311.1 (3.5)	67 (41)	3 (5)
2	3439	271 (146)	3.92 (2.03)	0.56 (0.30)	299.5 (6.0)	311.4 (3.6)	19 (12)	5 (9)
3	3944	253 (146)	3.91 (2.36)	0.53 (0.32)	300.0 (5.6)	311.8 (4.0)	14 (8)	10 (6)
4	2311	225 (160)	4.67 (2.31)	0.58 (0.35)	296.8 (6.6)	310.6 (4.8)	9 (10)	23 (17)
5	1124	348 (150)	1.72 (1.73)	0.74 (0.72)	298.5 (6.4)	303.8 (6.9)	3 (8)	16 (12)
6	3046	203 (116)	3.77 (1.68)	0.33 (0.35)	302.4 (3.8)	314.1 (3.3)	37 (25)	14 (9)
7	2325	194 (114)	4.00 (2.23)	0.33 (0.31)	301.7 (4.1)	314.0 (4.1)	31 (34)	13 (17)
8	1085	238 (166)	3.46 (2.19)	0.65 (0.65)	293.3 (6.7)	303.4 (5.3)	35 (22)	18 (16)
9	371	232 (151)	3.79 (1.73)	0.53 (0.23)	292.8 (8.4)	304.0 (6.9)	55 (37)	16 (19)
10	333	353 (28)	2.40 (0.52)	0.15 (0.05)	303.6 (0.4)	311.3 (1.7)	48 (30)	17 (10)
11	806	255 (193)	3.69 (1.79)	0.24 (0.22)	296.9 (11.8)	307.9 (8.5)	2 (3)	36 (28)
12	2529	186 (92)	2.81 (1.61)	0.35 (0.27)	301.9 (4.0)	310.7 (3.9)	39 (11)	47 (23)

Table 4.3: Table summarizing the number of trajectories flowing at least for one time step over the 12 macroareas of Fig. 4.16 during the event of November 2000. The average values (along with the respective variances) of the height above the surface, of the specific humidity, of the potential vorticity, of the potential temperature, of the equivalent potential temperature and of the height of the surface underneath are reported for the the air parcels staying over the various macroareas. The last column gives the average number of time steps spent by trajectories over each area.

	δz[dam]	$\delta q[\frac{g}{kg}]$	δPV[PVU]	$\delta\theta$[K]	$\delta\theta_e$[K]	δh[dam]	$\delta Q_{TOT}[\frac{kg}{m^2 h}]$
1	52 (47)	-0.60 (0.84)	0.01 (0.39)	1.34 (1.83)	-0.35 (1.86)	75 (60)	-0.022
2	13 (40)	0.03 (0.81)	0.01 (0.35)	-0.12 (1.41)	-0.06 (2.09)	-9 (24)	0.002
3	41 (59)	0.05 (1.32)	0.07 (0.44)	-0.53 (2.13)	-0.38 (3.21)	14 (18)	0.002
4	63 (132)	-0.71 (2.40)	0.19 (0.54)	2.23 (5.12)	0.21 (5.06)	-21 (34)	-0.014
5	-39 (76)	0.28 (0.94)	-0.10 (0.31)	-0.17 (1.94)	0.70 (3.08)	15 (25)	0.002
6	58 (105)	0.05 (1.55)	0.00 (0.41)	-0.74 (3.22)	-0.63 (3.36)	8 (33)	0.002
7	-13 (42)	0.52 (1.80)	0.03 (0.32)	-0.83 (1.86)	0.58 (4.32)	-7 (12)	0.014
8	-59 (105)	0.61 (1.97)	0.04 (0.55)	-1.56 (3.70)	0.08 (4.01)	5 (38)	0.008
9	-8 (68)	-0.18 (1.27)	0.12 (0.48)	-0.87 (2.56)	-1.43 (3.30)	48 (60)	-0.001
10	-52 (60)	-0.24 (0.36)	-0.01 (0.05)	-1.00 (0.77)	-1.75 (1.10)	-26 (25)	0.000
11	74 (122)	0.00 (2.11)	-0.14 (0.34)	0.80 (3.03)	0.71 (3.97)	-7 (12)	0.000
12	-50 (51)	1.27 (1.36)	0.02 (0.41)	-0.51 (2.95)	3.33 (3.66)	24 (22)	0.011

Table 4.4: The mean variations (as well as the respective variances) of the height of the trajectories in passing over various macroareas (Fig. 4.16) are reported for the event of November 2000. The same is done for the variations of the specific humidity, of the potential vorticity, of the potential temperature, of the equivalent potential temperature and of the height of the surface underneath of the parcels. The last column gives the quantity of water vapour (computed by the formula 4.6) gained or lost by all the trajectories over each area.

due to evaporation.

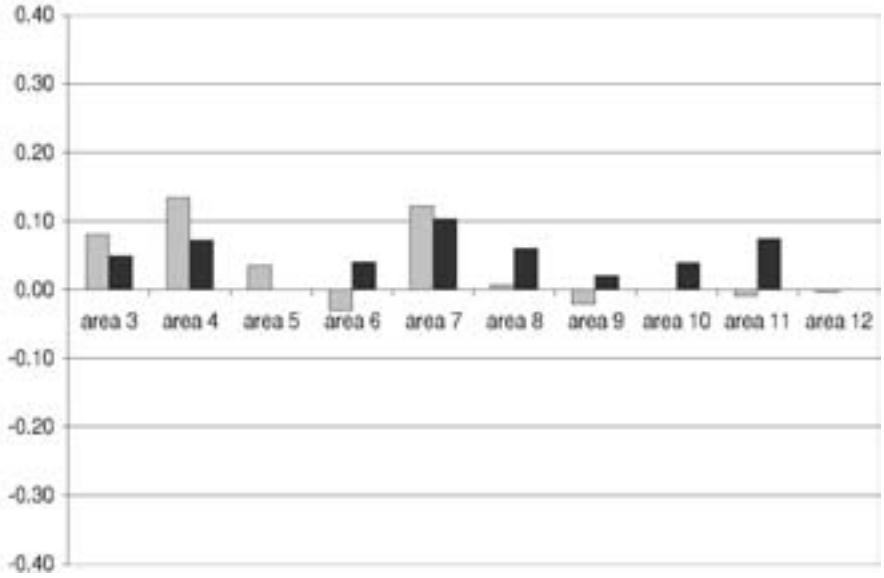

Figure 4.29: Average in time (over the period from 24/11/0218 UTC to 26/11/02 18 UTC) and in space of evaporation over various areas (x-axis). Lagrangian specific humidity variation in $kg\,m^{-2}h^{-1}$ over various areas computed following the refined method of Eq. 4.18) for the first phase of the 2002 event.

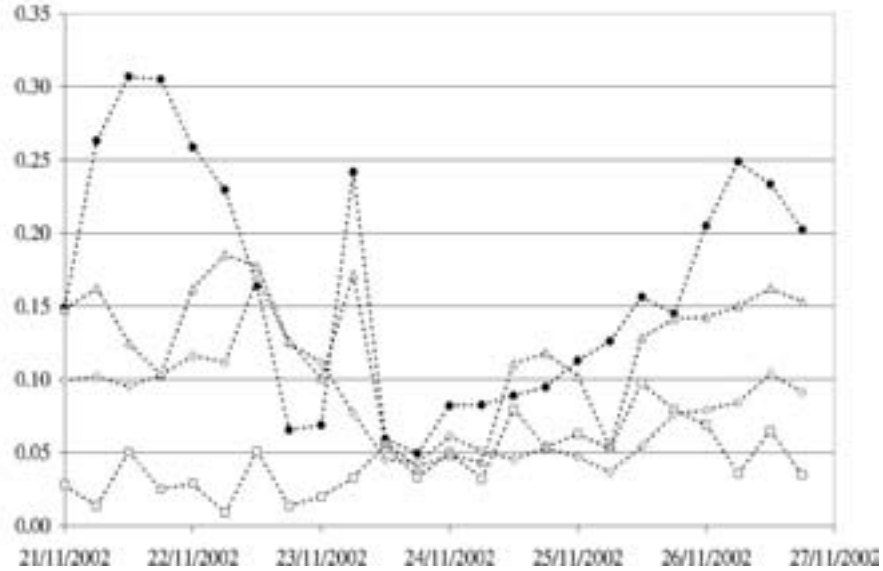

Figure 4.30: Evolution of mean evaporation rate ($kg\,m^{-2}h^{-1}$) over 4 areas (diamonds for area 3, triangles for area 4, squares for area 6 and bold circles for area 7) 24/11/0218 UTC to 26/11/02 18 UTC.

	N_k	$\overline{z}$[dam]	$\overline{q}[\frac{g}{kg}]$	$\overline{PV}$[PVU]	$\overline{\theta}$[K]	$\overline{\theta_e}$[K]	$\overline{h}$[dam]	t[h]
1	2760	360 (145)	3.34 (2.06)	0.41 (0.25)	302.2 (5.8)	312.4 (2.7)	65 (49)	3 (5
2	1699	268 (156)	4.51 (2.23)	0.44 (0.25)	299.4 (6.5)	312.9 (3.3)	19 (11)	4 (10
3	2229	270 (169)	3.99 (2.21)	0.38 (0.30)	300.6 (5.7)	312.7 (2.8)	20 (11)	9 (8
4	2348	309 (159)	2.89 (1.59)	0.27 (0.14)	302.5 (5.1)	311.5 (2.4)	12 (8)	13 (5
5	2136	382 (167)	1.94 (1.71)	0.32 (0.14)	303.1 (7.9)	309.1 (5.4)	3 (7)	23 (16
6	2561	286 (147)	2.87 (1.66)	0.29 (0.15)	303.2 (4.2)	312.1 (2.6)	68 (27)	17 (13
7	601	98 (67)	5.30 (1.74)	0.49 (0.34)	298.2 (3.4)	314.1 (2.5)	42 (43)	9 (10)
8	421	298 (140)	3.32 (1.49)	0.37 (0.20)	299.5 (7.6)	309.6 (6.9)	27 (21)	8 (8
9	310	386 (140)	2.56 (1.37)	0.34 (0.15)	301.8 (6.3)	309.8 (4.3)	38 (21)	4 (7
10	0	0 (0)	0.00 (0.00)	0.00 (0.00)	0.0 (0.0)	0.0 (0.0)	0 (0)	0 (0)
11	1022	322 (74)	4.14 (1.35)	0.44 (0.12)	301.2 (4.1)	313.7 (3.2)	1 (2)	45 (16
12	1557	228 (87)	2.82 (1.57)	0.33 (0.17)	305.2 (5.0)	314.1 (2.8)	45 (13)	43 (27

Table 4.5: Table summarizing the number of trajectories flowing at least for one time step over the 12 macroareas of Fig. 4.16 during the first phase of the event of November 2002. The average values (along with the respective variances) of the height above the surface, of the specific humidity, of the potential vorticity, of the potential temperature, of the equivalent potential temperature and of the height of the surface underneath are reported for the the air parcels staying over the various macroareas. The last column gives the average number of time steps spent by trajectories over each area.

	δz[dam]	$\delta q[\frac{g}{kg}]$	δPV[PVU]	$\delta\theta$[K]	$\delta\theta_e$[K]	δh[dam]	$\delta Q_{TOT}[\frac{kg}{m^2 h}]$
1	36 (48)	-0.51 (0.76)	0.00 (0.37)	1.34 (2.09)	-0.07 (2.17)	74 (63)	-0.013
2	26 (29)	-0.07 (0.56)	0.01 (0.39)	0.89 (1.07)	0.71 (1.58)	-15 (29)	-0.001
3	31 (49)	0.10 (0.89)	0.09 (0.39)	-0.25 (1.56)	0.02 (2.42)	14 (17)	0.002
4	15 (53)	0.44 (0.88)	-0.03 (0.23)	-0.69 (1.34)	0.61 (2.66)	-35 (31)	0.009
5	-39 (77)	0.62 (1.25)	0.02 (0.18)	-0.12 (3.12)	1.74 (4.90)	26 (23)	0.006
6	16 (71)	-0.04 (1.00)	0.02 (0.29)	-0.38 (2.07)	-0.50 (3.00)	15 (27)	-0.001
7	-20 (21)	1.37 (1.57)	0.06 (0.40)	-0.84 (1.02)	2.95 (3.99)	-13 (13)	0.008
8	-8 (44)	0.03 (0.77)	0.00 (0.19)	-0.53 (1.37)	-0.45 (2.03)	5 (24)	0.000
9	17 (36)	-0.13 (0.49)	-0.01 (0.18)	0.61 (1.26)	0.26 (1.07)	68 (57)	0.000
10	0 (0)	0.00 (0.00)	0.00 (0.00)	0.00 (0.00)	0.00 (0.00)	0 (0)	0.000
11	307 (160)	-4.11 (3.11)	-0.10 (0.36)	10.35 (7.10)	-1.07 (4.46)	-1 (6)	-0.003
12	-63 (54)	-0.15 (0.79)	-0.10 (0.18)	-1.42 (2.37)	-1.91 (3.13)	12 (17)	-0.001

Table 4.6: The mean variations (as well as the respective variances) of the height of the trajectories in passing over various macroareas (Fig. 4.16) are reported for the first phase of the event of November 2002. The same is done for the variations of the specific humidity, of the potential vorticity, of the potential temperature, of the equivalent potential temperature and of the height of the surface underneath of the parcels. The last column gives the quantity of water vapour (computed by the formula 4.6) gained or lost by all the trajectories over each area.

Second phase

In the second phase, simulated precipitation is underestimated by only 30 % (Fig. 4.11). Evaporation values computed with the Eulerian and with the Lagrangian method are not very different (Fig. 4.31).

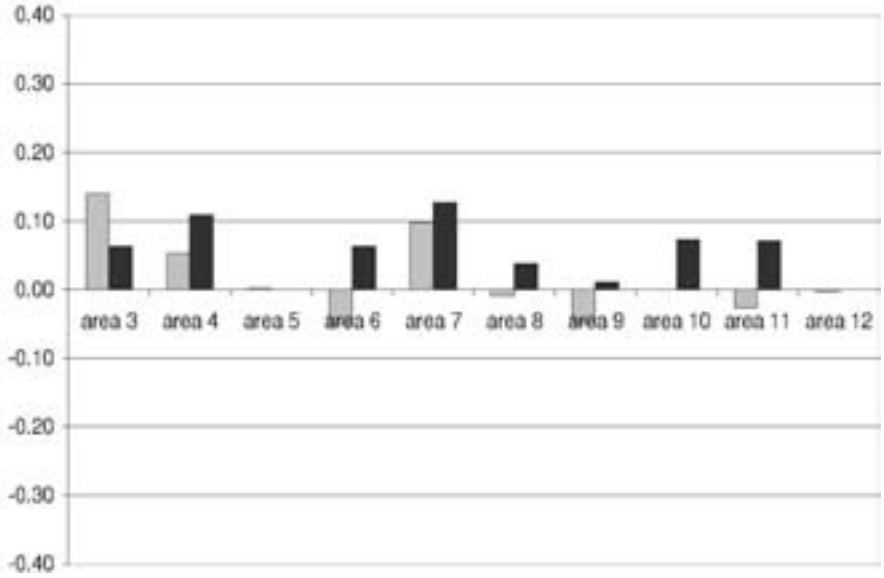

Figure 4.31: Average in time (over the period from 24/11/0218 UTC to 26/11/02 18 UTC) and in space of evaporation over various areas (x-axis). Lagrangian specific humidity variation in $kg\,m^{-2}h^{-1}$ over various areas computed following the refined method of Eq. 4.18) for the second phase of the 2002 event.

	N_k	$\overline{z}$[dam]	$\overline{q}[\frac{g}{kg}]$	$\overline{PV}$[PVU]	$\overline{\theta}$[K]	$\overline{\theta_e}$[K]	$\overline{h}$[dam]	t[h]
1	3220	349 (140)	4.20 (1.85)	0.45 (0.27)	303.0 (6.1)	315.9 (1.9)	63 (46)	3 (5
2	2394	247 (157)	5.34 (2.29)	0.38 (0.31)	300.1 (6.3)	316.1 (2.7)	16 (9)	5 (11
3	3201	241 (142)	4.59 (1.78)	0.34 (0.23)	301.4 (5.1)	315.4 (2.6)	14 (8)	13 (6
4	1030	297 (120)	3.33 (1.41)	0.35 (0.20)	302.9 (5.3)	313.3 (4.2)	25 (15)	5 (5
5	1192	306 (113)	2.82 (1.89)	0.20 (0.11)	306.6 (3.9)	315.6 (5.8)	7 (9)	34 (10
6	3071	210 (111)	3.78 (1.42)	0.27(0.23)	303.7 (4.1)	315.4 (3.7)	30 (12)	9 (4)
7	2913	209 (131)	3.97 (1.69)	0.32 (0.33)	302.8 (4.6)	315.1 (3.2)	24 (36)	8 (9
8	194	314 (135)	3.24 (1.54)	0.36 (0.19)	298.7 (6.9)	308.6 (7.2)	36 (17)	8 (8)
9	171	437 (72)	3.01 (0.89)	0.52 (0.16)	306.6 (3.1)	316.2 (1.6)	42 (22)	2 (1)
10	0	0 (0)	0.00 (0.00)	0.00 (0.00)	0.0 (0.0)	0.0 (0.0)	0 (0)	0 (0)
11	359	315 (66)	5.05 (1.46)	0.35 (0.11)	302.9 (3.4)	318.2 (2.9)	0 (1)	26 (11
12	3009	222 (106)	3.90 (1.95)	0.26 (0.13)	303.8 (5.5)	315.9 (5.0)	41 (10)	43 (19)

Table 4.7: Table summarizing the number of trajectories flowing at least for one time step over the 12 macroareas of Fig. 4.16 during the second phase of the event of November 2002. The average values (along with the respective variances) of the height above the surface, of the specific humidity, of the potential vorticity, of the potential temperature, of the equivalent potential temperature and of the height of the surface underneath are reported for the the air parcels staying over the various macroareas. The last column gives the average number of time steps spent by trajectories over each area.

	δz[dam]	$\delta q[\frac{g}{kg}]$	δPV[PVU]	$\delta\theta$[K]	$\delta\theta_e$[K]	δh[dam]	$\delta Q_{TOT}[\frac{kg}{m^2 h}]$
1	58 (56)	-0.87 (1.06)	0.01 (0.30)	1.85 (2.54)	-0.57 (1.76)	80 (66)	-0.024
2	21 (27)	0.08 (0.86)	0.06 (0.29)	0.38 (1.42)	0.60 (1.96)	-15 (23)	0.003
3	70 (78)	0.55 (1.55)	0.07 (0.44)	-0.97 (3.08)	0.56 (2.73)	19 (24)	0.017
4	17 (43)	0.19 (0.83)	-0.01 (0.18)	0.34 (1.60)	0.91 (2.07)	-27 (43)	0.002
5	-124 (125)	0.19 (1.41)	0.00 (0.13)	-1.55 (2.21)	-1.05 (4.33)	28 (14)	0.001
6	12 (57)	-0.17 (0.70)	0.08 (0.31)	-0.80 (1.10)	-1.34 (1.95)	-10 (32)	-0.005
7	0 (44)	0.36 (1.14)	0.01 (0.22)	-0.48 (1.32)	0.50 (3.03)	-9 (17)	0.011
8	5 (45)	-0.46 (0.90)	0.01 (0.13)	0.49 (1.63)	-0.78 (2.31)	3 (22)	0.000
9	57 (38)	-0.69 (0.50)	-0.02 (0.17)	2.32 (1.57)	0.30 (0.65)	75 (55)	-0.001
10	0 (0)	0.00 (0.00)	0.00 (0.00)	0.00 (0.00)	0.00 (0.00)	0 (0)	0.000
11	325 (105)	-5.03 (2.78)	-0.09 (0.19)	12.74 (5.23)	-1.11 (3.65)	0 (2)	-0.005
12	-27 (76)	-0.17 (1.26)	0.00 (0.22)	-0.32 (2.80)	-0.77 (3.71)	8 (11)	-0.002

Table 4.8: The mean variations (as well as the respective variances) of the height of the trajectories in passing over various macroareas (Fig. 4.16) are reported for the second phase of the event of November 2002. The same is done for the variations of the specific humidity, of the potential vorticity, of the potential temperature, of the equivalent potential temperature and of the height of the surface underneath of the parcels. The last column gives the quantity of water vapour (computed by the formula 4.6) gained or lost by all the trajectories over each area.

5 Cluster analysis: method and applications

The identification of the flow patterns which mostly contributed to precipitation events requires suitable gathering of ensembles of trajectories into few remarkable and representative bundles. Various classification methods and, in particular, clustering techniques are presented here. The attention is mainly focused on the adoption of the most suitable phase space where trajectories can be represented as points and the "distance" between two trajectories is easily the euclidean distance between the respective points. This allows for gathering together similar trajectories of the ensemble and obtaining fewer final clusters. Trajectories have often been used in the literature to decipher individual flow situations, but suitable methods of analysis to classify large sets of trajectories have been only recently developed (see next sections).

5.1 Flow climatologies

Trajectory analyses were first used for flow climatologies: large sets of 5 to 15-day back trajectories were calculated over a time span of several years and their transport directions and travel speeds were classified according to suitable criteria. These statistical criteria were defined to discriminate, for instance, between oceanic, clean continental and polluted continental air masses. An early example of this technique is the study of Miller (1981). He calculated more than 7000 back trajectories ending over Hawai Islands and classified them into five transport sectors. Many authors used variations of this technique, mostly to group air and precipitation chemistry data to roughly identify the source areas of air pollutants, namely those transport sectors associated with high pollutant concentrations at the receptor site (Henderson and Weingartner, 1982; Colin et al., 1989; Miller, 1987; White et al., 1994).

5.2 Classification of trajectories in CETs

A similar procedure has been later introduced to classify a large number of trajectories covering the same time period, but starting from a three dimensional domain (Schär and Wernli, 1993;

Wernli and Davies, 1997; Rossa, 1995). The analysis can yield limited ensembles of trajectories from the large pool depending on specific dynamically based criterion. Wernli and Davies (1997) classified the selection criteria as follows:

- *A priori* criteria based upon the spatial coordinates and physical properties of the air parcels at the reference time. For example the air parcel flowing in the stratosphere at the reference time must have a potential vorticity value exceeding 2 potential vorticity units (PVU).
- *A posteriori* criteria based upon the time trace either of the air-parcel paths (e.g. significant ascent, or significant increase of specific humidity) where *significant* means larger than a specified threshold.
- A combination of *a priori* and *a posteriori* criteria such as an *a priori* constraint to identify stratospheric air and an *a posteriori* constraint of significant descent.

Using suitable criteria and thresholds, the resulting ensemble of trajectories shows a coherent structure: in this case one can define a *coherent ensemble of trajectories* (CET). A powerful application of the trajectory models is the exploration of the extratropical cyclones to reveal the existence of coherent Lagrangian flow structures and to identify their nature (section 5.3).

5.3 The use of CET methods to analyse the structure of cyclones

Originating from the work of Browning (1971) and Carlson (1980), the conveyor-belt model is based (as shown above) on the analysis of the equivalent isentropic surface maps within a system-relative frame moving with the mean speed of the cyclone, assuming that the air parcels really remain on those surfaces (this is generally true above the ABL, but it can be misleading with latent heat fluxes).
Another concept, which is related to the air streams and purely based upon Eulerian analysis, is that of "tropospheric rivers" (Newell et al., 1992). These are filaments in the field of the vertically integrated water vapour flux

$$\mathbf{J}_q = g^{-1} \int_0 p_0 \mathbf{v} q dp \tag{5.1}$$

where $\mathbf{v}$ is the horizontal wind vector, p_0 is the pressure at the surface and q is the specific humidity. They persist for several days over the mid-latitude oceans: the main contribution to $\mathbf{J}_q$ stems from the lower troposphere ahead of surface cold fronts.
Wernli and Davies (1997) and Wernli (1997) adopted a Lagrangian-based strategy to test such Eulerian conceptual schemes. They first computed a large number of trajectories over a certain time period by starting from a three dimensional box encompassing the whole domain of interest;

then they selected coherent ensembles of trajectories by using the methods described in section 5.2. They showed that a CET can be related to the concepts of *conveyor belt* and *tropospheric river* and that it can be represented by the flowing of a single macro air parcel.

First of all Wernli (1997) focused on the moist ascending CETs during the cyclonic transition from an incipient frontal wave to a vertically coherent vortex. The geometrical criterion (ascent larger than 620 hPa) identified two distinct and parallel-flowing CETs (named X and Y). The physical criterion (decrease of specific humidity larger than 12 $g\,kg^{-1}$) selects only one CET, which corresponds qualitatively to CET X. The third criterion (water vapour flux larger than 0.17 $m\,s^{-1}$) identifies the CET R.

All the three ensembles, whose selection seems to have a small sensitivity to the threshold values, start from the ABL in the warm sector ahead of the cold front, but at different latitudes. CET Y starts moving northward only 200 km south-east of the growing cyclone; then, during the ascent, it bends around the north-eastern side of the depression close to the low center. In this phase most of the water vapour content condenses and the mean potential temperature values increase because of the diabating heating related to water vapour condensation. Moreover PV values first increase from typical atmospheric values up to 1-2 PVU in the saturation area (low-middle level positive PV anomaly) before returning to the original values (high level negative PV anomaly).

CET X is initially located 1400 km south of the incipient cyclone in the low-level jet region ahead of the cold front. It flows rapidly northward ascending in a rearward-sloping manner: in fact, after 1 day, it is flowing over the cold side of the surface polar front. Nevertheless, looking at the values of various physical variables, this ensemble experiences similar physical processes to those experienced by CET Y. It only differs for its higher decrease in specific humidity, which strongly contributes to the precipitation along the cold front of the cyclone.

The third CET (R) is slightly different, because its rapid ascent is limited to the second part of a 2-day period and reaches the middle troposphere, but not the tropopause (as well as CETs X and Y). In the first day, trajectories move in a sort of low level moist jet just ahead of the surface cold front. In the second day they approach the warm front east to the cyclone center entering the zone of upward motion and contributing to the precipitation over that area; after that they begin to fan out in an anticyclonic movement.

Wernli (1997) developed the above analyis in depth by studying the evolution of 2-day CET properties. He showed that early X-CETs are characterized by an anticyclonic path in agreement with the shape of the upper level trough. Later, parcels turn cyclonically around the vertically coherent vortex. Y-CETs are present only during the main cyclogenetic phase, whereas the R-CETs tend to be no more compact and coherent during the cyclone deepening. Moreover, an animated visualization of the CETs reveals the existence of airstreams ('flexible tubes') through which various

macro-parcels are ascending from the moist boundary layer into the upper troposphere. After comparing such airflows with the previous interpretation of moist airstream, Wernli (1997) concluded that the so called 'tropospheric rivers' mark a region of rapid and coherent passage, rather than constituting a Lagrangian entity by itself. Viceversa the moist ascending CETs resemble more the moist 'flexible tubes' of CETs.

Indeeed the Lagrangian analysis of Wernli (1997) allowed to refine the conceptual model of

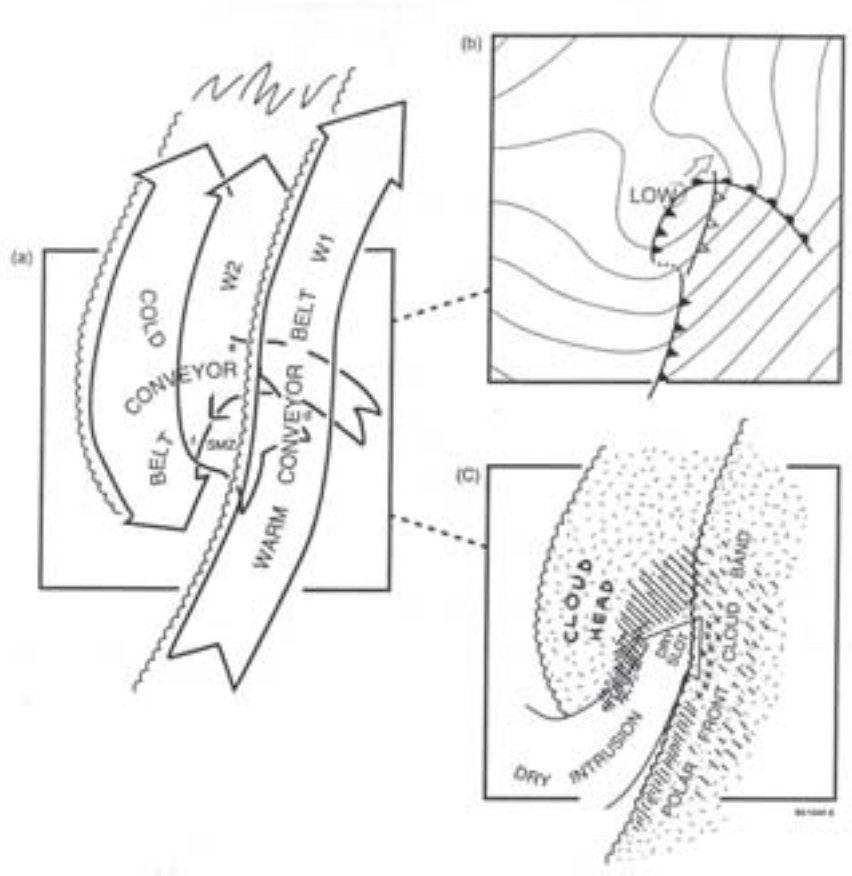

Figure 5.1: Airflow and precipitation within a developing extratropical frontal cyclone (based on Browning and Roberts, 1994). The main warm conveyor belt is labelled W1. The ascending cold conveyor belt (CCB) is responsible for a large portion of the cloud head. The lowest part of the warm conveyor belt is labelled W2: it peels off and ascends in the top part of the cloud head. The westward component of W2 and the CCB are associated with the ageostrophic transverse circulation.

the WCB, which bifurcates when approaching the cyclonic centre. The model, later proposed in Browning and Roberts, 1996 (Fig. 5.1), shows three stages in the evolution of bifurcating WCB in

association with the upper level vortex: at the end the W1 part overruns the tail of W2 and turns anticyclonically in the upper ridge, while the flow fanning out within W2 forms the top part of the emerging cloud head of the developing cyclone. Note that the W2 warm conveyor belt corresponds to Y-CET airstream in Wernli (1997), while the W1 warm conveyor belt includes both the X-CET and the R-CET airstreams.
Wernli (1997) applied the same analysis to the study of DI using the selection criterion that the descent must be larger than 350 hPa and that PV must have initial values larger than 2 PVU. Trajectory analysis resulted to be powerful to better characterize the tropopause folding and the intrusion of stratospheric air in the middle troposphere, but it did not modify the scheme of mid-latitude cyclone structure.

5.4 Cluster analysis

Cluster analysis is a multivariate statistical technique to split a data set into a number of groups by means of repeated gathering them in suitable clusters. The meteorological applications of this technique available in the literature are essentially restricted to the the field of the "ensemble forecasting". An "ensemble forecast" consists in a number of simulations (black trajectories in Fig.

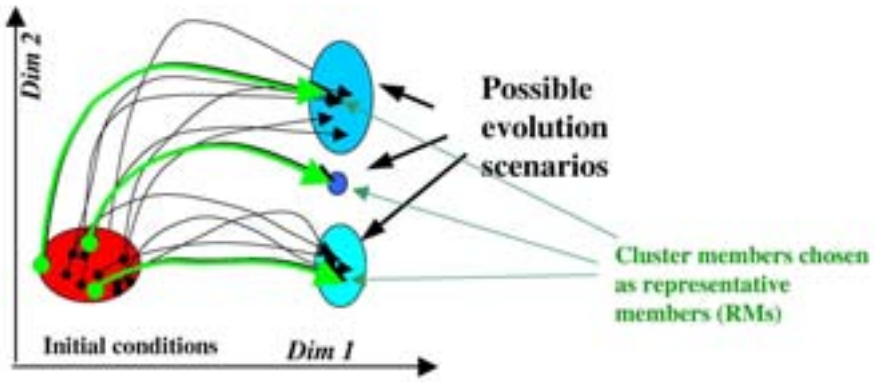

Figure 5.2: Ensemble forecasting: black trajectories are the various simulations undertaken with the same forcing, but where small perturbations to initial conditions have been introduced. The simulation ensemble can be classified by the clustering techniques in some scenarios (the light blue circles) representing the main possible evolutions of the atmospheric conditions. Each green trajectory is the average of all trajectories/simulations belonging to that cluster.

5.2) performed with the same boundary conditions, but where small perturbations to remote initial conditions have been introduced to estimate the uncertainty associated with the forecast. The

simulation ensemble can be classified by the clustering techniques in some scenarios representing the main possible evolutions of the atmospheric conditions.
Cluster analysis is commonly described as an objective classification method, but this is not true, since the selection of the clustering algorithm, the specification of the distance measure and the number of clusters remain, to some extent, subjective. Kalkstein et al. (1987), who evaluated three different clustering procedures for use in synoptic climatological classification, remarked the question of subjectivity: the selection of the proper clustering procedure to be used in the development of an objective synoptic methodology may have far-reaching implications on the composition of the final homogeneous groups. Various clustering procedures can be used in meteorological applications (see Kalkstein et al., 1987 for an introduction to this kind of methods). Moody and Galloway (1988) were the first authors to import clustering methods in the field of trajectory computation. In their works, trajectory clustering technique was applied to a wide set of computed forward/backward trajectories starting/ending from a target point over several years in order to identify the most recurrent flow patterns over the selected period. The motivation of that study was air chemistry monitoring and their focus was to relate on periods with high pollutant concentration with specific synoptic configurations favouring the advection of pollutants from the source regions to the target areas. In all the subsequent studies the same statistical approach has been followed; sometimes trajectory cluster analysis has been associated with Principal Component Analyses to better combine trajectory clusters with the most recurring synoptic conditions (Avila and Alarcon, 1999).
In this kind of studies each trajectory can be defined by its physical coordinates or even by the values of other dynamic and thermodynamic variables (humidity, potential vorticity, ...) which can better identify the state of the air parcel. This implies the adoption of a suitable trajectory phase space where each point represents one whole trajectory: accordingly its generalised coordinates will include, besides spatial coordinates of points reached at various time step, the values of additional dynamic and thermodynamic variables at the same times (the phase space adopted in the present work will be described in detail in section 5.5). In this hyperspace each trajectory is represented by a point and the clustering procedure is applied to these points: the Euclidean distances in the phase space are a measure of the difference or likelyness between various trajectories.
We report now a brief summary of the most used clustering techniques in the Lagrangian studies.

5.4.1 A non-hierarchical clustering method

The well known non-hierarchical trajectory clustering method was applied for the first time by Dorling et al. (1992). The best property of this algorithm is its low requirement for computational storage (Brankov et al., 1998). The various consecutive steps are as follows:

1. Choice of a number of "seed" trajectories corresponding to the number of wanted clusters: the choice is arbitrary (they can even be not real trajectories) but it is better to choose seed-trajectories well covering the spread of all the real trajectories.

2. Assign each of the real trajectories to that "seed" trajectory which is closest in term of an "a priori" defined distance (see Jain et al., 1996 and section 5.5 for the definition of distance in the phase space). After assignment of all the real trajectories, recalculate the "seed" or "average" trajectory in each cluster from its members (now it is highly probable that this "average" trajectory does not correspond to a real trajectory).

3. Recalculation of cluster mean trajectories may now result in some real trajectories being in the wrong cluster in terms of their distance from cluster means. Check each real trajectory in this regard and recalculate the cluster means again after completing the check. Several iterative "passes" through all the trajectories may be necessary, each time recalculating the cluster means at the end of each pass, before all real trajectories are correctly assigned.

All the procedure can be repeated for various numbers of searched clusters. The choice of the optimal number of cluster can then be fixed by the analysis fo the RMSD (Bertò et al., 2004).

5.4.2 The hierarchical clustering methods

The hierarchical clustering methods are well known algorithms. These "bottom-up" procedures develop following the steps reported below:

1. At the beginning, all the single trajectories are considered clusters, there are no "seed trajectories".

2. The couple of trajectories displaying the minimum distance are aggregated, i.e. are gathered into one cluster.

3. The coordinates of the mean trajectory, representing the cluster, are calculated as the average of the corresponding coordinates representing the two trajectories.

4. The distances between all possible couples of trajectories and between each trajectory and the cluster are evaluated. In fact various hierarchical clustering methods differ for the way they compute the distance between the single trajectory and a cluster of more trajectories (or later between two clusters).

    - In the case of the "centroid" method the distance is the distance between the two mean cluster trajectories (or centroids).

- In the case of the "complete-linkage" method the maximum distance is retained of the computed distances between all the possible couples of trajectories belonging to the two clusters.
- In the case of the "single-linkage" method the minimum distance is retained of the computed distances between all the possible couples of trajectories belonging to the two clusters.
- In the case of the "average-linkage" method the distance is the average of the distances between all the possible couples of trajectories belonging to the two clusters (Kalkstein et al., 1987; Cape et al., 2000; Lee and Merrill, 2002). It has been shown that "average-linkage" method is superior to both the single and complete linkage as it possesses the unique capability to minimize within-cluster variance and maximize between-cluster variance (Boyce, 1969).
- The Ward's method (Moody and Galloway, 1988; Moody et al., 1991; Harris et al., 1992; Lee and Merrill, 1994; Lin et al., 2001; Wyputta and Grieger, 1999) slightly differs from the others. It gathers together just the two elements so that the new within-cluster variance is minimized.

5. Following the chosen definition of distance, the two closest elements (trajectories or clusters) are gathered into a new, single cluster. The procedure is then iterated up to retain only one cluster: the clustering procedure agglomerates trajectories in a progressive way building a dendrogram.

5.4.3 Other clustering methods

Some authors use alternative clustering methods. Some of them (Frank and Seibert, 2003) found a sort of optimal combination between the two most commonly used algorithms. Other use completelly alternative methods such as "heuristic algorithms" (Best and Hege, 2002).

5.4.4 The number of clusters

In all the clustering methods described, there is no intrinsic rule to objectively define the total number of clusters, or to stop the agglomerative procedure at some point. Intuitively, the optimal number of cluster should be when the procedure is forced to agglomerate elements displaying very little "resemblance". A possible criterion to detect this breaking point is given by the the analysis of the dependence of variance on the number of clusters. The variance within the cluster is defined as the averaged square distance between each point representing a trajectory in the phase space

and the center of mass of the cluster. The average of the cluster variances is the Mean Square Deviation (MSD) and provides a suitable functional test. In order to minimize the variance within each cluster and to maximize the variance between different clusters, the changes occurring in the Root Mean Square Deviation (RMSD) can be analysed for various possible final numbers of clusters in order to detect sudden breaks.
Nevertheless, clustering is a wide branch of scientific research and probably only some classical approaches have been transferred ed in the meteorological field. For example, Giada and Marsili (2002) addressed the problem of data clustering by introducing a unsupervised, parameter-free approach based on maximum likelihood principle. Starting from the observation that data sets belonging to the same cluster share a common information, they construct an expression for the likelihood of any possible cluster structure. The likelihood, in turn, depends only on the Pearson's coefficient of the data. They discuss clustering algorithms that provide a fast and reliable approximation to maximum likelihood configurations. In the authors opinion, compared to standard clustering methods, their approach seems has the following advantages:

1. it is parameter free
2. the number of clusters need not be fixed in advance
3. the interpretation of the results is transparent.

If this method was really so powerful it could be certainly introduced for trajectory clustering.

5.5 Application of the clustering techniques to the present work

Each trajectory can be defined by the positions of the air parcel at them = 121 time steps if the 5-day back-trajectories are built by the Lagrangian model output every 1 hour. So each trajectory is defined by 3 $\times$m = 363 coordinates. In the following $x_{i,k}$, $y_{i,k}$, $z_{i,k}$ are the coordinates of the i-th trajectory ($i = 1,...,N_T$) at the k-th time step ($k = 1,...,M$) where N_T = 460. The time step $k = 1$ is the time of arrival of trajectory over Trentino, the $k-th$ time step denotes $t_k = -(k-1)$ hours before the time of arrival and hence $k = 121$ corresponds to $t_{121} = -120$ hours (5 days) before the time of arrival.
However, at each time step and for each trajectory, further quantities can be added to the set of variables needed to identify the state of the air parcel: these may be either dynamic and thermodynamic variables (such as the specific humidity $q_{i,k}$, the relative humidity $RH_{i,k}$, the equivalent potential temperature $\theta_{ei,k}$, the potential vorticity $PV_{i,k}$) or their rate of change. These additional coordinates will allow to identify more precisely the state of the air parcel and to distinguish between spatial trajectories lying close but displaying different physical properties (e.g. moisture

content).
This implies the adoption of a suitable trajectory phase space for clustering where each point represents one whole trajectory: accordingly its coordinates will be, besides spatial coordinates of points reached at various time step, the values of additional dynamic and thermodynamic variables at the same times. In principle this would imply the use of a hyperspace where all relevant quantities at all time steps provide the component of the vector identifying each trajectory. This would however produce relatively cumbersome objects and many variables that do not play any effective role might be included. The choice of the most appropriate coordinate subset for the phase space is a key issue in order to capture the conserved quantities relevant to the event: 2 possible ensembles of parameters have been tested and reported in the following subsections. Once trajectories have been reduced to points in the phase space, the "distance" between two trajectories is easily the euclidean distance between the respective points in the chosen phase space. Afterwards various hierarchical agglomerative clustering techniques can be adopted (Jain et al., 1996; Dorling and Davies, 1995; Brankov et al., 1998) to gather the "trajectory points" of the phase space in a small number of trajectory clusters. In the present work the Average-Linkage Clustering algorithm (Cape et al., 2000) has been selected due to its satisfactory performances for the purposes of the present study.
At the end of the agglomerative procedure only significant clusters, including more than 2 % of the total trajectory number, have been retained in order to avoid outliers.

5.5.1 Use of specific humidity to define the phase space

It has been anticipated that it might not be necessary to take into account the values of the various parameters of trajectories at all time steps. Aim of the present work is to find a relationship between high evaporation occurring where moist air masses originate and strong precipitation occurring in the ending areas. As a consequence, spatial coordinates of the physical space and the other physical variables at the intermediate trajectory stage (from 60h to 12h before the ending time) are not included as coordinates of the phase space used for the clustering.
Furthermore, since each quantity enters as a component with its own dimension, in order to make the ranges of all the variables comparable, suitable normalization has to be introduced. This is achieved by subtracting from each variable ξ_i of the phase space its average value

$$\overline{\xi} = \frac{\sum_{i=1}^{N_T} \xi_i}{N_T}$$

and normalizing with its variance

$$\sigma_\xi = \sqrt{\frac{\sum_{i=1}^{N_T}(\xi_i - \overline{\xi})^2}{N_T - 1}}.$$

On the basis of the above reasoning, the adopted multidimensional phase space will include as coordinates the following quantities:

- the specific humidity change in the 12 hours before trajectory arrival at target point ($\delta q_i = q_{i,13} - q_{i,1}$),
- the trajectory height at the 3 time steps over the last 6-hours time lags ($z_{i,1}$, $z_{i,7}$, $z_{i,13}$),
- the trajectory positions (latitude, longitude and height) at the 6 time steps over the beginning 12-hour time lags ($x_{i,121}$, $y_{i,121}$, $z_{i,121}$, $x_{i,109}$, $y_{i,109}$, $z_{i,109}$, $x_{i,97}$, $y_{i,97}$, $z_{i,97}$, $x_{i,85}$, $y_{i,85}$, $z_{i,85}$, $x_{i,73}$, $y_{i,73}$, $z_{i,73}$, $x_{i,61}$, $y_{i,61}$, $z_{i,61}$),

resulting in a total number of 22 degrees of freedom.
So the hypervector in the phase space will be as follows:

$$\begin{aligned}\overline{\Xi} = \Bigg(& \frac{\delta q_i - \overline{\delta q}}{\sigma_{\delta q}}, \frac{z_{i,1} - \overline{z_1}}{\sigma_{z_1}}, \frac{z_{i,7} - \overline{z_7}}{\sigma_{z_7}}, \frac{z_{i,13} - \overline{z_{13}}}{\sigma_{z_13}}, \frac{x_{i,61} - \overline{x_{61}}}{\sigma_{x_{61}}}, \frac{y_{i,61} - \overline{y_{61}}}{\sigma_{y_{61}}}, \frac{z_{i,61} - \overline{z_{61}}}{\sigma_{z_{61}}}, \\ & \frac{x_{i,73} - \overline{x_{73}}}{\sigma_{x_{73}}}, \frac{y_{i,73} - \overline{y_{73}}}{\sigma_{y_{73}}}, \frac{z_{i,73} - \overline{z_{73}}}{\sigma_{z_{73}}}, \frac{x_{i,85} - \overline{x_{85}}}{\sigma_{x_{85}}}, \frac{y_{i,85} - \overline{y_{85}}}{\sigma_{y_{85}}}, \frac{z_{i,85} - \overline{z_{85}}}{\sigma_{z_{85}}}, \\ & \frac{x_{i,97} - \overline{x_{97}}}{\sigma_{x_{97}}}, \frac{y_{i,97} - \overline{y_{97}}}{\sigma_{y_{97}}}, \frac{z_{i,97} - \overline{z_{97}}}{\sigma_{z_{97}}}, \frac{x_{i,109} - \overline{x_{109}}}{\sigma_{x_{109}}}, \frac{y_{i,109} - \overline{y_{109}}}{\sigma_{y_{109}}}, \frac{z_{i,109} - \overline{z_{109}}}{\sigma_{z_{109}}}, \\ & \frac{x_{i,121} - \overline{x_{121}}}{\sigma_{x_{121}}}, \frac{y_{i,121} - \overline{y_{121}}}{\sigma_{y_{121}}}, \frac{z_{i,121} - \overline{z_{121}}}{\sigma_{z_{121}}} \Bigg)\end{aligned}$$

Beside the choice of the most suitable phase space, clustering procedure leaves the possibility of weighing some coordinates of the phase space with an amplification or reduction factor to give them higher or lower importance in the clustering algorithm. For example, if most of the variance of the trajectory ensemble resides in the geographical position of trajectories, then all the coordinates of the phase space (except the first one) can be multiplied by a reduction factor to enhance the information deriving from the specific humidity variations. Yet, the chosen weighing should be tested and explained on a physical basis, so it has not been adopted in the present work.

5.5.2 A two step agglomerative algorithm

The previous choice was innovative and physically based since it aimed at outlining possible links between the intensity of precipitation along trajectories before arriving at the target area and the

water vapour source regions contributing to enrich trajectories (Bertò et al., 2004). Doubt still remained however that we were sometimes forcing trajectories to gather together by the uncontrolled mixing of two types of criteria: the geographical distance and the different size of specific humidity variations. To rationalize the procedure, a two step agglomerative algorithm has been adjusted:

1. In the first step the adopted multidimensional phase space includes as coordinates only geographical quantities: the trajectory height at the 3 time steps over the last 6-hours time lags $z_{i,1}$, $z_{i,7}$, $z_{i,13}$ and the trajectory positions (latitude, longitude and height) at the 6 time steps over the beginning 12-hour time lags $x_{i,121}$, $y_{i,121}$, $z_{i,121}$, $x_{i,109}$, $y_{i,109}$, $z_{i,109}$, $x_{i,97}$, $y_{i,97}$, $z_{i,97}$, $x_{i,85}$, $y_{i,85}$, $z_{i,85}$, $x_{i,73}$, $y_{i,73}$, $z_{i,73}$, $x_{i,61}$, $y_{i,61}$, $z_{i,61}$, resulting in a total number of 21 degrees of freedom. In this way N_T trajectories are gathered together in N_{C1} on the basis of purely "geographical" criteria.

2. In the second step the clustering algorithm is applied to each set of trajectories belonging to each one of the N_{C1} main clusters obtained in the first step. Now the adopted phase space includes only one coordinate: the specific humidity change in the 12 hours before trajectory arrival at target point $\delta q_i = q_{i,13} - q_{i,1}$. So the second step is made to select subclusters, inside a trajectory cluster originating over a specific region, characterized by different humidity variations before arriving over the target area. The number of subclusters selected inside one of the main clusters depends on the population of the main cluster itself through a simple algebric expression: such strategy has been chosen to avoid to compute subclusters inside already small main clusters. The total number of obtained subclusters will be N_{C2}.

Hereafter trajectory clustering performed in the above phase space will be called "final geographical clustering", while the procedure of Bertò et al. (2004) will be referred to as "direct clustering". Another strategy for the second step of the *geographical* approach is to adopt a phase space including only the specific humidity variation along trajectories in their first 4 days $\delta q_i = q_{i,121} - q_{i,25}$ as coordinate. This algorithm, herafter called "initial geographical clustering", aims to point out various sources of water vapour along trajectories without looking at the ending precipitation.

5.6 Clustering: an example

As an example of the application of the "direct clustering method" clusters of trajectories arriving over the target area on the 4th November 1966 00 UTC are reported in Fig. 5.3. The number of trajectories belonging to each cluster is reported in the figure.

The same analysis could be repeated for each ensemble of computed trajectories arriving over the

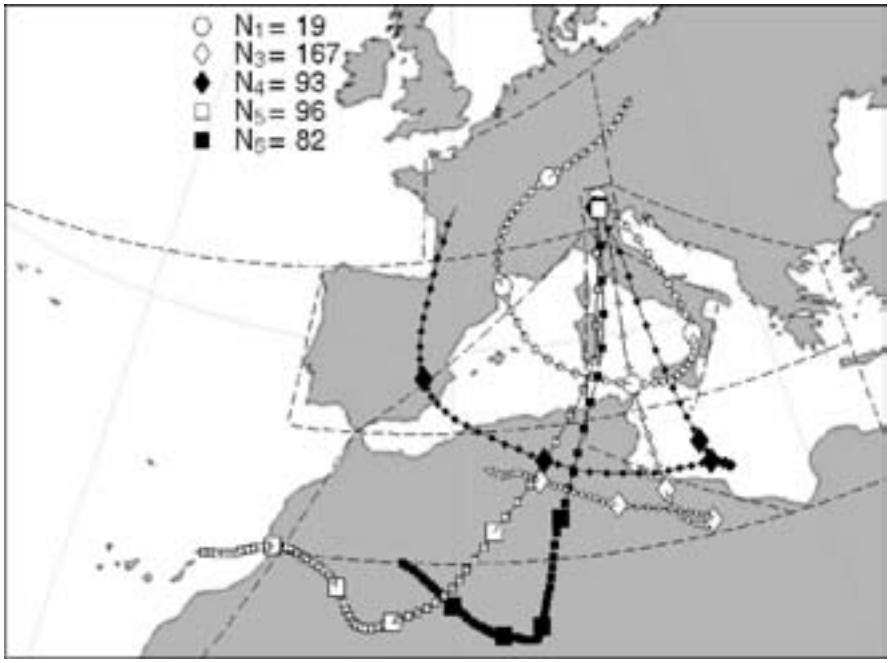

Figure 5.3: Cluster of trajectories arriving over Trentino at 00 UTC of 04/11/1966. Every curve is the average, in the physical space, of all trajectories belonging to that cluster.The average position every 6 hours is marked by a small circle, the position every 24 hours by a big one. The number of trajectories for each cluster is indicated in the figure.

target area every 3 hours during the entire duration of the event (e.g. from 03 November 00 UTC to 05 November 00 UTC for the flood event of 1966). This approach would generate too many figures and tables, which result to be dispersive. Nevertheless the analysis of cluster scenarios for ensembles of trajectories arriving over the target area every 12 or even every 24 hours would lead to loss or to misunderstand the evolution of the precipitation event.

So trajectory clustering analysis can be performed simultaneously on the all the ensembles of trajectories computed for the considered event. This is done by introducing the time as a further coordinate of the clustering phase space to avoid to gather in one cluster similar trajectories ending over Trentino at different times.

The optimal time window to perform the cluster analysis is not even the entire event. This approach would lead to catch all the typical types of air masses occuring during a whole cyclonic event (trajectories belonging to the "warm conveyor belt", other to the "cold conveyor belt" and other to the "dry intrusion"), but it would become hard to characterize these types of clusters without distinguishing smaller ensembles of trajectories inside them. So events lasting two or three days

have been broken a priori in more phases: the cluster analysis has been performed for each of the phases.
In Fig. 5.4 trajectory clusters are reported computed for the central phase of the 1966 precipitation event. In the subsequent figure (Fig. 5.5) there are all the trajectories belonging to each cluster:

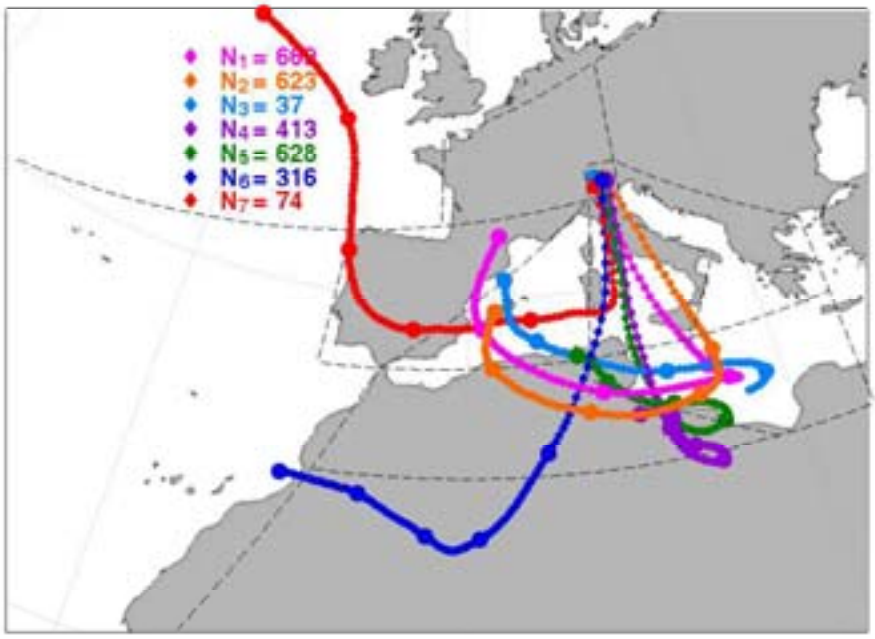

Figure 5.4: Clusters of trajectories arriving over Trentino in the period from 03/11/66 21 UTC to 04/11/66 12 UTC. Every curve is the average, in the physical space, of all trajectories belonging to that cluster.The average position every 1 hour is marked by a small circle, the position every 24 hours by a big one. The number of trajectories for each cluster is indicated.

this helps to appreciate both the power and the limits of a procedure trying to summarize all the information in a few representative paths. For example, it is not directly clear from Fig. 5.5 that some trajectories originate over Germany (orange cluster) or over the inland areas of Lybia (violet and green cluster) and that some clusters are not compact around their mean trajectory (green cluster).

In the next chapter as well as in the Appendix the following variables are plotted, beside the spatial projection of the average cluster trajectories:

1. for each cluster the evolution of its average height over the sea level as well as the average profile of the orography underneath its trajectories (see for example Fig. 5.6). In Fig. 5.7

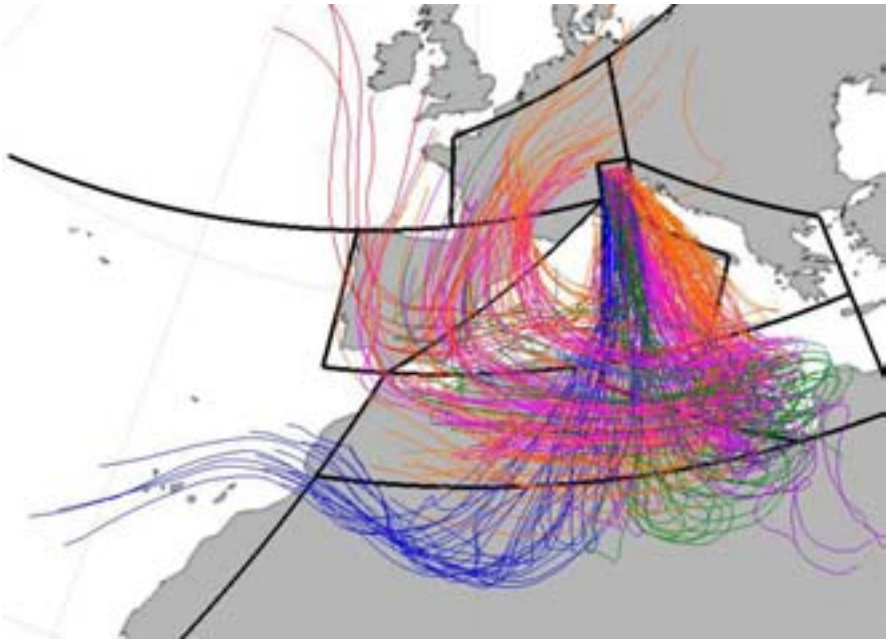

Figure 5.5: Individual trajectories arriving over Trentino in the period from 03/11/66 21 UTC to 04/11/66 12 UTC. They are marked by different colors according to Fig. 5.4. The average profile of the orography underneath each cluster trajectory is also reported.

an exemplified representation of the orography profile underneath a generic trajectory is plotted. Note that, at each time step, the average of a variable is computed as the average of the values of that variable along the trajectories belonging to the considered cluster. So, the average orography profile results to be very smoothed for densely populated clusters, while it is steeper for scarcely populated clusters. Similarly, the more compact is the airstream, the less smoothed is the average orography profile beneath.

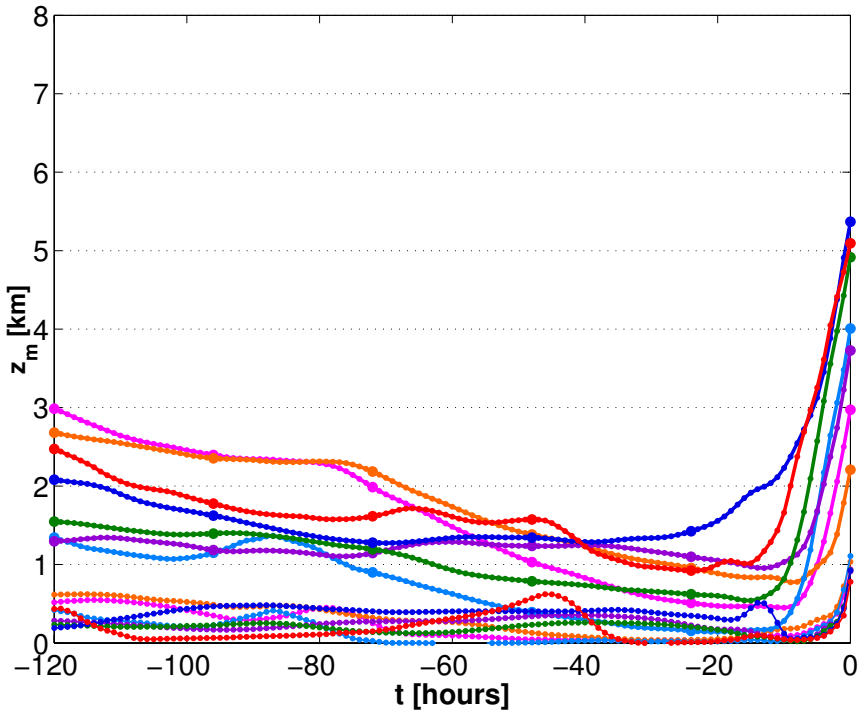

Figure 5.6: Height of trajectory clusters arriving over Trentino in the period from 03/11/66 21 UTC to 04/11/66 12 UTC. The height is marked by different colors and circles of different size according to Fig. 5.4

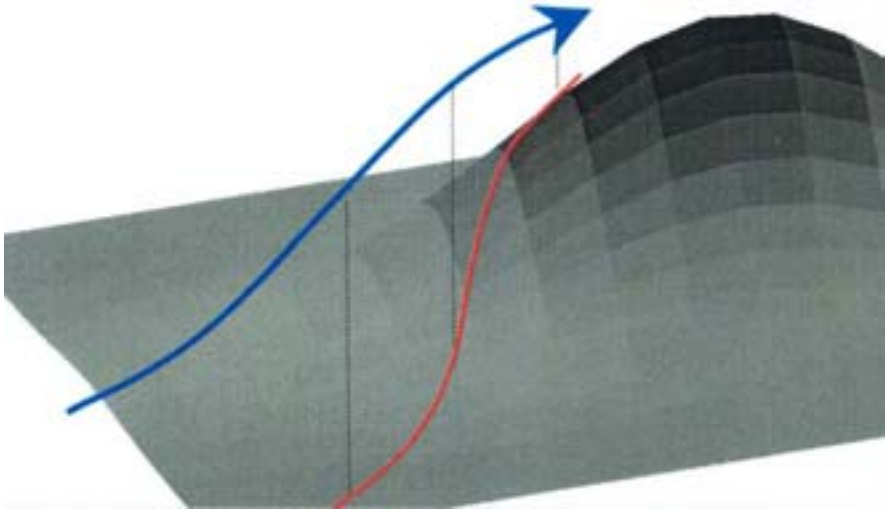

Figure 5.7: Exemplified representation of the orography profile underneath a generic trajectory.

2. for each cluster the evolution of its average water content (see for example Fig. 5.8) As specified in the Figure caption the sum of the specific humidity with the concentration of liquid and solid water parcels is plotted. This type of plot is almost equal to the plot of the specific humidity alone, since the concentration of liquid and solid water parcels is typically an order of magnitute less than the concentration of water vapour (Fig. 5.9).

3. for each cluster the evolution of its average relative humidity, potential vorticity, potential temperature and equivalent potential temperature (see for example Fig. 5.10)

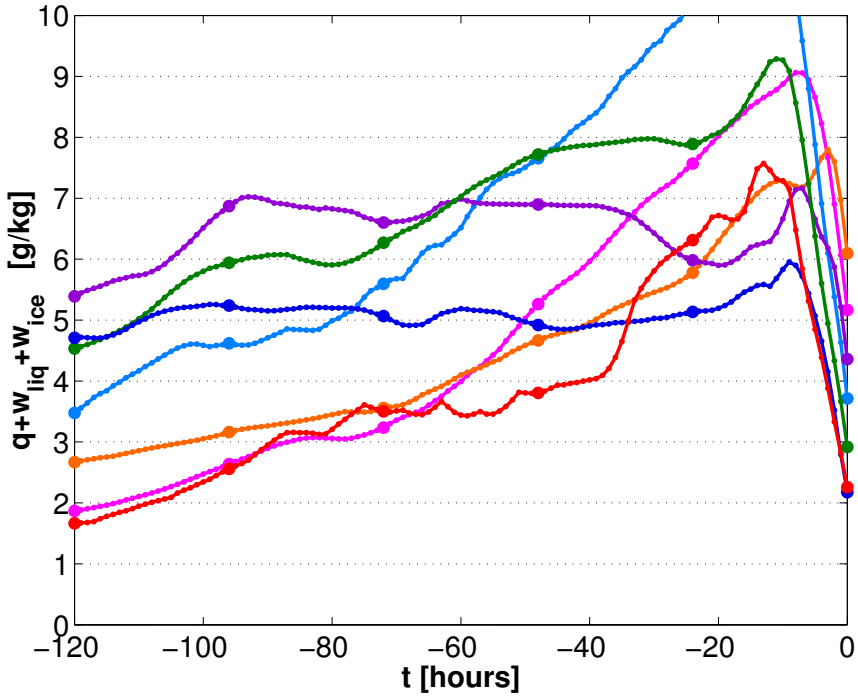

Figure 5.8: Specific humidity along trajectory clusters arriving over Trentino in the period from 03/11/66 21 UTC to 04/11/66 12 UTC. Colors and circles of different size have been used according to Fig. 5.4

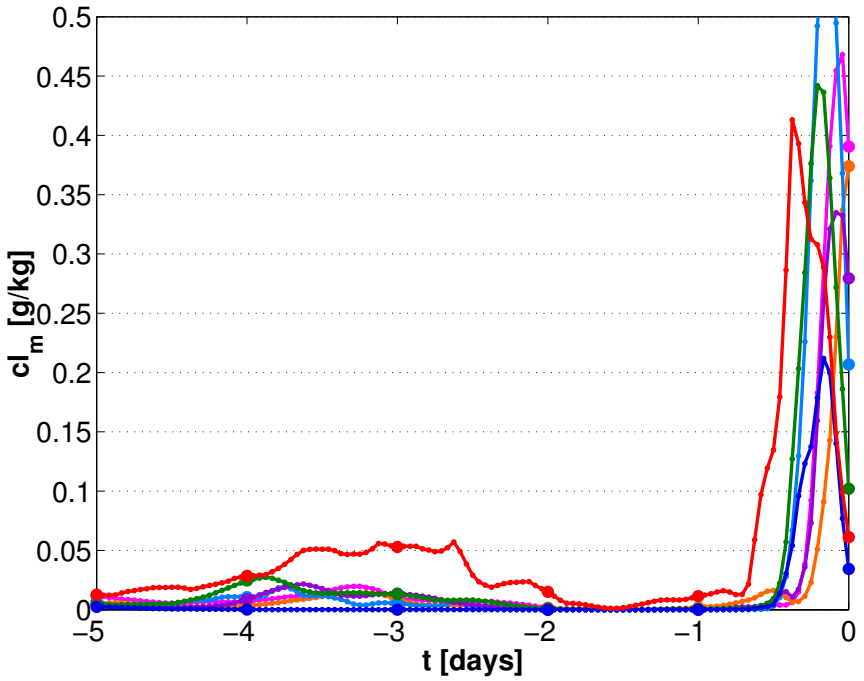

Figure 5.9: Concentration of liquid air parcels along trajectory clusters arriving over Trentino in the period from 03/11/66 21 UTC to 04/11/66 12 UTC. Colors and circles of different size have been used according to Fig. 5.4

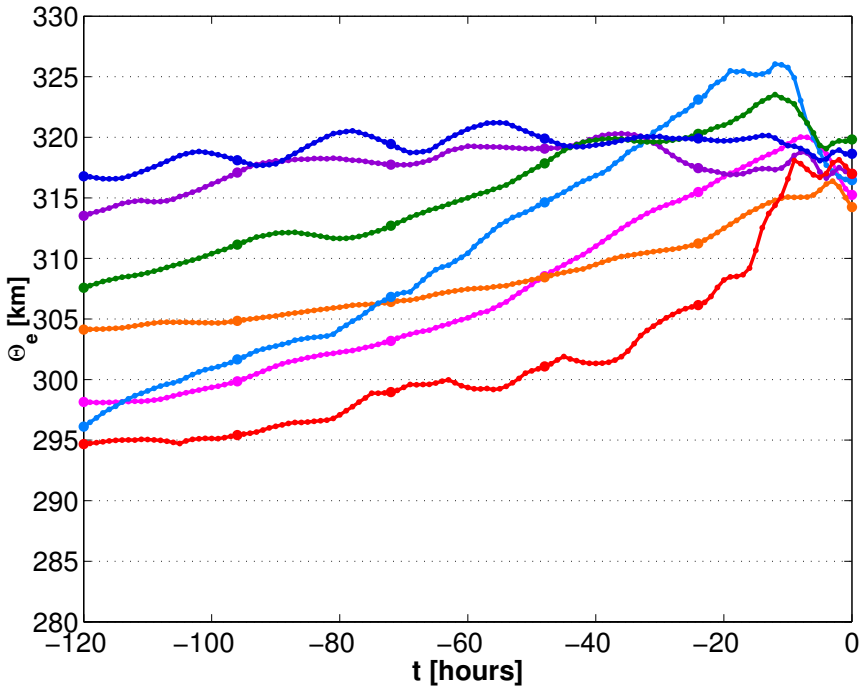

Figure 5.10: Equivalent potential temperature along trajectory clusters arriving over Trentino in the period from 03/11/66 21 UTC to 04/11/66 12 UTC. Colors and circles of different size have been used according to Fig. 5.4

Another possibility offered by the cluster analysis is to perform the budget (see also the previous chapter), using the average cluster trajectories instead of the whole set of trajectories (see Tab. 5.1 and Tab. 5.1 and compare them with Tab. 4.1 and Tab. 4.2). For example, note that the number of trajectories flowing over area 4 is largely overestimated using the "direct clustering algorithm" and that the average specific humidity variation over area 6 appears to be positive while it should be negative and so on. The analysis applied on the trajectory clusters has shorter computational times but introduces large approximations in the budget reconstruction. Thus it is useful: a) to compare various clustering algorithms: the best method should be very faightful to the budget computed starting from the ensemble of trajectories; b) to have an idea whether the computed clusters are representative of the whole set of trajectories or not. A comparison between tables and figures outlines that the procedure is very sensitive to the distance between cluster trajectories and the boundaries of various areas. For example in the event of 1966 (Figure 5.4) the orange cluster is inside area 4 only in the first time step (5 days before the ending time): if it had originated only slightly to the East, this would have drastically changed the analysis of that area because of the large population of the cluster.

	N_k	z_m[dam]	$q_m[\frac{g}{kg}]$	PV_m[PVU]	θ_m[K]	θ_{em}[K]	h_m[dam]	t[h]
1	2760	351 (127)	4.27 (1.63)	0.76 (0.08)	303.9 (6.1)	317.0 (1.8)	81 (9)	1 (2
2	2697	252 (151)	5.53 (1.85)	0.61 (0.25)	300.3 (6.5)	316.9 (2.1)	32 (16)	2 (9
3	2760	138 (70)	7.19 (0.94)	0.43 (0.17)	297.2 (3.2)	318.4 (3.3)	13 (3)	12 (6
4	2377	205 (43)	3.70 (0.77)	0.36 (0.07)	294.1 (1.9)	305.1 (1.9)	38 (23)	22 (44
5	367	198 (34)	4.52 (0.69)	0.46 (0.10)	299.9 (5.1)	313.7 (6.9)	21 (9)	7 (90
6	2618	150 (48)	5.30 (1.38)	0.25 (0.06)	295.3 (4.0)	311.0 (6.2)	27 (12)	21 (33
7	2393	100 (26)	6.49 (1.03)	0.18 (0.08)	295.0 (1.7)	314.1 (4.1)	15 (5)	32 (14
8	73	225 (156)	3.04 (1.65)	0.50 (0.07)	291.9 (5.7)	300.9 (5.2)	37 (16)	27 (69
9	10	738 (439)	0.09 (1.63)	0.61 (0.00)	307.9 (17.9)	308.3 (13.1)	26 (23)	13 (99
10	0	0 (0)	0.00 (0.00)	0.00 (0.00)	0.0 (0.0)	0.0 (0.0)	0 (0)	0 (0
11	73	282 (226)	1.91 (0.97)	0.61 (0.08)	292.0 (7.8)	297.7 (5.2)	14 (9)	40 (61
12	383	130 (28)	5.44 (1.01)	0.20 (0.07)	303.0 (2.3)	319.6 (0.4)	39 (6)	77 (37

Table 5.1: The same quantities shown in Tab.4.1 are reported for the event of November 1966. In the present table data have been computed starting from the cluster trajectories (obtained using the "direct clustering" algorithm) so as all trajectories gathered together into one cluster had the average position and the average properties of the cluster.

	δz[dam]	$\delta q[\frac{g}{kg}]$	δPV[PVU]	$\delta\theta$[K]	$\delta\theta_e$[K]	δh[dam]	$\delta Q_{TOT}[\frac{kg}{m^2 h}]$
1	58 (27)	-1.04 (0.60)	0.05 (0.10)	2.18 (0.95)	-0.70 (0.75)	43 (16)	-0.057
2	33 (41)	-0.37 (0.47)	0.04 (0.10)	1.06 (0.83)	0.02 (0.61)	17 (11)	-0.021
3	187 (238)	-2.04 (2.26)	0.44 (0.14)	5.06 (4.65)	-0.52 (2.26)	20 (14)	-0.093
4	-31 (32)	0.91 (0.47)	-0.06 (0.07)	-0.50 (1.81)	2.05 (2.05)	-13 (14)	0.041
5	-10 (13)	0.13 (0.17)	-0.16 (0.16)	-0.17 (0.71)	0.20 (0.27)	8 (33)	0.001
6	-24 (44)	0.48 (0.72)	-0.04 (0.13)	0.44 (1.05)	1.85 (2.69)	-8 (9)	0.036
7	-47 (64)	1.78 (1.30)	0.01 (0.10)	0.27 (1.13)	5.32 (3.37)	-5 (9)	0.122
8	-44 (84)	0.55 (0.19)	-0.19 (0.08)	0.91 (1.27)	2.56 (1.83)	40 (55)	0.001
9	-74 (82)	0.04 (0.08)	-0.13 (0.21)	-2.55 (0.40)	-2.39 (0.54)	32 (41)	0.000
10	0 (0)	0.00 (0.00)	0.00 (0.00)	0.00 (0.00)	0.00 (0.00)	0 (0)	0.000
11	-97 (102)	1.70 (1.32)	-0.04 (0.01)	-1.89 (1.19)	3.00 (2.59)	-34 (37)	0.002
12	-43 (56)	0.04 (0.56)	-0.21 (0.14)	2.42 (0.92)	2.74 (2.32)	5 (9)	0.000

Table 5.2: The same quantities shown in Tab.4.2 are reported for the event of November 1966. In the present table data have been computed starting from the cluster trajectories (obtained using the "direct clustering" algorithm) so as all trajectories gathered together into one cluster had the average position and the average properties of the cluster.

6 Discussion of results

In the present, chapter the results are discussed, based on both the budget and the cluster analysis. A conceptual model describing the airstreams flowing over the Mediterranean basin during heavy precipitation events is proposed. This provides a preliminary basis for the classification of meteorological situations producing intense precipitation events over the Alps. Finally a preliminary test of the sensitivity of the trajectory method to the resolution of input data is reported.

6.1 Detailed Lagrangian analysis of the three case studies

The synoptic scenarios described in chapter 4 for each one of the 3 considered events and the relative budget studies can be read in the light of the clustering analysis. Furthermore, it is possible to recognize the most considerable components of the airflows originating over various areas and characterized by various water vapour contents.

6.1.1 Event of November 2000

In the this section all the figures and the tables obtained from cluster analysis of the event of November 2000 will be ispected. Analysis of figures 6.1, 6.2and 6.3 obtained from the "initial geographical clustering" method indicates that:

- There are two predominant air streams: the first one (in light blue color) comes from the Sahara desert, the second one (in green color) flows around a restricted area over the Mediterranean Sea. They start from different regions but from the same height above sea level (2km). In the last 2 days, the light blue cluster rises up to 2 km higher than the green one.
- The two main clusters experience a first strong ascent a day before the arrival: the light blue cluster over Area 6 (i.e. in the north of Algeria before and while crossing the Atlas), the green cluster over the Area 3 (i.e over Sardinia). Whilst the first rising is undoubtly due to the rising motion in the cyclone (see Fig. 6.2), in the last 6 hours before the end time "all the

clusters" are also subjected to the orographic lifting (see the terrain profile beneath cluster trajectories).

- Both clusters have an initial specific humidity of 3.5 g/kg. Then they gain humidity just in the 2 days before experiencing the strong cyclonic ascent: note that the maximum in specific humidity occurs halfway through the ascent.

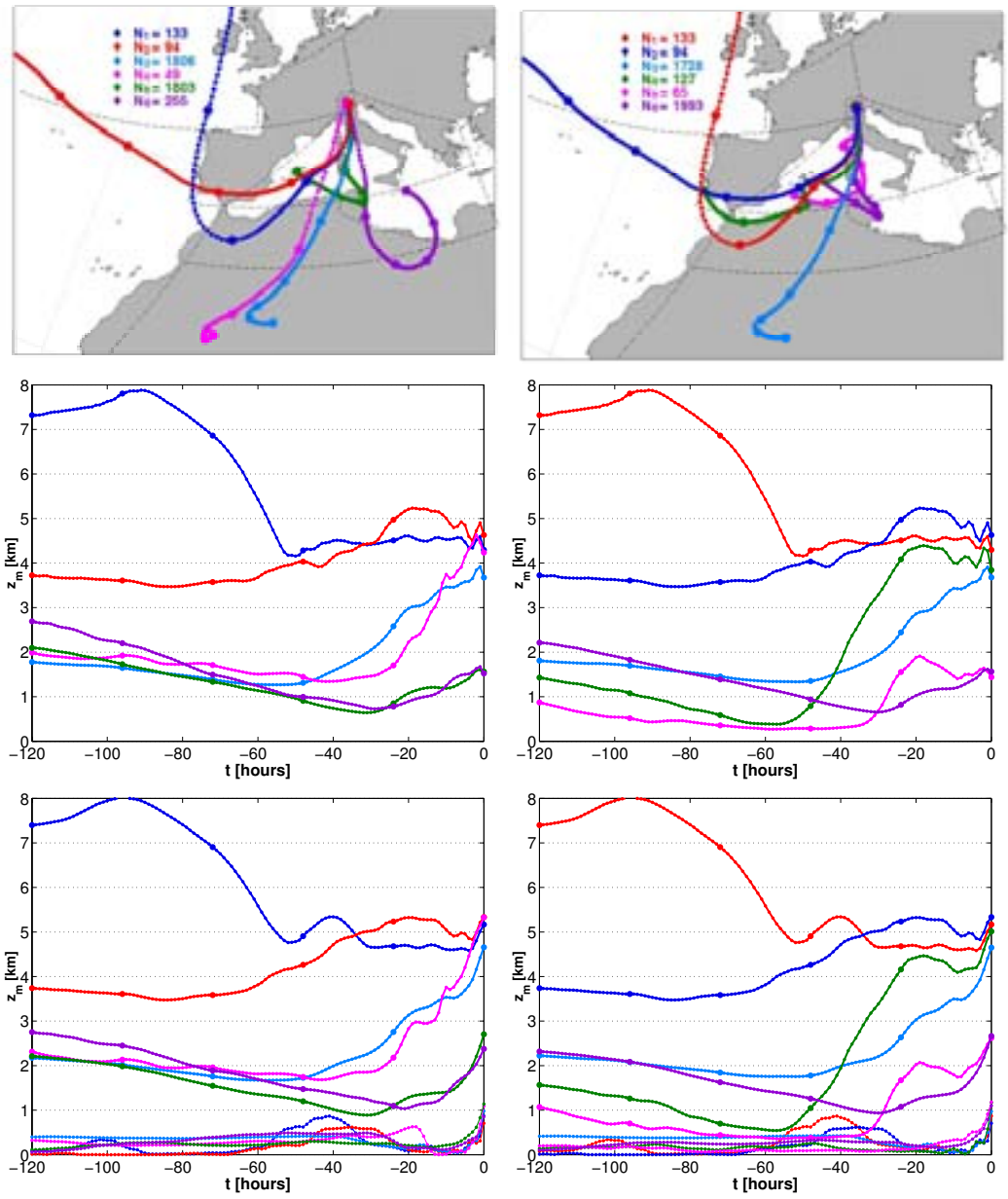

Figure 6.1: Clusters of trajectories arriving over Trentino in the period from 16/11/00 18 UTC to 17/11/00 18 UTC. On the left handside there are the clusters obtained from the "final geographical clustering", on the right handside there are the clusters obtained from the "initial geographical clustering". In the first couple of plots each curve is the average, in the physical space, of all trajectories belonging to that cluster. The average position every hour is marked by a small circle, the position every 24 hours by a big one. The number of trajectories for each cluster is reported. In the second and in the third couple of plots there are the average height of the clusters above the surface and the average height above the mean sea level of the cluster and of the terrain beneath them respectively.

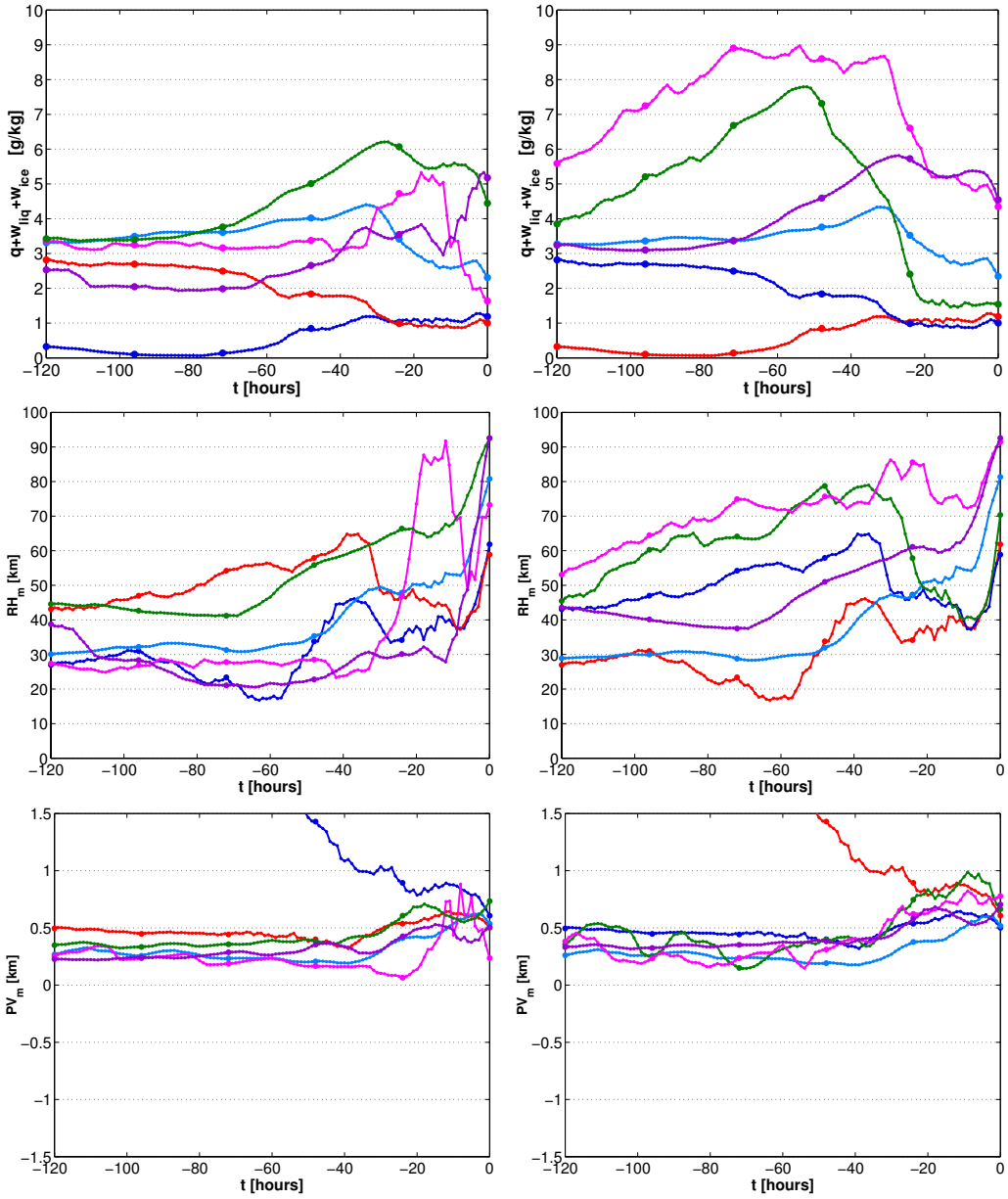

Figure 6.2: Clusters of trajectories arriving over Trentino in the period from 16/11/00 18 UTC to 17/11/00 18 UTC. On the left handside there are the clusters obtained from the "final geographical clustering", on the right handside there are the clusters obtained from the "initial geographical clustering". In the first, in the second and in the third couple of plots there are the average water concentration ($q + w_{liq} + w_{ice}$), the average relative humidity (RH_m), and the average potential vorticity (PV_m) of the clusters respectively. The clusters have been marked by different colors and circles of different size according to figure 6.1.

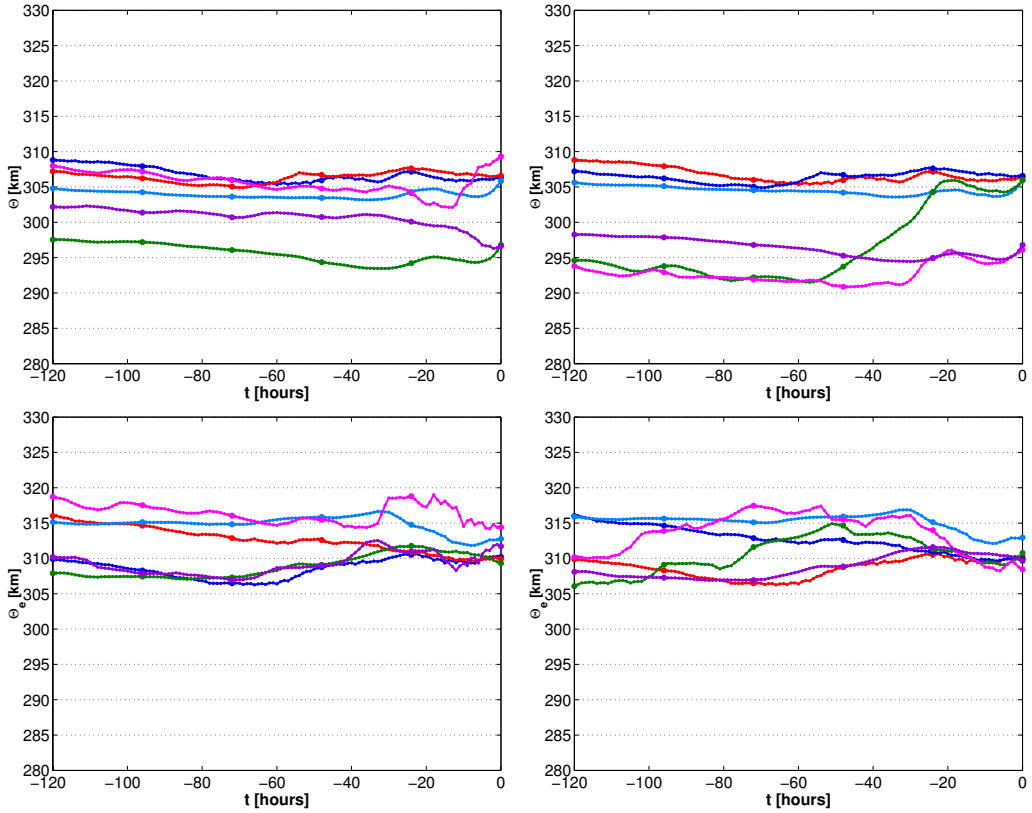

Figure 6.3: Clusters of trajectories arriving over Trentino in the period from 16/11/00 18 UTC to 17/11/00 18 UTC. On the left handside there are the clusters obtained from the "final geographical clustering", on the right handside there are the clusters obtained from the "initial geographical clustering". In the first and in the second couple of plots there are the average potential temperature (θ) and the average equivalent potential temperature (θ) of the clusters respectively. The clusters have been marked by different colors and circles of different size according to figure 6.1.

By looking at the synoptic charts from the Met Office (see Fig. 4.9), it is possible to see a cold front approaching the Mediterranean Sea between the 14th and 15th of November. The meridional tail of this cold front favoured the development of a surface weak low near Gibraltar (15th November 00 UTC). Subsequently the low moved eastward north of Algeria (16th November 00 UTC) and then eastward and northward toward Sardinia (17th November 00 UTC) and the Gulf of Genoa (18th November 00 UTC). Because of the cyclonic development the cold front manifested peculiar properties: north of the cyclonic center it changed to a warm front, whereas in its meridional part it seemed to remain stationary, sliding north-eastward along its axis.
The above synoptic evolution explains the observed "cyclonic" rising of the light blue cluster: it moves inside the warm conveyor belt and is slightly enriched in humidity (probably deriving from the evaporation following intense precipitations occurred over the north of Algeria). After that, it contributes to the precipitation over the coasts and over the mountains of Algeria. The green cluster starts eastward of the developing low center, so it gains humidity because of evaporation from the sea (it is flowing in the ABL) or because of re-evaporation of precipitation falling from higher levels. It is reasonable to guess that the air stream represented by the light blue cluster, flowing 2 km above the green cluster and losing humidity, is a persistent feature over North Algeria for 24 - 48 hours. In the last day, the green cluster, captured by the warm conveyor belt, moves northward at low levels and is associated with precipitation, first over Sardinia, later over northern Italy.
By looking at figures 6.2 and 6.3, it possible to draw out further observations:

- The values of relative humidity for the described air streams are far from saturation: 50-60% one day before the arrival, 80-90% at the arrival. This apparently anomalous feature can be explained in different ways:

  1. The relative humidity of a populated cluster is the average of the RH values of many trajectories. Far away from the target area, the cluster is heterogeneous: since it is reasonable to expect that the saturation conditions occur only in restricted areas, the mean values of RH are never close to 100%. Conversely, this is possible over the target area, i.e. at the ending time of trajectories.
  2. If a precipitation area is characterized by embedded convection, it is possible to have a strong heterogeneity in precipitation as well as in relative humidity fields. Mean values report precipitation as well as absence of saturation.

  In this case there is probably the contribution of both the effects over the north of Algeria (with frontal convection).

- Precipitation is accompanied by diabatic PV production (see green and light blue cluster in

figure 6.2)

- In general, potential temperature seems to decrease when a descent of clusters is observed (the first three days), whereas it increases with precipitation because of the released latent heat. Morover, the initial height and the specific humidity being equal, the light blue cluster coming from the Sahara is warmer than the green one (which suggests stable atmosphere).
- The figure of equivalent potential temperature outlines that the increase of specific humidity of the green cluster in the first three days is due to evaporation (θ is constant, while θ_e increases), but the increase in the fourth day is due to re-evaporation of precipitating droplets since θ_e is constant, q increases and θ decreases (vaporization latent heat). It is hard to explain the decrease of equivalent potential temperature of the light blue cluster during precipitation. It could be possible to explain that effect with embedded convection (there is a net transfer of energy from the higher levels of atmosphere to the lower levels). Another possibility is that a decrease of θ_e (expressed by the classical formula) is due to the sensible heat transferred to the droplets during condensation: generally this effect is quite small if precipitation is not very large.

The other clusters are not so populated. Still, it is interesting to note the followings:

- The blue cluster is related to a dry stratospheric intrusion following the cold front
- The violet cluster is a dry air stream flowing over Area 7 and 6 for 4 days. It starts at 3 km of height but descends slowly in the boundary layer where it gains humidity by evaporation (over the coasts of Lybia). In the last day it experiences a further increment in specific humidity content and a decrease in the potential temperature: this suggest that at the lowest levels of troposphere there is re-evaporation of precipitation.

Another possibility of clustering is the "final geographical clustering". Figure 6.1 shows that some clusters are equivalent to the clusters obtained from the previous "initial geographical clustering". They are the clusters which are born from the first "geographical phase" of the clustering procedure and that are not affected by a sub-division in the second "humidity phase". Moreover it is possible to note that the new violet cluster is very similar to the green one. In the new analysis, a cluster starting from Lybia does not emerge, but two new clusters appear (the green one and the magenta one) starting from the west of the Mediterranean Sea. They were moist and cold air masses at low levels affected by the passage of the cold front: quickly advected at medium levels they produced precipitation. Their "zig-zag" movement is symptomatic of both their small population and of their passage near the center of the low. Finally it is clear from figure 6.2 how the clustering method

works: the new clusters differ for specific humidity variations in the first 2-3 days, the cluster of the previous methods for variations in the last 12 hours.
The last clustering method adopted in the present work is the "direct clustering". All the resulting clusters differs from the clusters of the previous methods, since the phase space for clustering is different. An unexpected property is the homogeneity of cluster population which gives an equal importance to trajectories having different courses and different specific humidity contents. Note that:

- The red and the violet clusters are similar to the clusters outlined by the "initial geographical clustering method" (the green one and the magenta one in that case): they gather together trajectories flowing close and around the cyclonic center, forced to a rapid ascent and to precipitation production. After that they flow in the rear of the front: while the red cluster is very dry, the violet cluster is still sufficiently humid to guarantee condensation after orographic lifting.

- The green cluster is a bit similar to the light blue one of the previous method: it is very dry and warm; it gains 1 g/kg of specific humidity over the desert of Sahara (note a through in the synoptic chart of 16 November), rises uniformely of more than 2 km producing precipitation over the north of Italy.

- The light blue cluster partially reminds of the violet cluster of the "final geographical clustering method"

- The magenta cluster reminds of the green cluster of the first method and the violet cluster of the second method

The analysis of trajectory clusters clarifies the dynamical reasons of data reported in budget tables 4.3 and 4.4:

- Air masses flowing over Area 12 and coming from tropical regions are quite dry (the mean values of q is only 2.81 g/kg for trajectories close to the ABL) and warm. Initial mean values of θ for cluster green in Fig. 8.3 is 308 K (the lower average value of 302 K over the whole area is conditioned by cold air masses in the rear of the cold front flowing from the North toward Morocco and then turning north-eastward). Over Area 12 southerly air masses increase a lot their water vapour content because of strong evaporation (mean increments of 3.33°C in θ_e); a residual contribution from re-evaporation of clouds or precipitation droplets could justify the negative variations in potential temperature. Cluster trajectories in Figure 8.3 clearly restrict the evaporation area just below the 30° of latitude and to a temporal window of 24 hours (on 15th of November).

- Air masses flowing over area 7 gather the easterly component of air streams from the desert (light blue cluster in Figure 6.1), the originally dry but colder air flow starting in the middle troposphere over the Central Mediterranean (violet cluster in Figure 8.3) and the low airstream flowing around anticyclonically over the Gulf of Gabes (Figure6.1). Globally these air masses are moister (the mean values of q is 4.00 g/kg) and slightly colder. They receive a lot of water vapour by evaporation and re-evaporation (the second one is probably more pronounced in the north western corner). It is interesting to note that the values of δq are smaller in comparison to δQ. The δq value is computed as the average variation of q along trajectories while flowing over the considered Area: if trajectories cross the Area more than once (as it happens for Area 7) δq is the average over all trajectories and over all the times. So if the crossing is short , δq is more underestimated: the same conclusions can be drawn for computed values of δPV, $\delta\theta$, $\delta\theta_e$, etc.

- Air masses over Areas 5 and 8 are cold and dry since they come from the north of Europe: because of this they gain a relatively large amount of water vapour over those areas. Over area 8 water vapour essentially comes from re-evaporation of cloud or precipitation droplets cumulated in the lower levels after the passage of the cold front.

- Air masses flowing over area 4, related to the passage of the cold front, are moist (4.67 g/kg) and not very warm. They produce a considerable precipitation marked by the strong ascent, the increase in potential temperature and the production of PV.

- It is hard to give an interpretation of the mean values of various variables for Area 6 since it is affected by both evaporation in the southerly part near Area 12 and precipitation at the boundary with Area 4. Morover, the dynamics of air masses changes because of the movement of the cold front inside that area. These air masses consist of warm air streams flowing from the South in the mid troposphere (light blue cluster in Fig 6.1) and lower and moister air streams ahead of the cold front flowing from the West over the Algerian coasts and mountains (red and violet clusters).

- Area 3 is crossed by almost all trajectories, which are still moist, but do not release much precipitation.

Figure 4.10 shows that evaporation estimated by the Lagrangian budget is almost negligible compared to real evaporation.

- Air masses flowing over area 4 and ending over the target area are mostly in the warm side of the cold front and are affected by cyclonic ascent and precipitation. They cannot take into

account strong evaporation occurring over the Mediterranean Sea near the coasts of Spain and France where a post-frontal dry wind blows over the sea surface favouring strong latent heat fluxes from the earth to the atmosphere.

- Trajectories flowing over area 7 experience the westerly boundary domain inside Area 7, which is not representative of the whole area (remember that this is the evaporation for time unit: the total computed evaporation over area 7 is not negligible since trajectories spend a lot of time over that area)

6.1.2 Event of November 2002

By looking at the synoptic charts from the Deutscher Wetterdienst (see Fig. 4.15) it is clear that Italy is affected by a series of fronts driven by the deep low Xara centred to the East of Ireland. The "first cold front" reaches Italy on 22 November, while its southerly tail slides zonally along the northward slopes of Atlas, without crossing the mountains. Subsequently, Gibraltar, approached by a "second cold front", is characterized by persistent cyclogenesis. A first low center, "Andrea", moves toward France on the 24th of November, thus favouring the formation of a warm front over the Alps on 25 November (Fig. 4.15) which characterizes the "**first phase**" of the event: 24 November 18 UTC - 25 November 09 UTC. The second low center, "Cornelia", moves toward Sardinia, hitting Italy on 26 November: the "**second phase**" of the event covers the period from 25 November 21 UTC to 26 November 12 UTC. On 25-26 November the part of the "second cold front" to the south of "Cornelia" low center breaks through Morocco, Algeria and Lybia channelling cold air over the North Africa. This uses up the energy reserves over Sahara resulting to be the last important autumnal precipitation event over that Mediterranean area.
The deepening of "Cornelia" on the 25th of November 2002 and the contemporary reinforcement of the high pressure area over the Eastern Mediterranean and over the East of Europe produces a strong zonal pressure gradient over Libia and the south of Italy (Fig. 4.15). The north of Italy is affected by a quasi-stationary warm front. Unlike other events (November 1966, November 2000 and the first phase of 2002) on 26 November 00 UTC the warm front is not leant against the Alps, but it extends north-eastward from the low center to Austria. This implies more marked easterly flow components in the lower tropospheric layers over the North and Central Italy.
The paragraph reports detailed observations and comments, derived from the cluster analysis of the "**first phase**" of the 2002 event (24 November 18 UTC - 25 November 09 UTC), as it has been done for the event of 2000.

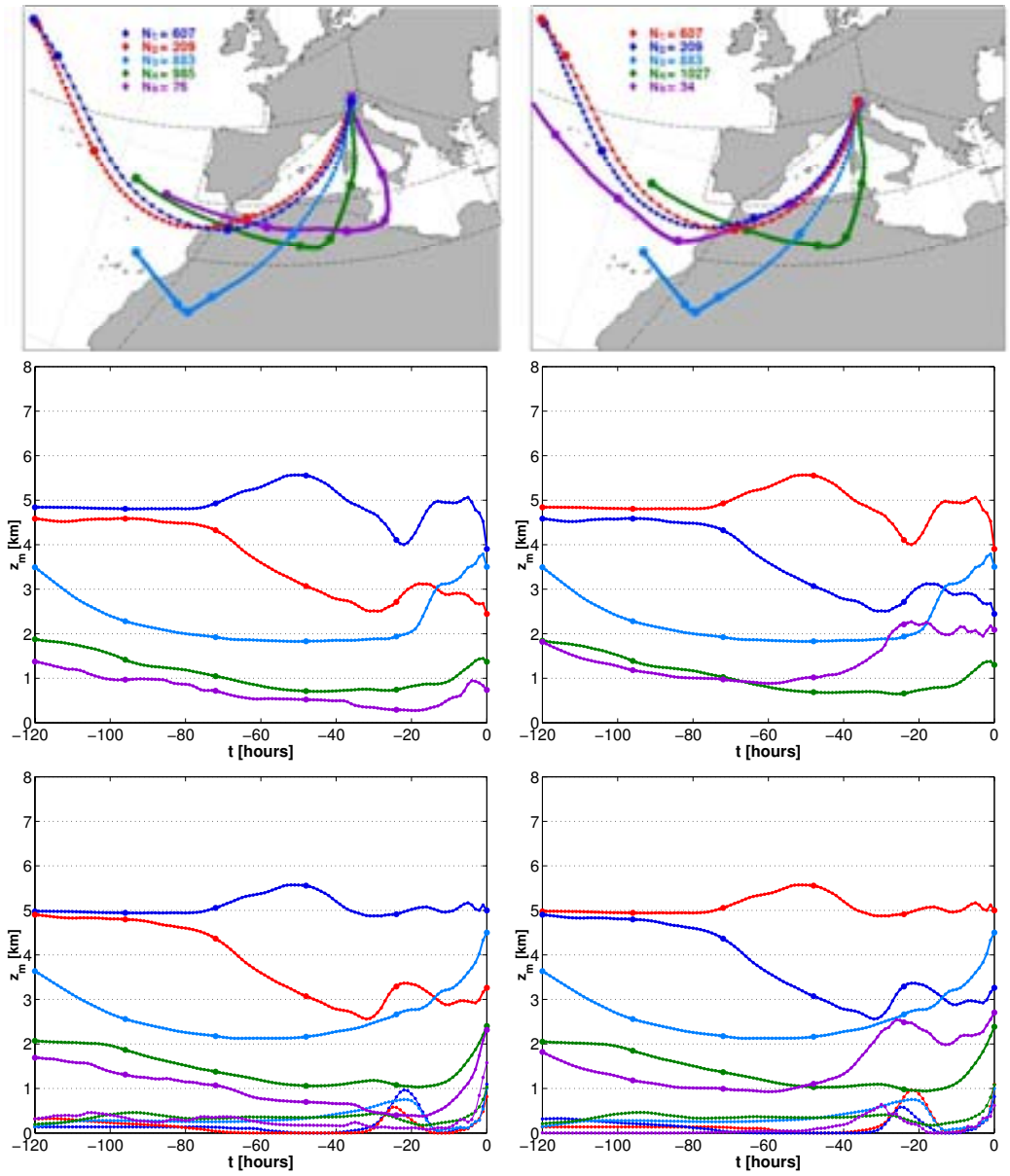

Figure 6.4: Clusters of trajectories arriving over Trentino in the period from 24/11/02 18 UTC to 25/11/02 09 UTC. On the left handside there are the clusters obtained from the "final geographical clustering", on the right handside there are the clusters obtained from the "initial geographical clustering". In the first couple of plots each curve is the average, in the physical space, of all trajectories belonging to that cluster. The average position every hour is marked by a small circle, the position every 24 hours by a big one. The number of trajectories for each cluster is reported. In the second and in the third couple of plots there are the average height of the clusters above the surface and the average height above the mean sea level of the cluster and of the terrain beneath them respectively.

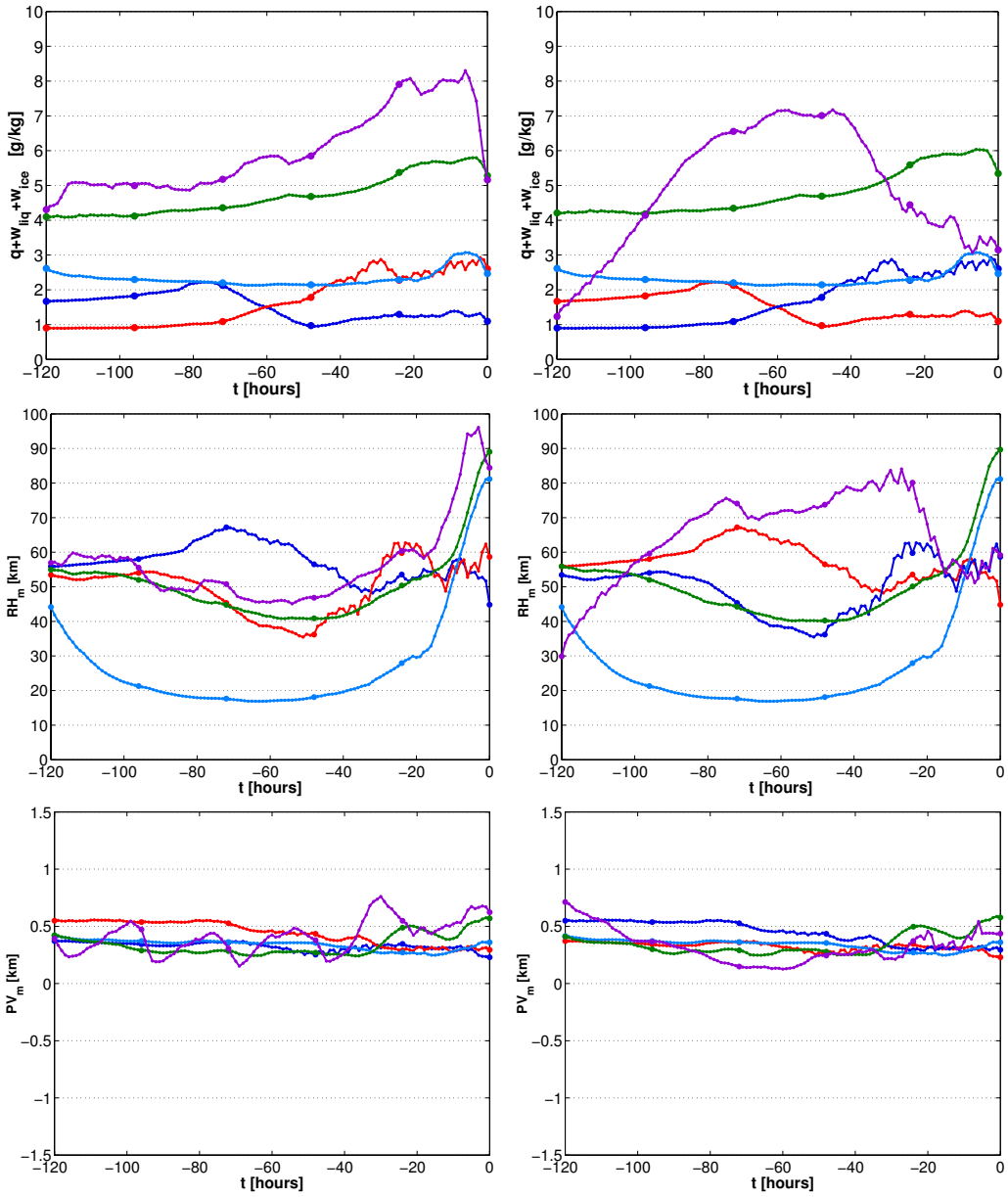

Figure 6.5: Clusters of trajectories arriving over Trentino in the period from 24/11/02 18 UTC to 25/11/02 09 UTC. On the left handside there are the clusters obtained from the "final geographical clustering", on the right handside there are the clusters obtained from the "initial geographical clustering". In the first, in the second and in the third couple of plots there are the average water concentration ($q + w_{liq} + w_{ice}$), the average relative humidity (RH_m), and the average potential vorticity (PV_m) of the clusters respectively. The clusters have been marked by different colors and circles of different size according to figure 6.4.

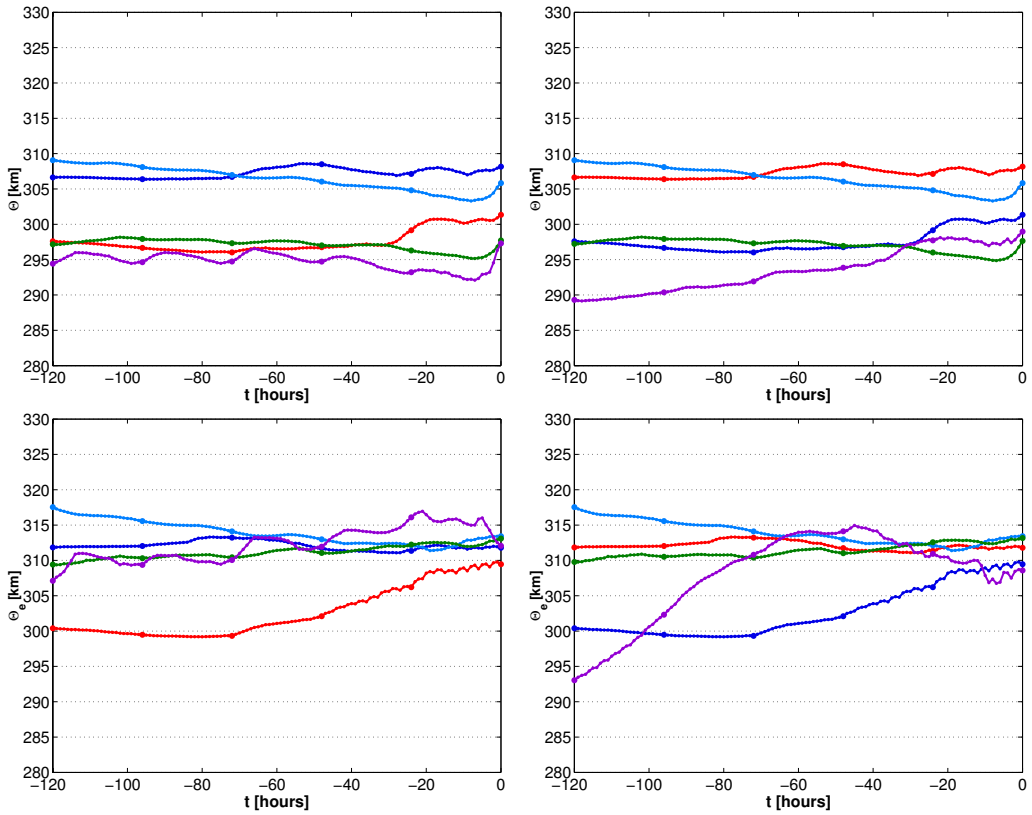

Figure 6.6: Clusters of trajectories arriving over Trentino in the period from 24/11/02 18 UTC to 25/11/02 09 UTC. On the left handside there are the clusters obtained from the "final geographical clustering", on the right handside there are the clusters obtained from the "initial geographical clustering". In the first and in the second couple of plots there are the average potential temperature (θ) and the average equivalent potential temperature (θ) of the clusters respectively. The clusters have been marked by different colors and circles of different size according to figure 6.4.

Figures 6.4, 6.5 and 6.6, stemmed from the application of the "initial geographical clustering", suggest that the first phase of 2002 precipitation event is characterized by an intense zonal flow from the Atlantic Ocean to the Mediterranean basin (air parcels move quickly from West to East). Inside the zonal flow three main airstreams can be identified: an upper level jet (the red and dark blue clusters) originating in the West Atlantic Ocean and flowing at a mean velocity of 40 m/s; a lower level airstream (the green and violet clusters) originating in the East Atlantic between the Azores Islands and Morocco, crossing the Atlas, bending to the north over Tunisia and flowing over the Tyrrhenian Sea; an airstream (the light blue cluster) originating over the coast of Morocco, flowing at first south-east of the Atlas chain, then crossing the north of Algeria and Sardinia. The three airflows have about the same trajectory population (one third of the total number), but they are characterized by different features:

(a) The upper level airstream flows at almost constant height, without being affected by orographic perturbation introduced by the Atlas and the Alps. It does not contribute to precipitation because of the low values of relative humidity.

(b) The airstream flowing at the lower levels (green and violet clusters) greatly contributes to precipitation over the Alps. By comparing the position of the air parcels along this airstream with the position of the "first cold front" on 22 November 00 UTC, it is clear that over the southern side of the Atlas the air masses are flowing ahead, but on the fringes of the front. In fact, during this phase, their motion and their feature do not resemble the typical feature of the WCB. Subsequently, on 23 November, a zonal pressure gradient arises over the Central Mediterranean area. The airmasses flow at low levels (1km) over Tunisia which, on the contrary, has been directly affected by the previous cold front (on 22 November) and where the specific humidity of trajectories is increased.

(c) The airstream originating east of Morocco flows at medium levels and has rather low RH values. These are explained by the high values of potential temperature (310 K) and the middle values of specific humidity (2.5 g/kg). Nevertheless, the strong ending ascent during the last day brings the air masses to saturation, thus contributing to precipitation.

On 25 November the WCB over Italy, occurring ahead of the "second cold front" and delimited by the warm front over the Alps, is formed by two airstreams, the moist low level airstream described above (green and violet clusters) and the light blue cluster. In fact, by comparing trajectories of the higher clusters (red and the dark blue) with the position of the cold front system indicates that these clusters represent cold air masses flowing behind the cold front (which explains their partial descent).

The surface pressure chart valid on 25 November 2002 00 UTC (Fig. 4.15) indicates that there is a sort of double cold front over the Mediterranean Sea. The westerly front is the real surface cold front, the other one is not on the surface but at a middle altitude in the troposphere (verifiable by observing cross section analysis -not reported here-). Such sort of upper level front (Browning, 1990 for further details) develops as an upper level cold intrusion (the red cluster in such case) breaks through the warmer air ahead of the surface front (the light blue cluster above and the green one below) . In fact light blue air masses are potentially warmer (see Fig. 6.6): 24 hours before the ending time the red cluster, flowing at a mean height of 3.2 km, has lower θ values with respect to the light blue cluster (flowing at a mean height of 2.5 km). So the blue trajectories are forced to rise over the red trajectories during the period from 20 to 10 hours before arrival, after they pass the Algerian Mediterranean coasts and before they flow over the Gulf of Genoa (essentially over macroarea 4), reaching saturation. In the last 20 hours, the red air masses represent a dry layer between 2 precipitating airstreams.

Note that the light blue trajectories register a clear increment in specific humidity although they experience strong vertical lifting over there; moreover they are characterized by a mean decrease in θ and a mean increment of 0.61 K in θ_e. This is explained by the development of convective conditions, which determine a net exchange of water vapour with the lower airstreams. A further contribution to the increase of moisture along the light blue trajectories (over area 4) is re-evaporation of the precipitation falling from higher layers.

Using other clustering methods, similar results and conclusions have been obtained (results are reported in the Appendix).

The mean values of various variables obtained from the budget analysis (Tab. 4.5 and 4.6) show the properties of trajectories flowing over various macroareas, which help us to define the aforementioned scenario of the trajectory features. First of all, it is clear that, in this case, a few macroareas are crossed by trajectories: in fact they follow a narrow route starting from the Atlantic, flowing over Gibraltar, northern Africa, to finally bend northward toward the Alps. Less than a quarter of the total number of trajectories flows over Area 7 (mostly over its north-westerly corner) and even less over Area 9. Nevertheless, area 7 is characterized by strong evaporation. Trajectories flowing in the ABL, whose mean altitude is less than 1 km, have strong specific humidity increments as well as marked positive variations in the equivalent potential temperature.

The 1022 trajectories flowing over Area 11 belong to the red and dark blue clusters in Fig. 6.4. Over area 11, these trajectories have been previously involved in a cyclonic event, and rise from low to high levels, thus yielding high rainfall rate. This explains the high equivalent potential temperature values for the high level trajectories.

By contrast airstreams flowing over Area 12 (the light blue cluster in Fig. 6.4) are very warm and

dry. In fact, these trajectories originate as already warm air parcels over the Canary Islands (Area 5) at an elevation of 3.5 km and then they slowly descend to an height of 2 km over Morocco without gaining any specific humidity increments.
Finally, trajectories flowing over area 4 have high specific humidity increments because of convection along the cold front (see above).

Results are now discussed from the cluster analysis of the "**second phase**" of the 2002 event from 25 November 21 UTC to 26 November 12 UTC.

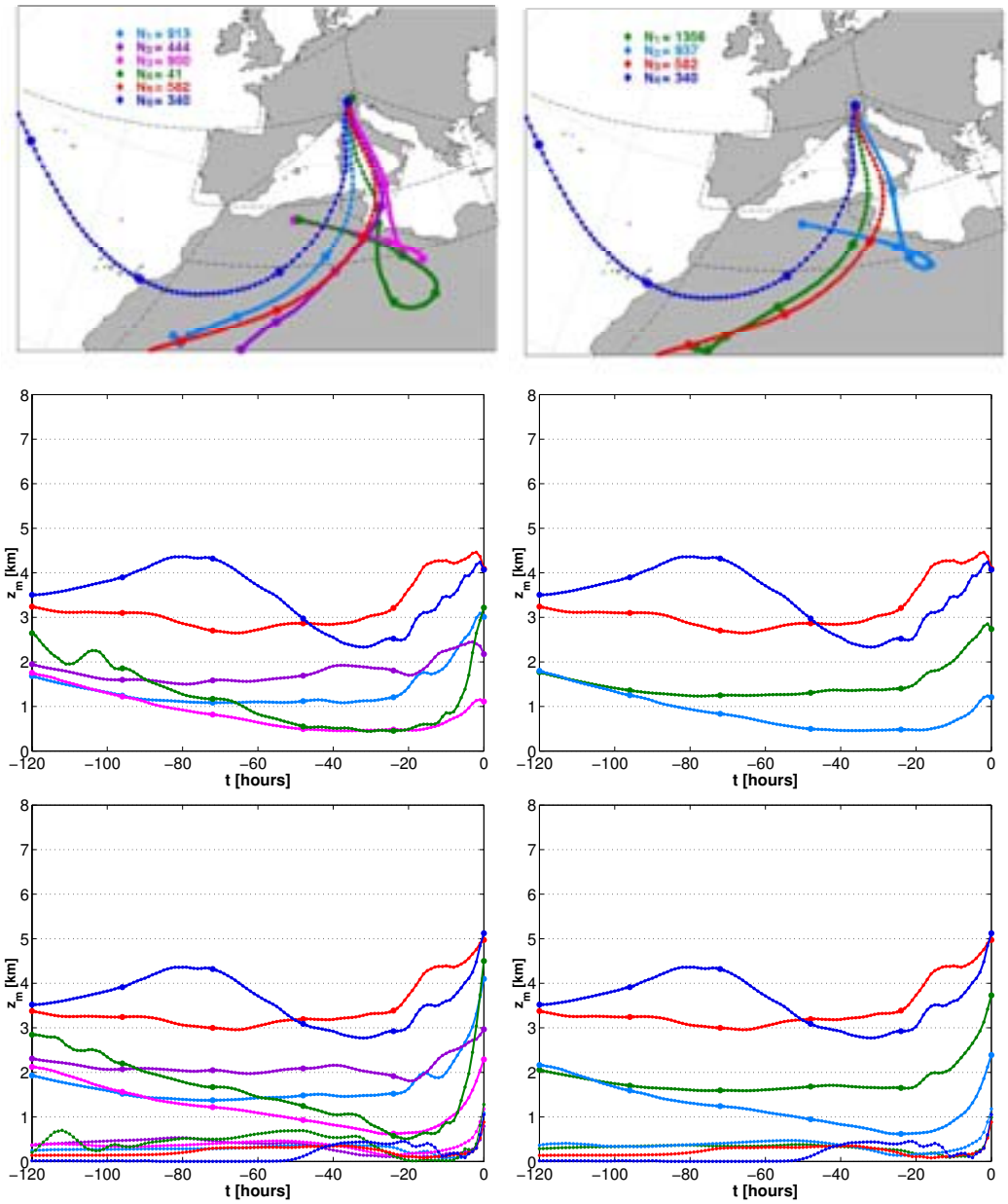

Figure 6.7: Clusters of trajectories arriving over Trentino in the period from 25/11/02 21 UTC to 26/11/02 15 UTC. On the left handside there are the clusters obtained from the "final geographical clustering", on the right handside there are the clusters obtained from the "initial geographical clustering". In the first couple of plots each curve is the average, in the physical space, of all trajectories belonging to that cluster. The average position every hour is marked by a small circle, the position every 24 hours by a big one. The number of trajectories for each cluster is reported. In the second and in the third couple of plots there are the average height of the clusters above the surface and the average height above the mean sea level of the cluster and of the terrain beneath them respectively.

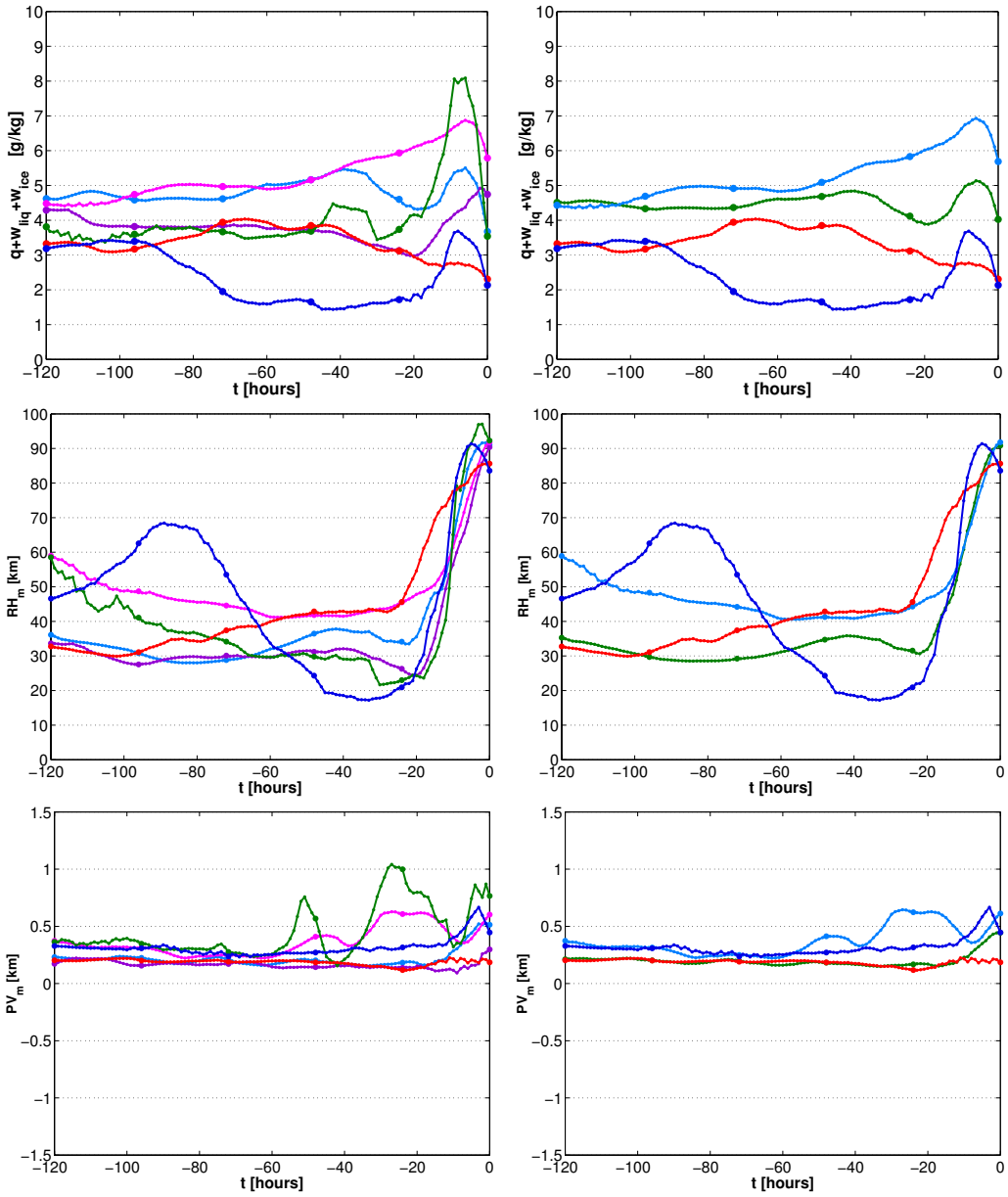

Figure 6.8: Clusters of trajectories arriving over Trentino in the period from 25/11/02 21 UTC to 26/11/02 15 UTC. On the left handside there are the clusters obtained from the "final geographical clustering", on the right handside there are the clusters obtained from the "initial geographical clustering". In the first, in the second and in the third couple of plots there are the average water concentration ($q + w_{liq} + w_{ice}$), the average relative humidity (RH_m), and the average potential vorticity (PV_m) of the clusters respectively. The clusters have been marked by different colors and circles of different size according to figure 6.7.

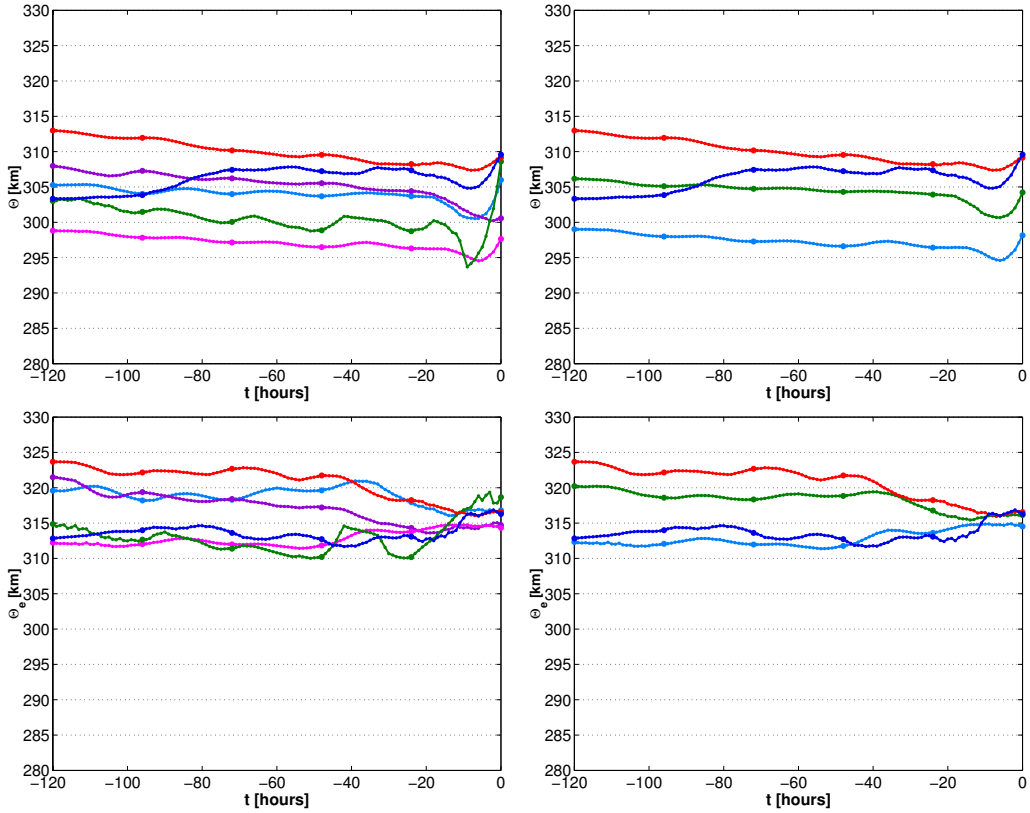

Figure 6.9: Clusters of trajectories arriving over Trentino in the period from 25/11/02 21 UTC to 26/11/02 15 UTC. On the left handside there are the clusters obtained from the "final geographical clustering", on the right handside there are the clusters obtained from the "initial geographical clustering". In the first and in the second couple of plots there are the average potential temperature (θ) and the average equivalent potential temperature (θ) of the clusters respectively. The clusters have been marked by different colors and circles of different size according to figure 6.7.

By analysing trajectory clusters obtained through the "initial geographical clustering" methods (Fig. 6.7, 6.8 and 6.9) it is possible to derive the following considerations:

1. All the air masses arriving over Trentino in the time lag between 25th November 21 UTC and 26th November 12 UTC belong to the WCB ahead of the cold front progressively moving from the area of Spain and Morocco to the north of Africa and to the Central Mediterranenan Sea.

2. The air masses can be classified into 3 different air streams:

   (a) Upper level airmasses (the dark blue and the red clusters) originating respectively over the western Atlantic Ocean and over the western coast of Africa (near Capo Verde and Senegal), flowing at a mean altitude of 3-4 km. The dark blue trajectories flow at the westernmost boundary of the cold front on the 23 November 2002; during the following day they descend from 4.5 km of height to 2.5 km crossing the Balearic Islands on 24th November; finally, they travel over the Atlas and are driven toward Italy always close to the surface cold front. The red trajectories represent the upper part of the warm conveyor belt, which flows less close to the cold front. Because of that they do not show any altimetric descent in the previous days.
   To sum up, the upper level trajectories have the typical features of the W1 warm conveyor belt (see section 5.3).

   (b) Middle level airmasses (the light blue and violet clusters) originating over a large area covering Mauritania and Mali. The light blue cluster flows quite low in the first 3-4 days (1.1 km), but it is rapidly lifted up in the last day before the arrival (25 November 2002). The violet one, flowing more easterly, is farther from the cold front (see for example its position on 25 November 00 UTC) and moves at a mean altitude of 2.7 km without undergoing strong final cyclonic ascent.

   (c) Low level airmasses (the magenta cluster) originating over the northern part of Algeria, moving eastward under the weak forcing of the "first cold front" (on 22-23 November, but without a direct involvement), turning anticyclonically over Lybia (an anticyclone formed on 24th November) at a height of 0.5 km and finally flowing toward Italy when the low center "Cornelia" draws on.

3. During the final day all trajectories enter an area of cyclonic ascent (over the north of Algeria, Tunisia, the Channel of Sicily and the Tyrrhenian Sea) which is not induced by the orographic forcing. The effect is stronger and earlier for upper and middle level clusters.
   With the exception of the most easterly trajectories the lifting occurs during 2 phases: the

ascent is weaker or null in an intermediate time lag (from 15 to 10 hours before the arrival) which corresponds to the period of maximum increasing in the specific humidity. This happens in the region between the coasts of Tunisia, Sardinia and Sicily and can be explained only by a very deep convection occurring in an area where water vapour at the sea surface is uplifted to 3-4 km of height.

4. Air masses converging over the target area have a high content of specific humidity with respect to the previous "atlantic phase" and to the event of November 2000. This is due to the lower trajectories (i.e. the magenta cluster) which are very moist since the beginning (note that they originate over an area characterized by the passage of the low "Yvonne" on 21 and 22 November 2002) and which gain further humidity from evaporation over the sea. Moreover the airmasses coming from the south of Algeria are particularly moist (4-5 gkg^{-1}) in comparison with the typical values of specific humidity (2-3 gkg^{-1}) registered along trajectories flowing over the desert. The latter airstream can be classified as a moist tropical plume originating over the equatorial regions near the ITCZ (section 2.2.2). Nevertheless its effect is moderate because of the extremely high values of temperature (the relative humidity is far from saturation). In fact the initial values of potential temperature for the red and light blue clusters are respectively 313 K and 305 K: higher than the values of θ for the light blue cluster of the first phase (Fig. 6.6) and for the light blue cluster for the event of November 2000 (Fig. 6.1). The higher moisture of these airmasses results from the values of the equivalent potential temperature (320-325 K), which are higher by at least 5 degree than in the other events.
   The driest airstreams are the violet cluster originating in the internal regions of the desert and the dark blue one which is cold and dry.

5. The warm conveyor belt appears to be stable with the exception of the dark blue and of the light blue clusters which produce conditional instability conditions.

More information can be derived from the "direct clustering" algorithm (Fig. 8.7 and 8.8). First of all, it is clear that not only the easternmost airstream but some others originate close to the Atlas chain, move eastward in the first day, rotate slowly anticyclonically undergoing a downward vertical displacement and finally are rapidly forced to move northward, which partially explains the higher moisture of this cluster. Tables derived from the budget analysis (Tab. 4.7 and 4.8) help to focus on the two most important sources of moisture:

1. Area 7, which is crossed by trajectories moving at very low heights;

2. Area 3, where airmasses mostly increase their moisture content by re-evaporation of liquid

droplets, since θ decreases (-0.97 K) while θ_e is constant. Moreover note that over this area trajectories undergo a strong vertical ascent (an average of 700 m).

Viceversa it is also clear from this table that a minor loss of moisture over Area 12 and 6 probably due to ABL turbulence fluxes, which are enhanced by the intensity of the low level winds, occurs.

6.1.3 Event of November 1966

Figures (Fig. 6.10, 6.11, 6.12) obtained from the "initial geographical clustering" method tell us that there are three air streams during the central phase of the event:

- a very little populated trajectory cluster (the red one) originating in the West of Ireland 5 days before the ending time;
- another one (dark blue) originating over the Canary Islands;
- the main airstream (96% of all trajectories) converging over Area 7 just one day before the ending time and then quickly flowing to the North toward Italy.

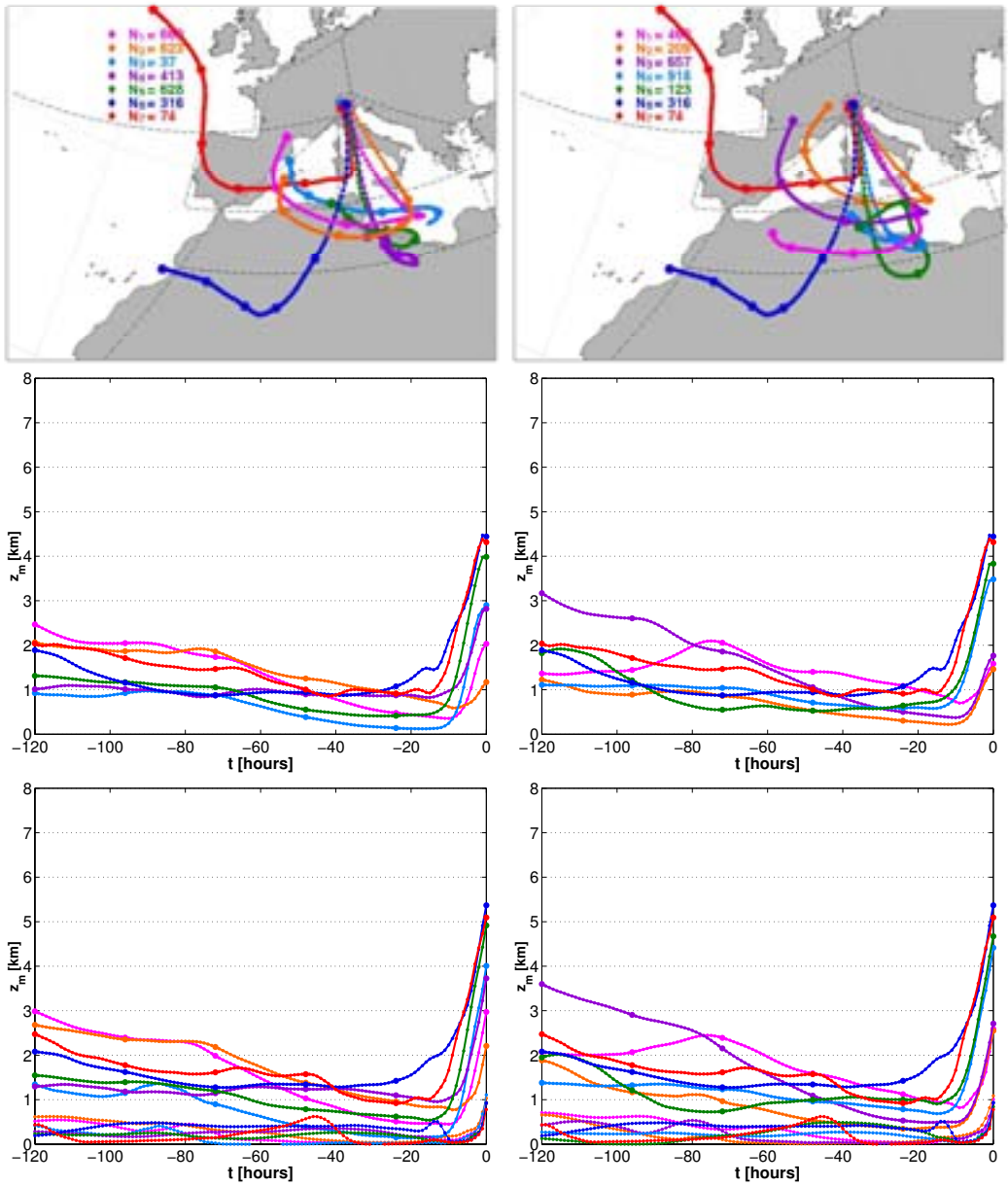

Figure 6.10: Clusters of trajectories arriving over Trentino in the period from 03/11/66 21 UTC to 04/11/66 12 UTC. On the left handside there are the clusters obtained from the "final geographical clustering", on the right handside there are the clusters obtained from the "initial geographical clustering". In the first couple of plots each curve is the average, in the physical space, of all trajectories belonging to that cluster. The average position every hour is marked by a small circle, the position every 24 hours by a big one. The number of trajectories for each cluster is reported. In the second and in the third couple of plots there are the average height of the clusters above the surface and the average height above the mean sea level of the cluster and of the terrain beneath them respectively.

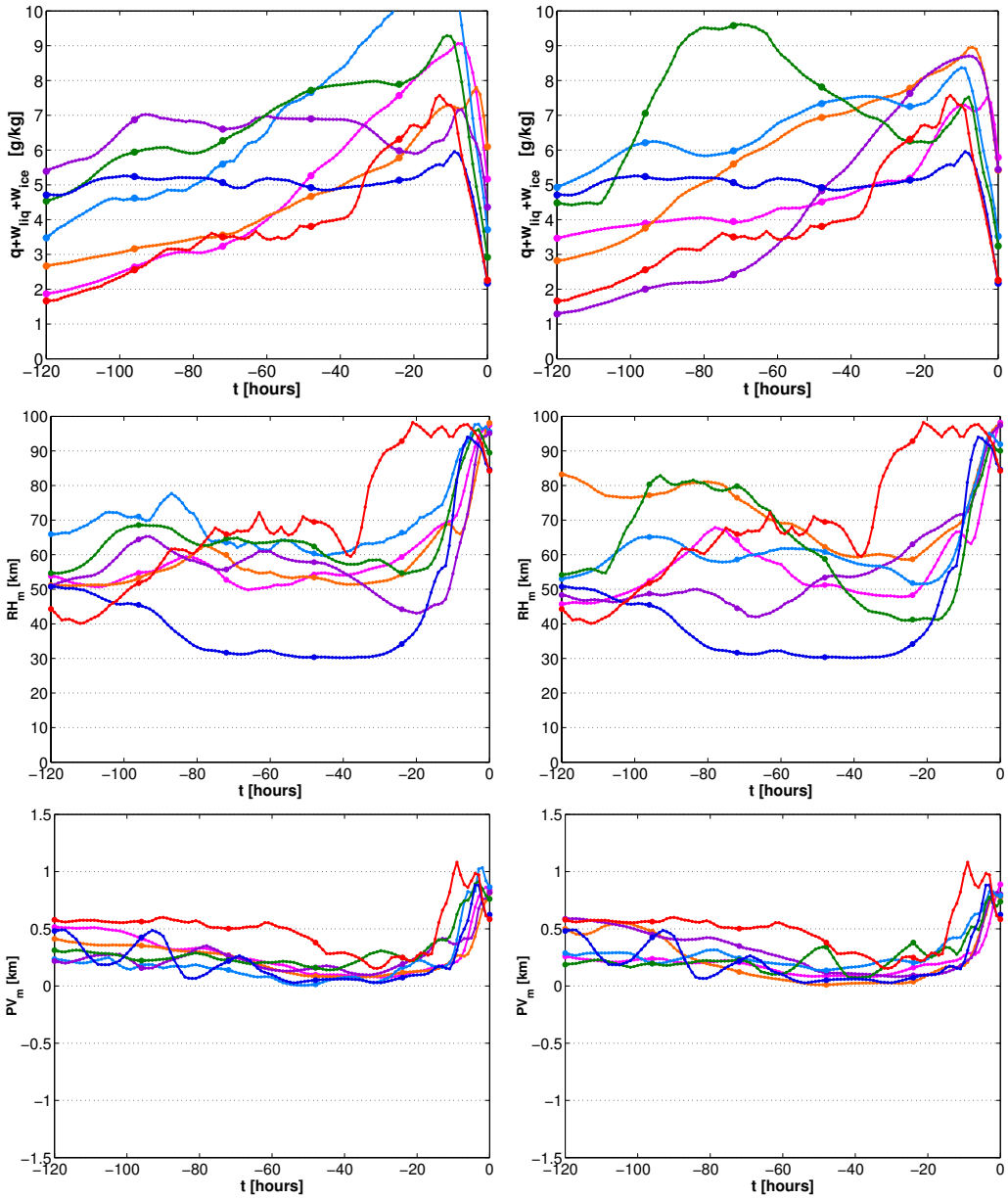

Figure 6.11: Clusters of trajectories arriving over Trentino in the period from 03/11/66 21 UTC to 04/11/66 12 UTC. On the left handside there are the clusters obtained from the "final geographical clustering", on the right handside there are the clusters obtained from the "initial geographical clustering". In the first, in the second and in the third couple of plots there are the average water concentration ($q + w_{liq} + w_{ice}$), the average relative humidity (RH_m), and the average potential vorticity (PV_m) of the clusters respectively. The clusters have been marked by different colors and circles of different size according to figure 6.10.

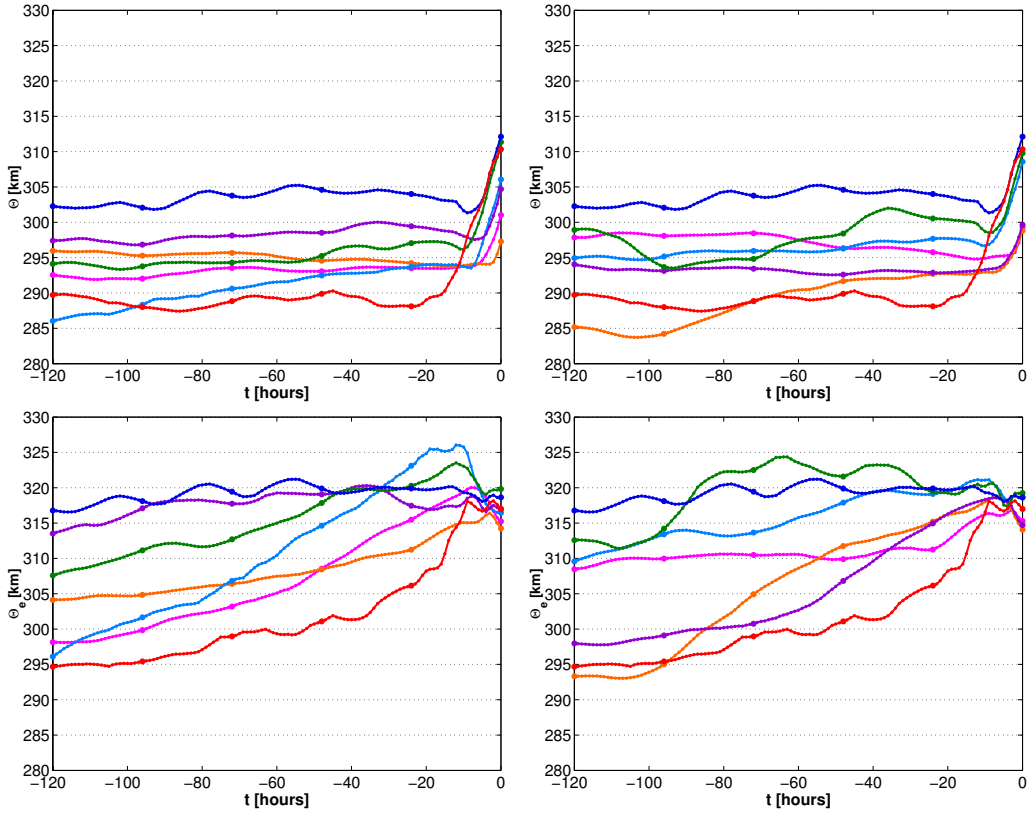

Figure 6.12: Clusters of trajectories arriving over Trentino in the period from 03/11/66 21 UTC to 04/11/66 12 UTC. On the left handside there are the clusters obtained from the "final geographical clustering", on the right handside there are the clusters obtained from the "initial geographical clustering". In the first and in the second couple of plots there are the average potential temperature (θ) and the average equivalent potential temperature (θ) of the clusters respectively. The clusters have been marked by different colors and circles of different size according to figure 6.10.

All these air masses originate and move at very low levels. One day before the arrival, the average height of all the clusters is less than 1 km above the surface.
So in the event of November 1966 the portion of the warm conveyor belt producing precipitation over Trentino is a homogeneous airstream originating in the lowest atmospheric layers over Area 7 between 02 November 21 UTC and 03 November 12 UTC (i.e one day before the phase of strongest precipitation). This homogeneity is remarked by the variations of various physical and thermodynamical properties having a similar value along all the trajectory clusters during the last 24-48 hours. By contrast, the surface wind in the previous days (96-48 hours before the ending time) is so weak that the trajectory airstreams are completely heterogeneous. Because of that it is possible to affirm that the real origin of the air masses (seen as the origin of the main air stream with homogeneous features) is over area 7. It would have been the same in the other events if the target area had been affected only by the lower air masses: the green and violet cluster in November 2000 (representing the 50% of all trajectories -Fig. 6.1-), the green cluster in the first phase of November 2002 (the 38% of all trajectories -Fig. 6.4-) and the light blue, magenta and green clusters in the second phase of November 2002 (the 66% of all trajectories -Fig. 6.4-).
The coherence of the whole precipitating airstream in the event of November 1966 is explained by the strong and persistent values of the vertical velocity over the north of Italy 6.17 which causes the whole air volume above the target area to be affected by air masses rising up from the lowest levels. Note that the lifting seems essentially to be the result of the cyclonic dynamics since the elevation of the model orography above sea level represents only $\frac{1}{4}$ (for the highest trajectories) or $\frac{1}{3}$ (for the lowest trajectories) of the whole trajectory cluster ascent.
Nevertheless two slightly different airflows within the main airstream can be distinguished:

- the airmasses flowing in the easternmost side over Italy (the orange and the magenta clusters): they originate over a vast region between the western Mediterranean Sea, Spain and France at a height of 2 or 2.5 km above the surface; in the first 3 days they move toward the central region of Area 7 where they are just above the sea surface (0.5 km); then they bend to 330° North and flow rapidly over Sicily, the eastern side of the Tyrrhenian Sea, Central Italy (Lazio, Umbria) to end over Trentino. The ending ascent of these clusters is moderate so that their final altitude is 1-2 km above the mountains.

- the airmasses flowing in the westernmost side over Italy close to the cold front (the green and violet clusters): they originate over a region between Tunisia, the north of Lybia and the gulf of Gabes at an height of 1.2 km above the surface. In the first four days they move very slowly south-eastward at the boundary between Area 7 and Area 12 over the coasts of Lybia remaining almost at the same level; then they are forced to move quickly northward over the

Gulf of Gabes, east of Tunisia, west of Sicily, over the central part of the Tyrrhenian Sea, Tuscany and to finally end over Trentino. This airstream rises in the last 12 hours from 0.2 up to 3-4 km above the surface.

Note that the most easterly clusters start as very dry (2g/kg) and then continuosly gain specific humidity before the last 4-8 hours, particularly over Area 7. The westerly clusters start with higher moisture content (5g/kg) which increases at a lower rate although the green cluster reaches mean maximum values of 9 g/kg of specific humidity (11 hours before the arrival).
Looking at figures 6.10 it is clear that trajectories flowing in the lowest warm conveyor belt describe a corkscrew movement in the last 12-24 hours before the ending time. Air masses flowing more westerly, close to the approaching cold front (Fig. 6.17) are the first to rise and to move quickly northward: in fact there are trajectories which cover the largest distances in the last hours. Air masses flowing on the eastern side are the last to ascend: they do not move exactly northward, but they have a small westward component and thus they tend to thread beneath the other trajectories. Their meridional movement is a bit slower since they remain closer to the surface where the wind speed values are smaller. The corkscrew movement is confirmed by the values of the height variance computed for trajectories flowing over each one of the 12 macro-areas (Tab. 4.1). The variance of trajectory altitude over area 1 (1.4 km) is larger than the variance over area 3 (0.8 km) and even higher than the value for areas 7 and 12 (0.5 km). This simply means that trajectories over Area 7 represent a thin and extended air volume close to the sea surface, while over Area 1 the same trajectories cover a smaller area but represent a thicker volume.
Further features or difference between trajectories belonging to the mean airstream are emphasized by the "initial geographical clustering":

- The orange cluster moves from the Atlantic and crosses France, flows to the easternmost and northern side of the area covered by trajectories one day before ending over the target area (i.e south-east of Sicily). Because of flowing in the ABL from the beginning it continuosly increases its moisture content. Despite this, at the end it is one of the clusters with the lowest θ_e. Moreover it has the lowest θ too although its flowing in the ABL is not at all adiabatic).

- The violet cluster originates over Pyrenees at a high altitude (3.5 km). Its adiabatic descent is strong and particularly conspicuous in the third and in the second day before the end when its specific humidity values rapidly increases.

- The magenta cluster originates over the Atlas mountains, at the border between Algeria and Morocco. It experiences a weaker descent (in particular in the first 2 days) and gains moisture after several hours. In the last three days it undergoes a weak decrement in θ and has low values of θ_e (with respect to the other trajectories).

- The green cluster is peculiar since its trajectory and the strong increment in specific humidity between 30 October 12 UTC and 31 October 12 UTC over the Gulf of Gabes. Changes in θ and θ_e suggest evaporation over the sea or re-evaporation of low level condensed droplets. A similar behaviour is shown by the light blue cluster.

The "direct clustering" method does not tell us more information than the "ending geographical clustering" algorithm.
By having a look at the maps derived from ECMWF analysis (Fig. 6.13, 6.14, 6.15, 6.16) valid on 30 and 31 October 1966 (00 UTC and 12 UTC) it is possible to better understand the properties of the trajectories during their first 2 days. From the geopotential height of the 850 hPa surface it is clear that a low center is over the north of Italy driving cold and dry air masses from the north of Europe into the Mediterranean basin through the Rhone Valley. The low level jet accounts for the enhanced evaporation at the sea surface over the Gulf of Lyons, the southern Tyrrhenian Sea and the western Gulf of Syrte. A secondary low center briefly developes on the lee-side of the Atlas and moves eastward towards the Gulf of Syrte, thus favouring a front formation at very low latitudes (Algeria and Lybia). The strong evaporation and the cyclonic deepening (driving moist air masses at the mean levels from Morocco) favours an increment of the specific humidity content at 950 hPa level.

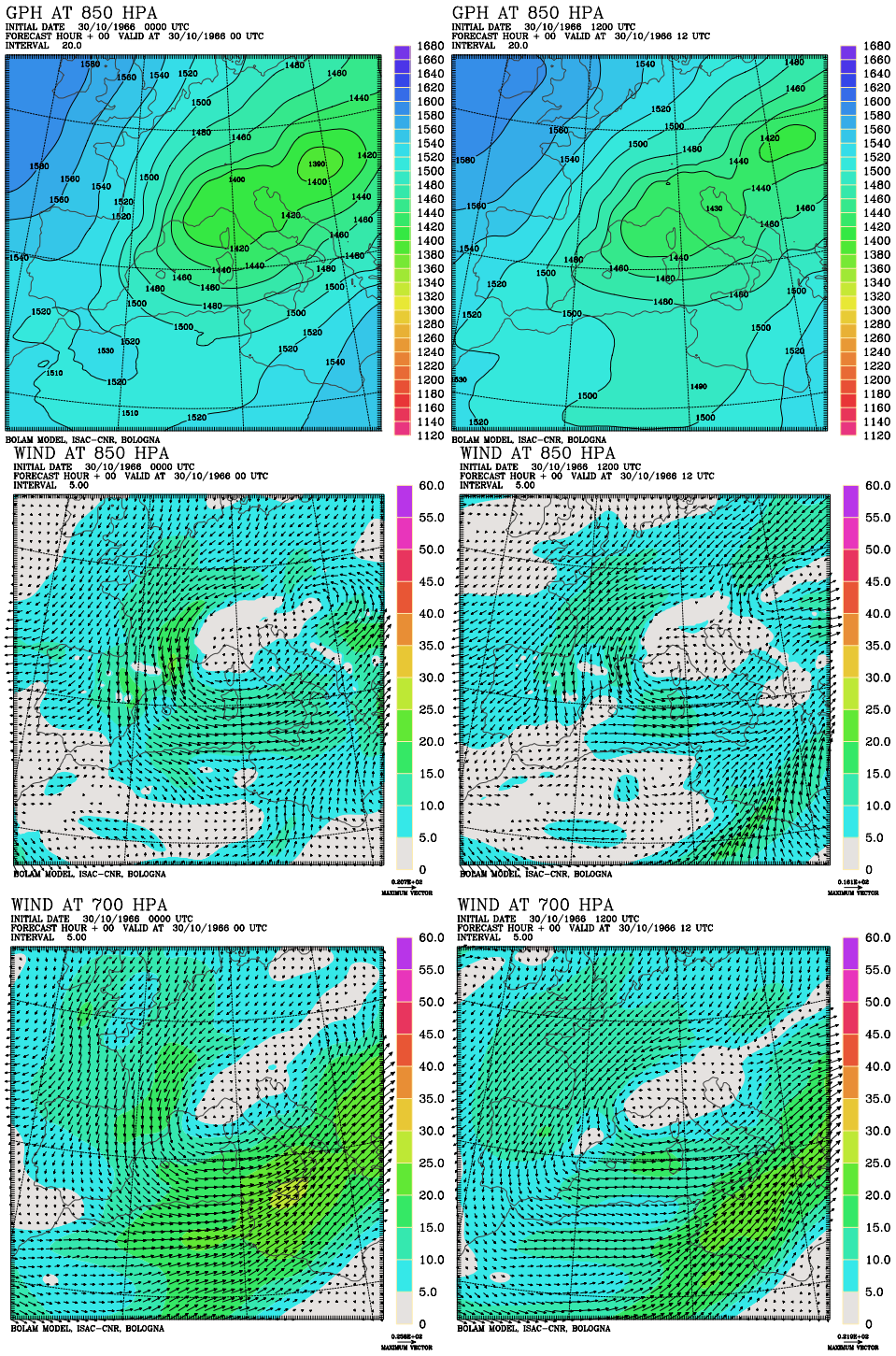

Figure 6.13: Geopotential height at 850 hPa, wind field at 850 hPa and at 700 hPa remapped to a resolution of $0.16° \times 0.16°$ starting from ERA40 analyses valid on 30 November 00 UTC (left handside) and 30 November 12 UTC (right handside)

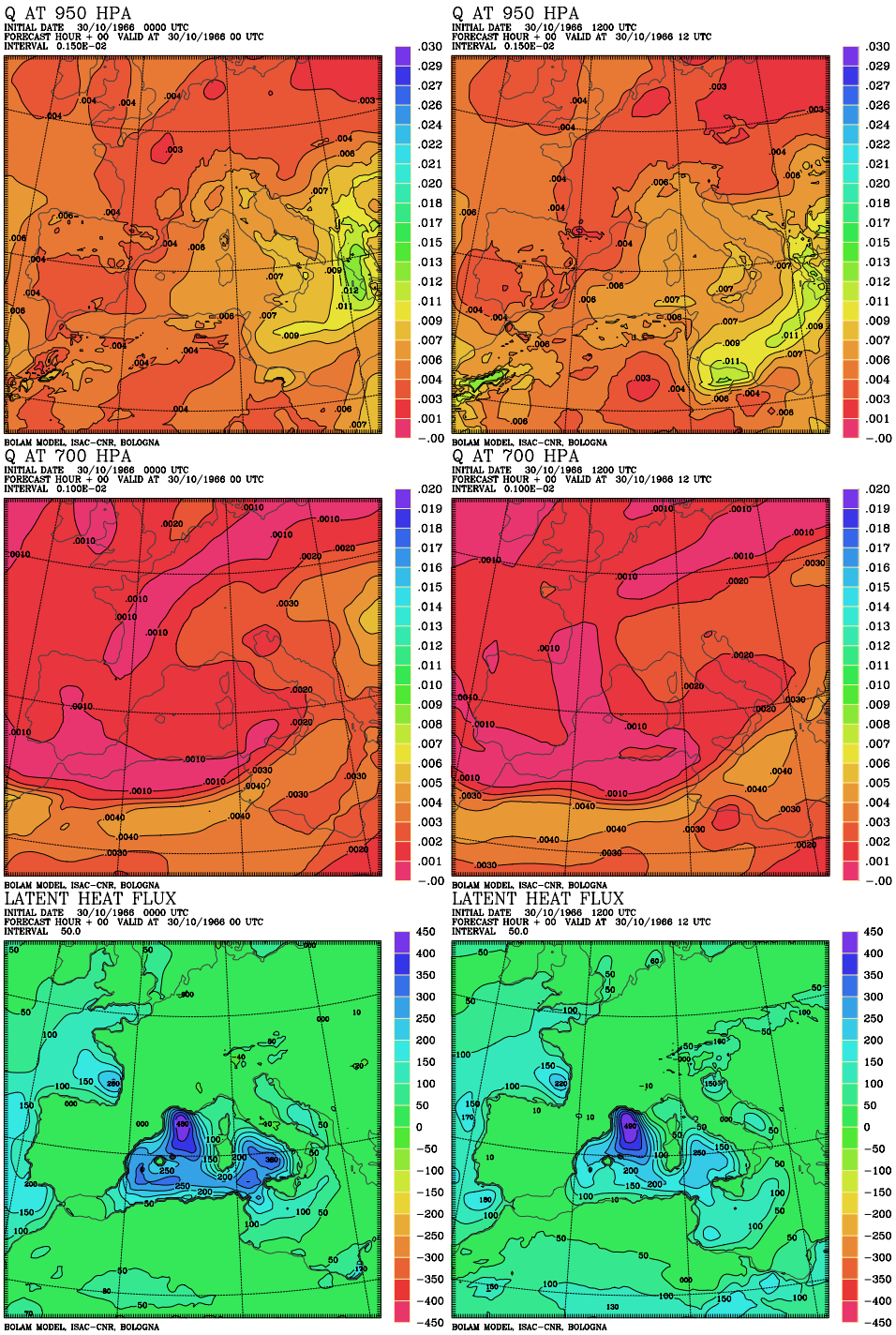

Figure 6.14: Specific humidity at 950 hPa and at 700 hPa, latent heat fluxes remapped to a resolution of $0.16^\circ \times 0.16^\circ$ starting from ERA40 analyses valid on 30 November 00 UTC (left handside) and 30 November 12 UTC (right handside)

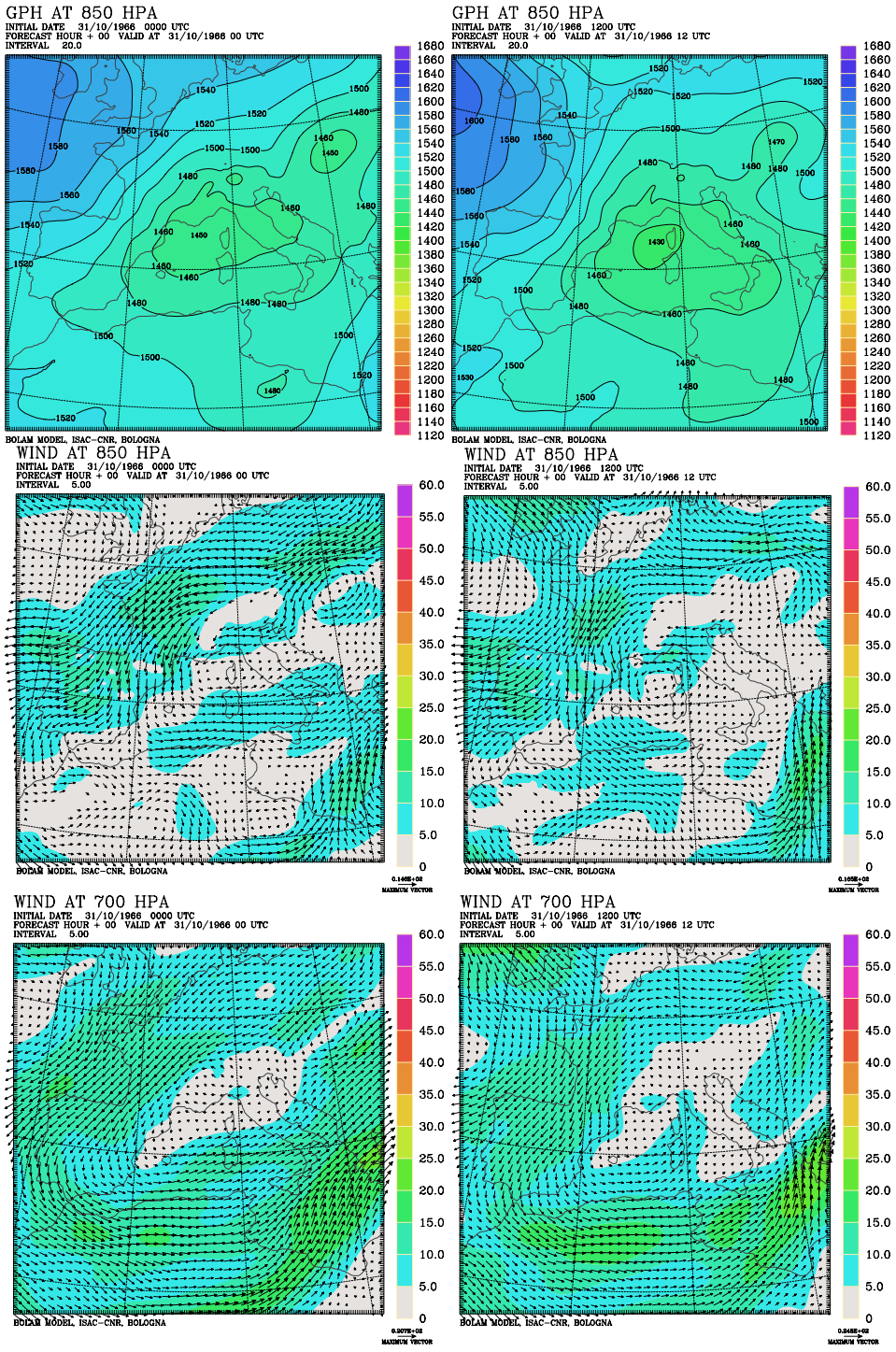

Figure 6.15: Geopotential height at 850 hPa, wind field at 850 hPa and at 700 hPa remapped to a resolution of $0.16° \times 0.16°$ starting from ERA40 analyses valid on 31 November 00 UTC (left handside) and 31 November 12 UTC (right handside)

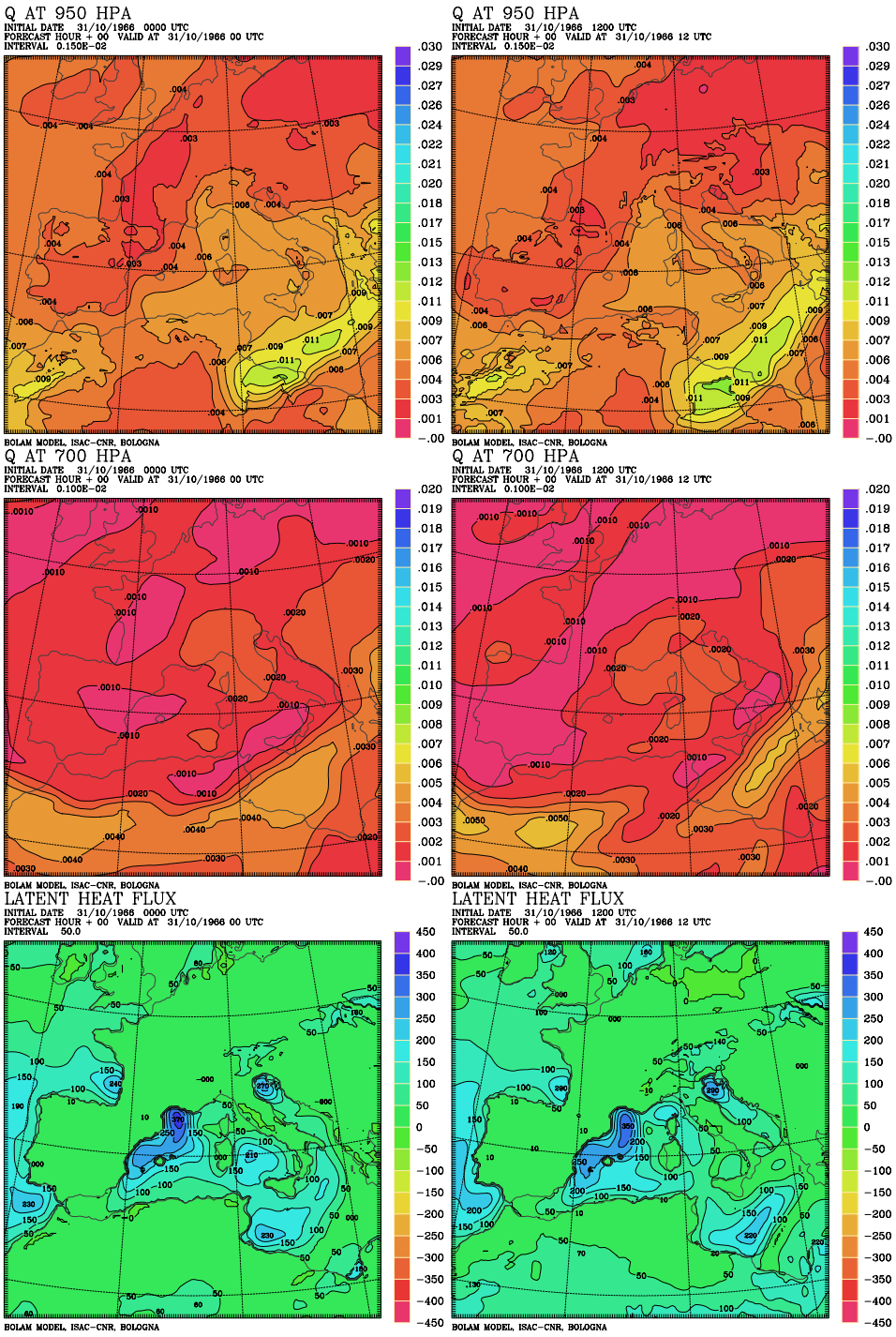

Figure 6.16: Specific humidity at 950 hPa and at 700 hPa, latent heat fluxes remapped to a resolution of $0.16^\circ \times 0.16^\circ$ starting from ERA40 analyses valid on 31 November 00 UTC (left handside) and 31 November 12 UTC (right handside)

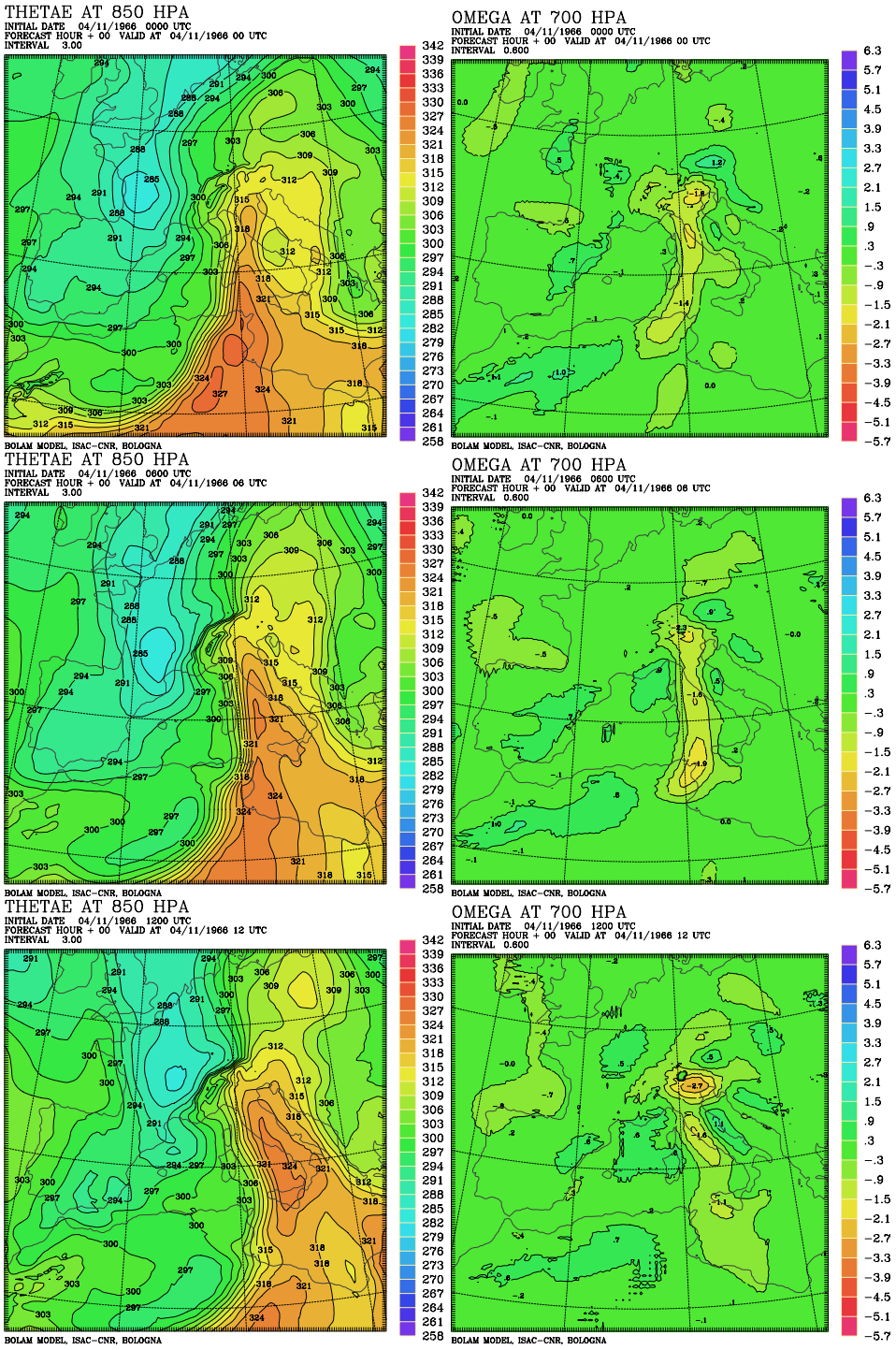

Figure 6.17: Equivalent potential temperature at 850 hPa and vertical velocity at 700 hPa remapped to a resolution of $0.16^\circ \times 0.16^\circ$ starting from ERA40 analyses valid on 04 November 00 UTC, 06 UTC and 12 UTC.

6.1.4 Some further comments

For all the events, budget tables have been also computed starting from clusters (see Appendix) in order to estimate:

1. the errors related to the schematization of the real airmass flow with the cluster airstreams: the better the clustering method is working, the closer are the budget values derived from clusters to the budget values derived from all trajectories;

2. the best clustering method able to represent synthetically the atmospheric properties.

For example in the case of the second phase of the 2002 event it is possible to observe that:

1. all the methods overestimate the moisture increments over area 3 (see the values of δQ_{TOT} in Tab. 8.29, 8.32, 8.35);

2. the "geographical clustering methods" fail to estimate the evaporation over Area 7 as well as the loss of specific humidity over Area 6, but the "direct method" yields good results for both these evaluations;

3. the "direct method" seems to have better performances in the estimation of trajectory height and specific humidity, while it is weaker in the computation of potential and equivalent potential temperature of trajectories flowing over a specific region.

In fact, it is not possible to understand what is the best clustering method among the three options without performing a climatology: a small displacement in the mean cluster trajectory is sufficient to change the assignment of tens of trajectories and of their properties from a region to another one. So in the present work the three adopted clustering algorithms have been essentially used to outline various properties of the airstreams, to have the possibility to argue about the failure of one of these methods and to retain the one with better performance in each case. For example, for the flood event of 2002 (2^{nd} phase) it is convenient to chose the "direct clustering method" as the best one, whereas in the other cases "geographical clustering" is to be preferred.

For each flood event further detailed tables (e.g. Tab. 8.9) have been derived (for further details see the Appendix). In fact, by looking at the evolution in time of various variables it appears that they commonly have a slow increasing/decreasing or stationary state in a first longer phase and a rapid, opposite change in a second shorter phase (illustrated in Fig. 6.11). Actually, this is particularly true for trajectories coming from the African continent: over there synoptic or mesoscale precipitation events typical of temperate regions rarely occur; moreover the wind field

is generally not intense enough for trajectories to cross the desert area of Africa during a period of 5 days. Thus, the detailed tables (Tab. 8.9, 8.3, 8.6, ...) report, for each variable and for each cluster, the timestep $\bar{t}$. $\bar{t}$ is the time when the variable reaches the maximum or the minimum value (along the 5 computation days). The variation in the values of that variable (for each cluster) from the ending time to $\bar{t}$ and from this $\bar{t}$ to the starting time are reported in the same table. Note that:

- in this table the computation time scale is used, so that a timestep 1 indicates the ending time when all trajectories are over Trentino, whereas a timestep 121 means 5 days (or 121 hours) before arrival
- generally, the mean height of trajectories decreases in time to rise up in the last hours, the same occurs for potential temperature and relative humidity, thus the minimum is computed for these variables
- potential vorticity and equivalent potential temperature generally remain constant and increase in the last hours
- by contrast, specific humidity increases at the beginning and then decreases over Italy, so the maximum is computed for this variable

Summarizing the results from all the studied events the ranges reported in Tab. 6.1 are observed for various $\bar{t}$:

$\bar{t}_z$	$\bar{t}_q$	$\bar{t}_\theta$	$\bar{t}_{PV}$	$\bar{t}_{RH}$	$\bar{t}_{\theta_e}$
4-20	8-30	18-35	23-70	50-90	8-70

Table 6.1: Typical values (registered over all the studied events) of time steps in which maximum or minimum values of various variables are registered

In the case of November 1966 the first variables to experience increments are relative humidity and potential vorticity (2 days before the arrival). After that, trajectories start to rise up (1 day before the arrival); loss of specific humidity, loss of equivalent potential temperature and increase in potential temperature occur 8 hours before the ending time. The evolution in time of various variables during the flood event of November 1966 is so marked that the features of airmasses during this event can be considered as the basis to derive a conceptual model of the WCB during extreme precipitation events.
In the other events, airstreams are less compact: various trajectory clusters undergo different dynamical and thermodynamical processes.
Morover cluster lifting to upper levels seems to begin after that trajectory clusters start to lose

specific humidity and to change the potential temperature. This is due to an evaluation error of $\overline{t}_z$: in most clusters the trajectory ascent is stopped for an intermediate time lag, which causes to erroneously shift the computed $\overline{t}_z$ toward the ending time.

The last type of analysis has been used to derive roughly the conceptual model reported in the following section (6.2). However, it should be applied to a larger number of case studies in order to have good statistic of the WCB properties for precipitation events occurring over Italy. Moreover, some improvements should be introduced in the computation of the $\overline{t}$ time steps: this is one of the possible developments of the techniques developed in the present thesis.

6.2 Conceptual model

The comparison of the three case studies helps to propose a conceptual model for the airstreams occurring when intense precipitation events affect the Alps.

6.2.1 Deep convection

Table 8.9 shows that in November 1966 each trajectory cluster attains maximum specific humidity after its ascent to higher elevations. Trajectories start to rise 21 hours before the arrival (in the south-east of the Tyrrhenian Sea), while they reach maximum moisture 8 hours before the arrival (more or less above the cold front). The maximum values of RH are reached even later, or just at the ending time. Note that in the event of November 1966 the whole air volume above the target area was at saturation and the same phenomenon occurred in the second phase of November 2002: this was not true in the event of 2000 and in the first phase of November 2002.
By checking maxima of θ_e and relative minima of θ, it appears that they almost correspond to the maxima of specific humidity. Before reaching saturation, therefore, air masses still gain moisture by evaporation from the sea surface, which is enhanced by the high wind-speed. So it is highly probable that along the cold front over the north of the Tyrrhenian Sea and over Tuscany deep convection occurred, which was caused by almost neutral stability conditions (see the values of θ_e along cluster trajectories during the last hours). By contrast, at the end of Autumn and with bad weather conditions, the typical ABL height over the sea should be much smaller. Note that a similar feature can be found in the behaviour of air masses arriving over Trentino during the second phase of the 2002 event (in particular the light blue, dark blue and green clusters of the right Fig. 6.8). In that case a net drop in θ can be read as a sign of precipitation or cloud particles re-evaporation. Nevertheless, both the absence of the above precipitating layer (most trajectory clusters undergo the same changes although they flow one above the other) and a weak drop in θ

supports the hypothesis of deep convection.
Although the event in November 1966 and the second phase of the event in November 2002 have such similar features, they differ because:

1. in 2002 there were trajectories (the red cluster) lacking the aforementioned effect;

2. in 2002 the hypothesized deep convection occurred over Tunisia and the Sicily Channel (not over the Tyrrhenian Sea) since the low center so as the cold front had a more southerly position;

3. the position of the low center and the strenght of the zonal pressure gradient during the event of 1966 favour the convergence over the target area of those air masses that originated at low levels over the Central Mediterranean Sea, i.e. of relatively cold and moist airmasses. In 2002 airmasses coming from North-Africa, being generally hot and dry, delay saturation conditions inhibiting possible deep convection.

6.2.2 Specific humidity

Further observations can be derived from the comparison of the average values of specific humidity.
The average values of specific humidity along trajectories, 5 days before the ending time, are quite similar in the 3 case studies (Fig. 6.11, 6.2, 6.5, 6.5). Nevertheless in the event of 1966 both a previous precipitation event over the Central Mediterranean Sea and over the north of Africa and the strong wind blowing over the Gulf of Gabes and over the Gulf of Syrte (Fig. 6.13, 6.14, 6.15, 6.16) favoured extreme values of evaporation over Area 7 (in particular at the boundary with Area 12) in the days before the event (see the map of latent heat flux in Fig. 6.16). In fact in the event of 1966 almost all trajectories flowed over Area 7 (Tab. 4.1): trajectories originating more or less over that region increased their specific humidity especially in the first 2 days (120-72 h before the ending time); trajectories originating over the West Mediterranean Sea gained moisture especially in the third and in the fourth day (72-24 h before the ending time). In 2002 the specific humidity increments were smaller because:

1. the latent heat fluxes over the sea were weaker (the surface wind was not so strong and no surface low was recorded in the previous days over North Africa);

2. about $\frac{2}{3}$ of total number of trajectories originated in the tropical regions of North Africa. Flow over the Mediterranean Sea lasted only 12-24 h, which prevented gaining of moisture by evaporation;

	θ_i[K]	θ_f[K]	θ_{ei}[K]	θ_{ef}[K]	RH_i[%]	RH_f[%]
1966	293-298	297-312	303-310	313-320	50-70	90-100
2000	297-308	297-307	308-316	308-316	30-40	60-90
2002(1)	297-310	297-310	305-316	310-314	50-60	50-90
2002(2)	303-300	300-310	310-323	313-318	20-40	85-95

Table 6.2: Range of values for the potential temperature, for the equivalent potential temperature and for the relative humidity in the 4 case studies at the ending time (θ_f and θ_{ef}) and 5 days before the arrival (θ_i and θ_{ei})

3. a part of the trajectories came from the inner areas of North Africa flow above the ABL: their capacity to gain moisture was smaller.

6.2.3 Potential temperature and relative humidity

Table 6.2 summarizes the range of values of θ, θ_e and *RH* for the 4 events at the ending time and 5 days before the arrival. The final values of the potential temperature over the target area are almost always the same. In 1966 the mean values of the potential temperature 5 days before the ending time are 10 degrees less than in the other cases, that is 10 degrees less than the typical values over the target area at the ending time (295 K against 305 K). In 1966, thus, there is a net heating of the air mass system related to the final precipitation. In the other cases there is small and slow cooling in the first days and a contained ending heating. The recurrent feature of slow cooling of air masses during the first days is not easy to be explained. It could be radiative cooling or re-evaporation of low layer clouds.
In the 3 case studies the average values of θ at the ending time are quite similar. On the contrary the values of equivalent potential temperature (θ_e) over the target area are very different: it is colder in the event of November 2000 and in the first phase of the 2002 event, while it is warmer in the second phase of the 2002 and in the 1966 event. The reason for the difference has to be found in their specific humidity conten at the ending time. This justifies the saturation of the air masses at the ending time in 1966 and in the second phase of 2002; saturation is not reached in the other cases. Regarding the evolution of θ_e along the trajectories, in 1966 there is a net heating during the event (from 305 K to 315 K), while in the other cases there is no substantial change in the mean equivalent potential temperature. By comparing the values of specific humidity and of the potential temperature, it is reasonable to reconstruct that in 1966 mean value of the relative humidity is close to the 60% even before the final ascent. By contrast, in 2002 it is about 30-40%. In fact the $\frac{2}{3}$ of trajectories originating in the tropical regions of North Africa in 2002 show rather high values of specific humidity, considering the negligible evaporation fluxes above the desert: they probably represent a warm and moist air plume coming from the ITCZ and crossing

the tropical anticyclonical band. They are also particularly warm since their average θ is the same as in the event of 2000, and as in the first phase of 2002, but their initial average height is lower (2 km against 2.5 - 3 km). However, in 1966 the airmasses over the Mediterranean Sea and over the coastal regions of Africa are much colder and moister: this explains the higher relative humidity initial values (see also tables 4.1 and 4.2 for more details).

6.2.4 Vertical lifting

By observing the vertical displacement of cluster trajectories in the 4 case studies (δz values in Tab. 4.2, 4.4, 4.6, 4.8) it results that they experience a strong ascent over areas 1, 2 and 3. By contrast, they undergo a weak descent over all the other analysis areas, especially over areas 7, 8, 9 and 11, although their average altitude is quite low (trajectories over area 7 already start from 1000m of altitude). This feature is more evident in the case of 1966 when trajectory flowing is similar to the flight of a "Canadair" airplane while it is recharging its water reserves over a lake or over the sea.

Trajectory ascent over Area 3 is substantial (and it is accompanied by PV production) both in the case of 1966 and in the second phase of 2002 (Tab. 6.3). In 2002 trajectories flow inside the WCB, but farther eastward of the cold front and of the low center. This is the effect of the circular shape of the low center and of the elongated and oblique position of the warm front which explains the smaller values of vertical lifting. By recalling the cyclone structure discussed in chapter 2, this type of WCB can be classified as W1. In fact, in the last 2-4 hours trajectories tend to move anti-cyclonically eastward. By contrast, in 1966 the cyclonic center has an elongated form, driving the whole WCB to a short warm front extending only along the italian slopes of the Alps (probably the warm front, plotted in the synoptic maps of the time - Fig. 4.4-, was in fact the border line between the WCB and a pool of low level and cold air blocked in front of the Alps). This WCB can be classified as W2 with a rearward component over the surface cold front and a marked vertical ascent. The surface wind jet and the vertical lifting over the Tyrrhenian Sea are emphasized by the North-west to South-east trend of the Apennines. In fact, the warm and moist air masses are forced to flow in a funnel-shaped corridor between the meridional cold front, which slowly moves to the East and the mountains. The effect is stronger for trajectory clusters close to the cold front. Afterward, the airmasses cross the Apennines, gather with the airflow from the Adriatic Sea and hit the Eastern Alps. The convergence of the WCB airmasses over the north of Italy and the homogeneity of this airstream make the temperature profile almost neutral. In fact the airparcel rising over the Alps (see Tab. 6.3) is larger than the orographic rise beneath trajectories. The cyclonic lifting would probably be concentrated only over the Tyrrhenian Sea if it did not have the mountain barrier.

	air parcel lifting	orographic rise	air parcel lifting	orographic rise
1966	570	480	1470	140
2000	520	750	410	140
2002(1)	360	740	310	140
2002(2)	580	800	700	190

Table 6.3: Mean value of the air parcel lifting as well as of the orographic rise underneath trajectories flowing over area 1 (target area) and over area 3 (Tyrrhenian Sea)

In 2002 the air parcel ascent over the target δz is not equal to the terrain profile δh. The vertical compression is due to the absence of horizontal convergence and to the stability of the temperature profile as determined by the medium level warm and dry airstream flowing from the tropical African regions.

6.2.5 The simplified model

By summarizing all the observations reported in the previous paragraphs, a simplified conceptual model is here proposed, which describes the WCB of cyclones producing extreme precipitation events over the North-east of Italy. Indeed the presence of the orography modifies so strongly the dynamics and the synoptic of the fronts, that the classical cyclone model has not only to be adapted but also to be changed.
Generally, the surface low center moves over the Tyrrhenian Sea (sometimes north-eastward of the Gulf of Genoa, sometimes eastward from the Balearic Islands to Sardinia). The surface cold front is oriented along meridians from the north of Africa to the low center. The WCB originates over Africa and the Central Mediterranean Sea and flows from South to North over the Tyrrhenian Sea, crosses the Apennines and reaches the Alps. The strong southerly wind inside the WCB, impinging against the Alps, and the low level cold and easterly flow in the Po Valley produce blocking conditions in front of the Alpine chain. The lo level surface between the WCB and the pool of cold air blocked in front of the mountains resembles a warm front.
In the case of 2002, the whole ensemble of trajectories can be classified into two main airstreams (Fig. 6.18):

1. a higher airstream ($\frac{2}{3}$ of trajectories) flowing from Africa to the Alps: it is warm and relatively dry and its ascent is moderate. Probably, the contribution of this airstream (W1) to the precipitation over the Alps is not as strong as that of the Oceanic cyclones because of the long period spent over the Sahara desert. In other words, the effectiveness of moist tropical plumes from ITCZ in enhancing the mid-latitude cyclones seems to be reduced over the Mediterranean area.

2. a lower airstream ($\frac{1}{3}$ of trajectories) flowing from the Central Mediterranean Sea to the Alps (W2): it has a lower potential temperature and it is very moist, its ascent is very large. This airstream gives the largest contribution to the precipitation when a Mediterranean cyclone deepens over Italy.

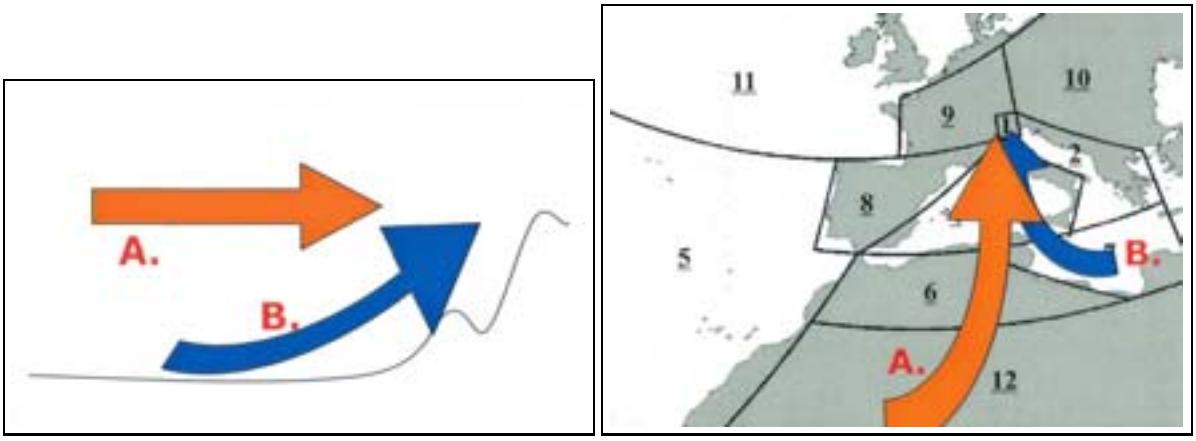

Figure 6.18: Conceptual model describing the main features of the WCB for extreme precipitation events occurring over the Alps. The airstreams ending at the lower(A.) / higher(B.) levels over Trentino have the characteristics of W2 / W1 conveyor belts.

In the event of 1966 the first type (W1) is essentially absent. Because of the high values of the vertical velocity in front of the Alps (Fig. 6.17) between 3 and 4 November, all the trajectories belong to W2 which causes the intense precipitations over the Alps.
The trajectory population of the two portions of WCB is the crucial point controlling the precipitation production (see also the next paragraph section 6.2.6). The larger the vertical lifting over the southerly slopes of Alps, the larger is the amount of airmasses belonging to W2, that is to the portion of WCB closer to the surface, and the larger is the expected amount of precipitation.

6.2.6 Risk index

The conceptual model can also help to point out a meteorological scenario, precursor of extreme precipitation events: for example the occurrence of strong surface wind blowing from South to North over area 7. The risk is even larger if an other precipitation event has hit area 7 in the previous days.

Alternatively it is possible to propose a sort of "risk index", as the following:

$$i = \frac{N_{area7}}{N_{TOT}} \frac{1}{\overline{z}_{area7}} \tag{6.1}$$

The simple formula tells that strong precipitation occurrs if a high percentage of the total number of trajectories flows over area 7 having a low average altitude. The formula has been tested over the 4 case studies: the correlation diagram is reported in Fig. 6.19, where to the left the linear regression between the risk index and the estimated precipitation is reported and to the right that between the risk index and the measured precipitation. Obviously, the highest correlation is found with the estimated precipitation, as the risk index is a product of the trajectory analysis and of the analysis fields. The gap between analysis and reality is also a feature of the risk index. Anyway results are very satisfactory, though the test should be extended to many case studies to be robust.

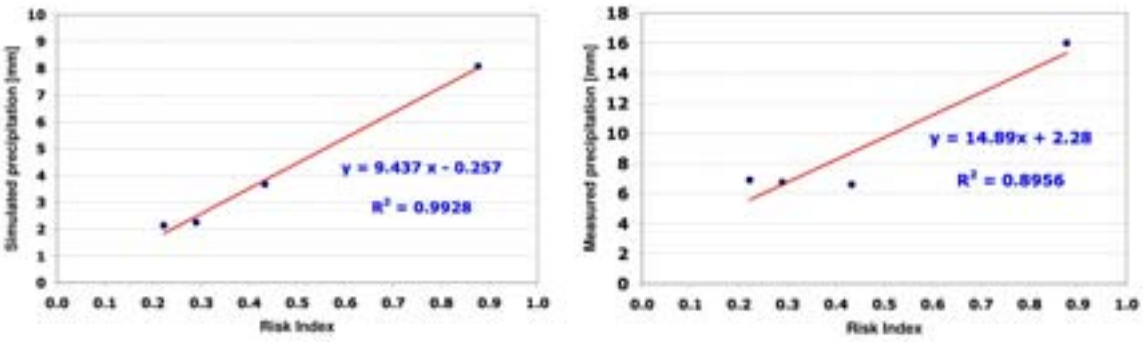

Figure 6.19: Linear regression between the risk index (on the x-axis) and the estimated (left) / measured (right) precipitation

6.3 Trajectories with BOLAM

Uncertainty in the trajectory computation based on the analysis fields of the global model has been tested. Analogous simulations have been performed using the output data of the LAM model BOLAM nested on the ECMWF analyses. The various fields of BOLAM forecast are given on 31 sigma vertical levels and on a regular grid with a horizontal resolution of 12.5 km (note that the orography of the model has the same horizontal resolution). A description of the numerical schemes implemented in BOLAM to describe the atmospheric physical and dynamical processes can be found in Buzzi and Malguzzi (1998); Buzzi and Foschini (2000).

The use of the output of a forecast model to compute trajectories has been tested because the analyses are close to the real atmospheric conditions, but they have a low spatial resolution and a

coarse schematization of physics and dynamics. By contrast, the weakness of the forecast model is that the more distant is the forecast time t from the initialization time t_0 of the model, the larger are the forecast errors.
To overcome the problem of the forecast errors, BOLAM has been used to perform a series of subsequent short forecasts: 8 run of 18 hours for totally 144 forecast hours. The initial fields of each short forecast (the analysis) are not retained for the trajectory computation, but they are replaced by the +18 h forecast fields of the previous short forecast. The technique is quite complex, but it allows to obtain high resolution forecast fields, which remain close to the global analyses during the whole event. It is a sort of dynamical interpolation of analyses, useful for the computation of high resolution trajectories. In fact, in section 3.1.2 it has been remarked that it is important to increase both the spatial and the temporal resolution of the input data to reduce the trajectory errors.
The Lagrangian model FLEXTRA has been adjusted to read the forecast data and to integrate trajectories by interpolating the wind fields available on sigma-levels of BOLAM. The remaining of the set-up methodology (ending points of the ensemble of trajectories, trajectory clustering algorithm, ...) has not been substantially modified.

6.3.1 High resolution trajectories for the event of 1966

In the present section the results obtained from the analysis of the event of 03-05 November 1966 are reported. BOLAM forecasts have been produced for the period from 30 October 1966 00 UTC to 05 November 1966 00 UTC with a temporal resolution of 3 hours. Six ensembles of 5 day back-trajectories have been computed ending over the target area from 03 November 21 UTC to 04 November 12 UTC every 3 hours.
By comparing Tab. 6.4 and Tab. 6.5 with Tab. 4.1 and Tab. 4.2, it is easy to recognize that back trajectories keep many characteristic features. The main differences are listed here:

- there is a smaller number of trajectories flowing over area 7 (from 2516 to 1547) and over area 6 (from 2123 to 1332), whereas the number of trajectories flowing over area 4 is increased (from 1309 to 2217);

- on average, the square roots of variances are larger than in the case of trajectories computed starting from analyses data. The coherence of the trajectory ensemble is reduced by the higher wind field resolution. It is intuitive that the coarser are the input data, the more homogeneous are the computed trajectories, because the numerical interpolation tends to smooth out the details and to remove the small-scale variability.

- on average, trajectories flow at a slightly lower height over areas 1, 2, 3 and 4, whereas they are much higher over area 6. By looking at their average vertical displacement, it is clear that the vertical lifting over area 1 (target area) is much larger, while it is limited over area 3 (Tyrrhenian Sea). By contrast, the descent of trajectories over areas 6 and 7 is considerable (north of Africa and Central Mediterranean Sea);

- side by side with the different vertical displacements a change in the specific humidity variations can be found. A large fall in the average specific humidity occurs over area 1 and a smaller reduction over area 3. Instead δQ_{TOT} does not feel such a large effect over area 1: this can be explained by the longer time the trajectories take to flow over the target area (in fact they are a bit slower).

- the average increment of specific humidity over area 7 is larger than in the previous computation (3.10 $\frac{g}{kg}$ instead of 2.78 $\frac{g}{kg}$) but δQ_{TOT} is much lower. Possible reasons are both the smaller number of trajectories flowing over area 7 and the longer period the trajectories spend over that area.

	N_k	z_m[dam]	$q_m[\frac{g}{kg}]$	PV_m[PVU]	θ_m[K]	θ_{em}[K]	h_m[dam]	t[h]
1	2760	286 (143)	5.46 (1.88)	0.28 (2.00)	301.1 (7.4)	317.5 (3.7)	89 (64)	3 (6)
2	2431	108 (132)	7.33 (1.94)	0.57 (0.69)	294.3 (6.2)	315.0 (4.5)	12 (17)	9 (14)
3	2681	127 (98)	6.56 (2.14)	0.36 (0.35)	293.5 (5.3)	311.2 (6.6)	19 (12)	11 (8)
4	2217	199 (140)	3.72 (2.42)	0.36 (0.31)	292.5 (7.2)	303.0 (8.3)	10 (13)	14 (9)
5	-	-	-	-	-	-	-	-
6	1332	305 (107)	1.58 (2.26)	0.38 (0.12)	298.4 (3.4)	303.2 (5.0)	59 (34)	23 (13)
7	1547	114 (89)	5.89 (2.24)	0.14 (0.21)	294.5 (4.7)	310.7 (6.8)	18 (37)	30 (20)
8	1450	193 (110)	2.19 (1.26)	0.70 (0.34)	287.4 (5.8)	293.0 (4.8)	35 (17)	9 (4)
9	764	261 (93)	2.60 (2.05)	0.75 (0.26)	292.7 (3.6)	300.4 (4.9)	50 (27)	14 (11)
10	-	-	-	-	-	-	-	-
11	-	-	-	-	-	-	-	-
12	-	-	-	-	-	-	-	-

Table 6.4: Table summarizing the number of trajectories flowing at least for one time step over the 12 macroareas of Fig. 4.16 during the event of November 1966. The average values (along with the respective variances) of the height above the surface, of the specific humidity, of the potential vorticity, of the potential temperature, of the equivalent potential temperature and of the height of the surface underneath are reported for the the air parcels staying over the various macroareas. The last column gives the average number of time steps spent by trajectories over each area.

This is supported by figure 6.20. The average "estimated evaporation" along trajectories flowing over area 7 is reduced by one half and the same is true for the "estimated precipitation" over area 3. A net increment in the average "estimated evaporation" over area 4 is shown.

	δz[dam]	$\delta q[\frac{g}{kg}]$	δPV[PVU]	$\delta\theta$[K]	$\delta\theta_e$[K]	δh[dam]	$\delta Q_{TOT}[\frac{kg}{m^2 h}]$
1	182 (149)	-2.60 (2.31)	0.03 (2.78)	8.01 (6.76)	1.14 (3.10)	117 (109)	-0.059
2	-4 (67)	0.80 (1.38)	0.15 (1.04)	0.08 (3.03)	3.02 (4.33)	-4 (47)	0.024
3	53 (142)	-0.21 (2.91)	0.23 (0.66)	2.90 (5.54)	2.69 (5.65)	18 (27)	0.000
4	-13 (86)	0.72 (1.65)	0.04 (0.44)	0.88 (4.22)	2.07 (5.13)	-8 (52)	0.013
5	-	-	-	-	-	-	-
6	-160 (99)	1.02 (1.50)	-0.04 (0.36)	-3.19 (3.11)	-0.02 (4.11)	-27 (42)	0.004
7	-100 (103)	3.10 (3.16)	-0.03 (0.33)	-1.01 (3.73)	6.96 (7.49)	-21 (36)	0.038
8	-89 (59)	0.66 (1.18)	-0.47 (0.62)	-3.48 (3.87)	-1.71 (4.29)	-57 (42)	0.005
9	-41 (61)	0.22 (0.75)	0.38 (0.43)	-1.47 (2.80)	-1.24 (2.97)	-14 (51)	0.000
10	-	-	-	-	-	-	-
11	-	-	-	-	-	-	-
12	-	-	-	-	-	-	-

Table 6.5: The mean variations (as well as the respective variances) of the height of the trajectories in passing over various macroareas (Fig. 4.16) are reported for the event of November 1966. The same is done for the variations of the specific humidity, of the potential vorticity, of the potential temperature, of the equivalent potential temperature and of the height of the surface underneath of the parcels. The last column gives the quantity of water vapour (computed by the equation4.6) gained or lost by all the trajectories over each area.

In Fig. 6.21 and Fig. 6.22 the trajectory clusters which have been computed applying the "final

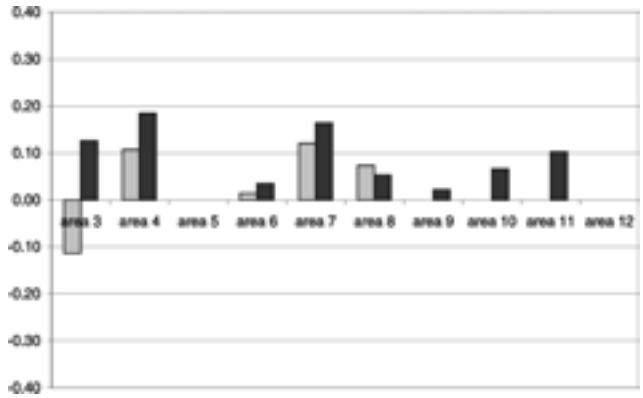

Figure 6.20: Average in time and in space of evaporation and of Lagrangian specific humidity variation (computed following the refined method of Eq. 4.18) in $kg\,m^{-2}h^{-1}$ over various areas (x-axis) in the period from 31/10/66 00 UTC to 04/11/66 00 UTC. The ensemble of trajectories has been computed starting from the output of the BOLAM model.

geographical clustering" algorithm to the whole set of trajectories are reported. By comparing these figures with Fig. 6.10, 6.11 and 6.12 it is clear that the most trajectories reach the boundary of the BOLAM domain before the 5 days integration has come to the end. Because of that

the green cluster in Fig. 6.21 does not show the slow anticyclonically movement of air masses which is clearly visible in the violet and green clusters in Fig. 6.10 ("final geographical clustering" algorithm). The most relevant information is that the warm conveyor belt is not completely homogeneous any more.

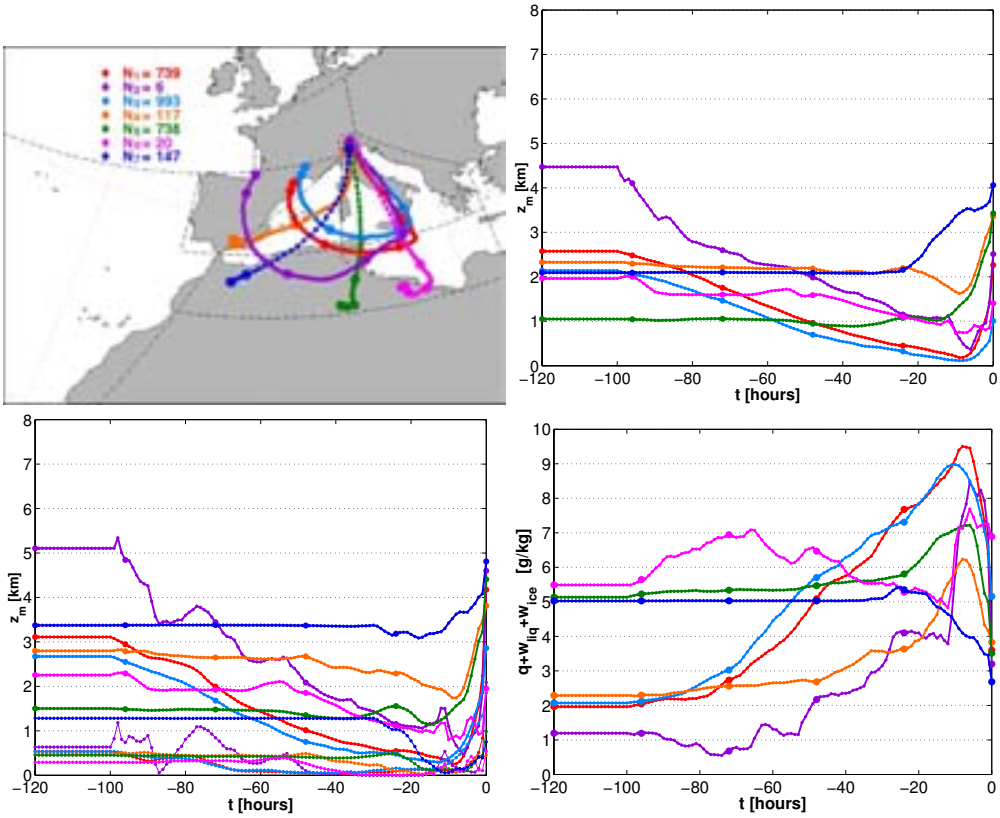

Figure 6.21: Clusters of trajectories arriving over Trentino in the period from 03/11/66 21 UTC to 04/11/66 12 UTC obtained from the "final geographical clustering" algorithm. In the first plot each curve is the average, in the physical space, of all trajectories belonging to that cluster. The average position every hour is marked by a small circle, the position every 24 hours by a big one. The number of trajectories for each cluster is reported. In the following plots there are the average height of the clusters above the surface, the average height above the mean sea level of the cluster (and of the terrain beneath them) and the average water concentration. The ensemble of trajectories has been computed starting from the output of the BOLAM model.

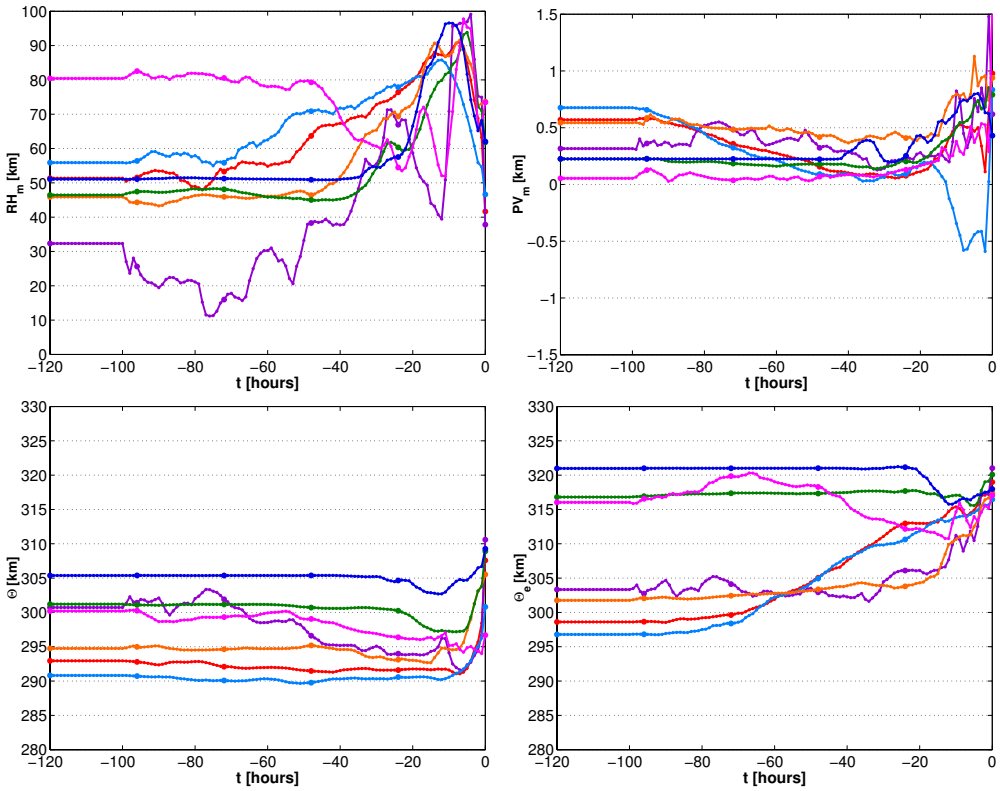

Figure 6.22: Clusters of trajectories arriving over Trentino in the period from 03/11/66 21 UTC to 04/11/66 12 UTC obtained from the "final geographical clustering" algorithm. In the plots there are the average relative humidity, the average potential vorticity respectively, the average potential temperature and the average equivalent potential temperature of the clusters. The clusters have been marked by different colors and circles of different size according to figure 6.21. The ensemble of trajectories has been computed starting from the output of the BOLAM model.

Differences in the two airstreams, which have been already pointed out in section 6.2, are emphasized in the followings:

1. In a 2 day period (85-13 h before the ending time) the red and the light blue cluster trajectories flow northward over the north of Tunisia, the Sicily Channel, the Ionic Sea and the south of Italy gaining much of their specific humidity (from $3.5\frac{g}{kg}$ to $9\frac{g}{kg}$) since they are in the ABL. Side by side with the specific humidity their mean equivalent potential temperature rises by 20 degrees. Then, in the last day they are over the eastern side of the Tyrrhenian Sea, cross the Apennines over Central Italy, flow along the Adriatic Sea and end over the Alps.

2. The green cluster flowing in the last day close to the cold front originates over the north of Africa. Unfortunately the actual dimension of the BOLAM domain does not allow to

compute full 5 days back-trajectories. Thus, it is not possible to verify if they gain the moisture from area 7 as suggested in the previous Lagrangian study.

It is possible to hypothesize that both the LAM model resolution of physics and dynamics and the higher resolution orography (in BOLAM) induce a stronger wind vertical component over the target area in front of the Alpine chain (on Fig. 6.17 the analysis vertical wind component is reported), which is suggested by the higher increments of the mountain orography beneath the trajectories (on average +1770m against +480m of the previous analysis). Most of the airmasses ending over Trentino are lifted from the lower levels, where the wind has a clear westward component. Because of that air masses flowing at very low levels over the Adriatic Sea and over the south of Italy are driven over Trentino. The northerly position of these airmasses in the previous days explains the followings:

- the lowest contribution of the evaporation over area 7 to the final precipitation over Trentino;
- the apparent absence of precipitation over area 3. In fact over the northern part of the Tyrrhenian Sea (over Tuscany) the green cluster undergoes a strong lifting and produces precipitation in the last day. On the contrary, over the southern part the light blue cluster gains moisture in the last 2-3 days before the ending time.

So previous results about the water budget over the Mediterranean area are fundamentally confirmed. Computing trajectories using the outputs of a forecast model shows only a northward shift of the source-area where most of the water vapour comes from.
In order to better estimate the uncertainty of the trajectory computation related to the temporal and spatial resolution of the wind field it would be better to enlarge the domain of BOLAM, especially southward. This would avoid to stop the numerical integration of most trajectories and to lose further valuable data.

7 Conclusions

7.0.2 Overview of the work

The present thesis aims at the reconstruction and the analysis of the moist airstreams governing the transport of water vapour over the Mediterranean basin and producing precipitation over the southerly slopes of the Alps. A Lagrangian methodology has been set and tested on some extreme precipitation events that occurred in the area of the Province of Trento (section 3.3.2). Results have been reported for the flood events of 3-5 November 1966, 16-18 November 2000 and 24-26 November 2002. In particular ensembles of back trajectories have been computed by using the model FLEXTRA. This model is already a widely used instrument, which would need some further test only in the spatial interpolation algorithms (chapter 3). To compute back trajectories, ECMWF analyses have been used because:

1. they are the global analyses with the highest spatial and temporal resolution available today;
2. they are available for all the events in the last four decades (ERA40 for 1966 event);
3. they are available on hybrid vertical coordinates allowing for a precise calculation of the vertical wind speed.

The forecast fields of the mesoscale model BOLAM have been also tested to compute higher resolution back-trajectories.

7.0.3 The set up of an analysis methodology

To provide, as far as possible, quantitative criteria consistent with a back-trajectory approach the whole surface domain, flown over by computed airflows, has been subdivided in suitable macroareas covering the European and Mediterranean regions (section 4.2). A simple statistical analysis of the meteorological variables along trajectories over various macroareas providing suitable averages and variances has proven to be a useful instrument to point out the occurrence of interesting meteorological features (e.g. deep convection, intense latent heat fluxes, atmospheric instability

or neutrality, ...). Although the analysis of singular meteorological events with a LAM model (i.e. from an Eulerian point of view) is generally more detailed and complete, the advantage of the lagrangian method consists in the capability of connecting them by airmass back trajectories. For example it is possible to say that on 03 November 1966 deep convection over the Tyrrhenian Sea contributed to reinforce water vapour fluxes to the lower atmospheric layer and finally to enhance the precipitation over Trentino. The choice of "macroareas" was intuitive and driven by subjective reasonings about areas of high (e.g. sea surface) or low evaporation (e.g. desertic areas); possible improvements based on more objective criteria can be tested as future developments (for example a finer detail can be given to the areal classification of the Central Mediterranean Sea).
Afterward, refined techniques of trajectory cluster analysis helped to identify and characterize airstreams driving the water vapour from the respective source regions to the Alps (chapter 5). In particular, in the present work a new two-step agglomerative algorithm has been adapted. The version finally adopted of this algorithm has solved some problems of the previous method (Bertò et al., 2004) arising from the use of different variables as general coordinates (e.g. geographical position and specific humidity variations) to define a suitable phase space for clustering. A final choice about the best clustering algorithm to be used in this kind of problems can be made after many case studies have been considered.
The method, howevers, appears to be relatively well tested, and ready to be used in further applications, such as the verification of NWP model forecasts. In fact, in the literature, quantitative precipitation forecasts are usually verified by means of pointwise comparisons between local measurements by rain gauges and model forecasts interpolated at the sites of observations. As a consequence, the distribution of rain gauges in the simulation domain plays a major role in verification, whose results mostly depend on the model performance in areas where the rain gauge network is denser. So cluster analysis can be adopted in this context as an objective method to create groups of rain gauges displaying interrelated measurements. Then for each group verification indexes shall be computed.

7.0.4 Results

The analysis of the three selected extreme precipitation events shows that precipitation over Trentino is strongly conditioned by the evaporation processes and by the airmasses properties over the Central Mediterranean area (see section 4.2.1). In particular, most of the water vapour contributing to the ending precipitation over the Alps originates over Tunisia, the coastal regions in eastern Algeria and in western Lybia, the Channel of Sicily, the Gulf of Gabes and the southern Tyrrhenian Sea (Fig. 7.1). The results deriving from the application of both the budget and the cluster analysis

Figure 7.1: Geographical area where most of the evaporation contributing to precipitation over Trentino (during the extreme events of 3-5 November 1966, 16-18 November 2000 and 24-26 November 2002) occurred.

outline different aspects which depend on the extreme precipitation event considered. Nevertheless, a simplified conceptual model has been proposed to visualize the traits of the moist airstreams within the Mediterranean cyclones (see chapter 6): a surface low slowly moves over the Tyrrhenian Sea (sometimes north-eastward of the Gulf of Genoa, sometimes eastward of the Balears and Sardinia), accompanied by a surface cold front, which is commonly meridionally oriented from North Africa to the low center. The WCB originates over Africa and the Central Mediterranean Sea and flows South to North over the Tyrrhenian Sea, crosses the Apennines and the Alps, forcing a pool of cold air to remain blocked in the Po Valley in front of the mountains. Airstreams ending at the lower levels over Trentino display typical characters of a W2 conveyor belt (Browning and Roberts, 1996): they originate over the Central Mediterranean Sea, are very moist and relatively cold; their lifting and precipitation production is generally enhanced by the Alpine chain. The airstreams ending at the higher levels over Trentino have the characteristics of a W1 conveyor belt, although their contribution to the precipitation over the Alps is moderate, because they flow for a long time over the Sahara desert.

The trajectory populations of the two portions of WCB is the crucial point controlling the precipitation production (section 6.2). The higher is the vertical lifting over the southerly slopes of Alps, the larger is the amount of airmasses belonging to W1 (i.e. to the portion of WCB closer to the surface) and the larger is the expected amount of precipitation.

Following this observation, a risk index of extreme precipitation over Trentino has been proposed, based on the path of the computed back trajectories (section 6.2.6). Note that the evaporation rate over the sea (related to the SST and to the surface wind speed) is one of the elements concurring to enhance the probability of precipitation. Nevertheless the results of the study show that the equation "higher evaporation = higher precipitation" is not always valid, and that the intensity and the dynamics of the low system are more crucial (chapter 4).
The uncertainty of back trajectory computation deriving from spatial and temporal resolution of the input wind fields has been tested. The conceptual model is not sapped although limited shifts of the evaporation areas can be present. The vertical motion, particularly sensitive to the orography resolution, is mostly responsible for this type of errors (see section 6.3).

Recently, some authors have looked at the tropical cyclones over the Atlantic Ocean as precursors of intense localized precipitation in the Mediterranean basin (Turato, 2003; Pinto et al., 2001). The reconstruction of longer back-trajectories (10-15 days) would be necessary to explore the water vapour budget on a wider domain, which includes the Atlantic Ocean and Northern America. However, the present study has shown a strong dispersion within the 5 days back-trajectory ensembles, which suggests that any reconstruction of correlated precursors at that time lag is difficult to be demonstrated. By contrast, a deeper investigation of the mesoscale mechanisms (such as orographic precipitation) over the Alps can lead to underestimating or neglecting the synoptic scale effects (Gheusi and Stein, 2002; Medina and Houze, 2003; Rotunno and Ferretti, 2001, 2003). The present analysis, therefore, focused on the description, and the quantification of the atmospheric water transport at the scale of the Mediterranean basin. This study considers for the first time the 3D airstream structure of the Mediterranean cyclones producing heavy precipitation events in order to outline both the orographic forcing of the mountains (the Alps, the Apennines and the Atlas) and the effect of the synoptic scale distribution of the continental, desertic and sea surfaces. So far, the methodology has been tested only on three selected events. In a near future it should be applied on a larger number of precipitation cases in order to reconstruct a climatology of both the WCBs and the evaporation areas contributing to the precipitation over the Alpine region.
As shown in the 2001 report of the Intergovernmental Panel on Climate Change, the average precipitation rate over the Northern Emisphere is increasing (ICCP, 2001). In fact with the "global warming" (Fig. 7.2), the surface energy budget tends to become increasingly dominated by evaporation, owing to the increase in the water holding capacity of the boundary layer. Globally there must be an increase in precipitation to balance the enhanced evaporation but "the processes by which precipitation is altered locally is not well understood". However, in the Mediterranean region several proxy data indicate that overall precipitation is decreasing. Thus, precipitation must

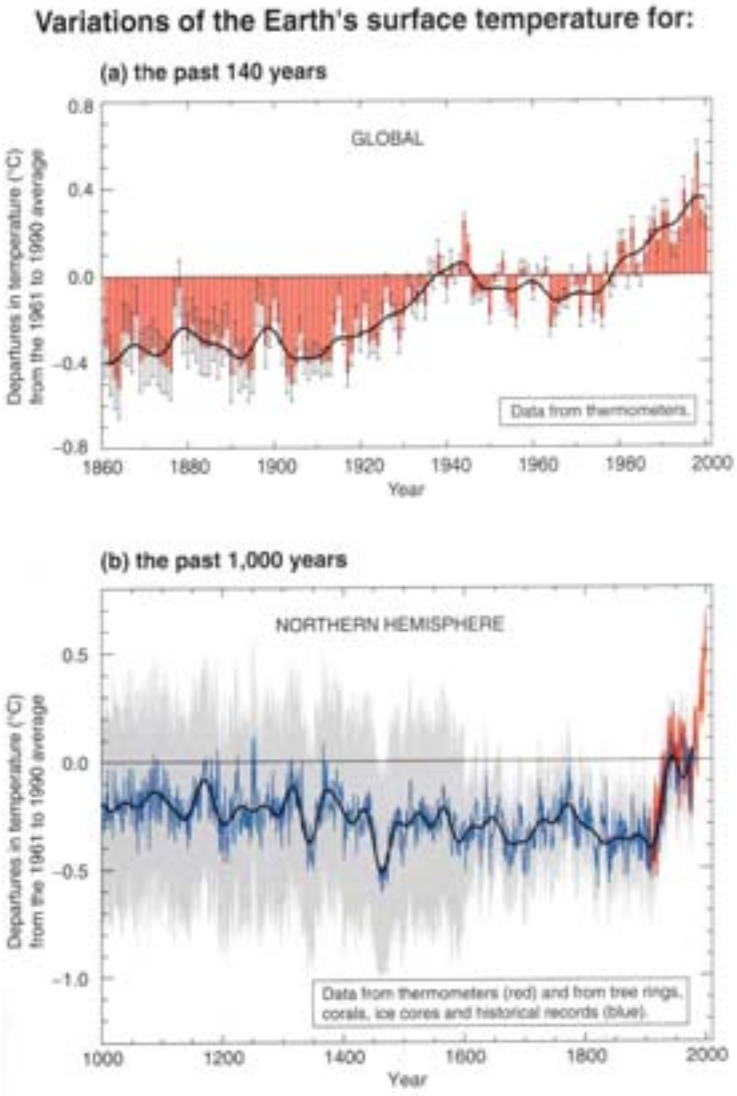

Figure 7.2: Variations of the Earth's surface temperature over the last 140 years and over the last millennium (ICCP, 2001). In a) the the annual values and the filtered evolution (black line) of the Earth's surface temperature are shown as derived from thermometers measurements. In b) the evolution of global temperature is reported as derived from "proxy-data".

have changed the distribution, both in space and in time. Instead of regular, seasonal precipitation distribution, we have "extreme events" and then periods when evapotranspiration prevails. Anyway the report adds that "where and when available, changes in annual streamflow often relate well to changes in total precipitation" (ICCP, 2001). Because of that the present work supplies an

instrument able to investigate and to estimate the changes in water vapour transport mechanisms over the Mediterranean area. A 40 years trajectory climatology starting from the ERA40 data would provide the possibility to point out the variations in the WCB structure due to the NAO index.
Otherwise enhanced precipitation rates cause also higher latent heat release. So global precipitation exibits small increments, but it becomes increasingly concentrated in fewer intense precipitation events, as observed to occurr in many parts of the world. In the CIPRA report (2002) (CIPRA, 2002) about the climate changes in the Alps it is reported that the average temperature in Switzerland has registered increments of more than 1 degree over the last century (Frei and Schär, 2001). Furthermore it is shown that an increment of 2 degrees in the global temperature would produce an increment of 20-40% in the extreme precipitation events. In fact the water vapour flux crossing the Marittime Alps and the Apennines during the flood event of October 2000 in Piedmont was comparable with water vapour amounts transported in the tropical regions. So it is clear that the lagrangian analysis can also help to explain the reasons of the explosion of such sudden extreme events.

Another development of the present work is the comparison of the trajectories results with the $\delta^{18}O$ isotopic content in the precipitated water (see chapter 2). Since the isotopic concentration over the sea surface is relatively well known, the $\delta^{18}O$ isotope will be essentially used as a material tracer to check the reliability of the computed trajectories. Moreover $\delta^{18}O$ is the isotopic content of the atmospheric water vapour, not generally of the air masses: so it would really be a tracer of the water vapour trajectories (section 3.1.3), which is the goal of the present research and of the project AQUAPAST. For example we should be able to understand if the specific humidity increment along trajectories over a specific macroarea is due to evaporation from the sea or to reevaporation of precipitation from higher levels. Another way to estimate the trajectory uncertainty is obviously the use of input wind field provided by various models and with various spatial and temporal resolutions. As anticipated in 6.3 this work is already in progress and only requires a better calibration of the LAM model domain and of graphical tools for data visualization.
Finally a new challenge will be the analysis and interpretation of $\delta^{18}O$ isotopic content in the carbonate of stalagmites (chapter 2). First of all the output of the GCM would be necessary to integrate air mass trajectories, then other elements should be taken into account such as the chemical reactions occuring in the soil when precipitating water seeps in the terrain. So the cooperation of a team of experts in various fields (geology, climatology and meteorology) will be necessary to reconstruct the big changes in the past of the atmospheric circulation over the Mediterranean Sea and over the Alps.

8 Appendix

8.1 Cluster analysis of the 1966 event

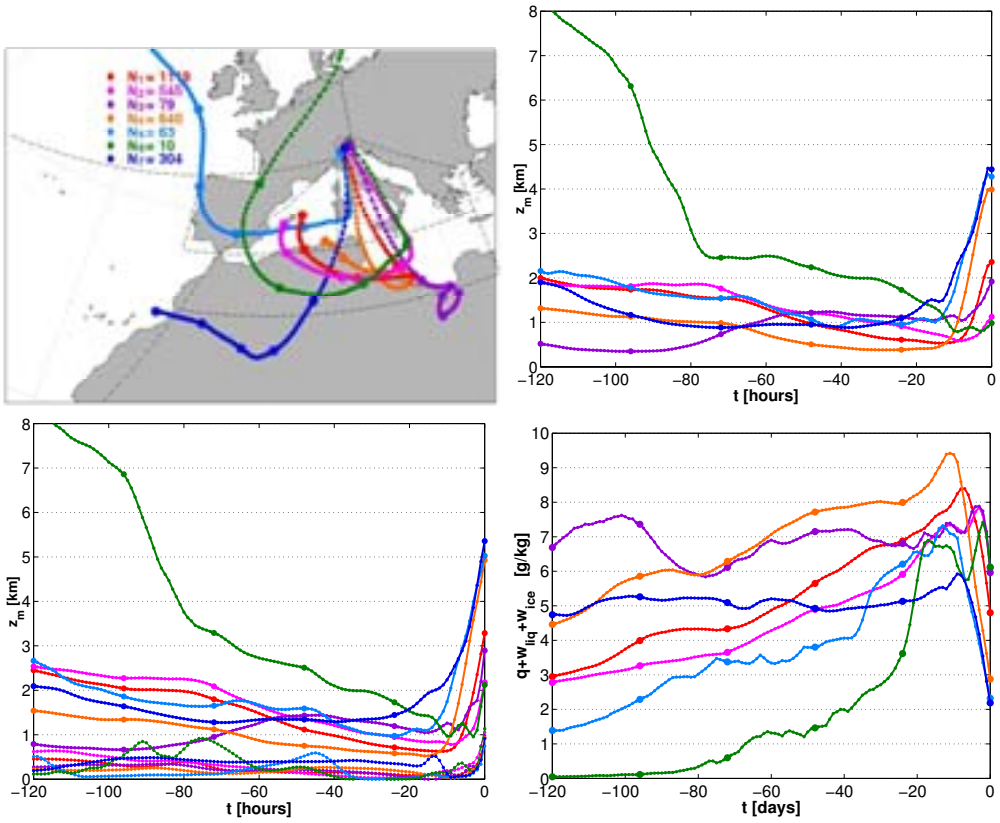

Figure 8.1: Clusters of trajectories arriving over Trentino in the period from 03/11/66 21 UTC to 04/11/66 12 UTC obtained from the "direct clustering" algorithm. In the first plot each curve is the average, in the physical space, of all trajectories belonging to that cluster. The average position every 1 hour is marked by a small circle, the position every 24 hours by a big one. The number of trajectories for each cluster is reported. In the following plots there are respectivelly the average height of the clusters above the surface, the average height above the mean sea level of the cluster (and of the terrain beneath them) and the average water concentration.

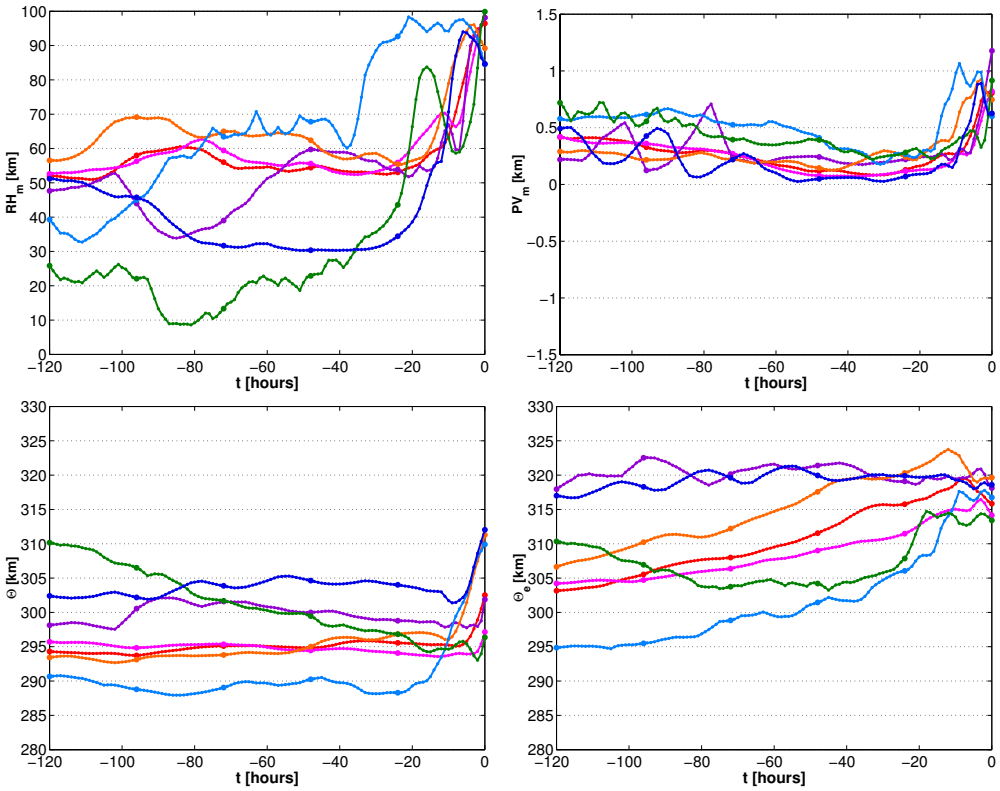

Figure 8.2: Clusters of trajectories arriving over Trentino in the period from 03/11/66 21 UTC to 04/11/66 12 UTC obtained from the "direct clustering" algorithm. In the plots there are the average relative humidity, the average potential vorticity, the average potential temperature and the average equivalent potential temperature of the clusters. The clusters have been marked by different colors and circles of different size according to figure 8.1.

	N_k	$\overline{z}$[dam]	$\overline{q}[\frac{g}{kg}]$	$\overline{PV}$[PVU]	$\overline{\theta}$[K]	$\overline{\theta_e}$[K]	$\overline{h}$[dam]	t[h]
1	2760	355 (125)	4.18 (1.54)	0.77 (0.07)	304.1 (6.2)	316.9 (2.0)	84 (10)	1 (1)
2	2760	254 (155)	5.47 (1.89)	0.61 0.26)	300.3 (6.7)	316.8 (2.2)	32 (17)	2 (9)
3	2760	138 (73)	7.20 (1.16)	0.43 (0.18)	297.1 (3.5)	318.3 (3.4)	12 (4)	13 (6)
4	2031	209 (49)	3.49 (1.00)	0.35 (0.07)	293.7 (2.2)	304.2 (3.1)	37 (23)	17 (49)
5	316	205 (23)	4.72 (0.65)	0.47 (0.09)	302.1 (1.6)	316.6 (3.6)	22 (9)	7 (91)
6	2649	149 (54)	5.39 (1.68)	0.24 (0.06)	296.5 (3.4)	312.6 (6.9)	29 (10)	25 (31)
7	2686	110 (37)	6.25 (1.07)	0.21 (0.08)	295.8 (2.8)	314.2 (4.6)	16 (12)	27 (17)
8	780	255 (43)	2.26 (0.65)	0.49 (0.09)	291.6 (1.8)	298.4 (2.3)	50 (6)	17 (78)
9	-	-	-	-	-	-	-	-
10	-	-	-	-	-	-	-	-
11	74	188 (178)	2.46 (1.18)	0.56 (0.12)	288.5 (6.8)	295.7 (3.5)	13 (8)	45 (55)
12	729	133 (11)	6.10 (0.90)	0.15 (0.07)	301.0 (2.4)	319.4 (0.5)	37 (7)	50 (31)

Table 8.1: The same quantities shown in Tab.4.1 are reported for the event of November 1966. In the present table data have been computed starting from the cluster trajectories (obtained using the "final geographical clustering" algorithm) so as all trajectories gathered together into one cluster had the average position and the average properties of the cluster.

	δz[dam]	$\delta q[\frac{g}{kg}]$	δPV[PVU]	$\delta\theta$[K]	$\delta\theta_e$[K]	δh[dam]	$\delta Q_{TOT}[\frac{kg}{m^2 h}]$
1	52 (23)	-0.93 (0.49)	0.02 (0.06)	2.03 (0.89)	-0.56 (0.53)	39 (15)	-0.060
2	38 (46)	-0.47 (0.42)	0.06 (0.13)	1.15 (0.75)	-0.18 (0.61)	20 (12)	-0.034
3	187 (238)	-1.98 (2.30)	0.43 (0.18)	5.07 (4.69)	-0.33 (2.52)	21 (14)	-0.106
4	-19 (22)	0.60 (0.59)	-0.07 (0.10)	0.21 (1.30)	1.91 (2.53)	-10 (11)	0.027
5	-8 (10)	0.07 (0.22)	-0.09 (0.07)	-0.27 (0.58)	-0.08 (0.01)	7 (34)	0.000
6	-23 (43)	0.39 (0.86)	-0.02 (0.13)	0.27 (0.96)	1.42 (2.98)	-11 (11)	0.034
7	-47 (72)	1.91 (1.77)	0.00 (0.12)	-0.02 (0.86)	5.41 (5.08)	-6 (9)	0.168
8	-42 (49)	0.45 (0.13)	-0.05 (0.17)	-0.31 (0.91)	0.97 (1.15)	0 (19)	0.008
9	-	-	-	-	-	-	-
10	-	-	-	-	-	-	-
11	-89 (93)	1.85 (1.28)	-0.07 (0.03)	-1.32 (0.53)	4.00 (3.12)	-30 (31)	0.003
12	-32 (44)	0.01 (0.55)	-0.17 (0.16)	1.78 (0.46)	1.96 (1.89)	8 (10)	0.000

Table 8.2: The same quantities shown in Tab.4.2 are reported for the event of November 1966. In the present table data have been computed starting from the cluster trajectories (obtained using the "final geographical clustering" algorithm) so as all trajectories gathered together into one cluster had the average position and the average properties of the cluster.

quantity	cluster 1	cluster 2	cluster 3	cluster 4	cluster 5	cluster 6	cluster 7	averadge
N	669	623	37	413	628	316	74	
$\bar{t}_q$	9	4	12	8	12	10	14	8.7
deltaq1	-7.20	-5.13	-7.69	-1.77	-4.75	-1.24	-5.91	-4.7
deltaq2	0.18	0.06	0.76	0.28	0.56	0.21	0.37	0.3
$\bar{t}_z$	1	1	2	2	3	4	4	1.9
deltaz1	252	143	386	275	428	408	373	293.7
deltaz2	-2535	-1902	-1192	-322	-907	-793	-1106	-1434.7
$\bar{t}_T$	109	14	121	99	103	10	87	72.9
deltaT1	7.2	3.2	12.2	7.1	15.1	10.8	18.2	8.9
deltaT2	1.3	-1.9	7.9	0.2	2.1	-0.9	2.5	0.5
$\bar{t}_{Te}$	9	4	13	37	13	56	3	18.2
deltaTe1	-4.8	-2.1	-9.5	-1.7	-3.4	-0.6	3.3	-2.8
deltaTe2	21.9	12.3	29.9	5.2	15.7	2.5	19.0	13.61
$\bar{t}_{RH}$	67	115	46	21	24	41	113	59.1424
deltaRH1	48	47	36	52	35	54	44	45.819
deltaRH2	-4	0	-6	-8	0	-21	-4	-4.7
$\bar{t}_{PV}$	30	37	52	34	46	55	32	39.0
deltaPV1	0.76	0.74	0.86	0.72	0.62	0.60	0.43	0.7
deltaPV2	-0.44	-0.34	-0.23	-0.12	-0.17	-0.45	-0.43	-0.3

Table 8.3: "Final geographical clustering" applied to 1966 event. For each variable and for each cluster $\bar{t}$ is reported as well as the variation in the values of that variable (for each cluster) from the ending time to $\bar{t}$ and from this $\bar{t}$ to the starting time (see section 6.1.4 for details). In the last column there is the weighted average over the cluster population.

	N_k	$\overline{z}$[dam]	$\overline{q}[\frac{g}{kg}]$	$\overline{PV}$[PVU]	$\overline{\theta}$[K]	$\overline{\theta_e}$[K]	$\overline{h}$[dam]	t[h]
1	2760	349 (113)	4.28 (1.39)	0.78 (0.07)	303.8 (5.4)	317.0 (1.7)	78 (7)	1 (1)
2	1842	222 (150)	6.17 (2.01)	0.62 (0.21)	298.9 (6.3)	317.2 (1.0)	33 (15)	2 (8)
3	2760	135 (74)	7.09 (1.16)	0.40 (0.19)	296.5 (4.0)	317.4 (4.2)	12 (3)	12 (7)
4	940	228 (82)	2.93 (1.58)	0.38 (0.10)	291.4 (3.3)	300.0 (4.1)	28 (13)	19 (46)
5	316	205 (23)	4.72 (0.65)	0.47 (0.09)	302.1 (1.6)	316.6 (3.6)	22 (9)	7 (91)
6	2477	149 (55)	5.45 (1.91)	0.23 (0.08)	296.9 (3.1)	313.1 (7.0)	30 (12)	32 (28)
7	2686	112 (34)	6.18 (0.97)	0.22 (0.08)	296.0 (2.6)	314.3 (4.4)	17 (13)	21 (19)
8	940	268 (87)	2.12 (0.89)	0.54 (0.03)	291.0 (3.9)	297.3 (2.2)	45 (5)	19 (77)
9	866	312 (78)	1.68 (0.68)	0.56 (0.08)	291.8 (4.0)	296.8 (2.2)	48 (8)	4 (102)
10	-	-	-	-	-	-	-	-
11	74	188 (178)	2.46 (1.18)	0.56 (0.12)	288.5 (6.8)	295.7 (3.5)	13 (8)	45 (55)
12	439	132 (20)	5.80 (1.22)	0.17 (0.05)	302.5 (2.2)	320.2 (1.5)	42 (1)	70 (37)

Table 8.4: The same quantities shown in Tab.4.1 are reported for the event of November 1966. In the present table data have been computed starting from the cluster trajectories (obtained using the "initial geographical clustering" algorithm) so as all trajectories gathered together into one cluster had the average position and the average properties of the cluster.

	δz[dam]	$\delta q[\frac{g}{kg}]$	δPV[PVU]	$\delta\theta$[K]	$\delta\theta_e$[K]	δh[dam]	$\delta Q_{TOT}[\frac{kg}{m^2 h}]$
1	63 (22)	-1.11 (0.47)	0.02 (0.06)	2.48 (0.86)	-0.63 (0.69)	46 (13)	-0.057
2	54 (60)	-0.82 (0.77)	0.11 (0.11)	1.48 (0.85)	-0.78 (1.32)	23 (10)	-0.032
3	170 (222)	-1.67 (1.87)	0.41 (0.17)	4.72 (3.88)	0.17 (2.10)	19 (15)	-0.079
4	-33 (35)	0.77 (0.85)	-0.09 (0.15)	1.11 (1.30)	3.38 (3.16)	4 (18)	0.013
5	-8 (10)	0.07 (0.22)	-0.09 (0.07)	-0.27 (0.58)	-0.08 (0.01)	7 (34)	0.000
6	-22 (42)	0.41 (0.65)	-0.04 (0.11)	0.50 (1.40)	1.75 (2.41)	-15 (21)	0.027
7	-39 (66)	1.71 (2.05)	0.01 (0.14)	-0.31 (1.13)	4.50 (5.72)	-5 (6)	0.147
8	-45 (50)	0.60 (0.14)	-0.10 (0.11)	-0.31 (0.92)	1.40 (0.94)	-8 (18)	0.011
9	-15 (22)	0.10 (0.09)	0.00 (0.07)	-0.38 (1.81)	-0.11 (1.77)	-1 (9)	0.002
10	-	-	-	-	-	-	-
11	-89 (93)	1.85 (1.28)	-0.07 (0.03)	-1.32 (0.53)	4.00 (3.12)	-30 (31)	0.002
12	-45 (57)	-0.45 (1.15)	-0.21 (0.24)	2.71 (1.27)	1.65 (2.80)	13 (14)	-0.003

Table 8.5: The same quantities shown in Tab.4.2 are reported for the event of November 1966. In the present table data have been computed starting from the cluster trajectories (obtained using the "initial geographical clustering" algorithm) so as all trajectories gathered together into one cluster had the average position and the average properties of the cluster.

quantity	cluster1	cluster 2	cluster 3	cluster 4	cluster 5	cluster 6	cluster 7	averadge
N	463	209	657	918	123	316	74	
$\overline{t}_q$	4	9	9	11	71	10	14	11.8
deltaq1	-4.04	-6.12	-7.42	-3.44	-5.13	-1.24	-5.91	-4.6
deltaq2	0.07	0.19	0.17	0.49	3.46	0.21	0.37	0.4
$\overline{t}_z$	1	1	1	2	5	4	4	1.9
deltaz1	177	217	221	372	367	408	373	295.6
deltaz2	-1251	-1503	-3102	-687	-945	-793	-1106	-1453.0
$\overline{t}_T$	14	104	52	103	94	10	87	64.5
deltaT1	4.0	5.9	6.2	11.9	14.6	10.8	18.2	8.9
deltaT2	-2.5	7.7	-0.6	1.7	-3.7	-0.9	2.5	0.4
$\overline{t}_{Te}$	4	7	9	13	64	56	3	17.0
deltaTe1	-1.5	-4.5	-3.9	-2.5	-3.8	-0.6	3.3	-2.5
deltaTe2	8.3	25.3	20.6	11.5	10.5	2.5	19.0	13.30
$\overline{t}_{RH}$	121	26	68	23	27	41	113	55.0312
deltaRH1	52	39	55	40	49	54	44	47.9806
deltaRH2	0	-25	-6	-1	-13	-21	-4	-6.9
$\overline{t}_{PV}$	37	51	30	49	40	55	32	42.4
deltaPV1	0.81	0.77	0.72	0.65	0.66	0.60	0.43	0.7
deltaPV2	-0.18	-0.49	-0.51	-0.15	-0.11	-0.45	-0.43	-0.3

Table 8.6: "Initial geographical clustering" applied to 1966 event. For each variable and for each cluster $\overline{t}$ is reported as well as the variation in the values of that variable (for each cluster) from the ending time to $\overline{t}$ and from this $\overline{t}$ to the starting time (see section 6.1.4 for details). In the last column there is the weighted average over the cluster population.

	N_k	$\overline{z}$[dam]	$\overline{q}[\frac{g}{kg}]$	$\overline{PV}$[PVU]	$\overline{\theta}$[K]	$\overline{\theta_e}$[K]	$\overline{h}$[dam]	t[h]
1	2760	351 (127)	4.27 (1.63)	0.76 (0.08)	303.9 (6.1)	317.0 (1.8)	81 (9)	1 (2)
2	2697	252 (151)	5.53 (1.85)	0.61 (0.25)	300.3 (6.5)	316.9 (2.1)	32 (16)	2 (9)
3	2760	138 (70)	7.19 (0.94)	0.43 (0.17)	297.2 (3.2)	318.4 (3.3)	13 (3)	12 (6)
4	2377	205 (43)	3.70 (0.77)	0.36 (0.07)	294.1 (1.9)	305.1 (1.9)	38 (23)	22 (44)
5	367	198 (34)	4.52 (0.69)	0.46 (0.10)	299.9 (5.1)	313.7 (6.9)	21 (9)	7 (90)
6	2618	150 (48)	5.30 (1.38)	0.25 (0.06)	295.3 (4.0)	311.0 (6.2)	27 (12)	21 (33)
7	2393	100 (26)	6.49 (1.03)	0.18 (0.08)	295.0 (1.7)	314.1 (4.1)	15 (5)	32 (14)
8	73	225 (156)	3.04 (1.65)	0.50 (0.07)	291.9 (5.7)	300.9 (5.2)	37 (16)	27 (69)
9	10	738 (439)	0.09 (1.63)	0.61 (0.00)	307.9 (17.9)	308.3 (13.1)	26 (23)	13 (99)
10	-	-	-	-	-	-	-	-
11	73	282 (226)	1.91 (0.97)	0.61 (0.08)	292.0 (7.8)	297.7 (5.2)	14 (9)	40 (61)
12	383	130 (28)	5.44 (1.01)	0.20 (0.07)	303.0 (2.3)	319.6 (0.4)	39 (6)	77 (37)

Table 8.7: The same quantities shown in Tab.4.1 are reported for the event of November 1966. In the present table data have been computed starting from the cluster trajectories (obtained using the "direct clustering" algorithm) so as all trajectories gathered together into one cluster had the average position and the average properties of the cluster.

	δz[dam]	$\delta q[\frac{g}{kg}]$	δPV[PVU]	$\delta\theta$[K]	$\delta\theta_e$[K]	δh[dam]	$\delta Q_{TOT}[\frac{kg}{m^2 h}]$
1	58 (27)	-1.04 (0.60)	0.05 (0.10)	2.18 (0.95)	-0.70 (0.75)	43 (16)	-0.057
2	33 (41)	-0.37 (0.47)	0.04 (0.10)	1.06 (0.83)	0.02 (0.61)	17 (11)	-0.021
3	187 (238)	-2.04 (2.26)	0.44 (0.14)	5.06 (4.65)	-0.52 (2.26)	20 (14)	-0.093
4	-31 (32)	0.91 (0.47)	-0.06 (0.07)	-0.50 (1.81)	2.05 (2.05)	-13 (14)	0.041
5	-10 (13)	0.13 (0.17)	-0.16 (0.16)	-0.17 (0.71)	0.20 (0.27)	8 (33)	0.001
6	-24 (44)	0.48 (0.72)	-0.04 (0.13)	0.44 (1.05)	1.85 (2.69)	-8 (9)	0.036
7	-47 (64)	1.78 (1.30)	0.01 (0.10)	0.27 (1.13)	5.32 (3.37)	-5 (9)	0.122
8	-44 (84)	0.55 (0.19)	-0.19 (0.08)	0.91 (1.27)	2.56 (1.83)	40 (55)	0.001
9	-74 (82)	0.04 (0.08)	-0.13 (0.21)	-2.55 (0.40)	-2.39 (0.54)	32 (41)	0.000
10	-	-	-	-	-	-	-
11	-97 (102)	1.70 (1.32)	-0.04 (0.01)	-1.89 (1.19)	3.00 (2.59)	-34 (37)	0.002
12	-43 (56)	0.04 (0.56)	-0.21 (0.14)	2.42 (0.92)	2.74 (2.32)	5 (9)	0.000

Table 8.8: The same quantities shown in Tab.4.2 are reported for the event of November 1966. In the present table data have been computed starting from the cluster trajectories (obtained using the "direct clustering" algorithm) so as all trajectories gathered together into one cluster had the average position and the average properties of the cluster.

quantity	cluster 1	cluster 2	cluster 3	cluster 4	cluster 5	cluster 6	cluster 7	averadge
N	1119	545	79	640	63	10	304	
$\overline{t}_q$	9	4	5	12	14	3	10	8.8
deltaq1	-4.05	-2.00	-2.34	-6.86	-5.12	-1.57	-3.93	-4.2
deltaq2	5.44	4.94	0.98	4.94	5.81	7.27	1.13	4.6
$\overline{t}_z$	2	1	10	3	4	1	4	2.2
deltaz1	27	14	22	43	36	11	41	29.5
deltaz2	-182	-175	-13	-94	-128	-740	-80	-144.9
$\overline{t}_T$	97	14	103	103	86	3	10	72.0
deltaT1	7.4	3.2	3.8	15.2	17.4	3.3	10.7	8.9
deltaT2	0.8	-1.7	0.0	2.6	1.9	-17.1	-1.0	0.4
$\overline{t}_{Te}$	9	4	96	13	3	19	56	16.5
deltaTe1	-3.6	-2.3	-2.7	-3.8	3.4	-0.9	-0.7	-2.9
deltaTe2	16.3	12.2	2.9	16.8	18.5	4.0	2.2	13.69
$\overline{t}_{RH}$	110	36	86	24	112	82	52	68.3145
deltaRH1	45	46	64	34	52	91	54	44.6569
deltaRH2	-1	0	-14	-1	-7	-17	-21	-3.6
$\overline{t}_{PV}$	33	38	97	46	32	34	55	41.2
deltaPV1	0.72	0.75	1.05	0.62	0.42	0.69	0.60	0.7
deltaPV2	-0.33	-0.35	-0.10	-0.16	-0.40	-0.50	-0.47	-0.3

Table 8.9: "Direct clustering" applied to 1966 event. For each variable and for each cluster $\overline{t}$ is reported as well as the variation in the values of that variable (for each cluster) from the ending time to $\overline{t}$ and from this $\overline{t}$ to the starting time (see section 6.1.4 for details). In the last column there is the weighted average over the cluster population.

8.2 Cluster analysis of the 2000 event

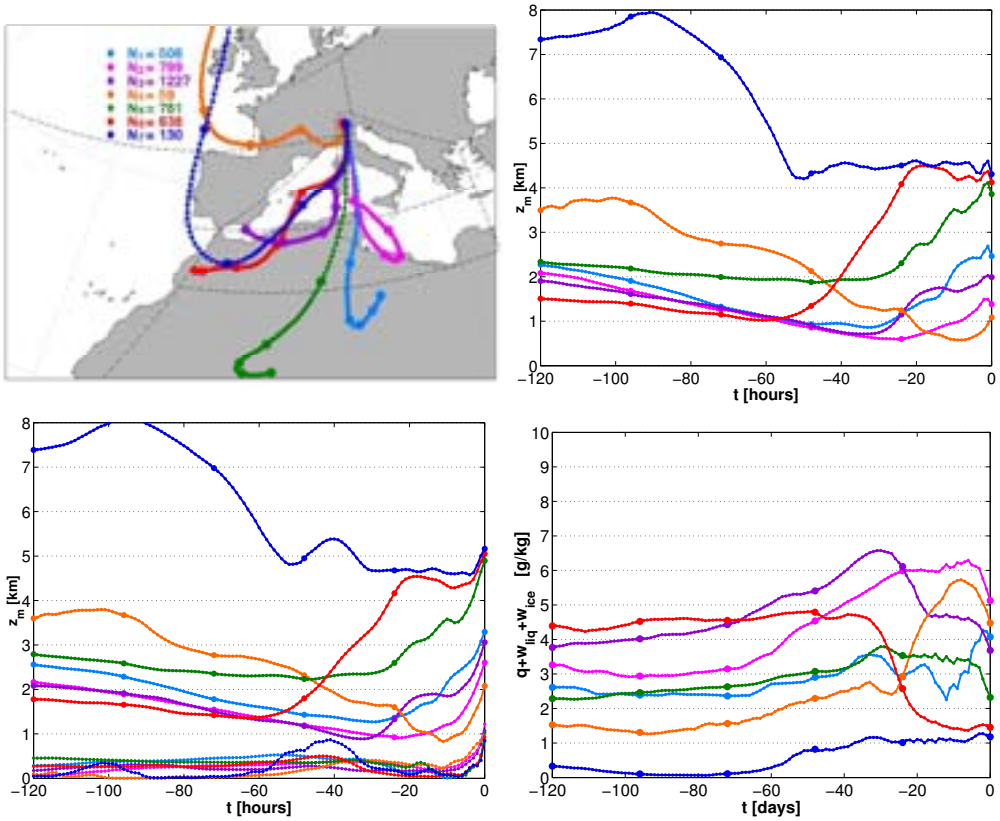

Figure 8.3: Clusters of trajectories arriving over Trentino in the period from 16/11/00 18 UTC to 17/11/00 18 UTC obtained from the "direct clustering" algorithm. In the first plot each curve is the average, in the physical space, of all trajectories belonging to that cluster. The average position every 1 hour is marked by a small circle, the position every 24 hours by a big one. The number of trajectories for each cluster is reported. In the following plots there are respectivelly the average height of the clusters above the surface, the average height above the mean sea level of the cluster (and of the terrain beneath them) and the average water concentration.

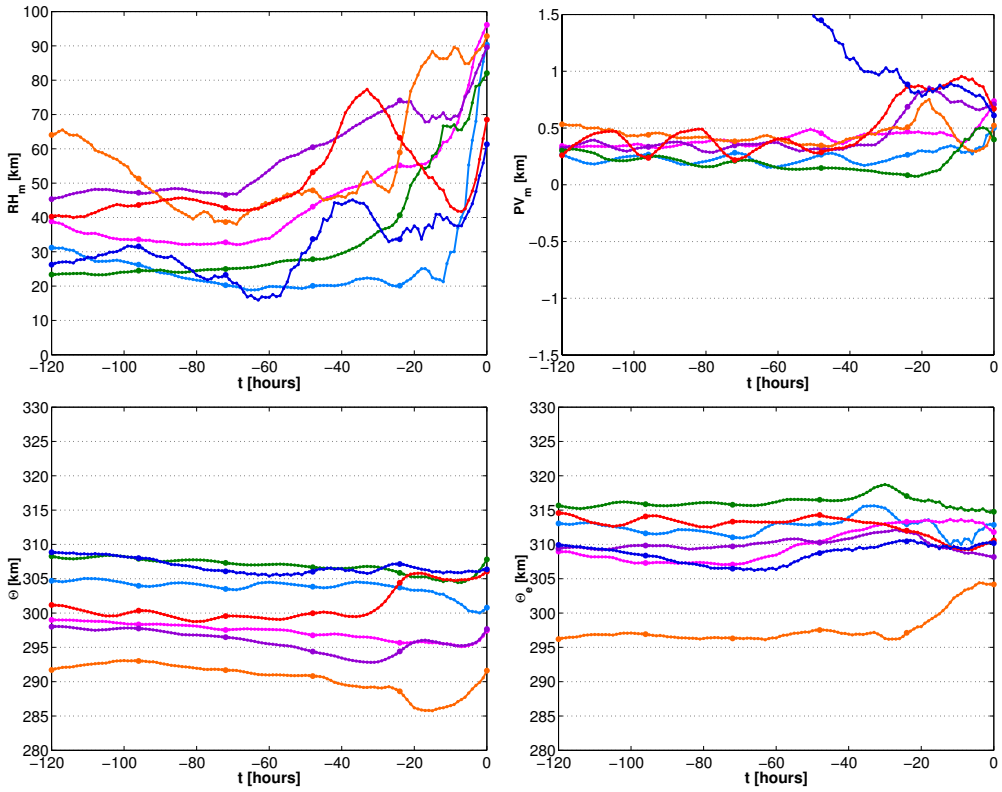

Figure 8.4: Clusters of trajectories arriving over Trentino in the period from 16/11/00 18 UTC to 17/11/00 18 UTC obtained from the "direct clustering" algorithm. In the plots there are the average relative humidity, the average potential vorticity, the average potential temperature and the average equivalent potential temperature of the clusters. The clusters have been marked by different colors and circles of different size according to figure 8.1.

	N_k	$\overline{z}$[dam]	$\overline{q}[\frac{g}{kg}]$	$\overline{PV}$[PVU]	$\overline{\theta}$[K]	$\overline{\theta_e}$[K]	$\overline{h}$[dam]	t[h]
1	4140	353 (111)	3.35 (1.29)	0.61 (0.08)	300.9 (4.8)	311.1 (1.6)	78 (14)	2 (2)
2	4140	310 (124)	3.77 (1.45)	0.60 (0.06)	299.9 (5.0)	311.4 (1.2)	39 (22)	1 (16)
3	4140	230 (114)	3.72 (1.31)	0.48 (0.11)	298.8 (4.4)	310.0 (2.7)	21 (9)	22 (21)
4	3885	283 (97)	2.96 (1.79)	0.41 (0.20)	301.3 (5.9)	310.5 (2.8)	19 (10)	17 (13)
5	227	511 (192)	0.88 (1.22)	1.62 (1.14)	305.5 (7.1)	308.4 (5.3)	18 (21)	14 (70)
6	2243	238 (80)	3.55 (0.91)	0.34 (0.22)	303.2 (1.4)	314.3 (2.9)	33 (12)	18 (15)
7	2058	160 (50)	3.67 (0.62)	0.36 (0.06)	297.1 (5.1)	308.1 (6.0)	22 (9)	29 (8)
8	227	498 (266)	0.94 (2.62)	1.33 (1.05)	306.0 (12.7)	309.1 (6.3)	25 (13)	8 (42)
9	-	-	-	-	-	-	-	-)
10	-	-	-	-	-	-	-	-)
11	227	596 (393)	1.19 (2.80)	1.69 (1.77)	307.2 (10.3)	311.0 (4.6)	7 (7)	42 (11)
12	2110	187 (6)	3.45 (0.78)	0.26 (0.09)	303.6 (1.9)	314.3 (4.3)	39 (2)	74 (38)

Table 8.10: The same quantities shown in Tab.4.3 are reported for the event of November 2000. In the present table data have been computed starting from the cluster trajectories (obtained using the "final geographical clustering" algorithm) so as all trajectories gathered together into one cluster had the average position and the average properties of the cluster.

	δz[dam]	$\delta q[\frac{g}{kg}]$	δPV[PVU]	$\delta\theta$[K]	$\delta\theta_e$[K]	δh[dam]	$\delta Q_{TOT}[\frac{kg}{m^2h}]$
1	45 (15)	-0.50 (0.30)	0.02 (0.08)	1.22 (0.52)	-0.23 (0.37)	56 (20)	-0.029
2	27 (28)	-0.19 (0.27)	0.01 (0.04)	0.43 (0.59)	-0.10 (0.27)	13 (23)	-0.010
3	36 (52)	0.26 (0.39)	0.11 (0.10)	-0.39 (0.65)	0.35 (0.94)	12 (8)	0.022
4	-4 (29)	-0.20 (0.64)	0.02 (0.17)	-0.36 (2.68)	-0.99 (1.34)	2 (27)	-0.009
5	-38 (76)	-0.09 (0.62)	-0.20 (0.16)	0.15 (0.71)	-0.04 (1.22)	20 (9)	0.000
6	83 (105)	-0.65 (0.93)	0.14 (0.25)	0.80 (1.74)	-1.09 (1.15)	-20 (29)	-0.019
7	-47 (50)	0.94 (0.73)	0.02 (0.02)	-1.33 (0.63)	1.30 (1.54)	-3 (11)	0.031
8	-1 (49)	0.07 (0.54)	-0.14 (0.18)	-0.07 (1.50)	0.11 (0.32)	20 (21)	0.000
9	-	-	-	-	-	-	-
10	-	-	-	-	-	-	-
11	-49 (50)	-0.17 (0.17)	-0.05 (0.09)	-2.34 (3.23)	-2.85 (3.65)	-3 (5)	0.000
12	-31 (39)	0.79 (0.50)	-0.05 (0.10)	-1.36 (0.92)	0.96 (2.44)	3 (22)	0.020

Table 8.11: The same quantities shown in Tab.4.4 are reported for the event of November 2000. In the present table data have been computed starting from the cluster trajectories (obtained using the "final geographical clustering" algorithm) so as all trajectories gathered together into one cluster had the average position and the average properties of the cluster.

quantity	cluster 1	cluster 2	cluster 3	cluster 4	cluster 5	cluster 6	averadge
N	133	94	1806	49	1803	255	
$\bar{t}_q$	4	120	34	19	29	2	31
deltaq1	-0.95	0.00	-1.09	-1.95	-2.78	-2.79	-1.91
deltaq2	-0.02	-1.75	0.30	-0.09	0.00	-0.01	0.09
$\bar{t}_z$	51	84	56	43	32	30	44
deltaz1	38	186	298	364	181	119	226
deltaz2	-261	-26	-50	-62	-132	-156	-99
$\bar{t}_T$	61	71	37	14	32	3	34
deltaT1	0.3	-0.6	2.6	6.6	3.2	0.2	2.6
deltaT2	-2.8	0.0	-1.6	-5.2	-3.9	-5.8	-2.9
$\bar{t}_{Te}$	24	120	34	19	25	34	32
deltaTe1	0.0	-6.1	-3.9	-4.6	-2.3	-0.3	-2.9
deltaTe2	0.3	0.0	1.5	0.3	3.7	1.8	2.4
$\bar{t}_{RH}$	64	9	121	43	76	65	93
deltaRH1	45	22	51	50	51	72	51
deltaRH2	-10	-6	0	-4	-3	-18	-3
$\bar{t}_{PV}$	1	40	40	25	103	109	70
deltaPV1	0.00	0.18	0.34	0.17	0.41	0.29	0.35
deltaPV2	-1.80	-0.18	-0.08	-0.19	-0.03	-0.01	-0.11

Table 8.12: "Final geographical clustering" applied to 2000 event. For each variable and for each cluster $\bar{t}$ is reported as well as the variation in the values of that variable (for each cluster) from the ending time to $\bar{t}$ and from this $\bar{t}$ to the starting time (see section 6.1.4 for details). In the last column there is the weighted average over the cluster population.

	N_k	$\overline{z}$[dam]	$\overline{q}[\frac{g}{kg}]$	$\overline{PV}$[PVU]	$\overline{\theta}$[K]	$\overline{\theta_e}$[K]	$\overline{h}$[dam]	t[h]
1	4140	353 (112)	3.35 (1.29)	0.61 (0.06)	300.9 (4.8)	311.1 (1.5)	78 (12)	2 (2)
2	4140	309 (124)	3.76 (1.44)	0.60 (0.06)	299.9 (5.0)	311.3 (1.3)	38 (21)	2 (16)
3	4140	233 (110)	3.70 (1.42)	0.48 (0.14)	299.0 (4.1)	310.1 (2.7)	20 (8)	18 (14)
4	4140	275 (89)	3.10 (1.78)	0.39 (0.21)	301.0 (5.5)	310.5 (2.8)	18 (9)	15 (15)
5	354	415 (196)	1.81 (1.74)	1.33 (0.99)	302.4 (6.5)	308.0 (4.8)	18 (19)	12 (72)
6	1988	247 (88)	3.78 (0.86)	0.36 (0.24)	303.4 (2.9)	315.0 (2.6)	29 (14)	20 (13)
7	1993	158 (37)	3.75 (0.25)	0.36 (0.03)	296.5 (5.2)	307.8 (6.2)	27 (4)	54 (25)
8	354	374 (219)	2.04 (2.12)	1.02 (0.85)	301.8 (10.2)	308.1 (5.4)	21 (15)	8 (41)
9	-	-	-	-	-	-	-	-
10	-	-	-	-	-	-	-	-
11	227	596 (393)	1.19 (2.80)	1.69 (1.77)	307.2 (10.3)	311.0 (4.6)	7 (7)	42 (11)
12	1728	196 (10)	3.47 (0.66)	0.25 (0.11)	304.7 (2.8)	315.6 (4.9)	40 (1)	82 (43)

Table 8.13: The same quantities shown in Tab.4.3 are reported for the event of November 2000. In the present table data have been computed starting from the cluster trajectories (obtained using the "initial geographical clustering" algorithm) so as all trajectories gathered together into one cluster had the average position and the average properties of the cluster.

	δz[dam]	$\delta q[\frac{g}{kg}]$	δPV[PVU]	$\delta\theta$[K]	$\delta\theta_e$[K]	δh[dam]	$\delta Q_{TOT}[\frac{kg}{m^2 h}]$
1	46 (13)	-0.49 (0.26)	0.02 (0.08)	1.22 (0.41)	-0.19 (0.36)	56 (19)	-0.027
2	27 (29)	-0.19 (0.23)	0.01 (0.05)	0.43 (0.56)	-0.10 (0.21)	13 (22)	-0.010
3	41 (59)	0.05 (0.12)	0.10 (0.10)	0.05 (0.62)	0.21 (0.72)	10 (7)	0.004
4	8 (64)	-0.34 (0.99)	0.04 (0.20)	0.06 (3.12)	-0.95 (1.49)	-1 (24)	-0.017
5	-30 (66)	0.02 (0.53)	-0.16 (0.14)	-0.09 (0.69)	-0.01 (1.09)	15 (11)	0.000
6	87 (103)	-0.66 (1.03)	0.11 (0.27)	0.65 (1.48)	-1.29 (1.75)	-22 (30)	-0.015
7	-97 (98)	1.96 (1.44)	0.05 (0.03)	-3.03 (2.20)	2.46 (1.88)	4 (11)	0.054
8	-4 (41)	0.18 (0.45)	-0.02 (0.17)	-0.25 (1.34)	0.24 (0.35)	14 (17)	0.001
9	-	-	-	-	-	-	-
10	-	-	-	-	-	-	-
11	-49 (50)	-0.17 (0.17)	-0.05 (0.09)	-2.34 (3.23)	-2.85 (3.65)	-3 (5)	0.000
12	-20 (25)	0.77 (0.50)	-0.08 (0.10)	-1.92 (1.41)	0.34 (2.99)	1 (23)	0.015

Table 8.14: The same quantities shown in Tab.4.4 are reported for the event of November 2000. In the present table data have been computed starting from the cluster trajectories (obtained using the "initial geographical clustering" algorithm) so as all trajectories gathered together into one cluster had the average position and the average properties of the cluster.

quantity	cluster1	cluster 2	cluster 3	cluster 4	cluster 5	cluster 6	averadge
N	133	94	1728	127	65	1993	
$\bar{t}_q$	4	120	34	54	55	28	33
deltaq1	-0.95	0.00	-1.06	-3.94	-3.38	-2.58	-1.89
deltaq2	-0.02	-1.75	0.19	3.09	3.17	-0.12	0.12
$\bar{t}_z$	5	8	5	6	6	3	4
deltaz1	38	186	289	447	226	173	227
deltaz2	-2615	-261	-469	-1024	-707	-1381	-993
$\bar{t}_T$	61	71	35	58	48	31	36
deltaT1	0.3	-0.6	2.3	13.9	4.4	2.2	2.5
deltaT2	-2.8	0.0	-2.0	-2.5	-2.1	-3.7	-2.8
$\bar{t}_{Te}$	24	120	32	52	73	25	32
deltaTe1	0.0	-6.1	-3.9	-3.7	-9.0	-1.9	-2.9
deltaTe2	0.3	0.0	1.0	8.4	7.2	3.4	2.4
$\bar{t}_{RH}$	64	9	69	11	121	73	68
deltaRH1	45	22	53	30	38	55	52
deltaRH2	-10	-6	-1	-5	0	-6	-4
$\bar{t}_{PV}$	1	40	40	72	55	103	70
deltaPV1	0.00	0.18	0.34	0.52	0.63	0.39	0.36
deltaPV2	-1.80	-0.18	-0.08	-0.21	-0.23	-0.02	-0.11

Table 8.15: "Initial geographical clustering" applied to 2000 event. For each variable and for each cluster $\bar{t}$ is reported as well as the variation in the values of that variable (for each cluster) from the ending time to $\bar{t}$ and from this $\bar{t}$ to the starting time (see section 6.1.4 for details). In the last column there is the weighted average over the cluster population.

	N_k	$\overline{z}$[dam]	$\overline{q}[\frac{g}{kg}]$	$\overline{PV}$[PVU]	$\overline{\theta}$[K]	$\overline{\theta_e}$[K]	$\overline{h}$[dam]	t[h]
1	4140	352 (108)	3.36 (1.33)	0.61 (0.12)	300.9 (4.8)	311.1 (2.5)	77 (14)	2 (2)
2	4140	308 (122)	3.80 (1.53)	0.60 (0.13)	299.8 (5.0)	311.4 (2.6)	38 (21)	2 (16)
3	4140	248 (110)	3.73 (1.47)	0.54 (0.22)	299.5 (4.3)	310.8 (2.8)	16 (7)	13 (5)
4	2054	217 (106)	4.24 (1.31)	0.47 (0.19)	297.7 (3.9)	310.4 (1.5)	19 (10)	26 (21)
5	130	564 (225)	0.35 (1.38)	2.04 (1.33)	305.7 (7.2)	306.9 (3.1)	25 (27)	7 (76)
6	4081	194 (79)	3.78 (0.67)	0.33 (0.20)	300.4 (4.0)	311.9 (3.6)	30 (11)	36 (24)
7	3313	177 (74)	4.07 (0.87)	0.32 (0.10)	299.2 (4.4)	311.5 (3.9)	24 (9)	13 (20)
8	189	411 (270)	1.73 (2.73)	1.59 (1.15)	299.4 (11.0)	304.5 (3.4)	21 (16)	3 (46)
9	59	170 (62)	2.81 (0.99)	0.48 (0.05)	288.9 (4.0)	297.1 (7.0)	34 (21)	29 (0)
10	-	-)	-)	-)	-)	-)	-)	-)
11	189	622 (422)	0.59 (3.18)	1.90 (1.94)	302.8 (9.3)	304.6 (6.3)	9 (8)	58 (15)
12	1287	223 (46)	2.71 (0.12)	0.20 (0.15)	306.1 (4.5)	314.8 (4.5)	40 (2)	92 (54)

Table 8.16: The same quantities shown in Tab.4.3 are reported for the event of November 2000. In the present table data have been computed starting from the cluster trajectories (obtained using the "direct clustering" algorithm) so as all trajectories gathered together into one cluster had the average position and the average properties of the cluster.

	δz[dam]	$\delta q[\frac{g}{kg}]$	δPV[PVU]	$\delta\theta$[K]	$\delta\theta_e$[K]	δh[dam]	$\delta Q_{TOT}[\frac{kg}{m^2h}]$
1	47 (16)	-0.52 (0.32)	0.02 (0.09)	1.27 (0.58)	-0.22 (0.46)	57 (19)	-0.028
2	27 (28)	-0.19 (0.26)	0.01 (0.05)	0.44 (0.59)	-0.09 (0.26)	13 (22)	-0.010
3	47 (67)	-0.02 (0.49)	0.01 (0.18)	-0.33 (1.09)	-0.41 (0.67)	12 (7)	-0.001
4	57 (97)	-0.68 (1.23)	0.28 (0.28)	1.01 (2.25)	-0.96 (2.08)	-10 (19)	-0.024
5	-72 (79)	0.22 (0.11)	-0.31 (0.23)	-0.11 (0.27)	0.64 (0.57)	23 (15)	0.001
6	-1 (54)	0.49 (0.76)	0.03 (0.12)	-1.20 (0.63)	0.15 (2.10)	1 (15)	0.027
7	-13 (26)	0.31 (0.53)	0.03 (0.02)	-0.62 (0.44)	0.22 (1.27)	2 (11)	0.017
8	-31 (40)	0.22 (0.43)	-0.15 (0.20)	0.11 (1.68)	0.77 (0.88)	4 (4)	0.001
9	-118 (119)	2.30 (2.51)	0.37 (0.25)	-4.93 (4.09)	1.53 (2.98)	9 (39)	0.002
10	-	-	-	-	-	-	-
11	-90 (91)	0.11 (0.47)	-0.11 (0.07)	-2.34 (3.29)	-2.05 (3.58)	3 (12)	0.000
12	-72 (89)	1.19 (0.25)	-0.15 (0.19)	-1.40 (1.18)	2.22 (1.11)	-4 (30)	0.017

Table 8.17: The same quantities shown in Tab.4.4 are reported for the event of November 2000. In the present table data have been computed starting from the cluster trajectories (obtained using the "direct clustering" algorithm) so as all trajectories gathered together into one cluster had the average position and the average properties of the cluster.

quantity	cluster 1	cluster 2	cluster 3	cluster 4	cluster 5	cluster 6	cluster 7	averadge
$\overline{t}_q$	3	7	32	9	31	51	4	25
deltaq1	-0.26	-1.40	-3.10	-1.41	-1.66	-3.41	-0.11	-2.08
deltaq2	1.58	2.97	2.78	4.17	1.51	0.39	0.92	2.02
$\overline{t}_z$	3	3	4	1	5	6	5	4
deltaz1	20	17	22	11	27	37	3	23
deltaz2	-127	-123	-119	-264	-56	-41	-256	-103
$\overline{t}_T$	3	8	33	16	9	82	61	28
deltaT1	0.8	2.3	4.8	4.5	1.1	6.2	0.3	3.2
deltaT2	-4.7	-3.9	-5.2	-4.6	-1.6	-1.3	-2.8	-3.5
$\overline{t}_{Te}$	34	13	28	5	31	121	24	40
deltaTe1	0.0	-1.7	-3.6	0.8	-4.0	-3.6	0.0	-2.7
deltaTe2	-0.2	4.5	2.4	7.1	3.1	-0.4	0.2	2.2
$\overline{t}_{RH}$	66	70	121	70	109	115	64	99
deltaRH1	71	64	44	55	59	29	45	52
deltaRH2	-12	-7	0	-26	0	0	-10	-4
$\overline{t}_{PV}$	64	94	79	6	23	73	1	65
deltaPV1	0.35	0.42	0.42	0.23	0.32	0.45	0.00	0.38
deltaPV2	-0.11	-0.02	-0.03	-0.24	-0.23	-0.04	-1.83	-0.14

Table 8.18: "Direct clustering" applied to 2000 event. For each variable and for each cluster $\overline{t}$ is reported as well as the variation in the values of that variable (for each cluster) from the ending time to $\overline{t}$ and from this $\overline{t}$ to the starting time (see section 6.1.4 for details). In the last column there is the weighted average over the cluster population.

8.3 Cluster analysis of the first phase of 2002 event

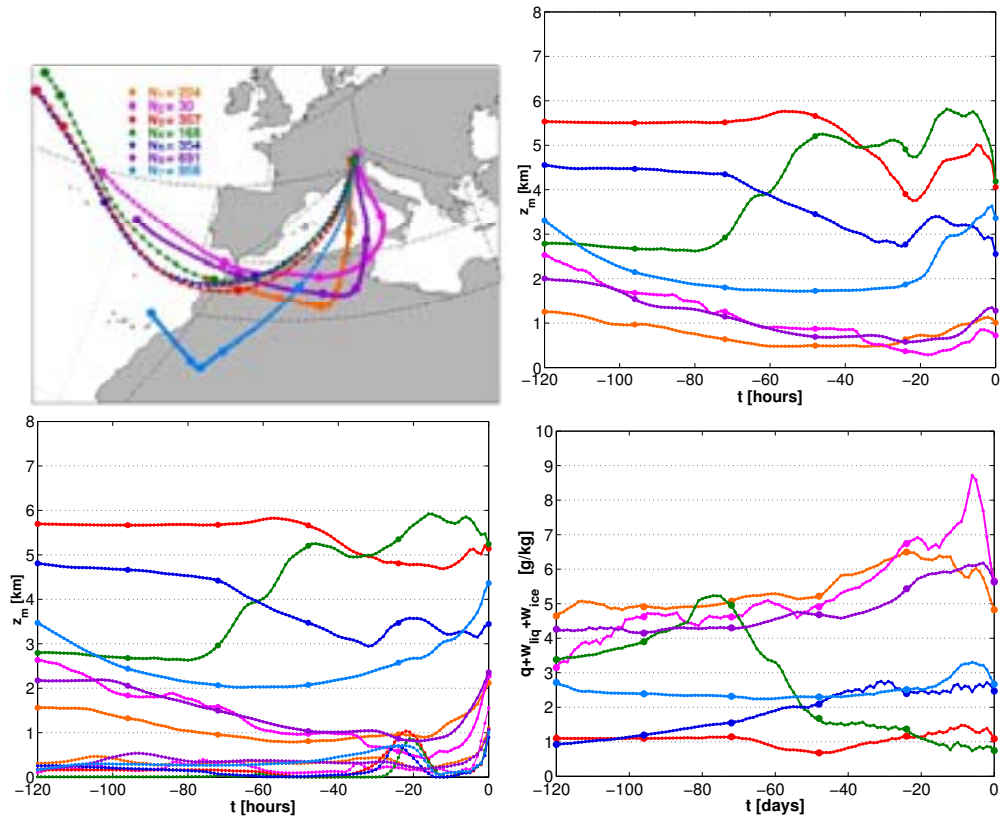

Figure 8.5: Clusters of trajectories arriving over Trentino in the period from 24/11/02 18 UTC to 25/11/02 09 UTC obtained from the "direct clustering" algorithm. In the first plot each curve is the average, in the physical space, of all trajectories belonging to that cluster. The average position every 1 hour is marked by a small circle, the position every 24 hours by a big one. The number of trajectories for each cluster is reported. In the following plots there are respectivelly the average height of the clusters above the surface, the average height above the mean sea level of the cluster (and of the terrain beneath them) and the average water concentration.

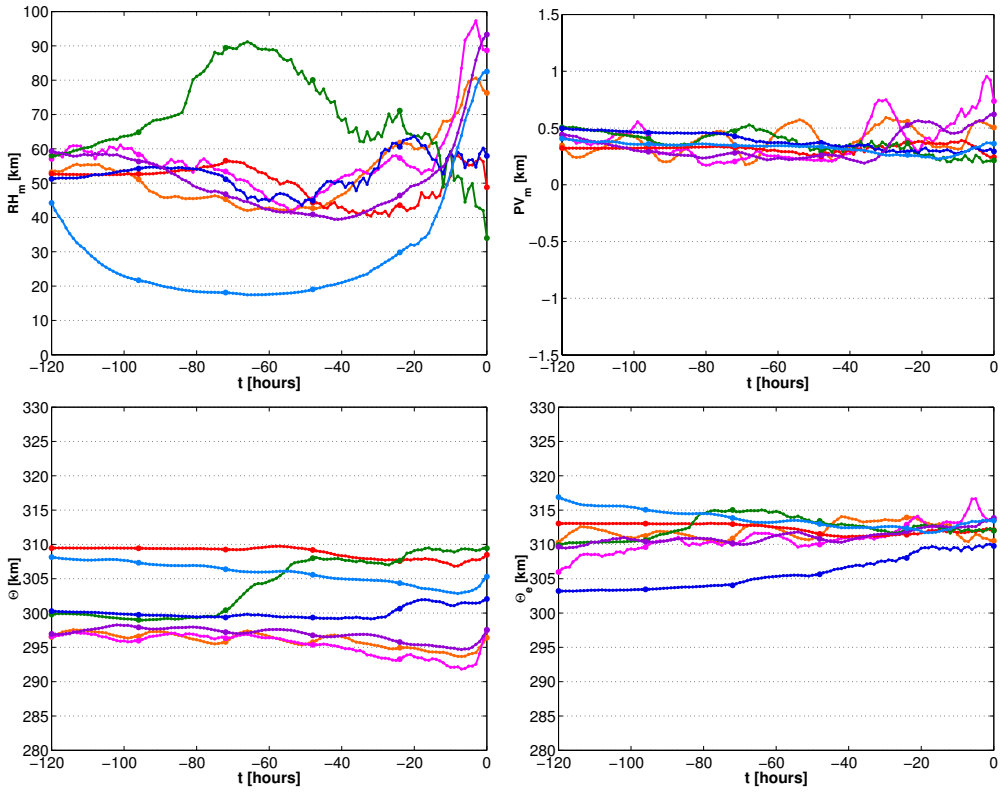

Figure 8.6: Clusters of trajectories arriving over Trentino in the period from 24/11/02 18 UTC to 25/11/02 09 UTC obtained from the "direct clustering" algorithm. In the plots there are the average relative humidity, the average potential vorticity, the average potential temperature and the average equivalent potential temperature of the clusters. The clusters have been marked by different colors and circles of different size according to figure 8.1.

	N_k	$\overline{z}$[dam]	$\overline{q}[\frac{g}{kg}]$	$\overline{PV}$[PVU]	$\overline{\theta}$[K]	$\overline{\theta_e}$[K]	$\overline{h}$[dam]	t[h]
1	2760	357 (126)	3.36 (1.80)	0.41 (0.14)	302.3 (4.9)	312.6 (1.0)	76 (12)	2 (3)
2	2760	326 (147)	3.67 (2.07)	0.40 (0.13)	301.3 (5.5)	312.5 (1.1)	34 (16)	1 (5)
3	2760	293 (159)	3.64 (1.82)	0.36 (0.09)	301.2 (4.9)	312.3 (1.2)	22 (5)	11 (11)
4	1699	378 (117)	2.17 (0.98)	0.29 (0.03)	304.7 (3.2)	311.6 (1.1)	14 (5)	12 (2)
5	2760	312 (132)	2.78 (1.44)	0.36 (0.05)	303.2 (5.4)	311.9 (4.6)	22 (20)	18 (23)
6	2760	269 (139)	2.92 (1.34)	0.29 (0.03)	302.2 (4.4)	311.2 (1.6)	56 (21)	32 (27)
7	1061	114 (21)	5.10 (0.39)	0.33 (0.16)	296.8 (1.4)	312.1 (2.0)	41 (6)	5 (21)
8	-	-	-	-	-	-	-	-
9	-	-	-	-	-	-	-	-
10	-	-	-	-	-	-	-	-
11	816	496 (176)	1.51 (2.65)	0.38 (0.10)	304.4 (5.6)	309.2 (7.1)	12 (11)	75 (27)
12	883	230 (2)	2.20 (0.62)	0.35 (0.02)	306.9 (1.7)	314.1 (0.1)	31 (14)	72 (30)

Table 8.19: The same quantities shown in Tab.4.5 are reported for the first phase of the event of November 2002. In the present table data have been computed starting from the cluster trajectories (obtained using the "final geographical clustering" algorithm) so as all trajectories gathered together into one cluster had the average position and the average properties of the cluster.

	δz[dam]	$\delta q[\frac{g}{kg}]$	δPV[PVU]	$\delta\theta$[K]	$\delta\theta_e$[K]	δh[dam]	$\delta Q_{TOT}[\frac{kg}{m^2h}]$
1	35 (29)	-0.47 (0.49)	0.01 (0.02)	1.30 (0.89)	0.01 (0.72)	60 (19)	-0.015
2	15 (19)	-0.07 (0.10)	0.01 (0.02)	0.36 (0.56)	0.16 (0.58)	11 (26)	-0.002
3	32 (45)	0.22 (0.39)	0.06 (0.09)	-0.30 (0.94)	0.29 (0.32)	8 (10)	0.008
4	33 (52)	0.44 (0.34)	0.01 (0.05)	-0.48 (0.31)	0.85 (0.94)	-35 (15)	0.008
5	-42 (53)	0.06 (0.66)	-0.05 (0.09)	0.14 (0.83)	0.36 (2.10)	29 (19)	0.002
6	-12 (55)	0.33 (0.55)	-0.02 (0.05)	-0.34 (1.19)	0.60 (1.57)	-4 (22)	0.011
7	-1 (6)	0.23 (1.16)	0.12 (0.07)	-0.35 (0.52)	0.30 (2.71)	2 (15)	0.003
8	-	-	-	-	-	-	-
9	-	-	-	-	-	-	-
10	-	-	-	-	-	-	-
11	-13 (88)	-0.29 (3.87)	-0.10 (0.01)	0.77 (9.64)	-0.03 (1.25)	-18 (19)	-0.002
12	-46 (52)	-0.12 (0.03)	-0.10 (0.00)	-3.42 (2.00)	-3.90 (1.98)	26 (13)	-0.001

Table 8.20: The same quantities shown in Tab.4.6 are reported for the first phase of the event of November 2002. In the present table data have been computed starting from the cluster trajectories (obtained using the "final geographical clustering" algorithm) so as all trajectories gathered together into one cluster had the average position and the average properties of the cluster.

quantity	cluster 1	cluster 2	cluster 3	cluster 4	cluster 5	averadge
$\overline{t}_q$	78	3	7	6	7	22
deltaq1	-0.55	-2.02	-0.46	-1.68	-3.99	-1.13
deltaq2	-0.67	-0.01	-0.20	-0.01	0.73	-0.20
$\overline{t}_z$	0	0	5	5	2	3
deltaz1	0	0	236	134	192	129
deltaz2	23	-1640	-1492	-1011	-1300	-993
$\overline{t}_T$	96	73	9	8	8	33
deltaT1	1.7	0.8	2.3	2.4	5.0	2.2
deltaT2	-0.1	3.0	-5.6	-1.9	-2.1	-2.3
$\overline{t}_{Te}$	78	2	121	1	22	57
deltaTe1	-1.5	-0.2	0.3	0.8	-3.8	-0.1
deltaTe2	1.5	9.3	-4.4	2.8	8.7	0.9
$\overline{t}_{RH}$	1	52	65	51	55	45
deltaRH1	0	23	64	48	39	41
deltaRH2	-11	-18	-27	-14	-12	-18
$\overline{t}_{PV}$	1	12	16	37	70	21
deltaPV1	0.00	0.01	0.11	0.33	0.47	0.17
deltaPV2	-0.14	-0.27	-0.17	-0.18	-0.24	-0.18

Table 8.21: "Final geographical clustering" applied to the first phase of 2002 event. For each variable and for each cluster $\overline{t}$ is reported as well as the variation in the values of that variable (for each cluster) from the ending time to $\overline{t}$ and from this $\overline{t}$ to the starting time (see section 6.1.4 for details). In the last column there is the weighted average over the cluster population.

	N_k	$\overline{z}$[dam]	$\overline{q}[\frac{g}{kg}]$	$\overline{PV}$[PVU]	$\overline{\theta}$[K]	$\overline{\theta_e}$[K]	$\overline{h}$[dam]	t[h]
1	2760	358 (124)	3.35 (1.78)	0.41 (0.14)	302.3 (4.8)	312.6 (1.1)	77 (13)	2 (2)
2	2760	327 (146)	3.66 (2.04)	0.40 (0.13)	301.3 (5.5)	312.5 (1.2)	34 (16)	1 (5)
3	2760	294 (159)	3.64 (1.80)	0.36 (0.08)	301.2 (4.9)	312.3 (1.2)	22 (5)	11 (11)
4	1733	375 (116)	2.20 (0.97)	0.29 (0.03)	304.5 (3.2)	311.6 (1.1)	13 (5)	13 (2)
5	2760	312 (133)	2.83 (1.51)	0.36 (0.05)	303.2 (5.4)	312.0 (4.7)	21 (20)	18 (24)
6	2760	271 (137)	2.90 (1.32)	0.29 (0.02)	302.2 (4.3)	311.2 (1.6)	57 (20)	32 (27)
7	1027	109 (11)	5.11 (0.19)	0.34 (0.15)	296.8 (1.4)	312.1 (2.0)	40 (2)	6 (19)
8	-	-	-	-	-	-	-	-
9	-	-	-	-	-	-	-	-
10	-	-	-	-	-	-	-	-
11	850	483 (175)	1.52 (2.64)	0.39 (0.11)	303.8 (6.0)	308.6 (7.9)	11 (11)	72 (27)
12	883	230 (2)	2.20 (0.62)	0.35 (0.02)	306.9 (1.7)	314.1 (0.1)	31 (14)	72 (30)

Table 8.22: The same quantities shown in Tab.4.5 are reported for the first phase of the event of November 2002. In the present table data have been computed starting from the cluster trajectories (obtained using the "initial geographical clustering" algorithm) so as all trajectories gathered together into one cluster had the average position and the average properties of the cluster.

	δz[dam]	$\delta q[\frac{g}{kg}]$	δPV[PVU]	$\delta\theta$[K]	$\delta\theta_e$[K]	δh[dam]	$\delta Q_{TOT}[\frac{kg}{m^2h}]$
1	34 (26)	-0.45 (0.25)	0.01 (0.01)	1.28 (0.77)	0.05 (0.23)	60 (16)	-0.015
2	15 (19)	-0.08 (0.09)	0.00 (0.01)	0.35 (0.57)	0.11 (0.61)	11 (27)	-0.002
3	33 (47)	0.22 (0.40)	0.06 (0.08)	-0.27 (0.92)	0.33 (0.35)	8 (9)	0.008
4	32 (52)	0.42 (0.39)	0.01 (0.05)	-0.48 (0.31)	0.77 (1.07)	-35 (15)	0.007
5	-41 (53)	0.09 (0.76)	-0.03 (0.08)	0.20 (1.04)	0.51 (2.70)	28 (19)	0.003
6	-13 (60)	0.28 (0.55)	-0.03 (0.06)	-0.39 (1.29)	0.40 (1.39)	-4 (22)	0.010
7	-1 (3)	0.28 (1.09)	0.14 (0.08)	-0.40 (0.44)	0.38 (2.57)	3 (16)	0.004
8	-	-	-	-	-	-	-
9	-	-	-	-	-	-	-
10	-	-	-	-	-	-	-
11	-13 (86)	-0.24 (3.92)	-0.10 (0.01)	0.75 (9.66)	0.09 (1.45)	-17 (19)	-0.002
12	-46 (52)	-0.12 (0.03)	-0.10 (0.00)	-3.42 (2.00)	-3.90 (1.98)	26 (13)	-0.001

Table 8.23: The same quantities shown in Tab.4.6 are reported for the first phase of the event of November 2002. In the present table data have been computed starting from the cluster trajectories (obtained using the "initial geographical clustering" algorithm) so as all trajectories gathered together into one cluster had the average position and the average properties of the cluster.

quantity	cluster 1	cluster 2	cluster 3	cluster 4	cluster 5	averadge
$\overline{t}_q$	78	3	7	7	46	23
deltaq1	-0.55	-2.02	-0.46	-1.83	-5.94	-1.17
deltaq2	-0.67	-0.01	-0.20	0.02	5.25	-0.14
$\overline{t}_z$	0	0	5	3	6	3
deltaz1	0	0	236	136	178	128
deltaz2	23	-1640	-1492	-1029	-892	-990
$\overline{t}_T$	96	73	9	8	119	34
deltaT1	1.7	0.8	2.3	2.7	4.8	2.2
deltaT2	-0.1	3.0	-5.6	-2.3	4.9	-2.4
$\overline{t}_{Te}$	78	2	121	1	46	57
deltaTe1	-1.5	-0.2	0.3	0.6	-6.4	-0.1
deltaTe2	1.5	9.3	-4.4	2.8	21.9	0.9
$\overline{t}_{RH}$	1	52	65	47	121	44
deltaRH1	0	23	64	50	29	41
deltaRH2	-11	-18	-27	-16	0	-18
$\overline{t}_{PV}$	1	12	16	67	61	32
deltaPV1	0.00	0.01	0.11	0.33	0.31	0.16
deltaPV2	-0.14	-0.27	-0.17	-0.16	-0.59	-0.17

Table 8.24: "Initial geographical clustering" applied to the first phase of 2002 event. For each variable and for each cluster $\overline{t}$ is reported as well as the variation in the values of that variable (for each cluster) from the ending time to $\overline{t}$ and from this $\overline{t}$ to the starting time (see section 6.1.4 for details). In the last column there is the weighted average over the cluster population.

	N_k	$\overline{z}$[dam]	$\overline{q}[\frac{g}{kg}]$	$\overline{PV}$[PVU]	$\overline{\theta}$[K]	$\overline{\theta_e}$[K]	$\overline{h}$[dam]	t[h]
1	2760	358 (125)	3.36 (1.80)	0.41 (0.14)	302.3 (4.9)	312.6 (1.3)	77 (12)	2 (3)
2	2403	301 (129)	4.00 (1.82)	0.42 (0.12)	300.4 (4.9)	312.5 (1.3)	36 (18)	1 (5)
3	2760	295 (159)	3.63 (1.79)	0.37 (0.09)	301.2 (4.9)	312.3 (1.2)	22 (5)	10 (10)
4	2039	338 (127)	2.73 (1.39)	0.31 (0.11)	303.3 (3.7)	311.9 (1.2)	16 (10)	12 (3)
5	2760	316 (127)	2.85 (1.50)	0.36 (0.05)	303.2 (5.0)	312.0 (4.3)	21 (20)	17 (26)
6	2760	273 (134)	2.93 (1.29)	0.29 (0.04)	302.2 (4.3)	311.3 (1.5)	58 (19)	30 (26)
7	925	101 (6)	5.12 (0.53)	0.31 (0.22)	296.5 (1.8)	311.7 (2.5)	34 (10)	8 (18)
8	30	189 (110)	4.57 (1.27)	0.53 (0.16)	295.9 (3.7)	309.3 (0.3)	18 (9)	3 (61)
9	-)	-)	-)	-)	-)	-)	-)	-)
10	-)	-)	-)	-)	-)	-)	-)	-)
11	879	475 (176)	1.63 (2.68)	0.38 (0.08)	304.1 (5.3)	309.2 (6.2)	12 (12)	73 (25)
12	956	222 (6)	2.33 (0.49)	0.34 (0.01)	306.4 (1.1)	313.9 (0.3)	32 (13)	74 (32)

Table 8.25: The same quantities shown in Tab.4.5 are reported for the first phase of the event of November 2002. In the present table data have been computed starting from the cluster trajectories (obtained using the "direct clustering" algorithm) so as all trajectories gathered together into one cluster had the average position and the average properties of the cluster.

	δz[dam]	$\delta q[\frac{g}{kg}]$	δPV[PVU]	$\delta\theta$[K]	$\delta\theta_e$[K]	δh[dam]	$\delta Q_{TOT}[\frac{kg}{m^2 h}]$
1	34 (29)	-0.46 (0.39)	0.01 (0.03)	1.29 (0.92)	0.03 (0.52)	59 (17)	-0.015
2	16 (20)	-0.07 (0.17)	0.01 (0.01)	0.38 (0.54)	0.19 (0.61)	11 (26)	-0.002
3	33 (45)	0.19 (0.56)	0.05 (0.10)	-0.21 (0.96)	0.29 (0.95)	13 (8)	0.007
4	29 (51)	0.40 (0.33)	0.02 (0.07)	-0.47 (0.30)	0.70 (0.82)	-32 (13)	0.009
5	-36 (51)	0.04 (0.69)	-0.05 (0.10)	0.08 (0.81)	0.24 (2.00)	27 (18)	0.001
6	-13 (66)	0.26 (0.47)	-0.02 (0.10)	-0.44 (1.35)	0.28 (1.16)	-4 (22)	0.009
7	0 (3)	0.29 (1.08)	0.15 (0.10)	-0.38 (0.48)	0.43 (2.53)	2 (16)	0.003
8	-8 (10)	0.06 (0.04)	0.01 (0.01)	-0.01 (0.53)	0.18 (0.63)	-3 (8)	0.000
9	-	-	-	-	-	-	-
10	-	-	-	-	-	-	-
11	-10 (128)	-0.08 (4.18)	-0.11 (0.05)	0.95 (10.03)	0.73 (2.77)	-17 (18)	0.000
12	-55 (61)	-0.05 (0.10)	-0.09 (0.01)	-2.93 (1.50)	-3.18 (1.27)	25 (12)	-0.001

Table 8.26: The same quantities shown in Tab.4.6 are reported for the first phase of the event of November 2002. In the present table data have been computed starting from the cluster trajectories (obtained using the "direct clustering" algorithm) so as all trajectories gathered together into one cluster had the average position and the average properties of the cluster.

quantity	cluster 1	cluster 2	cluster 3	cluster 4	cluster 5	cluster 6	cluster 7	averadge
$\overline{t}_q$	25	7	10	78	32	8	7	16
deltaq1	-1.76	-3.29	-0.42	-4.42	-0.29	-0.65	-0.74	-0.94
deltaq2	1.86	5.54	0.40	1.84	1.81	1.87	0.57	1.26
$\overline{t}_z$	4	2	2	8	0	2	5	4
deltaz1	12	18	3	26	0	15	23	15
deltaz2	-67	-219	-91	-16	-137	-133	-143	-120
$\overline{t}_T$	8	8	10	96	33	8	9	17
deltaT1	1.5	5.6	1.7	9.9	2.9	2.9	2.3	2.8
deltaT2	-1.6	-4.7	-2.6	-0.3	-1.1	-2.3	-5.1	-3.0
$\overline{t}_{Te}$	43	6	79	65	2	1	121	60
deltaTe1	-3.4	-3.0	0.3	-3.0	2.2	1.3	0.1	0.2
deltaTe2	3.7	10.6	-1.3	5.1	4.4	2.9	-3.5	0.6
$\overline{t}_{RH}$	67	55	33	1	52	42	67	50
deltaRH1	34	47	8	0	14	54	65	42
deltaRH2	-11	-16	-12	-24	-8	-20	-27	-19
$\overline{t}_{PV}$	70	81	2	4	12	37	16	23
deltaPV1	0.33	0.56	0.00	0.02	0.02	0.43	0.13	0.19
deltaPV2	-0.17	-0.27	-0.08	-0.31	-0.22	-0.25	-0.18	-0.20

Table 8.27: "Direct clustering" applied to the first phase of 2002 event. For each variable and for each cluster $\overline{t}$ is reported as well as the variation in the values of that variable (for each cluster) from the ending time to $\overline{t}$ and from this $\overline{t}$ to the starting time (see section 6.1.4 for details). In the last column there is the weighted average over the cluster population.

8.4 Cluster analysis of the second phase of 2002 event

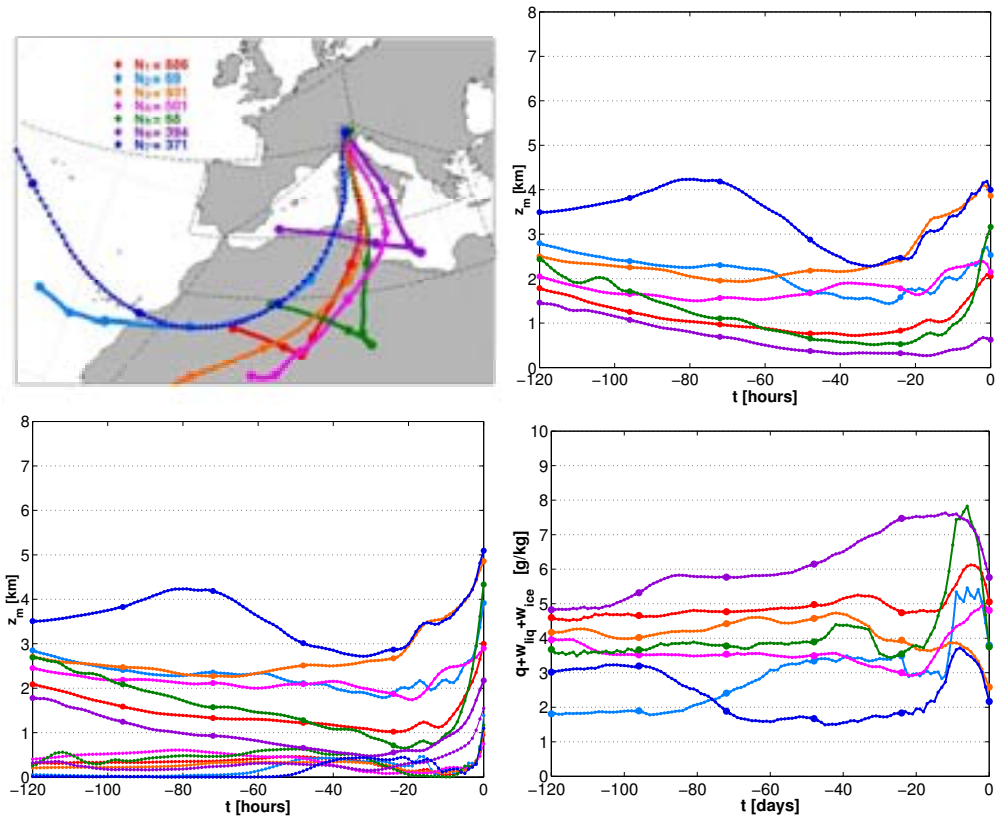

Figure 8.7: Clusters of trajectories arriving over Trentino in the period from 25/11/02 21 UTC to 26/11/02 15 UTC obtained from the "direct clustering" algorithm. In the first plot each curve is the average, in the physical space, of all trajectories belonging to that cluster. The average position every 1 hour is marked by a small circle, the position every 24 hours by a big one. The number of trajectories for each cluster is reported. In the following plots there are respectivelly the average height of the clusters above the surface, the average height above the mean sea level of the cluster (and of the terrain beneath them) and the average water concentration.

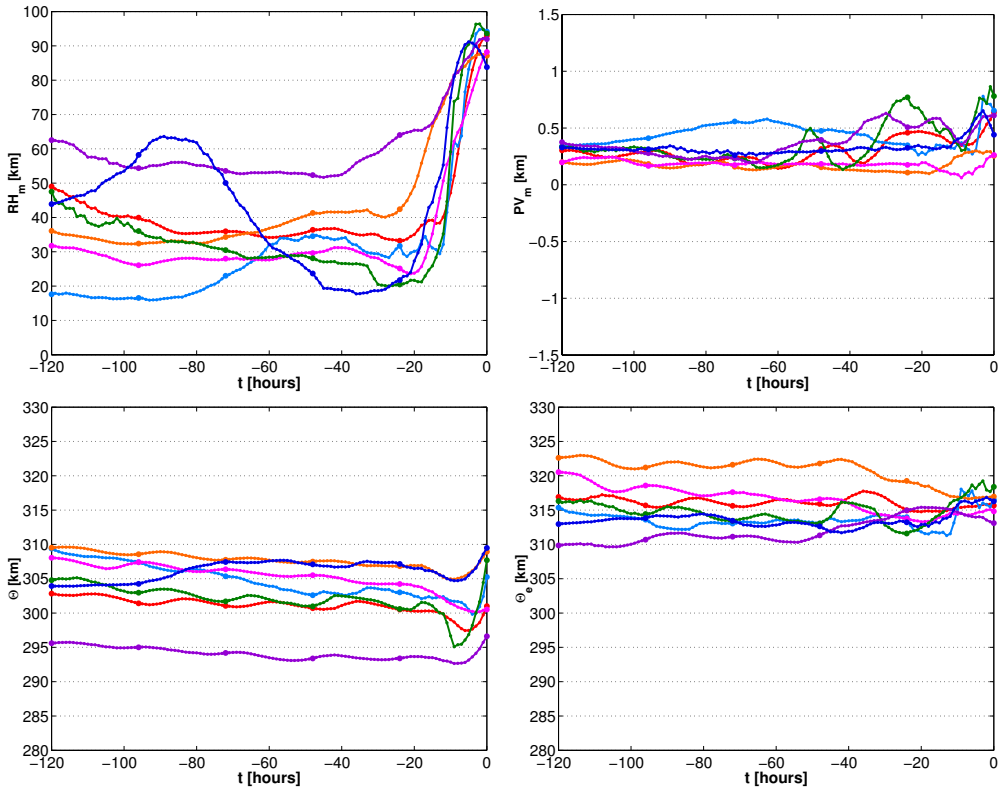

Figure 8.8: Clusters of trajectories arriving over Trentino in the period from 25/11/02 21 UTC to 26/11/02 15 UTC obtained from the "direct clustering" algorithm. In the plots there are the average relative humidity, the average potential vorticity, the average potential temperature and the average equivalent potential temperature of the clusters. The clusters have been marked by different colors and circles of different size according to figure 8.1.

	N_k	$\overline{z}$[dam]	$\overline{q}[\frac{g}{kg}]$	$\overline{PV}$[PVU]	$\overline{\theta}$[K]	$\overline{\theta_e}$[K]	$\overline{h}$[dam]	t[h]
1	3220	351 (118)	4.11 (1.49)	0.43 (0.14)	303.2 (5.0)	315.8 (1.0)	77 (17)	2 (2)
2	3220	304 (139)	4.66 (1.72)	0.39 (0.16)	301.7 (5.4)	315.9 (1.1)	33 (17)	2 (6)
3	3220	238 (131)	4.63 (1.33)	0.36 (0.15)	301.5 (4.2)	315.6 (1.1)	15 (4)	15 (5)
4	340	350 (53)	2.54 (0.79)	0.34 (0.02)	305.7 (2.8)	313.8 (0.5)	26 (1)	2 (25)
5	340	377 (70)	1.77 (1.06)	0.26 (0.06)	307.4 (0.8)	313.2 (2.4)	4 (3)	36 (21)
6	3220	191 (86)	4.16 (1.06)	0.26 (0.12)	301.9 (4.6)	314.7 (2.7)	31 (8)	16 (19)
7	3220	210 (116)	4.09 (1.23)	0.28 (0.17)	302.7 (4.1)	315.3 (1.6)	21 (9)	7 (19)
8	-	-	-	-	-	-	-	-
9	-	-	-	-	-	-	-	-
10	-	-	-	-	-	-	-	-
11	340	388 (74)	3.16 (1.89)	0.31 (0.04)	304.2 (1.3)	313.8 (4.4)	1 (1)	41 (34)
12	3220	193 (82)	4.16 (1.09)	0.22 (0.06)	304.0 (4.8)	316.9 (4.1)	36 (9)	66 (44)

Table 8.28: The same quantities shown in Tab.4.7 are reported for the second phase of the event of November 2002. In the present table data have been computed starting from the cluster trajectories (obtained using the "final geographical clustering" algorithm) so as all trajectories gathered together into one cluster had the average position and the average properties of the cluster.

	δz[dam]	$\delta q[\frac{g}{kg}]$	δPV[PVU]	$\delta\theta$[K]	$\delta\theta_e$[K]	δh[dam]	$\delta Q_{TOT}[\frac{kg}{m^2h}]$
1	51 (28)	-0.68 (0.47)	0.03 (0.09)	1.74 (1.16)	-0.13 (0.48)	59 (22)	-0.026
2	28 (32)	-0.24 (0.38)	0.03 (0.06)	0.72 (0.56)	0.03 (0.59)	16 (31)	-0.009
3	81 (93)	0.60 (0.64)	0.05 (0.23)	-0.94 (1.55)	0.73 (1.05)	13 (8)	0.024
4	3 (4)	0.44 (0.25)	0.02 (0.03)	-0.51 (0.86)	0.81 (0.10)	-18 (8)	0.001
5	-138 (148)	-1.05 (1.25)	0.02 (0.02)	0.32 (1.88)	-2.72 (1.67)	29 (1)	-0.003
6	-6 (46)	0.12 (0.50)	-0.05 (0.15)	-0.43 (0.74)	-0.09 (1.88)	-10 (8)	0.007
7	4 (28)	0.03 (0.42)	0.10 (0.15)	-0.45 (0.44)	-0.41 (1.11)	-7 (9)	0.002
8	-	-	-	-	-	-	-
9	-	-	-	-	-	-	-
10	-	-	-	-	-	-	-
11	84 (113)	-0.66 (4.38)	-0.07 (0.02)	3.33 (9.43)	1.73 (2.85)	-2 (1)	-0.002
12	-29 (36)	-0.04 (0.30)	0.02 (0.10)	-1.95 (2.19)	-2.10 (2.44)	9 (5)	-0.002

Table 8.29: The same quantities shown in Tab.4.8 are reported for the second phase of the event of November 2002. In the present table data have been computed starting from the cluster trajectories (obtained using the "final geographical clustering" algorithm) so as all trajectories gathered together into one cluster had the average position and the average properties of the cluster.

quantity	cluster 1	cluster 2	cluster 3	cluster 4	cluster 5	cluster 6	averadge
$\bar{t}_q$	40	3	7	10	67	9	27
deltaq1	-0.85	-0.63	-2.39	-4.25	-0.71	-0.50	-1.23
deltaq2	0.00	0.01	-0.03	-0.24	0.42	0.10	0.08
$\bar{t}_z$	4	8	4	3	7	3	5
deltaz1	264	93	151	360	202	235	196
deltaz2	-472	-280	-1340	-1949	-419	-750	-727
$\bar{t}_T$	8	3	7	10	9	121	19
deltaT1	1.9	0.3	3.1	14.9	-0.8	4.7	2.0
deltaT2	-1.2	-7.8	-4.3	-9.3	-3.0	1.5	-3.1
$\bar{t}_{Te}$	40	121	10	4	121	3	53
deltaTe1	-4.2	-0.3	-0.2	1.6	-6.2	-0.1	-2.4
deltaTe2	1.4	-6.5	2.3	2.2	-0.9	3.5	0.4
$\bar{t}_{RH}$	82	21	57	31	103	34	65
deltaRH1	63	66	51	71	56	66	59
deltaRH2	-8	-9	-18	-37	-3	-29	-13
$\bar{t}_{PV}$	35	10	64	43	24	70	41
deltaPV1	0.36	0.21	0.38	0.61	0.07	0.21	0.28
deltaPV2	-0.08	-0.08	-0.15	-0.21	-0.09	-0.10	-0.10

Table 8.30: "Final geographical clustering" applied to the second phase of 2002 event. For each variable and for each cluster $\bar{t}$ is reported as well as the variation in the values of that variable (for each cluster) from the ending time to $\bar{t}$ and from this $\bar{t}$ to the starting time (see section 6.1.4 for details). In the last column there is the weighted average over the cluster population.

	N_k	$\overline{z}$[dam]	$\overline{q}[\frac{g}{kg}]$	$\overline{PV}$[PVU]	$\overline{\theta}$[K]	$\overline{\theta_e}$[K]	$\overline{h}$[dam]	t[h]
1	3220	351 (113)	4.11 (1.45)	0.43 (0.12)	303.1 (7.1)	315.7 (5.6)	78 (16)	2 (3)
2	3220	305 (136)	4.68 (1.72)	0.41 (0.11)	301.6 (7.5)	315.8 (5.6)	34 (19)	1 (6)
3	3220	239 (131)	4.64 (1.28)	0.35 (0.14)	301.4 (6.8)	315.5 (5.6)	16 (4)	15 (5)
4	340	350 (53)	2.54 (0.79)	0.34 (0.02)	305.7 (2.8)	313.8 (0.5)	26 (1)	2 (25)
5	344	373 (75)	1.85 (1.25)	0.26 (0.06)	307.2 (1.7)	313.2 (2.4)	3 (3)	36 (21)
6	3219	187 (87)	4.17 (1.04)	0.26 (0.10)	301.9 (4.5)	314.7 (2.5)	31 (8)	16 (19)
7	3219	205 (116)	4.07 (1.16)	0.28 (0.17)	302.8 (4.1)	315.3 (1.5)	20 (9)	6 (20)
8	-	-	-	-	-	-	-	-
9	-	-	-	-	-	-	-	-
10	-	-	-	-	-	-	-	-
11	340	388 (74)	3.16 (1.89)	0.31 (0.04)	304.2 (1.3)	313.8 (4.4)	1 (1)	41 (34)
12	3215	194 (80)	4.15 (1.03)	0.22 (0.05)	304.0 (4.8)	316.8 (4.1)	35 (9)	67 (44)

Table 8.31: The same quantities shown in Tab.4.7 are reported for the second phase of the event of November 2002. In the present table data have been computed starting from the cluster trajectories (obtained using the "initial geographical clustering" algorithm) so as all trajectories gathered together into one cluster had the average position and the average properties of the cluster.

	δz[dam]	$\delta q[\frac{g}{kg}]$	δPV[PVU]	$\delta\theta$[K]	$\delta\theta_e$[K]	δh[dam]	$\delta Q_{TOT}[\frac{kg}{m^2h}]$
1	51 (25)	-0.70 (0.41)	0.03 (0.09)	1.76 (0.84)	-0.17 (0.49)	58 (23)	-0.028
2	26 (28)	-0.25 (0.35)	0.03 (0.06)	0.77 (0.41)	0.07 (0.57)	15 (31)	-0.009
3	81 (91)	0.62 (0.45)	0.07 (0.22)	-1.06 (1.11)	0.65 (0.88)	15 (7)	0.025
4	3 (4)	0.44 (0.25)	0.02 (0.03)	-0.51 (0.86)	0.81 (0.10)	-18 (8)	0.002
5	-136 (147)	-1.04 (1.24)	0.02 (0.03)	0.32 (1.88)	-2.69 (1.67)	29 (3)	-0.004
6	-10 (43)	0.05 (0.55)	-0.05 (0.14)	-0.32 (0.80)	-0.18 (1.94)	-9 (6)	0.004
7	15 (30)	0.06 (0.36)	0.09 (0.16)	-0.44 (0.34)	-0.30 (0.86)	-6 (10)	0.003
8	-	-	-	-	-	-	-
9	-	-	-	-	-	-	-
10	-	-	-	-	-	-	-
11	84 (113)	-0.66 (4.38)	-0.07 (0.02)	3.33 (9.43)	1.73 (2.85)	-2 (1)	-0.002
12	-31 (37)	0.03 (0.24)	0.03 (0.11)	-2.06 (2.24)	-2.02 (2.19)	6 (6)	0.001

Table 8.32: The same quantities shown in Tab.4.8 are reported for the second phase of the event of November 2002. In the present table data have been computed starting from the cluster trajectories (obtained using the "initial geographical clustering" algorithm) so as all trajectories gathered together into one cluster had the average position and the average properties of the cluster.

quantity	cluster 1	cluster 2	cluster 3	cluster 4	cluster 5	cluster 6	averadge
$\bar{t}_q$	7	58	7	31	67	9	18
deltaq1	-0.62	0.00	-2.50	-0.49	-0.71	-0.50	-1.17
deltaq2	0.04	0.00	-0.03	-3.41	0.42	0.10	0.09
$\bar{t}_z$	8	0	4	0	7	3	6
deltaz1	213	-4	162	0	202	235	198
deltaz2	-462	1412	-1394	1234	-419	-750	-753
$\bar{t}_T$	7	121	7	28	9	121	19
deltaT1	3.6	1.1	3.5	3.4	-0.8	4.7	2.9
deltaT2	-5.5	6.5	-4.4	-3.1	-3.0	1.5	-4.0
$\bar{t}_{Te}$	121	68	4	117	121	3	74
deltaTe1	0.1	-14.3	-0.2	-6.4	-6.2	-0.1	-1.2
deltaTe2	-4.2	19.1	2.4	-2.0	-0.9	3.5	-0.8
$\bar{t}_{RH}$	85	22	57	67	103	34	75
deltaRH1	62	53	51	71	56	66	58
deltaRH2	-7	-49	-18	-48	-3	-29	-12
$\bar{t}_{PV}$	34	1	64	13	24	70	45
deltaPV1	0.29	0.00	0.39	0.51	0.07	0.21	0.27
deltaPV2	-0.06	-0.57	-0.15	-0.64	-0.09	-0.10	-0.10

Table 8.33: "Initial geographical clustering" applied to the second phase of 2002 event. For each variable and for each cluster $\bar{t}$ is reported as well as the variation in the values of that variable (for each cluster) from the ending time to $\bar{t}$ and from this $\bar{t}$ to the starting time (see section 6.1.4 for details). In the last column there is the weighted average over the cluster population.

	N_k	$\overline{z}$[dam]	$\overline{q}[\frac{g}{kg}]$	$\overline{PV}$[PVU]	$\overline{\theta}$[K]	$\overline{\theta_e}$[K]	$\overline{h}$[dam]	t[h]
1	3220	350 (117)	4.13 (1.47)	0.44 (0.17)	303.1 (5.0)	315.8 (1.1)	77 (19)	2 (3)
2	3151	277 (145)	4.93 (1.73)	0.41 (0.15)	300.8 (5.6)	315.7 (1.4)	31 (17)	2 (6)
3	3220	237 (122)	4.64 (1.29)	0.34 (0.14)	301.5 (4.1)	315.6 (1.1)	15 (5)	14 (5)
4	834	251 (96)	3.71 (1.13)	0.34 (0.02)	300.6 (5.3)	311.9 (2.4)	30 (7)	6 (21)
5	440	349 (63)	1.84 (0.99)	0.31 (0.13)	307.2 (0.6)	313.2 (2.4)	4 (3)	42 (17)
6	2826	209 (82)	3.85 (0.94)	0.27 (0.15)	304.3 (2.7)	316.4 (2.4)	26 (7)	10 (22)
7	3220	212 (103)	3.97 (1.01)	0.28 (0.15)	302.7 (4.1)	315.0 (2.4)	17 (12)	13 (25)
8	-	-	-	-	-	-	-	-
9	-	-	-	-	-	-	-	-
10	-	-	-	-	-	-	-	-
11	371	379 (64)	3.02 (2.03)	0.31 (0.04)	304.5 (1.7)	313.7 (4.5)	1 (1)	39 (36)
12	2826	211 (50)	3.96 (0.99)	0.22 (0.07)	305.4 (3.2)	317.8 (3.6)	37 (9)	77 (50)

Table 8.34: The same quantities shown in Tab.4.7 are reported for the second phase of the event of November 2002. In the present table data have been computed starting from the cluster trajectories (obtained using the "direct clustering" algorithm) so as all trajectories gathered together into one cluster had the average position and the average properties of the cluster.

	δz[dam]	$\delta q[\frac{g}{kg}]$	δPV[PVU]	$\delta\theta$[K]	$\delta\theta_e$[K]	δh[dam]	$\delta Q_{TOT}[\frac{kg}{m^2 h}]$
1	51 (32)	-0.71 (0.59)	0.03 (0.09)	1.78 (1.31)	-0.19 (0.52)	59 (26)	-0.026
2	25 (30)	-0.23 (0.38)	0.03 (0.06)	0.61 (0.65)	-0.03 (0.70)	15 (31)	-0.009
3	78 (87)	0.65 (0.94)	0.07 (0.12)	-0.99 (1.93)	0.82 (1.38)	14 (7)	0.025
4	-10 (15)	0.23 (0.21)	-0.01 (0.03)	-0.33 (0.69)	0.35 (0.70)	-12 (17)	0.002
5	-120 (133)	-0.60 (1.18)	0.04 (0.07)	-0.73 (2.43)	-2.42 (1.39)	28 (3)	-0.002
6	16 (32)	-0.25 (0.29)	0.06 (0.10)	-0.72 (0.56)	-1.50 (1.13)	-17 (10)	-0.008
7	2 (45)	0.22 (0.66)	0.02 (0.07)	-0.45 (0.62)	0.13 (1.35)	-2 (7)	0.009
8	-	-	-	-	-	-	-
9	-	-	-	-	-	-	-
10	-	-	-	-	-	-	-
11	72 (101)	-0.51 (4.52)	-0.04 (0.04)	2.63 (10.12)	1.42 (2.53)	-1 (1)	-0.002
12	-45 (65)	0.11 (0.51)	-0.03 (0.06)	-1.83 (1.79)	-1.53 (2.22)	7 (6)	0.004

Table 8.35: The same quantities shown in Tab.4.8 are reported for the second phase of the event of November 2002. In the present table data have been computed starting from the cluster trajectories (obtained using the "direct clustering" algorithm) so as all trajectories gathered together into one cluster had the average position and the average properties of the cluster.

quantity	cluster 1	cluster 2	cluster 3	cluster 4	cluster 5	cluster 6	cluster 7	averadge
$\overline{t}_q$	6	7	43	3	7	13	9	17
deltaq1	-1.26	-1.89	-2.27	-0.19	-4.33	-2.08	-1.63	-1.60
deltaq2	1.50	3.65	0.56	0.91	4.01	2.80	0.69	1.30
$\overline{t}_z$	4	3	7	8	3	2	3	5
deltaz1	19	21	26	8	34	16	24	20
deltaz2	-96	-106	-44	-35	-175	-119	-79	-74
$\overline{t}_T$	7	5	10	4	10	10	115	20
deltaT1	3.5	4.1	1.3	0.3	11.6	3.6	4.8	2.7
deltaT2	-5.4	-8.2	-1.9	-7.9	-8.7	-2.6	0.8	-3.8
$\overline{t}_{Te}$	37	10	115	121	4	21	3	65
deltaTe1	0.1	-1.3	-5.4	-0.2	-0.3	-2.0	-0.1	-1.8
deltaTe2	-1.4	2.4	-0.2	-5.5	2.3	5.2	3.4	-0.2
$\overline{t}_{RH}$	25	94	99	22	28	46	37	51
deltaRH1	60	78	55	65	74	40	66	58
deltaRH2	-16	-2	-4	-8	-27	-11	-26	-12
$\overline{t}_{PV}$	61	22	19	10	43	68	70	42
deltaPV1	0.49	0.39	0.16	0.20	0.65	0.42	0.18	0.31
deltaPV2	-0.16	-0.08	-0.10	-0.14	-0.20	-0.18	-0.07	-0.13

Table 8.36: "Direct clustering" applied to the second phase of 2002 event. For each variable and for each cluster $\overline{t}$ is reported as well as the variation in the values of that variable (for each cluster) from the ending time to $\overline{t}$ and from this $\overline{t}$ to the starting time (see section 6.1.4 for details). In the last column there is the weighted average over the cluster population.

8.5 Budget analysis over the initial phase of the 1966 event

	N_k	$\overline{z}$[dam]	$\overline{q}[\frac{g}{kg}]$	$\overline{PV}$[PVU]	$\overline{\theta}$[K]	$\overline{\theta_e}$[K]	$\overline{h}$[dam]	t[h]
1	2760	363 (133)	3.04 (1.47)	0.48 (0.18)	299.5 (6.4)	308.8 (4.3)	77 (22)	2 (2)
2	1920	259 (140)	4.30 (1.65)	0.48 (0.26)	295.9 (6.6)	308.7 (4.7)	31 (11)	6 (13)
3	2509	202 (125)	4.77 (1.56)	0.36 (0.20)	295.0 (5.3)	309.2 (4.3)	14 (7)	16 (14)
4	2488	218 (78)	3.47 (2.03)	0.41 (0.18)	295.0 (5.2)	305.4 (7.4)	19 (13)	15 (10)
5	418	219 (43)	2.43 (1.652)	0.47 (0.14)	300.2 (2.8)	307.8 (6.8)	7 (11)	28 (24)
6	1779	172 (50)	4.00 (1.49)	0.22 (0.17)	297.5 (3.5)	309.7 (6.3)	53 (23)	32 (22)
7	913	115 (52)	4.57 (0.96)	0.18 (0.15)	293.8 (3.5)	307.4 (5.0)	34 (27)	11 (11)
8	1675	286 (107)	1.36 (1.01)	0.55 (0.25)	294.6 (6.9)	298.8 (5.1)	45 (18)	18 (11)
9	1475	405 (149)	1.19 (0.95)	0.61 (0.23)	296.4 (7.4)	300.2 (5.8)	35 (25)	19 (11)
10	398	280 (145)	2.13 (1.28)	0.60 (0.24)	290.5 (8.0)	296.9 (6.7)	41 (26)	20 (16)
11	979	510 (98)	0.58 (0.41)	0.59 (0.13)	301.4 (3.3)	303.4 (3.4)	7 (5)	19 (16)
12	698	131 (38)	4.64 (0.43)	0.17 (0.18)	300.0 (2.6)	314.2 (3.2)	42 (7)	42 (27)

Table 8.37: 1966 - First phase (03/11/1966 03UTC - 03/11/1966 18UTC): evaporation from area 6.

	δz[dam]	δq[g kg^{-1}]	δPV[PVU]	$\delta\theta$[K]	$\delta\theta_e$[K]	δoro[dam]	δQ_{TOT}[kg m^{-2}h^{-1}]
1	32 (28)	-0.44 (0.40)	-0.01 (0.17)	1.38 (1.28)	0.14 (1.38)	47 (31)	-0.017
2	45 (28)	-0.47 (0.75)	0.00 (0.19)	1.15 (1.62)	-0.16 (2.33)	15 (15)	-0.013
3	95 (76)	-0.42 (1.64)	0.14 (0.33)	2.34 (2.73)	1.20 (3.49)	16 (16)	-0.010
4	37 (95)	0.26 (1.38)	0.02 (0.24)	0.63 (2.83)	1.43 (4.24)	-15 (33)	0.014
5	-12 (42)	0.49 (1.20)	-0.06 (0.14)	-0.41 (2.51)	1.01 (3.40)	25 (19)	0.002
6	-19 (84)	0.89 (1.25)	-0.03 (0.26)	-1.47 (2.99)	1.07 (4.07)	0 (33)	0.028
7	-26 (23)	0.82 (1.12)	0.04 (0.10)	0.52 (1.18)	2.86 (7.03)	-16 (16)	0.013
8	-99 (81)	0.32 (0.52)	-0.14 (0.37)	-0.30 (2.00)	0.63 (2.67)	-8 (31)	0.008
9	-70 (70)	0.06 (0.42)	0.01 (0.36)	-2.76 (3.22)	-2.61 (2.63)	7 (23)	0.001
10	-3 (44)	-0.12 (0.92)	0.02 (0.36)	-1.09 (3.26)	-1.47 (4.15)	19 (27)	-0.001
11	-61 (67)	0.05 (0.34)	0.01 (0.19)	-1.12 (1.82)	-0.95 (5.47)	5 (20)	0.001
12	0 (54)	0.71 (0.78)	-0.11 (0.42)	0.97 (3.81)	3.11 (4.43)	5 (17)	0.007

Table 8.38: 1966 - First phase (03/11/1966 03UTC - 03/11/1966 18UTC): evaporation from area 6.

8.6 Budget analysis over the final phase of the 1966 event

	N_k	$\overline{z}$[dam]	$\overline{q}[\frac{g}{kg}]$	$\overline{PV}$[PVU]	$\overline{\theta}$[K]	$\overline{\theta_e}$[K]	$\overline{h}$[dam]	t[h]
1	1840	361 (140)	2.37 (1.96)	0.72 (0.41)	299.9 (6.7)	307.2 (6.6)	77 (20)	2 (2)
2	1264	316 (194)	3.49 (2.83)	0.68 (0.65)	298.6 (7.0)	309.1 (6.8)	29 (11)	3 (4)
3	1724	305 (181)	3.41 (2.72)	0.75 (0.53)	297.3 (6.1)	307.5 (6.0)	16 (8)	9 (8)
4	1780	311 (200)	2.62 (2.37)	0.80 (0.70)	294.8 (6.6)	302.6 (4.6)	14 (12)	16 (12)
5	611	357 (147)	1.31 (1.25)	0.84 (0.55)	296.5 (4.7)	300.6 (4.1)	2 (4)	12 (11)
6	346	270 (196)	3.14 (2.41)	0.74 (0.57)	297.7 (6.8)	307.0 (4.8)	54 (18)	26 (21)
7	360	250 (184)	3.70 (2.54)	0.65 (0.51)	297.7 (6.0)	308.8 (3.7)	38 (26)	13 (18)
8	1745	410 (205)	1.36 (1.46)	1.07 (1.03)	295.6 (6.9)	299.8 (5.1)	48 (20)	17 (13)
9	992	490 (230)	1.03 (1.41)	1.16 (1.29)	296.8 (8.2)	299.9 (6.2)	29 (20)	15 (9)
10	87	778 (203)	0.23 (0.68)	2.02 (1.83)	307.2 (9.5)	308.0 (8.1)	29 (14)	22 (10)
11	1460	502 (227)	0.78 (1.17)	1.09 (1.00)	297.0 (8.8)	299.4 (7.0)	18 (22)	45 (24)
12	32	67 (25)	4.90 (0.55)	0.75 (0.59)	298.5 (2.5)	313.3 (3.8)	45 (10)	36 (20)

Table 8.39: 1966 - Third phase (04/11/1966 15UTC - 05/11/1966 00UTC): evaporation from area 4.

	δz[dam]	δq[g kg^{-1}]	δPV[PVU]	$\delta\theta$[K]	$\delta\theta_e$[K]	δoro[dam]	δQ_{TOT}[kg m^{-2}h^{-1}]
1	20 (30)	-0.43 (0.89)	-0.06 (0.18)	0.90 (1.52)	-0.28 (2.14)	49 (31)	-0.014
2	7 (17)	-0.07 (0.56)	-0.01 (0.18)	0.28 (0.84)	0.07 (1.72)	17 (11)	-0.001
3	49 (92)	-0.30 (1.34)	0.00 (0.32)	3.16 (4.78)	2.41 (3.11)	14 (14)	-0.006
4	-52 (83)	1.07 (1.29)	-0.23 (0.73)	0.06 (3.29)	3.19 (5.27)	-12 (26)	0.036
5	- 7 (39)	0.59 (0.93)	-0.03 (0.19)	-0.62 (1.91)	1.12 (2.83)	6 (8)	0.006
6	-52 (94)	0.59 (1.40)	-0.03 (0.69)	0.02 (3.71)	1.86 (5.23)	15 (24)	0.003
7	11 (67)	0.35 (1.84)	0.02 (0.46)	1.92 (2.43)	2.97 (4.73)	-17 (14)	0.003
8	- 1 (97)	-0.01 (1.05)	0.09 (0.62)	1.00 (3.18)	0.99 (2.80)	5 (35)	0.000
9	-13 (78)	-0.19 (0.69)	0.23 (0.91)	-1.07 (2.22)	-1.65 (2.40)	6 (26)	-0.004
10	-25 (81)	0.00 (0.07)	0.35 (1.93)	-0.31 (5.38)	-0.30 (5.31)	-34 (39)	0.000
11	-65 (158)	0.25 (1.06)	-0.19 (1.01)	0.25 (4.43)	1.02 (5.35)	-50 (103)	0.006
12	-4 (17)	-0.20 (0.71)	0.34 (0.95)	4.39 (3.77)	4.11 (4.85)	5 (13)	0.000

Table 8.40: 1966 - Third phase (04/11/1966 15UTC - 05/11/1966 00UTC): evaporation from area 4.

8.7 Budget analysis over the whole 2002 event

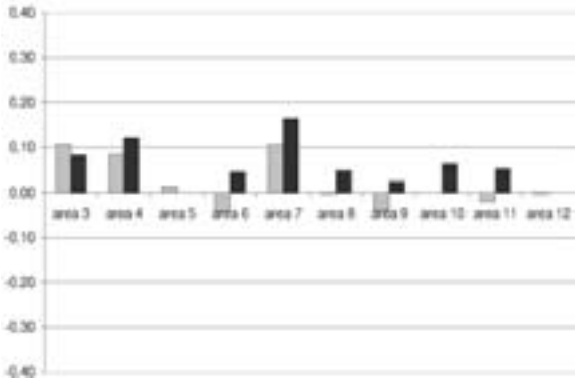

Figure 8.9: Average in time (over the period from 24/11/02 18 UTC to 26/11/02 18 UTC) and in space of evaporation over various areas (x-axis). Lagrangian specific humidity variation in $kg\,m^{-2}h^{-1}$ over various areas computed following the refined method of Eq. 4.18) for the whole event.

	N_k	$\overline{z}$[dam]	$\overline{q}[\frac{g}{kg}]$	$\overline{PV}$[PVU]	$\overline{\theta}$[K]	$\overline{\theta_e}$[K]	$\overline{h}$[dam]	t[h]
1	5980	354 (142)	3.80 (1.99)	0.43 (0.26)	302.6 (6.0)	314.3 (2.8)	64 (48)	3 (5)
2	4093	255 (157)	5.01 (2.31)	0.41 (0.29)	299.8 (6.4)	314.8 (3.3)	18 (10)	5 (11
3	5430	252 (154)	4.34 (1.99)	0.36 (0.26)	301.1 (5.3)	314.3 (3.0)	16 (10)	11 (7
4	3378	306 (150)	3.01 (1.56)	0.29 (0.16)	302.6 (5.2)	312.0 (3.1)	15 (12)	11 (6
5	3328	357 (155)	2.23 (1.82)	0.28 (0.14)	304.2 (7.0)	311.3 (6.3)	4 (8)	26 (15)
6	5632	246 (135)	3.35 (1.60)	0.28 (0.20)	303.4 (4.2)	313.9 (3.6)	48 (28)	13 (10
7	3514	191 (129)	4.18 (1.76)	0.35 (0.33)	302.1 (4.7)	314.9 (3.1)	27 (38)	8 (9)
8	615	301 (139)	3.30 (1.50)	0.37 (0.20)	299.3 (7.5)	309.4 (7.0)	29 (20)	8 (8)
9	481	404 (123)	2.72 (1.24)	0.40 (0.18)	303.5 (5.8)	312.1 (4.7)	40 (22)	3 (6)
10	-	-	-	-	-	-	-	-
11	1381	318 (70)	4.66 (1.48)	0.39 (0.12)	302.1 (3.8)	316.3 (3.8)	0 (1)	34 (16
12	4566	224 (99)	3.45 (1.88)	0.29 (0.15)	304.4 (5.3)	315.2 (4.3)	42 (11)	43 (23

Table 8.41: Table summarizing the number of trajectories flowing at least for one time step over the 12 macroareas of Fig. 4.16 during the whole event of November 2002. The average values (along with the respective variances) of the height above the surface, of the specific humidity, of the potential vorticity, of the potential temperature, of the equivalent potential temperature and of the height of the surface underneath are reported for the the air parcels staying over the various macroareas. The last column gives the average number of time steps spent by trajectories over each area.

	δz[dam]	$\delta q[\frac{g}{kg}]$	δPV[PVU]	$\delta\theta$[K]	$\delta\theta_e$[K]	δh[dam]	$\delta Q_{TOT}[\frac{kg}{m^2 h}]$
1	48 (54)	-0.71 (0.95)	0.01 (0.34)	1.62 (2.36)	-0.34 (1.98)	77 (65)	-0.037
2	23 (28)	0.02 (0.76)	0.04 (0.33)	0.58 (1.31)	0.65 (1.82)	-15 (26)	0.002
3	54 (70)	0.37 (1.34)	0.08 (0.42)	-0.68 (2.59)	0.34 (2.62)	17 (21)	0.020
4	15 (50)	0.38 (0.88)	-0.02 (0.22)	-0.42 (1.48)	0.69 (2.52)	-33 (35)	0.010
5	-67 (104)	0.48 (1.32)	0.01 (0.17)	-0.59 (2.93)	0.81 (4.90)	27 (20)	0.007
6	14 (64)	-0.11 (0.86)	0.05 (0.30)	-0.61 (1.63)	-0.95 (2.53)	1 (32)	-0.006
7	-3 (42)	0.52 (1.27)	0.02 (0.26)	-0.54 (1.28)	0.90 (3.33)	-10 (16)	0.019
8	-5 (44)	-0.07 (0.82)	0.00 (0.18)	-0.32 (1.48)	-0.52 (2.10)	5 (24)	0.000
9	31 (41)	-0.33 (0.56)	-0.02 (0.18)	1.22 (1.60)	0.28 (0.94)	70 (56)	-0.001
10	-	-	-	-	-	-	-
11	317 (131)	-4.63 (2.96)	-0.09 (0.28)	11.71 (6.21)	-1.09 (4.01)	0 (4)	-0.008
12	-42 (70)	-0.16 (1.09)	-0.04 (0.21)	-0.78 (2.69)	-1.24 (3.53)	10 (14)	-0.004

Table 8.42: The mean variations (as well as the respective variances) of the height of the trajectories in passing over various macroareas (Fig. 4.16) are reported for the whole event of November 2002. The same is done for the variations of the specific humidity, of the potential vorticity, of the potential temperature, of the equivalent potential temperature and of the height of the surface underneath of the parcels. The last column gives the quantity of water vapour (computed by the formula 4.6) gained or lost by all the trajectories over each area.

Bibliography

F. Apadula, A. Gott, A. Pigini, A. Longhetto, F. Rochett, C. Cassardo, S. Ferrarese, and R. Forza. Localization of source and sink regions of carbon dioxide through the method of the synoptic air trajectory statistics. *Atm. Env.*, 37:3757–3770, 2003.

L. L. Ashbaugh, W. C. Malm, and W. Z. Sadeh. A residence time probability analysis of sulfur concentrations at grand canyon national park. *Atm. Env.*, 19:1263–1270, 1985.

A. Avila and M. Alarcon. Relation between precipitation chemistry and meteorological situations at a rural site in ne spain. *Atm. Env.*, 33:1663–1677, 1999.

A. Ayalon, M. Bar-Matthews, and E. Sass. Rainfall-recharge relationships within a karstic terrain in the eastern mediterranean semi-arid region, israel: δ^{18}o and δd characteristics. *J. Hydrol.*, 207:18–31, 1998.

M. J. Bader, G. S. Forbes, J. R. Grant, R. B. Lilley, and A. Waters. In *Images in weather forecasting*. Cambridge University Press, 1990.

J. Baldini, F. McDermott, and I. J. Fairchild. Structure of the 8200-year cold event revealed by a speleothem trace element record. *Science*, 296:2203–2206, 2002.

K. Baumann and A. Stohl. Validation of a long-range trajectory model using gas balloon tracks from the gordon bennett cup 95. *J. Appl. Meteor.*, 36:711–720, 1997.

A. Bertò, A. Buzzi, and D. Zardi. Back-tracking water vapour contributing to a precipitation event over trentino: a case study. *Meteorol. Z.*, 13 (3):189–200, 2004.

C. Best and H. C. Hege. Visualizing and identifying conformational ensembles in molecular dynamics trajectories. *Computing in Science & Engineering*, (3):68–75, 2002.

J. Bjerknes. On the structure of moving cyclones. *Geofys. Pub.*, I (2):1–8, 1919.

P. Bougeault, P. Binder, A. Buzzi, R. Dirks, R. Houze, J. Kuettner, R. Smith, R. Steinacker, and H. Volkert. The map special observing period. *Bull. Am. Meteorol. Soc.*, 82:433–462, 2001.

A. J. Boyce. Mapping diversity: a comparatice study of some numerical methods. In A. J. Cole, editor, *Numerical Taxonomy*. Academic Press, 1969.

E. Brankov, S. T. Rao, and P. S. Porter. A trajectory clustering correlation methodology for examining the long-range transport of air pollutants. *Atm. Env.*, 32 (9):1525–1534, 1998.

K. A. Browning. Radar measurements of air motion near fronts - part two: Some categories of frontal air motion. *Weather*, 26:320–340, 1971.

K. A. Browning. Organization of clouds and precipitation in extratropical cyclones. In C. Newton and E. O. Holopainen, editors, *Extratropical cyclones - The Erik Palmen Memorial Volume*. American Meteorological Society, Boston, 1990.

K. A. Browning and J. Mason. Air motion and precipitation growth in frontal systems. *Pure Appl. Geophys.*, 119:577–593, 1981.

K. A. Browning and N. Roberts. Structure of a frontal cyclone. *Quart. J. Roy. Meteor. Soc.*, 120: 1535–1557, 1994.

K. A. Browning and N. Roberts. Variation of frontal and precipitation structure along a cold front. *Quart. J. Roy. Meteor. Soc.*, 122:1845–1872, 1996.

A. Buzzi and P. Alberoni. Analysis and numerical modelling of a frontal passage associated with thunderstorm development over the po valley and the adriatic sea. *Meteorol. Atmos. Phys.*, 48: 205–224, 1992.

A. Buzzi, M. D'Isidoro, and S. Davolio. A case study of an orographic cyclone south of the alps during the map sop. *Quart. J. Roy. Meteor. Soc.*, 129 B:1795–1818, 2003.

A. Buzzi and L. Foschini. Mesoscale meteorological features associated with heavy precipitation in the southern alpine region. *Meteorol. Atmos. Phys.*, 72:131–146, 2000.

A. Buzzi and P. Malguzzi. Modello meteorologico ad area limitata, manuale scientifico - bolam v.2. Bologna, 1998.

J. N. Cape, J. Methven, and L. E. Hudson. The use of trajectory cluster analysis to interpret trace gas measurements at mace head, ireland. *Atm. Env.*, 34:3651–3663, 2000.

T. N. Carlson. Airflow through midlatitude cyclones and the comma cloud pattern. *Mon. Wea. Rev.*, 108:1498–1509, 1980.

T. N. Carlson. *Mid-latitude weather systems*. HarperCollins Academic, 1991.

CIPRA. *Le changement climatique et les Alpes. Un rapport de synthèse.* AlpMedia rapport, 2002.

J. F. Clarke, T. L. Clark, J. K. Ching, P. L. Haagenson, R. B. Husar, and D. E. Patterson. Assessment of model simulation of long-distance transport. *Atm. Env.*, 12:2449–2462, 1983.

S. A. Clough, C. S. A. Davitt, and A. J. Thorpe. Attribution concepts applied to the omega equation. Joint Centre for Mesoscale Meteorology, Reading, UK, 1995.

J. L. Colin, D. Renard, V. Lescoat, J. L. Jaffrezo, M. J. Gros, and B. Strauss. Relationship between rain and snow acidity and air mass trajectory in eastern france. *Atm. Env.*, 23:1487–1498, 1989.

E. F. Danielsen. Trajectories: isobaric, isentropic and actual. *Journal of Meteorology*, 18:479–486, 1961.

E. F. Danielsen. Stratospheric source for unexpectedly large values of ozone measured over the pacific ocean during gametag, august 1977. *J. Geophys. Res.*, 85:401–412, 1980.

P. A. Dirmeyer and K. L. Brubacker. Contrasting evaporative moisture sources during the drought of 1998 and the of 1993. *J. Geophys. Res.*, 104:19383–19397, 1999.

S. R. Dorling and T. D. Davies. Extending cluster analysis - synoptic meteorology links to characterize chemical climates at six northwest european monitoring stations. *Atm. Env.*, 29:145–167, 1995.

S. R. Dorling, T. D. Davies, and C. E. Pierce. Cluster analysis: A technique for estimating the synoptic meteorlogical controls on air and precipitation chemistry - method and applications. *Atm. Env.*, 26A (14):2575–2581, 1992.

K. G. Doty and D. J. Perkey. Sensitivity of trajectory calculations to the temporal frequency of wind data. *Mon. Wea. Rev.*, 121:387–401, 1993.

W. H. Dove. Ueber das gesetz der stuerme. Berlin, 1840.

R. R. Draxler. Sensitivity of a trajectory model to the spatial and temporal resolution of the meteorological data during captex. *J. Climate Appl. Meteor.*, 26:1577–1588, 1987.

R. R. Draxler. The accuracy of trajectories during anatex calculated using dynamical model analyses versus rawinsonde observations. *J. Climate Appl. Meteor.*, 30:1446–1467, 1991.

R. R. Draxler. Trajectory optimization for balloon flight planning. *Weather and Forecasting*, 11: 111–114, 1996.

J. A. Dutton. Dover, New York, 1986.

G. Fea, A. Gazzola, and A. Cicala. *Prima documentazione generale della situazione meteorologica relativa alla grande alluvione del Novembre 1966*. 1968.

S. Ferrarese, A. Longhetto, C. Casssardo, F. Apadula, D. Bertoni, C. Giraud, and A. Gotti. A study of seasonal and yearly modulation of carbon dioxide sources and sinks, with a particular attention to the boreal atlantic ocean. *Atm. Env.*, 36:5517–5526, 2002.

A. H. Fink and P. Knippertz. An extreme precipitation event in southern morocco in spring 2002 and some hydrological implications. *Weather*, 58 (10):377–386, 2003.

R. Fitzroy. The weather book. a manual of practical meteorology. London, 1863.

A. Frank and P. Seibert. Diagnose von extremerignissen aus großräumigen meteorologische feldern. endbericht zum project startclim. 4. In *Teil des Endberichts zum Projekt: Startproject Klimaschutz: Erste Analysen extremer Wetterereignisse und ihre Auswirkungen in Österreich*. Institut für Meteorologie, Univ. für Bodenkultur, Vienna, 2003.

C. Frei and C. Schär. A precipitation climatology of the alps from high-resolution rain-gauge observations. *Int. J. Climatol.*, 18:873–900, 1998.

C. Frei and C. Schär. Detection probability of trends in rare events: Theory and application to heavy precipitation in the alpine region. *J. Climate*, 14:1568–1584, 2001.

S. Frisia, A. Borsato, and R. Miorandi. page AQUAPAST Internal report, 2004.

H. E. Fuelberg, R. O. Loring, M. V. Watson, M. C. Sinha, K. E. Pickering, A. M. Thompson, G. W. Sachse, D. R. Blake, and M. R. Schoeberl. Trace a trajectory intercomparison. 2. isentropic and kinematic methods. *J. Geophys. Res.*, 101:23927–23939, 1996.

D. Genty, D. Blamart, R. Ouhadi, M. Gilmour, A. Baker, J. Jouzel, and S. V. Exeter. Greenland ice core chronologies constrained by dansgaard-oescher events preserved in a sw france stalagmite (32-83 ka). *Nature*, 421:833–837, 2003.

F. Gheusi and J. Stein. Lagrangian description of airflows using eulerian passive tracers. *Quart. J. Roy. Meteor. Soc.*, 128:337–360, 2002.

L. Giada and M. Marsili. Algorithms of maximum likelihood data clustering with applications. *Physica A*, 315:650–664, 2002.

J. S. A. Green, F. H. Ludlam, and J. F. R. McIlveen. Isentropic relative-flow analysis and the parcel theory. *Quart. J. Roy. Meteor. Soc.*, 92:210–219, 1966.

P. L. Haagenson, K. Gao, and Y. H. Kuo. Evaluation of meteorological analyses, simulations, and long range transport using anatex surface tracer data. *J. Appl. Meteor.*, 29:1268–1283, 1990.

P. L. Haagenson, Y. H. Kuo, M. Skumanich, and N. L. Seaman. Tracer verification of trajectory models. *J. Climate Appl. Meteor.*, 26:410–426, 1987.

J. Hansen, M. Sato, and R. Ruedy. Radiative forcing and climate response. *J. Geophys. Res.*, 102: 6831–6864, 1997.

J. M. Harris, P. P. Tans, E. J. Dlugokencky, K. A. Masarie, P. M. Lang, S. Whittlestone, and L. P. Steele. Variations in atmospheric methane at mauna loa observatory related to long-range transport. *J. Geophys. Res.*, 97:6003–6010, 1992.

T. W. Harrold. Mechanisms influencing the distribution of precipitation within baroclinic disturbances. *Quart. J. Roy. Meteor. Soc.*, 99:232–251, 1973.

P. Haynes and M. McIntyre. On the evolution of isentropic distributions of potential vorticity in the presence of diabatic heating and frictional or other forces. *J. Atmos. Sci.*, 44:828–841, 1987.

J. L. Heffter. Air resources laboratories atmospheric transport and dispersion models (arl-atad). page 17 pp. Boulder, Colorado, U.S.A., 1980.

R. G. Henderson and K. Weingartner. Trajectory analysis of map3s precipitation chemistry data at ithaca, new york. *Atm. Env.*, 16:1657–1665, 1982.

K. Hoinka, M. Hagen, H. Volkert, and D. Heimann. On the influence of the alps on a cold front. *Tellus*, 42 A:140–164, 1990.

B. J. Hoskins, I. Draghici, and H. C. Davies. A new look at the *w*-equation. *Quart. J. Roy. Meteor. Soc.*, 104:31–38, 1978.

B. J. Hoskins, M. E. McIntyre, and A. W. Robertson. On the use and significance of isentropic potential vorticity maps. *Quart. J. Roy. Meteor. Soc.*, 111:122–129, 1985.

ICCP. *Climate Change 2001: The scientific basis*. Cambridge University Press, Boston, 2001.

H. Iskenderian. A 10-year climatology of northern hemisphere tropical cloud plumes and their composite flow patterns. *J. Climate*, 8:1630–1637, 1995.

A. K. Jain, M. N. Murty, and F. J. Flynn. Data clustering: a review. In K. Bowyer and N. Ahuja, editors, *Advances in Image Understanding: A Festschrift for Azriel Rosenfeld*. IEEE Computer Society Press, 1996.

P. James, A. Stohl, C. Forster, S. Eckhart, P. Seibert, and A. Frank. A 15-year climatology of stratosphere-troposphere exchange with a lagrangian particle dispersion model: 2. mean climate and seasonal variability. *J. Geophys. Res.*, 108:8522, doi:10.1029/2002JD002639, 2003.

J. D. Kahl, J. M. Harris, G. A. Herbert, and M. P. Olson. Intercomparison of three long-range trajectory models applied to arctic haze. pages 175–185. Plenum Press, New York, 1989a.

J. D. Kahl, J. M. Harris, G. A. Herbert, and M. P. Olson. Intercomparison of three long-range trajectory models applied to arctic haze. *Tellus*, 41B:524–536, 1989b.

J. D. Kahl and P. J. Samson. Uncertainty in trajectory calculations due to low resolution meteorological data. *J. Climate Appl. Meteor.*, 25:1816–1831, 1986.

J. D. Kahl and P. J. Samson. Uncertainty in estimating boundary-layer transport during highly convective conditions. *J. Appl. Meteor.*, 27:1024–1035, 1988.

L. S. Kalkstein, G. Tan, and J. A. Skindlov. An evaluation of three clustering procedures for use in synoptic climatological classification. *J. Climate Appl. Meteor.*, 26:717–730, 1987.

C. Keil, H. Volkert, and D. Majewski. The oder flood in july 1997: Transport routes of precipitable water diagnosed with an operational forecast model. *Geophys. Res. Lett.*, 40 (2):235–238, 1999.

D. Keyser. On the representation and diagnosis of frontal circulations in two and three dimensions. volume I, pages 193–207. Bergen, Norway, 1994.

R. Kistler, E. Kalnay, W. Collins, S. Saha, G. White, J. Woollen, M. Chelliah, W. Ebisuzaki, M. Kanamitsu, V. Kousky, H. van den Dool, R. Jenne, and M. Fiorino. The ncep-ncar 50-year reanalysis: Monthly means cdrom and documentation. *Bull. Am. Meteorol. Soc.*, 82 (2): 247–267, 2001.

P. Knippertz, A. H. Fink, A. Reiner, and P. Speth. Three late summer/early autumn cases of tropical-extratropical interactions causing precipitation in northwest africa. *Mon. Wea. Rev.*, 131:116–135, 2002.

B. M. Knudsen and G. D. Carver. Accuracy of the isentropic trajectories calculated for the easoe campaign. *Geophys. Res. Lett.*, 21:1199–1202, 1994.

B. M. Knudsen, J. M. Rosen, N. T. Kjome, and A. T. Whitten. Comparison of analysed stratospheric temperatures and calculated trajectories with long-duration balloon data. *J. Geophys. Res.*, 101:19137–19145, 1996.

I. Kuhnel. Tropical-extratropical cloudbands climatology based on satellite data. *Int. J. Climatol.*, 9:441–463, 1989.

I. Kuhnel. Tropical-extratropical cloudbands in the australian region. *Int. J. Climatol.*, 10:341–364, 1990.

J. H. Kuo, M. Skumanich, P. L.Haagenson, and J. S. Chang. The accuracy of trajectory models as revealed by the observing system simulation experiments. *Mon. Wea. Rev.*, 113:1852–1867, 1985.

G. Lee and J. T. Merrill. Variations of free tropospheric nitrate at mauna loa observatory, hawaii. *J. Geophys. Res.*, 99:12821–12831, 1994.

G. Lee and J. T. Merrill. Origin of observed acidic-alkaline rains ina wet-only precipitation study in a mediterranean coastal site, patras, greece. *Atm. Env.*, 36:3089–3099, 2002.

C. J. Lin, M. D. Cheng, and W. H. Schroeder. Transport patterns and potential sources of total gaseous mercury measured in canadian high arctic in 1995. *Atm. Env.*, 35:1141–1154, 2001.

A. Longinelli and E. Selmo. Isotopic composition of precipitation in italy: a first overall map. *J. Hydrol.*, 270:75–88, 2003.

G. S. Lorimer. The kernel method for air quality modelling - i. mathematical foundation. *Atm. Env.*, 20:1447–1452, 1986.

R. H. Maryon and C. C. Heasmann. The accuracy of plume trajectories forecast using the u.k. meteorological office operational forecasting models and their sensitivity to calculation schemes. *Atm. Env.*, 22:259–272, 1988.

A. Massacand, A. Wernli, and H. Davies. Heavy precipitation on the alpine south side: An upper level precursor. *Geophys. Res. Lett.*, 25:1435–1438, 1998.

F. McDermott, D. Mattey, and C. Hawkesworth. Centennial-scale holocene climate variability revealed by a high-resolution speleotherm ó18o record from sw ireland. *Science*, 294:1328–1331, 2001.

J. P. McGuirk, A. H. Thompson, and N. R. Smith. Moisture bursts over the tropical pacific ocean. *Mon. Wea. Rev.*, 115:787–798, 1987.

J. T. McQueen and R. R. Draxler. Evaluation of model back trajectories of the kuwait oil fires smoke plume using digital satellite data. *Atm. Env.*, 28:2159–2174, 1994.

S. Medina and R. A. J. Houze. Air motions and precipitation growth in alpine storms. *Quart. J. Roy. Meteor. Soc.*, 129:341–344, 2003.

J. T. Merrill, R. Bleck, and D. Boundra. Techniques of lagrangian trajectory analysis in isentropic coordinates. *Mon. Wea. Rev.*, 114:571–581, 1986.

J. T. Merrill and J. L. Moody. Synoptic meteorology and transport during the north atlantic regional experiment (nare) intensive: Overview. *J. Geophys. Res.*, 101(28):903–921, 1996.

J. M. Miller. A five-year climatology of back trajectories from the mauna loa observatory. *Atm. Env.*, 15:1553–1558, 1981.

J. M. Miller. The use of back air trajectories in interpreting atmospheric chemistry data: a review and bibliography. NOAA Technical Memo. ERL ARL-155, Air Resources Laboratory, Silver Spring, Maryland, U.S.A, 1987.

J. L. Moody and J. N. Galloway. Quantifying the relationship between atmospheric transport and the chemical composition of precipitation on bermuda. *Tellus*, 40B:463–479, 1988.

J. L. Moody, A. Pszenny, A. Gaudry, W. C. Keene, J. N. Galloway, and G. Polian. Precipitation composition and its variability in the southern indian ocean: Amsterdam island, 1980-1987. *J. Geophys. Res.*, 96:769–786, 1991.

J. Namias. The use of isoentropic analysis in short term forecasting. *J. Aeronautic. Sci.*, 6:295–298, 1939.

R. E. Newell, N. E. Newell, Y. Zhu, and C. Scott. Tropospheric rivers? - a pilot study. *Geophys. Res. Lett.*, 12:2401–2404, 1992.

C. W. Newton and E. H. (Eds.). In *Extratropical cyclones - The Erik Palmen Memorial Volume*. American Meteorological Society, Boston, 1990.

K. C. Nguyen, J. A. noonan, I. E. Galbally, and W. L. Physick. Prediction of plume dispersion in complexterrain: Eulerian versus lagrangian models. *Atm. Env.*, 31:947–958, 1997.

K. Nodop, editor. *Constant volume balloon model used to derive tracer plume trajectories (ETEX experiment first release)*, 1997a. European Commission EUR 17346.

K. Nodop, editor. *Constant volume balloon model used to derive tracer plume trajectories (ETEX experiment second release)*, 1997b. European Commission EUR 17346.

I. Orlanski. A rational subdivision of scales for atmospheric processes. *Bull. Am. Meteorol. Soc.*, 56:527–530, 1975.

E. Palmén. On the dynamics of cold air outbreaks in the westerlies. University of Chicago, Dept. Meteorol., Off. Naval Res., 1953.

P. Perrson. Simulation of the potential vorticity structure and budget of fronts 87 iop8. *Quart. J. Roy. Meteor. Soc.*, 121 (525):1041–1081, 1995.

S. Petterssen. In *Weather Analysis and Forecasting*, pages 221–223. McGraw-Hill, New York, 1940.

K. E. Pickering, A. M. Thompson, D. P. McNamara, and M. R. Schoeberl. An intercomparison of isentropic trajctories over the south atlantic. *Mon. Wea. Rev.*, 122:864–879, 1994.

J. G. Pinto, M. Klawa, U. Ulbrich, R. Rudari, and P. Speth. Extreme precipitation events over northwest italy and their relationship with tropical-extratropical interactions over the atlantic. Baja Sardinia, Italy, 2001.

S. T. Rao, J. Pleim, and J. Czapaski. A comparative study of two trajectory models of long-range transport. *Journal of Air Pollution Control Association*, 33:32–41, 1983.

O. Reale, L. Feudale, and B. Turato. Evaporative moisture sources during a sequence of floods in the mediterranean region. *Geophys. Res. Lett.*, 28 (10):2085–2088, 2001.

J. Reiff, G. S. Forbes, F. T. M. Spieksma, and J. J. Reynders. African dust reaching northwestern europe: a case study to verify trajectory calculations. *J. Climate Appl. Meteor.*, 25:1543–1567, 1986.

H. Rodean. *Stochastic Lagrangian models of turbolent diffusion*, volume 26 (48). American Meteorological Society, Boston, USA, 1996.

G. D. Rolph and R. R. Draxler. Sensitivity of three-dimensional trajectories to the spatial and temporal densities of the wind field. *J. Appl. Meteor.*, 29:1043–1054, 1990.

A. M. Rossa. The impact of latent heat release on the dynamics of extratropical cyclogenesis. Phd-thesis, Institute for Atmospheric Science, ETH, Zuerich, 1995.

C. G. Rossby. Isentropic analysis. *Bull. Am. Meteorol. Soc.*, 18:201–209, 1937.

C. G. Rossby. The scientific basis of modern meteorology. In E. B. F. A. Berry and N. R. Beers, editors, *Handbook of meteorology*, pages 501–529. McGraw-Hill, 1945.

R. Rotunno and R. Ferretti. Mechanisms of intense alpine rainfall. *J. Atmos. Sci.*, 58:1732–1749, 2001.

R. Rotunno and R. Ferretti. Orographic effects on rainfall in map cases iop 2b and iop 8. *Quart. J. Roy. Meteor. Soc.*, 129 B:373–391, 2003.

F. Rubel and B. Rudolf. Global daily precipitation estimates proved over the european alps. *Meteorol. Z.*, 10:407–418, 2001.

F. Sanders and J. R. Gyakum. Synoptic-dynamic climatology of the 'bomb'. *Mon. Wea. Rev.*, 108: 1589–1606, 1980.

J. Schmidli, C. Schmutz, C. Frei, H. Wanner, and C. Schär. Mesoscale precipitation variability in the region of the european alps during the 20th century. *Int. J. Climatol.*, page In press, 2002.

C. Schär and H. Wernli. Structure and evolution of an isolated semi-geostrophic cyclone. *Quart. J. Roy. Meteor. Soc.*, 119:57–90, 1993.

P. Seibert. Convergence and accuracy of numerical methods for trajectory calculations. *J. Appl. Meteor.*, 32:558–566, 1993.

P. Seibert. Inverse dispersion modelling based on trajectory-derived source-receptor relationships. *Proceedings of the 22nd International Technical Meeting on Air Pollution Modelling and its Applications*, 1997.

P. Seibert, H. Kromp-Kolb, U. Baltensperger, D. T. Jost, and M. Schwikowski. Trajectory analysis of highalpine air pollution data. pages 595–96. Plenum Press, New York, 1994a.

P. Seibert, H. Kromp-Kolb, U. Baltensperger, D. T. Jost, M. Schwikowski, A. Kasper, and H. Puxbaum. Trajectory analysis of aerosol measurements at high alpine sites. pages 689–693. Academic Publishing, Den Haag, 1994b.

M. A. Shapiro and D. Keyser. Fronts, jet streams and the tropopause. extratropical cyclones, the erik palmén memorial volume. In C. Newton and E. O. Holopainen, editors, *Extratropical cyclones - The Erik Palmen Memorial Volume*, pages 167–191. American Meteorological Society, Boston, 1990.

W. N. Shaw. The meteorological aspects of the storm of february 26-27, 1903. *Quart. J. Roy. Meteor. Soc.*, 29:233–262, 1903.

W. N. Shaw and R. G. K. Lempfert. The life history of surface air currents. a study of the surface trajectories of moving air. volume 174. National Meteorological Library, Bracknell, 1906.

U. Stein and P. Alpert. Factor separation in numerical simulations. *J. Atmos. Sci.*, 50 (14):2107–2115, 1993.

A. Stohl. On the use of trajectories for establishing source-receptor relationships of air pollutants. University of Vienna, 1996.

A. Stohl. Computation, accuracy and applications of trajectories - a review and bibliography. *Atm. Env.*, 32 (6):947–966, 1998.

A. Stohl, O. R. Cooper, and P. James. A cautionary note on the use of meteorological analysis fields for quantifying atmospheric mixing. *J. Atmos. Sci.*, 61:1446–1453, 2004.

A. Stohl, L. Haimberger, M. P. Scheele, and H. Wernli. An intercomparison of results from three trajectory models. *Meteor. Appl.*, 8:127–135, 2001.

A. Stohl and P. James. A lagrangian analysis of the atmospheric branch of the global water cycle. part i: Method description, validation, and demonstration for the august 2002 flooding in central europe. *J. Hydrometeor.*, 5:656–678, 2004.

A. Stohl and P. Seibert. Accuracy of trajectories as determined from the conservation of meteorological tracers. *Quart. J. Roy. Meteor. Soc.*, 124:1465–1484, 1998.

A. Stohl and G. Wotawa. A method for computing single trajectories representing boundary layer transport. *Atm. Env.*, 29:3235–3239, 1995.

A. Stohl, G. Wotawa, P. Seibert, and H. Kromp-Kolb. Interpolation errors in wind fields as a function of spatial and temporal resolution and their impact on different types of kinematic trajectories. *J. Appl. Meteor.*, 34:2149–2165, 1995.

B. J. B. Stunder. An assessment of the quality of forecast trajectories. *J. Appl. Meteor.*, 35: 1319–1331, 1996.

D. J. Thomson. Criteria for the selection of stochastic models of particle trajectories in turbulent flows. *J. Fluid. Mech.*, 180:529–556, 1987.

S. Tibaldi, A. Buzzi, and A. Speranza. Orographic cyclogenesis. In C. Newton and E. O. Holopainen, editors, *Extratropical cyclones - The Erik Palmen Memorial Volume*, pages 107–127. American Meteorological Society, Boston, 1990.

B. Turato. Large scale forcing of intense localized precipitation events in the mediterranean basin. Ph.D. thesis, DIAM, University of Genoa, 2003.

L. W. Uccellini. Organization of clouds and precipitation in extratropical cyclones. In C. Newton and E. O. Holopainen, editors, *Extratropical cyclones - The Erik Palmen Memorial Volume*, pages 81–105. American Meteorological Society, Boston, 1990.

M. Uliasz. Lagrangian particle dispersion modeling in mesoscale applications. *Environmental Modeling*, II:71–101, 1994.

J. von Hardenberg, K. Fraedrich, F. Lunkeit, and A. Provenzale. Transient chaotic mixing during a baroclinic life cycle. *Chaos: An Interdisciplinary Journal of Nonlinear*, 10 (1):122–134, 2000.

J. M. Wallace and P. V. Hobbs. *Atmospheric science*. Academic Press, 1977.

J. L. Walmsley and J. Mailhot. On the numerical accuracy of trajectory models for long-range transport of atmospheric pollutants. *Atmos.-Ocean*, 21:14–39, 1983.

D. W. Waugh and R. A. Plumb. Contour advection with surgery: a technique for investigating Þnescale structures in tracer transport. *J. Atmos. Sci.*, 51:530–540, 1994.

H. Wernli. A lagrangian-based analysis of extratropical cyclones. ii: A detailed case study. *Quart. J. Roy. Meteor. Soc.*, 123:1677–1706, 1997.

H. Wernli and H. Davies. A lagrangian-based analysis of extratropical cyclones. i: The method and some applications. *Quart. J. Roy. Meteor. Soc.*, 123:467–489, 1997.

H. Wernli, S. Dirren, M. Liniger, and M. Zillig. Dynamical aspects of the life cycle of the winter storm "lothar". *Quart. J. Roy. Meteor. Soc.*, 128:405–429, 2002.

P. W. White, editor. *IFS documentation. ECMWF Tech. Rep.* 2002.

W. H. White, E. S. Macias, J. D. Kahl, P. J. Samson, J. V. Molenar, and W. C. Malm. On the potential of regional-scale emissions zoning as an air qality management tool for the grand canyon. *Atm. Env.*, 28:1035–1045, 1994.

J. D. Wilson and B. L. Sawford. Review of lagrangian stochastic models for trajectories in the turbulent atmosphere. *Bound. Layer Meteor.*, 78:191–210, 1996.

WMO. *Scientific Assessment of Ozone Depletion:1998. global Ozone research and Monitoring Project*. Geneva, Switzerland, 1999.

U. Wyputta and B. Grieger. Comparison of eastern atlantic atmospheric trajectories for present day and last glacial maximum. *Palaeogeography, Palaeoclimatology, Palaeoecology*, 146:53–66, 1999.

M. V. Young, G. A. Monk, and K. A. Browning. Interpretation of satellite imagery of a rapidly deepening cyclone. *Quart. J. Roy. Meteor. Soc.*, 113:1089–1115, 1987.

B. Ziv. A subtropical rainstorm associated witha tropical plume over africa and the middle-east. *Theor. Appl. Climatol.*, 69:91–102, 2001.